Employing nitrogen-vacancy centers in diamond for scanning probe microscopy from cryogenic to room temperature

Stefan Ernst - PhD thesis

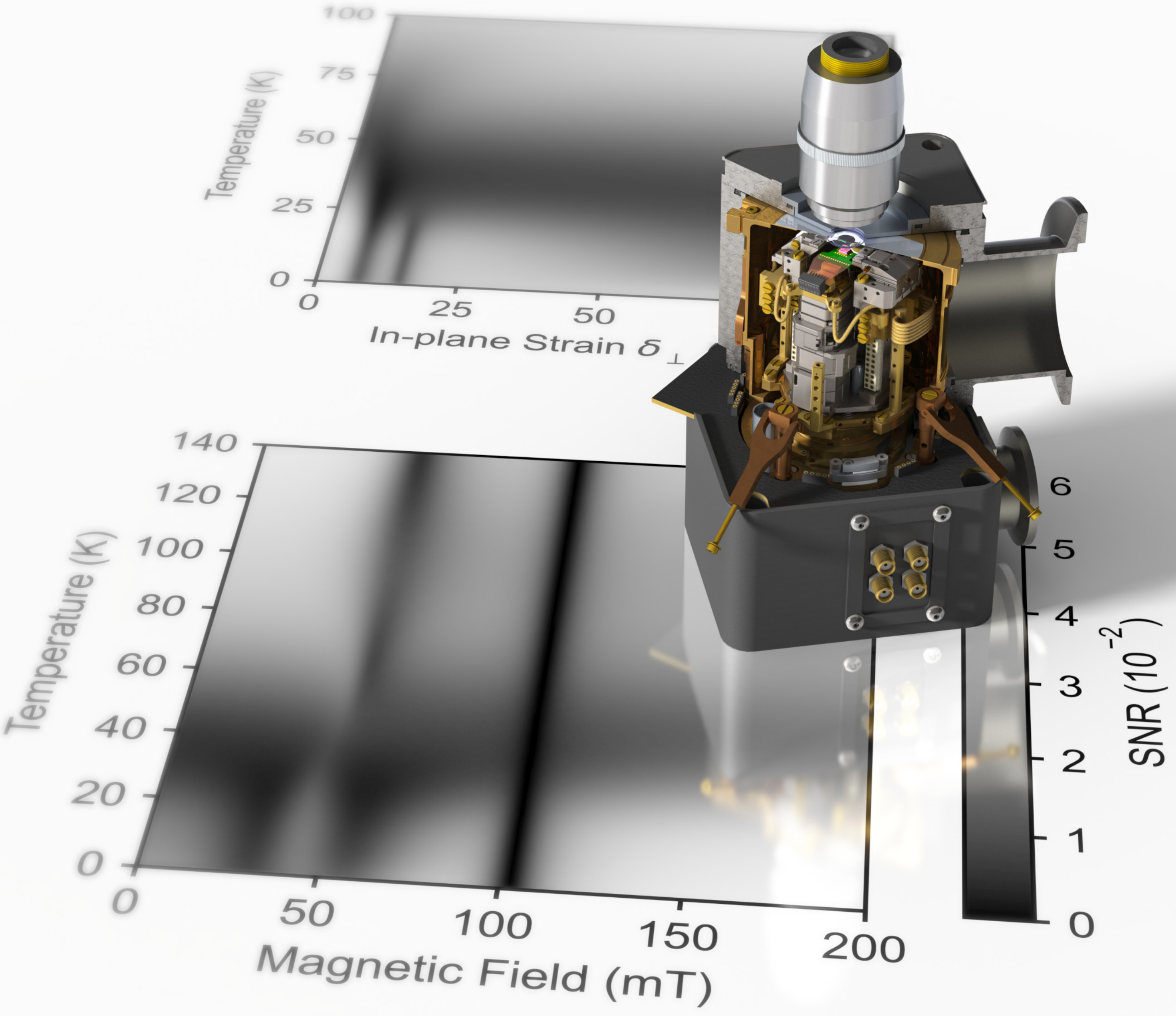
100
75
50
25
0
Temperature (K)
0
25
50
In-plane Strain δ ⊥
140
120
100
80
60
40
20
0
Temperature (K)
0
50
100
150
200
Magnetic Field (mT)
6
5
4
3
2
1
0
SNR (10^{-2})

ETH zürich

DISS. ETH NO. 30156

DISS. ETH NO. 30156

Employing nitrogen-vacancy centers in diamond for scanning probe microscopy from cryogenic to room temperature

A thesis submitted to attain the degree of
DOCTOR OF SCIENCES
(Dr. sc. ETH Zurich)

presented by

Stefan Ernst
M.Sc., Technische Universität München

born on 24.07.1991

accepted on the recommendation of
Prof. Dr. Christian L. Degen, examiner
Prof. Dr. Friedemann Reinhard, co-examiner

2024

Abstract

The negatively charged nitrogen-vacancy (NV^-) center is a crystal lattice defect in diamond. It exhibits a spin-1 ground state that is widely used in quantum metrology and quantum information. This prominence stems from its favorable spin and optical properties, which span a wide temperature range from zero to over 600 K. In the field of scanning probe microscopy, for example, the NV center is used as a quantum sensor that is raster-scanned in nanoscopic steps over a sample surface. This technique is versatile since it is applicable at all temperatures, and thus, a wide variety of samples and temperature-dependent phenomena can be studied. In this thesis, the engineering of such a variable-temperature (7 K to 350 K) scanning NV microscope is described. The base temperature of 7 K is achieved with a very compact cryostat design. The involved challenges in temperature management are addressed. Furthermore, a critical step in accomplishing uninterrupted operation was the design of an improved vacuum system, which avoids contamination aggregation on the sample surface under the scanning tip. Besides the experimental challenges, a fundamental lack of understanding impeded scanning NV experiments at variable temperature: despite the NV center's role in quantum applications, its photo-physics were incompletely understood, especially at intermediate temperatures between 10 K to 100 K where phonons become activated. This poses a key problem as the NV center's quantum state is initialized and read out via its photo-physical properties. Crucially, a prominent dip in the sensing performance is observed between 30 K to 60 K. The core subject of this thesis is to present a rate model that can describe the cross-over from the low-temperature to the high-temperature regime, including the dip at intermediate temperatures. Key to the model is a phonon-driven hopping between the two orbital branches in the electronic excited state, which causes a spin-lattice relaxation via an interplay with the spin precession. The model is extended to include magnetic and electric fields as well as crystal strain, allowing simulation of the population dynamics over a wide range of experimental conditions. The model recovers existing descriptions for the low- and high-temperature limits and successfully reproduces observations from previous literature. Additionally, a large and diverse set of data is used to deduce system parameters by fits with the model. Based on these parameters, the model allows for predicting various experimental observables relevant to quantum applications — in particular, the photoluminescence intensity, spin contrast, and spin initialization fidelity. The new understanding allows for probing of the electron-phonon interaction of the NV center and reveals a gap between the current understanding and recent experimental findings. Finally, with the required simulation tools at hand, improvements to the common optical initialization and readout scheme are found and compared with experiments. The model is made openly accessible as a Python library and can be used as a predictive tool for optimizing experimental conditions in NV center applications.

Zusammenfassung

Das negativ geladene Stickstoff-Fehlstellenzentrum (NV^-) ist ein Kristallgitterdefekt in Diamant. Es weist einen Spin-1 Grundzustand auf, und ist in der Quantenmetrologie und Quanteninformation weit verbreitet. Diese Bekanntheit ist bedingt durch seine günstigen Spin- und optischen Eigenschaften, die einen weiten Temperaturbereich von Null bis über 600 K umfassen. Im Bereich der Rastersondenmikroskopie, beispielsweise, wird das NV-Zentrum als Quantensensor verwendet, der in nanoskopischen Schritten über eine Probenoberfläche gerastert wird. Diese Technik ist vielseitig, da sie bei allen Temperaturen anwendbar ist und somit eine Vielzahl von Proben und temperaturabhängigen Phänomenen untersucht werden kann. In dieser Arbeit wird die Konstruktion eines solchen NV-Rastersondenmikroskops mit variabler Temperatur (7 K bis 350 K) beschrieben. Die Basistemperatur von 7 K wird mit einem sehr kompakten Kryostatdesign erreicht. Die damit verbundenen Herausforderungen im Temperaturmanagement werden besprochen. Ausserdem war ein entscheidender Schritt zur Erreichung eines unterbrechungsfreien Betriebs die Entwicklung eines verbesserten Vakuumsystems, welches die Bildung von Verunreinigungen unter der Rastersonde verhindert. Neben den experimentellen Anforderungen wurden NV-Rastersondenexperimente bei variabler Temperatur durch einen grundlegenden Mangel im Verständnis gebremst: trotz der Rolle des NV-Zentrums in Quantenanwendungen war seine Photophysik nur unvollständig verstanden, insbesondere bei mittleren Temperaturen von 10 K bis 100 K, wo Phononen aktiviert werden. Dies stellt ein zentrales Problem dar, da der Quantenzustand des NV-Zentrums über seine photophysikalischen Eigenschaften initialisiert und ausgelesen wird. Insbesondere wird zwischen 30 K und 60 K ein starker Einbruch in der Messleistung beobachtet. Das Kernthema dieser Arbeit ist die Vorstellung eines Ratenmodells, welches diesen Übergang vom Tieftemperatur- zum Hochtemperaturbereich, einschließlich des Einbruchs bei Zwischentemperaturen, beschreiben kann. Der Schlüssel zum Erfolg dieses Modells ist ein phononengetriebenes Hüpfen zwischen den beiden Orbitalzweigen im elektronisch angeregten Zustand, welches eine Spin-Gitter-Relaxation durch ein Zusammenspiel mit der Spin-Präzession erzeugt. Das Modell wird um magnetische und elektrische Felder, sowie Kristallspannung, erweitert, was die Simulation der Populationsdynamik über einen weiten Bereich an experimentellen Bedingungen ermöglicht. Das Modell geht korrekt in die bestehenden Beschreibungen für die Tief- und Hochtemperatur über, und reproduziert erfolgreich Beobachtungen aus früherer Literatur. Zusätzlich wird ein großer und vielfältiger Datensatz verwendet, um Systemparameter durch Ausgleichungsrechnung mit dem Modell abzuleiten. Auf der Basis dieser Parameter ermöglicht das Modell die Vorhersage verschiedener experimenteller Messgrößen, welche für Quantenanwendungen relevant sind – insbesondere die Photolumineszenzintensität, den Spin-Kontrast und die Spin-Initialisierungsfidelität. Das neue Verständnis ermöglicht es, die Elektron-Phonon-Wechselwirkung des NV-Zentrums zu untersuchen und zeigt eine Lücke zwischen dem derzeitigen Verständnis und den jüngsten experimentellen Ergebnissen auf. Zuletzt werden, danke der Verfügbarkeit des erforderlichen Simulationswerkzeugs, Verbesserungen in dem üblichen optischen Initialisierungs- und Ausleseschema gefunden und mit Experimenten verglichen. Das Modell wurde als Open-Access Python-Bibliothek zugänglich gemacht und kann als Vorhersageinstrument zur Optimierung der Versuchsbedingungen in Anwendungen mit NV-Zentren verwendet werden.

Acknowledgements

First, I want to thank my entire research group, the Spin Physics group at ETH Zurich, and my supervisor, Christian Degen, for providing such a pleasant working atmosphere. Everyone was always happy to help or share their expertise with great dedication, even without any direct profit. Also, I enjoyed the high level of freedom and the absence of unnecessary additional pressure. This created space to explore and find enduring solutions or new scientific projects. I believe that this was an essential ingredient for the work I will present in this thesis.

Second, I want to thank those with whom I worked closely on the projects during my doctoral studies. I want to thank Sebastián Guerrero and Luca Lorenzelli for the great teamwork on the setup, which we operated together. I also want to thank Patrick Scheidegger and Simon Diesch, my photo-physics project collaborators, for their endurance, amazing setup work, and countless fruitful discussions. Further, I am grateful for the motivation and excellent work that Tobias Hächler and Leo Šutevski provided during their semester projects on improved optical schemes for the NV center. Also, I want to thank Marcela Giraldo for her support in the $ErMnO_3$ *project and Marius Palm for his mentoring in the initial phase of the hydrodynamic transport project, as well as his continuous help on the setup. Further, I want to thank Francesco Poggiali and Dominik Irber from Friedemann Reinhard's group for our collaboration and discussions in the early phase of the photo-physics project. Lastly, I am pleased that Gregory D. Fuchs and Friedemann Reinhard gave me the chance to enter the exciting field of NV centers during my previous graduate studies.*

Third, I greatly appreciate numerous people's technological and scientific assistance throughout my doctoral studies. Here, I want to explicitly thank our technician Urs Grob, my office mates Pol Welter, William Huxter, and Nils Prumbaum, and the advice and exchange with Konstantin Herb, Jan Rhensius, Laura Alicia Voelker, Jonathan Zopes, and Erika Janitz. Further, I want to thank Andreas Stuker, Willy Staubli, and Kurt Jakob from our mechanical workshop – their work and expertise were essential to the setup improvements described in this thesis. Also, the technicians Peter Märki, Thomas Michlmayr, Martin Klöckner, and Robert Janz provided important support for the engineering of our cryostat.

Fourth, I am grateful to Christian Degen, Simon Diesch, Sebastián Guerrero, William Huxter, Erika Janitz, Friedemann Reinhard, Stephan Roschinski, Patrick Scheidegger, and Laura Alicia Voelker for their very helpful review of this thesis.

Finally, I want to thank the taxpayers and governments for believing in the importance of scientific progress, even if most steps are incremental and the outcome of projects is uncertain.

List of abbreviations

NV center	nitrogen-vacancy center in diamond
SPM	scanning probe microscope
AFM	atomic force microscope
MW	microwave
ODMR	optically-detected magnetic resonance
SNR	signal-to-noise ratio
PI(D) controler	proportional-integral(-derivative) controller
FWHM	full width at half maximum
IR	infra-red
CAD	computer-aided design
PCB	printed circuit board
(U)HV	(ultra-)high vacuum
NEG	non-evaporable getter
SMP	a radio-frequency wire connector type
D-sub	D-subminiature (an electrical connector type)
OFHC copper	oxygen-free high thermal conductivity copper
PTFE	polytetrafluoroethylene (a.k.a. Teflon™)
PEEK	polyether ether ketone
GS	electronic ground state of the NV$^-$center
SS	shelving state of the NV$^-$center (metastable singlet states)
ES	electronic excited state of the NV$^-$center
E_x/E_y	lower/upper-lying orbital branch of the ES
ISC	intersystem crossing from the ES to the SS
LAC	level-anti-crossing
ZPL	zero phonon line of the NV$^-$center
ZFS	zero field splitting of the spin states
PL	photoluminescence
RTN	random telegraph noise
NMR	nuclear magnetic resonance
HIMBI	a dilution refrigerator setup in our group
VarTMa	the variable-temperature setup re-engineered in this thesis
PWM	pulse-width-modulation

See Tab. 4.1 for an overview of essential parameter symboles.

Contents

Abstract iii

Zusammenfassung v

Acknowledgements vii

List of abbreviations ix

Contents xi

1 Introduction and outline 1

2 The NV center as a nano-scale sensor 3
- 2.1 Basics of the NV center . . . 3
- 2.2 Pulse sequence . . . 5
- 2.3 Performance characterization . . . 8
  - 2.3.1 Magnetic sensitivity . . . 8
  - 2.3.2 Signal-to-noise ratio . . . 9
  - 2.3.3 Approximation . . . 10
- 2.4 Temperature-dependent photo-physics . . . 10
- 2.5 Exemplary samples: multiferroic rare-earth manganites . . . 11

3 Design of a cryogenic scanning probe microscope 13
- 3.1 Design goals . . . 14
- 3.2 Components and choice of materials . . . 15
  - 3.2.1 4 K system . . . 15
  - 3.2.2 30 K system . . . 18
  - 3.2.3 Optical access . . . 19
- 3.3 Electrical design . . . 22
  - 3.3.1 Instrumentation . . . 22
  - 3.3.2 AFM distance control and tuning fork holder . . . 22
  - 3.3.3 Sample holder . . . 24

3.3.4 Choice of cables 25
3.3.5 Cable organization 26
3.4 Mechanical design 28
3.4.1 Microwave holder 28
3.4.2 Vibration isolation 29
3.4.3 Permanent magnet on stages 30
3.4.4 Expansion matching design 32
3.5 Temperature management 34
3.5.1 Welded joints 34
3.5.2 Bolted joints 35
3.5.3 Cooling braids 36
3.5.4 Wires 36
3.5.5 Radiation 37
3.5.6 Overall achieved improvement 39
3.6 Vacuum System 41
3.6.1 Motivation 41
3.6.2 Mitigating ice formation 42
3.6.3 Design 43
3.6.4 Achieved Improvement 46
3.7 Performance summary 49
3.8 Measurements on $ErMnO_3$ 49

4 Modeling temperature-dependent dynamics in the NV excited state 53

4.1 Need for a unifying model covering all temperatures 54
4.2 Rate model 55
4.2.1 Level structure 55
4.2.2 Transition rates under optical excitation 59
4.2.3 Phonon-induced transition rates 62
4.2.4 Lindblad master equation 63
4.2.5 Jump operators 64
4.2.6 Experimental observables 67
4.3 Phonon-induced orbital hopping 68
4.3.1 Fermi's Golden Rule 68
4.3.2 One-phonon process 69

4.3.3 Two-phonon process 71
4.3.4 Phonon wavelength considerations 74
4.4 Simulation of spin-lattice relaxation and orbital averaging 76
4.4.1 Temperature dependence 76
4.4.2 Comparison to phenomena in the field of NMR 79
4.4.3 Strain dependence 83
4.4.4 Magnetic field dependence 87
4.4.5 Combination of strain and magnetic field 90
4.4.6 Laser polarization and orbital branch selectivity 96
4.5 Classical rate models 97
4.5.1 Classical model at cryogenic temperature 97
4.5.2 Classical model at room temperature 100

5 Comparing measurements from literature with the model 103
5.1 Intersystem crossing rates at cryogenic temperatures 103
5.2 ES Strain dependence at room temperature 104
5.3 Probing electron-phonon interactions 107

6 Fitting model parameters to tailored measurements 111
6.1 Experiment overview 112
6.2 Measurement types 112
6.2.1 PL vs. B 114
6.2.2 Time-resolved pulsed ODMR 114
6.2.3 Saturation measurement 115
6.2.4 Shelving state lifetime 115
6.2.5 Laser characterization 117
6.3 Computational implementation of the models 118
6.4 Data evaluation 119
6.4.1 Overview 119
6.4.2 Calibration process 120
6.4.3 Implementation of data handling 121
6.4.4 Discussion of calibration results 123
6.5 Comparison of simulations with data 126
6.6 Further results 130

7 Examination of spin initialization and readout schemes 133

7.1 Laser power dependence of spin initialization and readout 134

7.1.1 Spin initialization fidelity 135

7.1.2 Spin readout fidelity 137

7.2 Implications of ES spin relaxation for other schemes 138

7.3 Improved spin initialization by a second laser power 139

7.4 Improved spin initialization by fast laser pulses 142

7.4.1 Optimization concept 142

7.4.2 Simulation results 144

7.4.3 Experimental results 147

7.4.4 Utilizing the improved scheme 151

8 Conclusion and Outlook 153

Bibliography 157

Curriculum vitae 169

CHAPTER 1

Introduction and outline

The negatively charged nitrogen-vacancy (NV^-) center in diamond has become one of the most studied solid-state spin defects [1] owing to its wide range of potential applications in quantum metrology [2] and quantum information [3]. Essential for its success is an extraordinarily long spin coherence time [4] in the electronic ground state combined with an optical initialization and readout of the spin state [5–9]. Importantly, both properties are maintained at cryogenic temperature (down to the millikelvin [10] regime), as well as at and above room temperature (up to around 700 K [11]).

Around room temperature, the NV center is commonly used for magnetic [12, 13] and electric [14] field sensing, as a temperature sensor [15, 16], as scanning near-field sensor [17, 18], and even for multi-qubit quantum information applications [19]. At temperatures below 20 K, resonant optical excitation [8] allows to use the NV center for quantum networks [20]. In the field of scanning NV magnetometry [21–23], which is the focus of the engineering part of this thesis, a large body of work has emerged since the first scans at room temperature [13, 24, 25]. In the last years, scanning NV setups have also been employed to investigate nanoscopic samples at cryogenic temperature [10, 26–31]. Recently, the interest in sample phenomena at intermediate temperatures, *i.e.* between cryogenic and room temperature, has also moved into focus. Examples intended to be studied with the setup built in this thesis are multiferroic order [32] (*e.g.* 80 K for $ErMnO_3$) or hydrodynamic current flow in graphene [33] (*e.g.* around 120 K). But at these intermediate temperatures, the photo-physics employed for initialization and readout of the NV center are not fully understood [34], impeding further progress.

This is a core topic of this thesis: it focuses on closing the gap in understanding the NV center's photo-physics, which existed between the two regimes, cryogenic and room temperature. Since these considerations are of a fundamental nature, their significance extends beyond scanning probe microscopy and is potentially even applicable to other solid-state spin defects. Recent experimental and theoretical work by our [35, 36] and other [37–39] research groups have addressed this topic, building on initial work by Rogers *et al.* [40], Fu *et al.* [41], and Fuchs *et al.* [42] on the dynamic Jahn-Teller effect in NV centers, which is responsible for the crossover between the two regimes. A rate model was developed in this thesis to simulate the photo-physics, and thus the performance of the NV center, over a large range of temperature, magnetic and electric fields, as well as crystal strain. A rich and unexpected dependence is found, with — most importantly — a significant drop in performance at around 35 K. The development of this rate model resulted in a publicly accessible GitHub Python library [43] to easily simulate the photo-physics of the NV center and plan experiments and expected performance accordingly.

The subject matter of this thesis is constructing a variable-temperature scanning NV microscope and understanding the performance of such an instrument. Beyond the theoretical work, a variable-temperature scanning NV magnetometer was developed further in this thesis. The initial setup [44] was re-engineered to access the full temperature range from cryogenic to room temperature and to allow for a reliable and fast turn-around operation. Following a brief general introduction to scanning NV magnetometry in Ch. 2, this engineering process is described in the first part of this thesis in Ch. 3. In the second part of this thesis, the above-mentioned theory and numerical model are explained in Ch. 4. Subsequently, the model is compared with and verified by previous experimental findings in Ch. 5 and our own tailored experiments in Ch. 6. Finally, improvements of the common initialization and readout schemes are examined in Ch. 7. The results obtained in this thesis are summarized in the last Ch. 8.

CHAPTER 2

The NV center as a nano-scale sensor

Parts of the text and figures in this chapter were published in Refs. [35, 36]. The contributions to this work are described at the beginning of chapter 4 and 6, which cover the model and data regarding the temperature-dependent photo-physics of the NV center.

In this chapter, the NV center is introduced as a scanning sensor for magnetic fields in Sec. 2.1. Then, a common pulse sequence to obtain a measurement result from the NV center is presented in Sec. 2.2. Based on this, Sec. 2.3 discusses how the performance of the NV center in the context of this thesis is characterized. Sec. 2.4 will create an initial overview of a core topic of this thesis: the temperature dependence of the NV center performance *e.g.* as a magnetic field sensor. Finally, Sec. 2.5 aims to illustrate the interest in a variable-temperature scanning NV microscope by presenting our current field of application: multiferroic rare-earth manganites. Early-stage measurements will be shown in Ch. 3.8 to present the successful engineering work.

2.1 Basics of the NV center

The lattice structure of the diamond crystal around the NV center is depicted in Fig. 2.1(a). The electronic structure of the NV^- center arises as an additional electron is captured from donors in the lattice. This electron, together with the three electrons from the nearest-neighbor carbon atoms and the two electrons from the nitrogen itself, form a spin-1-system [45, 46]. The coherent quantum state of this spin-1 system can be used [47, 48] as a qubit (a quantum bit for information purposes) or as a sensor. Due to its long coherence time of up to milliseconds [4], this quantum state degrades only slowly, allowing for logical operations or a sensing sequence within this time. Additionally, the energy level structure of the NV^- defect allows for preparation (“initialization”) and readout of this quantum spin state. It should be noted that the NV center can also occur in or switch to its neutral charge state NV^0, which is useless for our purposes. In this thesis, the neutral charge state is largely ignored, but the implications of its existence are discussed in cases where it becomes relevant.

To understand how the experimentalist in the macroscopic world can interface with the nanoscopic quantum state of the NV^- through simple illumination, we look at the level diagram in Fig. 2.1(b): Upon optical excitation from the ground state (GS), which is commonly done by a green laser, the excited electronic state (ES) decays

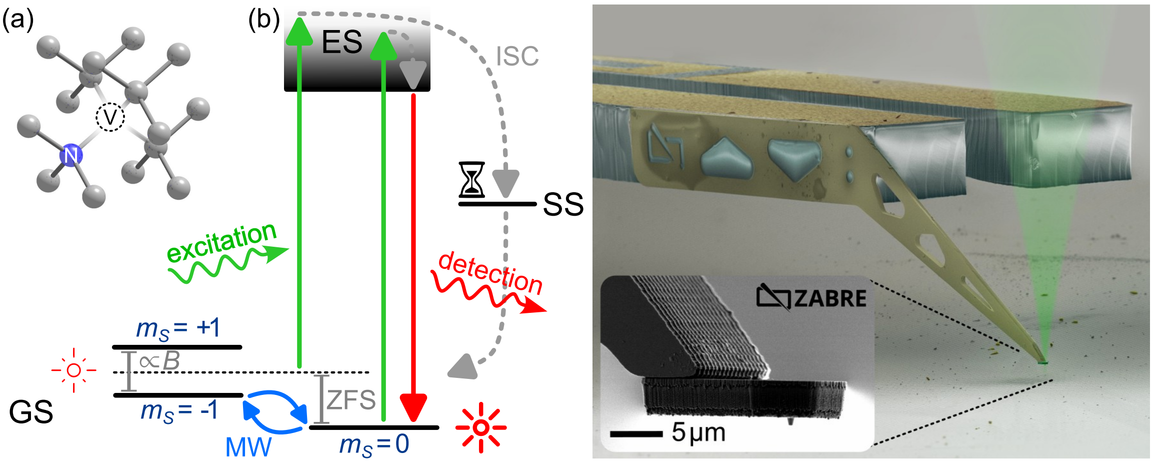

Figure 2.1: Basic functioning of the NV$^-$ center as a scanning sensor. (a) Lattice structure around the NV center, which is a point defect in the diamond crystal. Carbon atoms are gray, the nitrogen atom is blue, and the lattice vacancy is transparent. Picture property of C. Degen. (b) Schematic level diagram and functional principle of the NV center as a magnetic field sensor. A magnetic field causes a Zeeman splitting of the $m_S = \pm 1$ spin states. Coherent transitions between the quantum spin state can be made by microwave (MW) pulses. The ground state (GS) can be excited by *e.g.* a green laser. Decay of the excited state (ES, depicted with phonon sideband) can occur by the emission of a red photon or via an intersystem crossing (ISC) to the long-lived (hourglass symbol) shelving state (SS). This transition is simplified here for clarity [1]. The ISC is spin selective, favoring decay out of $m_S = \pm 1$, and rendering the $0/\pm 1$ spin state bright/dark under continuous excitation (indicated by sun symbols). A more complete picture of the photo-physics will be given later in Fig. 4.2(d). (c) Electron micrograph of a scanning NV tip for a scanning probe microscope (SPM). The NV center is located in the tip of the diamond pedal, which is glued to a silicon cantilever that is attached to a tuning fork (millimeter-sized). A local field measurement can be performed once the tip is brought into a soft contact with the sample surface. For this, the NV center is excited with a focused green laser (cone outline), and its photoluminescence (PL) is observed with a confocal microscope. Picture property of QZabre LLC.

either radiatively by emission of a photon or non-radiatively (at least within the visible range) via an intersystem crossing (ISC) to a metastable singlet state [1] — also called the shelving state (SS). The optical decay gives rise to a photoluminescence (PL) intensity, which is in the visible red to near infra-red (IR) wavelength range. Since the excitation is typically done off-resonantly with green light, a dichroic mirror is used to separate the optical excitation and collection path. An ES spin state with $m_S = 0$ will dominantly decay by the emission of a red photon (on the order of ten nanoseconds). Mostly, it will not take the path via the SS and thus maintain its m_S value. A spin state $m_S = \pm 1$, on the other hand, is likely to decay non-radiatively via the SS. This is a comparably slow process due to the long lifetime of the SS (on the order of a hundred nanoseconds). Thus, the spin selectivity of the ISC process leads to the generation of a spin contrast C in the PL intensity. The selectivity further leads to a preferential population of the $m_S = 0$ spin state after prolonged optical excitation, which is used to initialize the spin state.

The spin state of the NV$^-$ can be used as a sensor. The fundamental idea here is that the eigenstates of the spin system change with external parameters. Coherent control of the spin state by microwaves (MW) allows to investigate the eigenstates or, more precisely, their transition energies. By quantitative knowledge of the coupling to an external parameter, the values of the transition energies can be used for a calibration-free, quantitative measurement of the external parameter. Today, measuring magnetic fields is the most common use case for the NV center as a sensor. If a magnetic bias field B_0 is applied along the N-V-axis, the projection of a small additional field ΔB onto the N-V-axis can be measured by the Zeeman effect as a change in the GS eigenenergies ΔE as [1]

$$\Delta E/h = \frac{\mu_\mathrm{B} g_\mathrm{GS}}{h} \cdot \Delta B = 28.03\,\mathrm{MHz\,mT^{-1}} \cdot \Delta B\,, \tag{2.1}$$

where μ_B is the Bohr magneton, h is the Planck constant, and g_GS the electronic g-factor. The Zeeman splitting of the $m_\mathrm{S} = \pm 1$ levels is sketched in Fig. 2.1(b).

Apart from being a sensitive magnetometer, the NV center has another feature as a sensor: its atomic size. Used in a scanning probe microscope (SPM), this atomic size can be employed to achieve images with nanometer resolution. A visual impression of this is given in Fig. 2.1(c): The NV center is located at the apex of a diamond tip, in a depth of only on the order of 10 nm. It is softly engaged on a sample mounted on a piezo stage. Since piezo crystals enable us to do nanometer-sized steps, an image with a resolution of the standoff distance of the NV center from the sample surface can be recorded pixel by pixel. Scanning NV magnetometry achieves field resolutions down to 5 nT (for AC fields) at around 50 nm to 100 nm spatial resolution [49].

2.2 Pulse sequence

We will now look in more detail at a very common sensing scheme and understand how it is used to measure the DC magnetic field at the atomic-size position of the NV center. This scheme is called “pulsed optically detected magnetic resonance” (pulsed ODMR) and will serve us as a representative for all kinds of sensing schemes [50].

The pulse sequence of an ODMR measurement is depicted in Fig. 2.2(a):

First, the spin state is initialized by a green laser pulse of duration t_LaserOn, followed by a waiting time $t_\mathrm{LaserWait}$ much longer than the SS lifetime τ_S. After $t_\mathrm{LaserWait}$, all populations of the levels in Fig. 2.1(b) have decayed to the GS. The resulting spin state is defined as the $m_\mathrm{S} = 0$ initialized state. Note that due to a small chance of the excited $m_\mathrm{S} = 0$ state also decaying to the SS, the $m_\mathrm{S} = 0$ initialized state is a classical mixture of dominantly quantum spin state $|0\rangle$ and minor $|\pm 1\rangle$ population. Thus, the spin state $m_\mathrm{S} = 0$ expectation value is $\langle m_\mathrm{S} = 0\rangle \approx 0.7 < 1$ in Fig. 2.2(a) at $t \approx 2\,\mu\mathrm{s}$. We will refer to $\langle m_\mathrm{S} = 0\rangle$ as the total probability of $m_\mathrm{S} = 0$ in the NV$^-$ system, *i.e.* the sum of the GS and ES, and use it as the spin initialization fidelity.

Second, a microwave pulse with a certain frequency f is applied. We will assume, at first, that the energy $E = hf$ of the photons in this microwave pulse is resonant to the level spacing between the $m_\mathrm{S} = 0$ and the $m_\mathrm{S} = -1$ (or $m_\mathrm{S} = +1$) levels. This allows for a quantum gate called “π-pulse”, which swaps the population of the two levels. We therefore obtain the $m_\mathrm{S} = -1$ (or $+1$) initialized state.

Finally, a second laser pulse is applied, and the PL of the $m_\mathrm{S} = 0$ ($m_\mathrm{S} = \pm 1$) initialized state is integrated over a certain integration time t_int to obtain the average $\mathrm{PL}_{m_\mathrm{S}=0}$ ($\mathrm{PL}_{m_\mathrm{S}=\pm 1}$) count rate. The spin contrast C (normalized blue shaded area in Fig. 2.2(a)) is then defined by

$$C = 1 - \frac{\mathrm{PL}_{m_\mathrm{S}=\pm 1}}{\mathrm{PL}_{m_\mathrm{S}=0}}\,. \tag{2.2}$$

If the frequency f of the microwave pulse was not in resonance with the level spacing, no state swap would occur, and we would not see a drop in the PL during t_int. In Fig. 2.2(b), a sweep of f is plotted. At the resonances

$$f_\pm = D_\mathrm{GS}(T) \pm 28.03\,\mathrm{MHz\,mT^{-1}} \cdot (B_0 + \Delta B)\,, \tag{2.3}$$

the PL shows a drop and reveals the strength of the magnetic field ($B_0 + \Delta B$) along the N-V-axis [5]. Since this equation follows from Eq. 2.1, the same assumptions as made there account here. In Eq. 2.3, the $D_\mathrm{GS}(T)$ is the temperature-dependent zero field splitting (ZFS) [16, 51, 52], for which the heuristic polynomial expression from Ref. [51] is used in this thesis.

In Fig. 2.2(b), each resonance $f_\pm$ has an additional hyperfine structure with a splitting of 3.05 MHz [53], which arises from the interaction with the nuclear spin state of the implanted ^{15}N isotope of the NV center. The fact that both hyperfine resonances can be observed means that during the averaging duration of the experiment, both nuclear spin states are populated. To increase the contrast and thus improve the readout in magnetometry scans, we sweep a pair of microwave frequencies at f and $f + 3.1\,\mathrm{MHz}$. This “two-tone drive” will result in three dips per resonance $f_\pm$: two satellite dips with the former contrast and a central dip at $f_\pm$ with up to double the former contrast [54, 55]. An alternative option is to polarize the nuclear spin, as addressed further in Ch. 6.6.

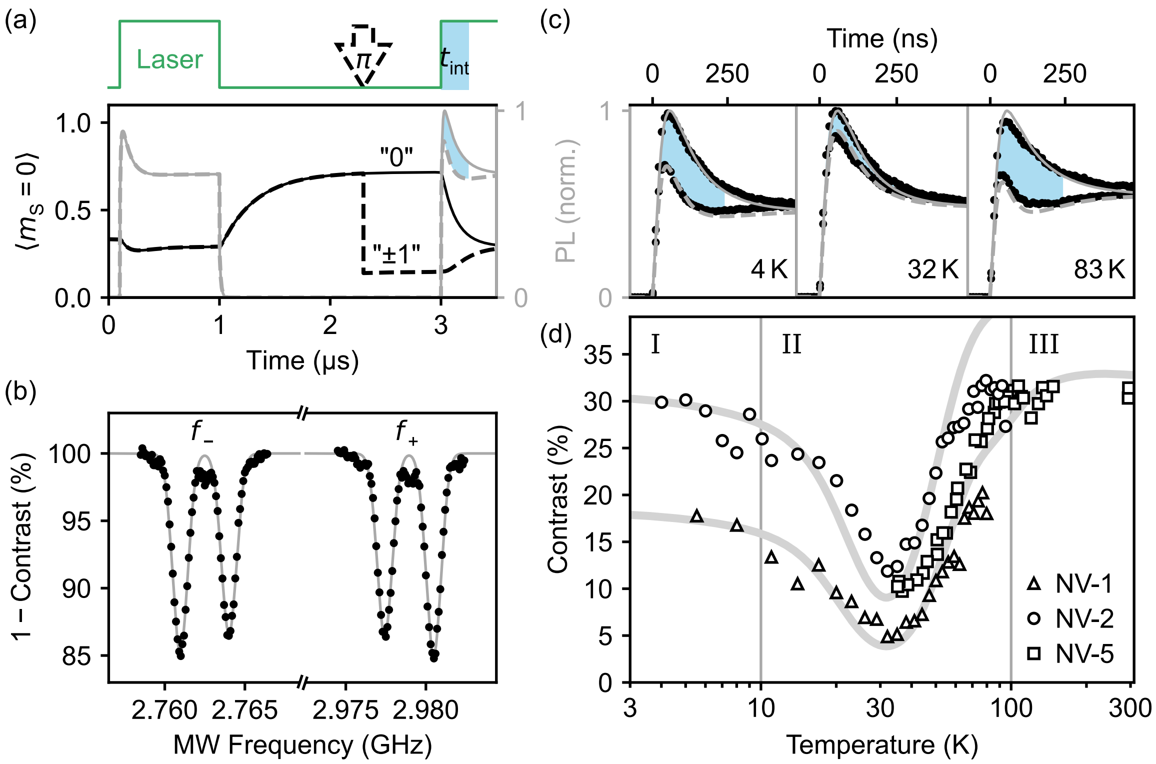

Figure 2.2: Pulsed optically-detected magnetic resonance (ODMR). (a, top) Pulse sequence of an ODMR measurement. (a, bottom) Simulation of the expectation value $\langle m_S = 0 \rangle$ (sum of GS and ES, black) and PL(t) (gray) during the sequence from above. We start in a thermal state and obtain the spin state defined as the $m_S = 0$ initialized state (solid traces) by a laser pulse of duration t_{LaserOn}, followed by a waiting time $t_{\text{LaserWait}}$. The state defined as the $m_S = \pm 1$ initialized state (dashed traces) is obtained by an additional π-pulse (MW pulse at the spin resonance frequency $f_\pm$). In a second laser pulse, the integration time t_{int} for the spin-state readout is marked by the blue shaded area. The spin contrast C is given by the relative difference between the two curves (blue shading). For simplicity, the duration of the MW pulse is plotted instantaneously. Generally, the time after $t_{\text{LaserWait}}$ is t_{sens}. Parameters as later given in Tab. 4.1 are used for the simulation ($T = 0\,\text{K}$). (b) Pulsed ODMR spectrum with hyperfine resolution of the ^{15}N coupling. Data recorded with NV-5 at 294 K (also used in part (d), right), averaged for 6.7 min. The deviation from the Gaussian fit arises from the MW square pulse, which gives the ODMR spectrum the shape of a sinc function convoluted with the Gaussian spin resonances. (c) Stacked ODMR time traces (as in part (a), right), measured on NV-2 at low, intermediate, and high temperatures. The gray traces are fits to the PL dynamics (see Ch. 6). (d) Spin contrast versus temperature for three NV centers. Three distinct regimes (I–III) can be identified, roughly corresponding to the respective selected measurements presented in part (c). In regime (II), *i.e.* at intermediate temperatures, an unexpected drastic reduction in the contrast is observed. Solid traces show corresponding simulations for NV-1 and NV-2 (see Ch. 6). For NV-5, the contrast of the two hyperfine resonances as shown in part (b) are added up.

2.3 Performance characterization

This thesis aims to quantitatively compare the performance of the NV^- center over a vast range of parameters. To that end, defining a quantity that describes the performance is necessary. Motivated by the case of scanning NV magnetometry, the magnetic sensitivity s could be used as a measure of NV performance. In Sec. 2.3.1, we will first derive this magnetic sensitivity for the pulsed ODMR scheme to gain an intuitive picture of the NV performance in a sensing task. However, the findings discussed in this thesis extend beyond the field of scanning NV microscopy and are directly applicable to NV center experiments in general. Therefore, we will define the generalized signal-to-noise ratio (SNR) in Sec. 2.3.2. This definition of the SNR will later be used as a measure of the NV performance. Finally, in Sec. 2.3.3, we will give an intuitive approximation for the role of the spin contrast C and the PL in the sensitivity s and the SNR.

For the scope of this thesis, the NV performance will be viewed from the perspective of photo-physics. As we will see below, another critical parameter for the sensitivity (or quantum information tasks) is the coherence time. Also, for sensing applications, NV^- charge state stability is often an important parameter. This thesis will not address the dependence of these two parameters on various experimental conditions. Probably the most influential factor to name for these two parameters is the immediate environment around the NV center — like the diamond surface [56–58].

2.3.1 Magnetic sensitivity

We now use the pulsed ODMR scheme introduced above to derive an equation for the magnetic sensitivity. Before we can do so, we need to address the shape of the dips in the ODMR spectrum. This shape is given by the Fourier transform of the microwave pulse convoluted with the intrinsic shape of the resonance [59] (Gaussian in the case of inhomogeneous broadening). Assuming a short square pulse, the shape will thus be a sinc function [60]. A longer π-pulse, which has lower power, gives a smaller width of the since function until the inherent Gaussian linewidth of the resonance dominates. The latter is determined by its spin coherence time T_2 (often called $T_2^\star$ to differentiate from a slower dephasing under dynamical decoupling). Since a smaller width of the ODMR dips gives better sensitivity, as we will see next, one should ideally choose the length of the microwave pulses to be about T_2 [60].

We now derive the sensitivity of a pulsed ODMR experiment to measure the magnetic field component along the NV axis [60]. The magnetic sensitivity

$$s = \Delta B_{\mathrm{min}} \sqrt{t} \tag{2.4}$$

is defined by the minimal magnetic field change ΔB_{min}, which can be measured within time t. Note that increasing the averaging time t improves $\Delta B_{\mathrm{min}} \propto 1/\sqrt{t}$ (*i.e.* reduces it), while s is constant. Ideally, the microwave frequency f dependent photon counts $\mathcal{S}(f)$ have the shape of a Gaussian (*cf.* one dip in Fig. 2.2(b)) with

$$\mathcal{S}(f) = \left[1 - e^{-4\ln(2)(f-f_0)^2/\nu^2}\right] \mathcal{S}_{m_\mathrm{S}\,=\,0}\,, \tag{2.5}$$

where f_0 is the resonance frequency at which a π-pulse between two levels can happen, and ν is the full-width at half maximum (FWHM) of the Gaussian (and related to the inverse spin coherence time $T_2 \propto \nu^{-1}$ [60]). The $\mathcal{S}(f)$ ($\mathcal{S}_{m_\mathrm{S}\,=\,0}$) are the total collected counts that fall into the integration window t_int with (without) a microwave pulse applied before the second laser pulse (see Fig. 2.2(a)). Since f_0 shifts with the magnetic field as $\Delta B = \Delta f\, 2\pi/\gamma = \Delta f/28.025\,\mathrm{MHz\,mT^{-1}}$, the best sensitivity (*i.e.* smallest s) is achieved at the frequency f_s of the highest slope of $\mathcal{S}(f)$. At this frequency, a pulsed ODMR experiment is performed, repetitively consisting of a π-pulse and a subsequent laser pulse for readout and re-initialization. Assuming a shot noise $\Delta\mathcal{S} = \sqrt{\mathcal{S}}$ limited readout at f_s, the slope of Eq. 2.5 at f_s can be used to translate $\Delta\mathcal{S}$ to Δf and finally to ΔB in Eq. 2.4. One then finds for the sensitivity

$$s = \frac{2\pi}{\gamma} m_G^{-1} \frac{\nu\sqrt{r}}{C\sqrt{\mathrm{PL}_{m_\mathrm{S}\,=\,0}}\sqrt{\mathrm{DC}}}\,. \tag{2.6}$$

Due to the Gaussian shape, the slope factor $m_G^{-1} = 0.700$ and $r = r_G = 1 - 0.607\,C$ [60]. Further, $\mathrm{PL}_{m_\mathrm{S}\,=\,0} = \mathcal{S}_{m_\mathrm{S}\,=\,0}/(t_\mathrm{int} N_\mathrm{seq})$ is the average PL count rate during t_int, with $N_\mathrm{seq} = t/T_\mathrm{seq}$ the number of repetitions of the pulsed ODMR sequence of duration

$$T_\mathrm{seq} = t_\mathrm{LaserOn} + t_\mathrm{LaserWait} + t_\mathrm{sens} \tag{2.7}$$

and the time intervals as given in Fig. 2.2(a). Finally, the readout duty cycle $\mathrm{DC} = t_\mathrm{int}/T_\mathrm{seq}$ and the spin contrast $C = 1 - \mathcal{S}(f_0)/\mathcal{S}_{m_\mathrm{S}\,=\,0}$ as in Eq. 2.2.

2.3.2 Signal-to-noise ratio

Next, we will view the readout of the spin state in a generalized and ideal scheme as in Ref. [61]. For this, we consider the SNR of a single initialization and readout cycle

$$\mathrm{SNR} = \sqrt{\mathrm{PL}_{m_\mathrm{S}=0}\, t_\mathrm{int}} \frac{C}{\sqrt{2-C}}\,. \tag{2.8}$$

This is equivalent to our finding in Eq. 2.6 for $r = 1 - 0.5\,C$. Up to constants and the coherence time T_2, one thus finds

$$s \propto \mathrm{SNR}^{-1}\sqrt{T_\mathrm{seq}}\,. \tag{2.9}$$

Note that a single sequence repetition gives on average only $\mathcal{S}_{m_\mathrm{S}\,=\,0} = \mathrm{PL}_{m_\mathrm{S}=0}\, t_\mathrm{int} = 0.06$ collected counts with an integration time of $t_\mathrm{int} = 300\,\mathrm{ns}$ at a count rate of $\mathrm{PL}_{m_\mathrm{S}\,=\,0} = 200\,\mathrm{kcps}$. With Eq. 2.8, SNR values of only around 5×10^{-2} result, as often seen in plots in this thesis. To obtain histograms like the ones presented in Fig. 2.2(c), the sequence has to be repeated many times N_seq until a reasonable integrated SNR is obtained.

2.3.3 Approximation

For a more intuitive picture, we can compare Eq. 2.6 and 2.8 and find that the inverse sensitivity is proportional to the SNR and approximately

$$s^{-1} \propto \mathrm{SNR} \approx C\sqrt{\mathrm{PL}_{\mathrm{inf}}}\,, \tag{2.10}$$

with the common observables spin contrast C and steady-state PL (just here called $\mathrm{PL}_{\mathrm{inf}}$ for clarity) used throughout this thesis. The steady-state PL is reached in Fig. 2.2(a) between roughly 0.5 µs to 1 µs. Importantly, both C and PL enter into s and the SNR and can, therefore, not be used separately for a complete characterization of the NV performance. We also note that the quality of spin initialization, as well as the spin readout, enter into s and the SNR.

2.4 Temperature-dependent photo-physics

Above, we saw that coherent operations on the spin states of the GS are essential for using the NV^- for sensing. The same accounts for applications in quantum information — the π-pulse discussed above, for instance, is a logical NOT gate. But not only the outstanding coherence time $T_2 \propto \nu^{-1}$ of the GS and the ability to apply quantum gates with high fidelity are relevant in NV center applications. The DiVincenzo criteria [62] prominently outline that the ability to initialize the quantum state as well as reading it out after some operations is equally essential. Here, the ES and the optical cycle come into play, as described above. Importantly, a fast spin-state relaxation in the ES can impair the ability to initialize by laser illumination. And if the spin state relaxes faster than a spin contrast in the PL can build up, the readout is also compromised. In this thesis, such a strong spin-state relaxation in the ES will be identified in the intermediate temperature regime. As a teaser for the theoretical (Ch. 4) and experimental (Ch. 6) findings, Fig. 2.2(c,d) shows how the spin contrast exhibits a severe dip around 35 K in the temperature regime (II), and better performance is found in the room temperature regime (III) compared to the cryogenic regime (I). In Fig. 2.2(c), the same pulse sequence as in Fig. 2.2(a) is measured and simulated at different temperatures. The deduced contrast values are plotted in Fig. 2.2(d) for different NV centers. An understanding of the origin of this spin relaxation will be developed in the second part of this thesis, which allows us to discuss ways to mitigate it.

The reduction from $C \approx 30\,\%$ to $C \approx 10\,\%$ of NV-5 in Fig. 2.2(d) means a nine-fold increase in measurement time for the same minimal detectable magnetic field according to Eq. 2.4 and 2.10, and the dip is also present in the PL (not shown in Fig. 2.2). Imaging the local magnetic fields on the surface of samples is currently the most common task of a scanning NV microscope. Hence, the temperature dependence of the NV photo-physics are of great importance for such an instrument. For this reason, we will closely examine the temperature dependence of PL and C in the second part of this thesis. But these findings are relevant not only to NV centers employed in SPM but also to the entire field of NV centers.

2.5 Exemplary samples: multiferroic rare-earth manganites

One of the systems we are exploring with our variable-temperature scanning NV magnetometer is the multiferroic order on the surface of rare-earth hexagonal manganites [63]. Here, we aim to resolve different magnetic and electric domain wall types at their inherent length scale — the nano-scale — and to monitor their evolution with temperature. The goal is to improve the understanding of the coupling between them. This section will briefly motivate the investigation of multiferroic order.

In recent years, the discovery and investigation of new thin-film materials has boosted research in the field of multiferroics again [64]. As formerly, electric control of the magnetic state is of huge technological interest. The two most prominent examples to name here are direct electrical reading and writing of magnetic bits and non-volatile four-state memories, which use both, magnetic and electric states, to store information. The former, for instance, promises smaller, faster, and more energy-efficient memory devices. Thin-film multiferroics are especially well suited as the electric order can be switched at feasibly low voltages. And stacked in heterostructures, interface and layer design allows for novel behavior. Beyond a mere technological interest, the physics behind the coupling of magnetic and electric domains in these novel multiferroic systems are under investigation. In so-called "type I" multiferroics, the electric and magnetic order have separate phase transitions. However, observed tendencies for overlapping domain walls hint towards a form of system-specific coupling.

We are investigating the bulk surface of the rare-earth hexagonal manganites like $ErMnO_3$ [65]. Below a transition temperature of $\sim 1430\,\mathrm{K}$, they form structural domains. The lattice distortions of this trimerization lead to a net electric polarization ($\sim 6\,\mathrm{\mu C\,cm^{-2}}$), causing ferroelectric and structural domain walls to coincide [66]. Remarkably, the ferroelectric domain pattern was found to be organized in cloverleaf-like vortices [67]. Below the Néel temperature of $\sim 80\,\mathrm{K}$, the Mn^{3+} spins undergo a phase transition from paramagnetic to antiferromagnetic order, rendering rare-earth hexagonal manganites multiferroic. Surprisingly, the ferroelectric domain walls were found to (mostly) coincide with antiferromagnetic ones [68].

Conventionally, second harmonic generation microscopy is used to image both the electric and magnetic order. But being a far-field optical technique, it suffers from low resolution [65]. Electron microscopy and piezoelectric force microscopy are used to image the electric and structural domains only. On field-cooled $ErMnO_3$, Geng *et al.* [32] used magnetic force microscopy (not quantitative) and resolved a net magnetic moment at ferroelectric domain walls. They attributed their signal dominantly to Er^{3+} spins, which couple by Dzyaloshinskii-Moriya interactions to the Mn^{3+} spins [69]. However, as discussed in Ch. 3.8, our first quantitative magnetometry scans on $ErMnO_3$ seem to match the theoretical prediction for the magnetic moment of slightly canting [70] Mn^{3+} spins in the A_2 symmetric phase alone. A scanning NV center is a uniquely suited tool for further investigations here, given its non-invasiveness, functionality from cryogenic to room temperature, high spatial resolution, and capability for multi-modal and quantitative imaging of both the magnetic and electric fields. By sweeping the temperature across the antiferromagnetic ordering, we hope to watch the pinning process of magnetic to electric domain walls. This is of particular interest as a few of the antiferromagnetic domain walls do not show pinning to the ferroelectric ones and relocate with every cooldown through the Néel temperature [65]. At room temperature, our research group has already demonstrated the ability to image the ferroelectric domains on $YMnO_3$ with scanning NV electrometry [71].

CHAPTER 3

Design of a cryogenic scanning probe microscope

A previous version of this setup was described by Lorenzelli [44]. I joined Luca Lorenzelli on the setup. Together, we achieved the first cryogenic magnetometry scans presented in Ref. [44] and Fig. 3.16(a). However, several problems existed with the setup that continuously disrupted the measurements. I re-designed several parts of the setup. This chapter describes this process and its results. In this process, the exchange with and great work done by the ETH D-PHYS mechanical workshop was essential. In particular, the work with Willy Staubli on the PEEK parts, Kurt Jakob on the welding, and Andreas Stuker on multiple design aspects is to be emphasized here. Our group's technician, Urs Grob, helped in many aspects of the process and made the main contribution to the design of the radiation shield. Further, other technicians at the D-PHYS department of ETH provided important input for the mechanical and electrical design: Peter Märki, Thomas Michlmayr, and Martin Klöckner. Finally, Robert Janz from Quantum Design GmbH (representing our cryostat manufacturer Montana Instruments®) repeatedly provided crucial support throughout the process. For the assembly of the new design, Sebastián Guerrero joined me on the setup. We worked together on the vacuum, mechanical, and thermal aspects, but in particular on the wiring, the last update of the mechanical excitation design for the AFM control (see Sec. 3.3.2 second paragraph), and restoring an operational state after the upgrade, Sebastián Guerrero made the main contributions. The setup's optics were initially built by Luca Lorenzelli and later improved by Sebastián Guerrero. Large parts of the control hardware and software used in the setup are also found in other setups in our group. On the software side, the main part of this work was done by Pol Welter [72]. On the electronic hardware side, three main contributors to this setup were Kevin Chang, Marius Palm, and Pol Welter. The measurements on $ErMnO_3$ presented in Fig. 3.16(a) were recorded by Lorenzelli [44]. Together, we planned and conducted the experimental work contained in Ref. [44]. I re-evaluated the data for the purpose of this thesis. The project was supported and suggested by Marcela Giraldo, Thomas Lottermoser, and Manfred Fiebig from the Laboratory for Multifunctional Ferroic Materials at ETH Zurich. Their group provided the $ErMnO_3$ sample, which stems from a single-crystalline rod (#1290) grown by the high-pressure floating-zone technique by Edith Bourret at the Lawrence Berkeley National Laboratory [73]. After finalizing the upgrade of the setup, the $ErMnO_3$ project was taken over by Sebastián Guerrero. He recorded and fitted the new $ErMnO_3$ scan in Fig. 3.16(b) as part of the ongoing project.

During this thesis, a first-generation Montana Instruments® cryostation s50 was modified to become an operative variable-temperature scanning NV microscope. The first steps in this engineering process and further details on the setup were previously reported by Lorenzelli [44]. We will refer to this setup as "Variable Temperature Magnetometer", or short VarTMa, in the following. Experimental data recorded on other setups is also evaluated in this thesis, but only the engineering aspects of VarTMa are discussed in this chapter.

In this chapter, we will first motivate the design goals of VarTMa in Sec. 3.1 and give an overview of the design in Sec. 3.2. Critical steps in the engineering process are presented, grouped into the topics electrical design (Sec. 3.3), mechanical design (Sec. 3.4), temperature management (Sec. 3.5), and vacuum system design (Sec. 3.6).

3.1 Design goals

The design goals of VarTMa are the following:

1. Ready access to the full temperature range from cryogenic ($< 10\,\mathrm{K}$) to room temperature.
2. Fast turnaround times from sample mounting over initial cryogenic measurements to sample exchange.
3. User-friendly design to reduce setup-work overhead and to gain accessibility for non-experts of the setup.

Point 1 allows to study a large variety of samples and monitor the evolution of phenomena like phase transitions as a function of temperature. An example of such a potential study was motivated in Ch. 2.5. Further, it allows the use of the NV^- in the temperature regimes (I) and (III), where Fig. 2.2(d) shows the best sensing performance.

Point 2 is facilitated by the small form factor of the cryostat. The outer dimensions of the cryostation chamber in Figs. 3.1 and 3.2 are only $(9\,\mathrm{cm})^2$ x $8\,\mathrm{cm}$ (user accessible space). A small air volume and reduced surface area for water adsorption/out-gassing allow for a fast pump-down to the high vacuum regime — a cooldown can only start once a high vacuum is reached. Additionally, a compact design reduces the amount of material that has to be cooled down to and warmed up and thus accelerates the turnaround. In practice, this is particularly useful when testing different experimental approaches for their feasibility or when a sample or the scanning tip breaks at cryogenic temperature.

Point 3 summarizes a series of experimental challenges that come with the operation of a cryogenic scanning NV setup compared to a common room-temperature setup. It includes the additional vacuum system, which was improved to avoid obstructive, gradual ice formation on the sample surface, but also the common elements of a scanning NV setup. Regarding the latter, VarTMa is, for example, equipped with a microscope objective that is placed outside the cryostat (see Fig. 3.1). This allows the operator to easily position the objective by hand while the tip and sample are cold. The ability to move the objective outside of the cryostat allows for the common room-temperature design where the tip is fixed in space and the sample is scanned underneath it (see Figs. 3.1, 3.2). Another design aspect similar to our room-temperature setups is the magnetic bias field generation. VarTMa possesses a second stack of attocube closed-loop positioners next to the sample stack to position a permanent magnet (see Fig. 3.2). This way, bias fields are limited to around 100 mT, but the field generation is free from additional challenges that come with electronic vector magnets.

3.2 Components and choice of materials

The Gifford-McMahon cryo-cooler head has two stages [44]. Stage 1 is connected to the radiation shield, and the entire system is referred to as the 30 K *system*. It has a higher cooling power and is used as an intermediate temperature layer to shield its inside. Stage 2 is connected to the cryostat core, and this system is referred to as the 4 K *system* (despite not being at 30 K/4 K in all cases). The two systems are described in the following. The choice of materials is also presented, as it is a central design aspect of a cryostat. Subsequent sections discuss further details of functionalities.

As an overview, a render of our computer-aided design (CAD) model is shown in Figs. 3.1, 3.2 (all CAD images presented in this thesis are made with SoildWorks®) with labels of the various parts: The cold finger of stage 2 is connected via the platform (*1*) to the user-accessible inside of the cryostat. Part of the platform is our platform heater (*1a*), which has to be pressed into thermal contact by a self-designed clamp (*1b*). The stage 1 shields this cold finger and terminates in the radiation shield socket (*2q*). Part of this socket ring are two charcoal absorbers (*2a*) and two thermal clamps (*2k*)(*2l*). The radiation shield socket and the platform, together with the vacuum housing (*7*), are designed by Montana Instruments. All other parts are home-built (excluding the attocube motors).

3.2.1 4 K system

We start with the 4 K *system*. On top of the cold finger, the platform (*1*) is fixed with four M3 brass screws — generally, almost all screws used are made of brass. The platform has large venting holes to pump down the air volume underneath it rapidly. Just like the entire cooling structure (*3*), the platform is made from oxygen-free high thermal conductivity (OFHC) copper and was gold-plated. Since the bottom surface of the platform is critical for the thermal link to the cold finger, it was lapped to achieve optimal surface planarity and low, mirror-like roughness. Right after, it was gold-coated by sputtering. The gold plating of all other copper surfaces was done by the Doerrer AG in Zurich. To achieve a mirror effect for IR heat radiation, a gold thickness of around 0.5 µm was chosen. Before galvanization, the native oxide layer of the copper parts was chemically removed, and an adhesion and barrier layer of

1	platform	Fig. 3.1
1a	platform heater	Fig. 3.1
1b	clamp	Fig. 3.1

2	radiation shield	Fig. 3.1
2a	charcoal absorbers	Fig. 3.1/3.2
2b	lower halves	Fig. 3.1/3.2
2c	cylinder surface	Fig. 3.1
2d	lid	Fig. 3.1
2e	cover tape	Fig. 3.1/3.8
2f	window	Fig. 3.1/3.8
2g	shield mounting posts	Fig. 3.1/3.2
2h	clamps	Fig. 3.1/3.2
2i	arms	Fig. 3.1/3.2
2k	thermal clamps for SMP	Fig. 3.1
2l	thermal clamps for sample	Fig. 3.2
2m	own thermal clamp left	Fig. 3.2/3.3
2n	own thermal clamp right	Fig. 3.2
2o	handles	Fig. 3.2
2p	clamp springs	Fig. 3.2
2q	radiation shield socket	Fig. 3.1

3	cooling structure	Fig. 3.1
3a	cooling posts	Fig. 3.1
3b	cooling braids	Fig. 3.1/3.10
3c	ankers	Fig. 3.1/3.10
3d	mounting plate	Fig. 3.1/3.10
3e	posts	Fig. 3.1
3f	sample holder	Fig. 3.3/3.5
3g	sample thermometer	Fig. 3.3
3h	sample heater	Fig. 3.3
3i	sample	Fig. 3.3
3k	sample PCB	Fig. 3.1/3.5
3l	sample pin battery	Fig. 3.3

4	titanium frame structure	Fig. 3.1
4a	springs	Fig. 3.1
4b	spacer (only to align)	Fig. 3.1
4c	counter-acting screws	Fig. 3.1
4d	baseplate	Fig. 3.1
4e	pin batteries	Fig. 3.1/3.6
4f	scanner head (*5*+*6*)	Fig. 3.14
4g	magnet mounting plate	Fig. 3.2
4h	magnet attocube stack	Fig. 3.2
4i	sample attocube stack	Fig. 3.1
4k	SMP cables tuning fork	Fig. 3.3
4l	SMP cables MW	Fig. 3.3
4m	flexible SMP cables	Fig. 3.3

5	microwave holder	Fig. 3.1/3.3
5a	antenna	Fig. 3.3/3.7
5b	cable clamp	Fig. 3.1
5c	micropositioner	Fig. 3.1/3.7

6	tuning fork holder	Fig. 3.3
6a	tuning fork	Fig. 3.3/2.1
6b	QZabre chip	Fig. 3.3/3.8
6c	dither piezo	Fig. 3.3

7	vacuum housing	Fig. 3.1
7a	lid	Fig. 3.1
7b	top window	Fig. 3.1/3.8
7c	SMP panel	Fig. 3.1
7d	PCB	Fig. 3.1
7e	PCB pulgs inside	Fig. 3.1/3.3
7f	PCB pulgs outside	Fig. 3.3
7g	O-rings	Fig. 3.1
7h	50-KF flange	Fig. 3.1/3.13
7i	cryo-cooler	Fig. 3.3
7k	guiding rods	Fig. 3.14
7l	25-KF panel for D-sub	Fig. 3.1/3.14

8	permanent magnet	Fig. 3.2/3.8

9	microscope objective	Fig. 3.1/3.8

10	D-sub feed-through	Fig. 3.13
10a	drain tube	Fig. 3.13/3.14

11	vacuum system holder	Fig. 3.13/3.15
11a	63-CF T-piece	Fig. 3.13/3.15
11b	guiding rail	Fig. 3.13/3.15
11c	slider	Fig. 3.13
11d	support wedges	Fig. 3.13
11e	springs	Fig. 3.13
11f	yokes	Fig. 3.13
11g	guiding slot	Fig. 3.13
11h	adjustment wedges	Fig. 3.13

12	getter pump	Fig. 3.13/3.15
12a	getter pump valve	Fig. 3.13/3.15
12b	50-KF bellow	Fig. 3.13/3.14

13	turbopump	Fig. 3.13
13a	pressure gauge	Fig. 3.13/3.15
13b	turbo pump valve	Fig. 3.13/3.15
13c	40-KF flexible tube	Fig. 3.13

14	optical table	Fig. 3.13
14a	microscope head mount	Fig. 3.13
14b	posts below optics	Fig. 3.13/3.15

Table 3.1: Setup component labels and where to find them. Parts of the 4 K *system*: *1*, *3*, *4*, *5*, *6*, *8*. Parts of the spring-mounted structure: *4*, *5*, *6*, *8*, partly *3*. Parts of the 30 K *system*: *2*.

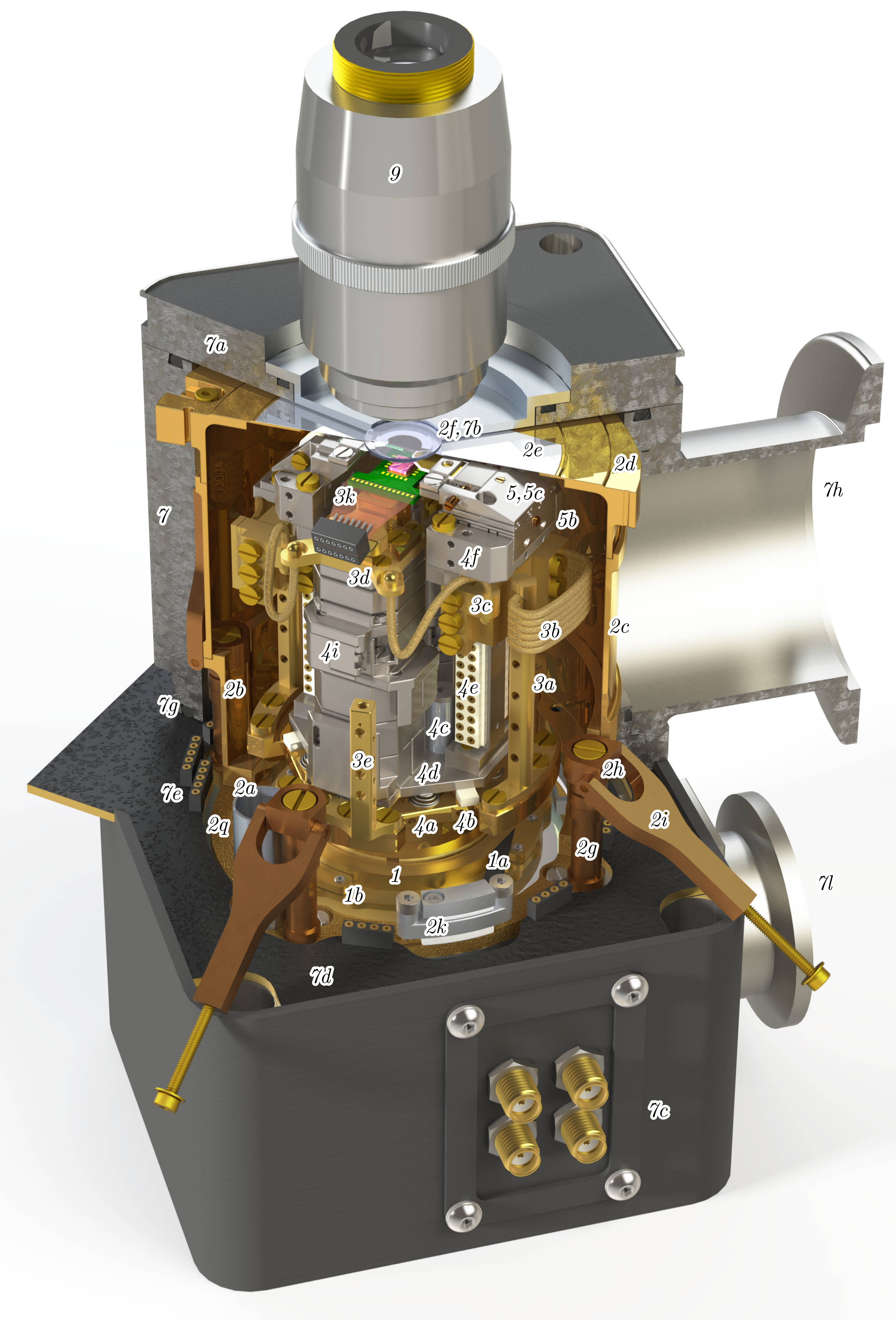
9
7a
2f, 7b
2e
2d
7h
3k
5, 5c
5b
7
4f
3d
3c
3b
2c
4i
4e
3a
2b
7g
4c
2h
3e
4d
7e
2a
2i
4a
4b
2q
2g
1a
7l
1
1b
2k
7d
7c

Figure 3.1: CAD design of the VarTMa setup (front view of Fig. 3.2). For clarity of presentation, the flexible part of the sample PCB (*3k*) is rendered transparent, and the microscope objective (*9*) is retracted by 6 mm. Electrical cables are shown in Fig. 3.3. Component labels are defined in Tab. 3.1. Some CAD files are property of Montana Instruments®.

Ni0.85/Ph0.15 was added. This thin adhesion layer is, in principle, magnetic. But we have not found a sign of magnetism in practice and thus conclude that it is effectively non-magnetic for our applications.

On top of the platform sits the spring-mounted structure, which contains the sample and the probe. The two attocube stacks (*4h*)(*4i*), on which the permanent magnet (*8*) and the sample holder (*3f*) are mounted, are surrounded by the titanium frame structure (*4*). On top of the latter sits the detachable scanner head (*4f*) with the tuning fork holder (*6*) and microwave holder (*5*) (see Fig. 3.3). All titanium parts are made from titanium grade 2, mostly by electrical discharge machining. After fabrication, the surface is rough, gray, and oxidized. Therefore, all titanium parts were electropolished by the Steiger Galvanotechnique SA in Châtel-St-Denis to obtain a shiny surface finish. This required a removal of 50 µm to 100 µm per surface. Thus, the change in size and alignment of stacks of several titanium parts became relevant for the tolerance of our assembly, which is less than 0.1 mm in some cases. Also, threads and through-holes became a bit looser. For future parts, this change in size should be considered already in the design process.

The cooling structure must provide a good thermal link between the platform and the sample holder. However, it may not be a rigid connection since, first, the springs (*4a*) mechanically decouple the cryostat vibrations from the tip and sample, and second, the attocube stack must be able to move the sample. Therefore, flexible OFHC copper cooling braids (*3b*) are used, which were also gold-plated. Two posts (*3a*) fixed with each three M2 brass screws to the platform are connected to the titanium frame structure by each six cooling braids. From there, the ankers (*3c*) of two separate cooling braids are connected, which constitute the thermal link to the mounting plate (*3d*) of the sample holder. The top surface of this sample mounting plate, as well as the bottom surface of the sample holders, were also lapped for planarity and low roughness. They are bolted by two M2 screws. Another cooling braid is connected to the magnet mounting plate (*4g*) and its attocube stack to speed up the thermalization and lower temperature gradients.

3.2.2 30 K system

The radiation shield (*2*) consists of several parts. Two lower halves (*2b*) have the same diameter as the radiation shield socket, onto which they are pressed by clamps (*2h*) on mounting posts (*2g*). The upper cylinder surface (*2c*) has a larger diameter and is put on top of the lower halves. It is easily removable to access the 4 K *system.* The lower halves, in contrast, are usually not taken off. Crucially, they host two additional thermal clamps (*2m*)(*2n*), which create a force for thermal lagging by each two springs (*2p*). The springs are bought from the Durovis AG in Perlen and are made of beryllium bronze, which offers a fairly temperature-independent and linear compression force of around $7\,\mathrm{N\,mm^{-1}}$.

The radiation shield is closed by a lid (*2d*). To obtain good thermalization, the lid and cylinder surface are pressed down onto the lower halves by arms (*2i*). These arms can be flipped to the side while working on the 4 K *system.* The lower halves, the cylinder surface, the lid, and the thermal clamps are made of gold-plated OFHC copper. The fastening parts of the radiation shield, namely the mounting posts, clamps, and arms, are made of bronze (CuSn6).

3.2.3 Optical access

A central challenge in the design of the radiation shield is optical access. The Nikon CFI L Plan EPI 50XCR microscope objective (*9*) has a coverglass correction ring and a working distance (here: front lens to focal plane) of around 4.15 mm for our setting with the vacuum housing window (*7b*) and radiation shield window (*2f*). Both windows are from Montana Instruments, have a thickness of 0.5 mm, and are made from fused silica with an anti-reflection coating. The height of the QZabre LLC up-configuration chip (*6b*) plus tuning fork (*6a*) and cantilever (see Fig. 2.1(c)), on which the tip is mounted, is 0.9 mm. Moreover, it is desirable to be able to view the sample surface by widefield microscopy while the scanning tip is still far from the sample. This way, the sample can be moved by the attocube steppers, and the region of interest on the sample can be found. Due to a potential tilt of the sample, bonding wires, and other structures on the sample, a sufficient tip-to-sample distance is desirable (~ 0.5 mm). This leaves only about 1.4 mm between chip and vacuum housing window. Within this distance, the chip-clamp structure of the scanner head, and the radiation shield window and lid are fitted (see Fig. 3.8). Since the temperature gradient from the 4 K *system* to ambient happens over this distance, no mechanical contact may exist between any of the three structures. Precise machining allowed us to realize the assembly with the distances depicted in Fig. 3.8. To obtain the right height of the spring-mounted structure, spacers with the correct size are placed between the platform and the titanium plate of the spring-mounted structure while tightening the two counter-acting screws (*4c*). Afterward, the spacers are removed to leave the top suspended on the springs. Since the radiation shield lid has to be very thin above the tip, the solid copper part has a large hole which is covered by a 80 µm thick cover tape (*2e*) (3M™ 1170 Tape: Aluminum Foil with Conductive Adhesive). On top of a small hole in this tape sits the radiation shield window (*2f*).

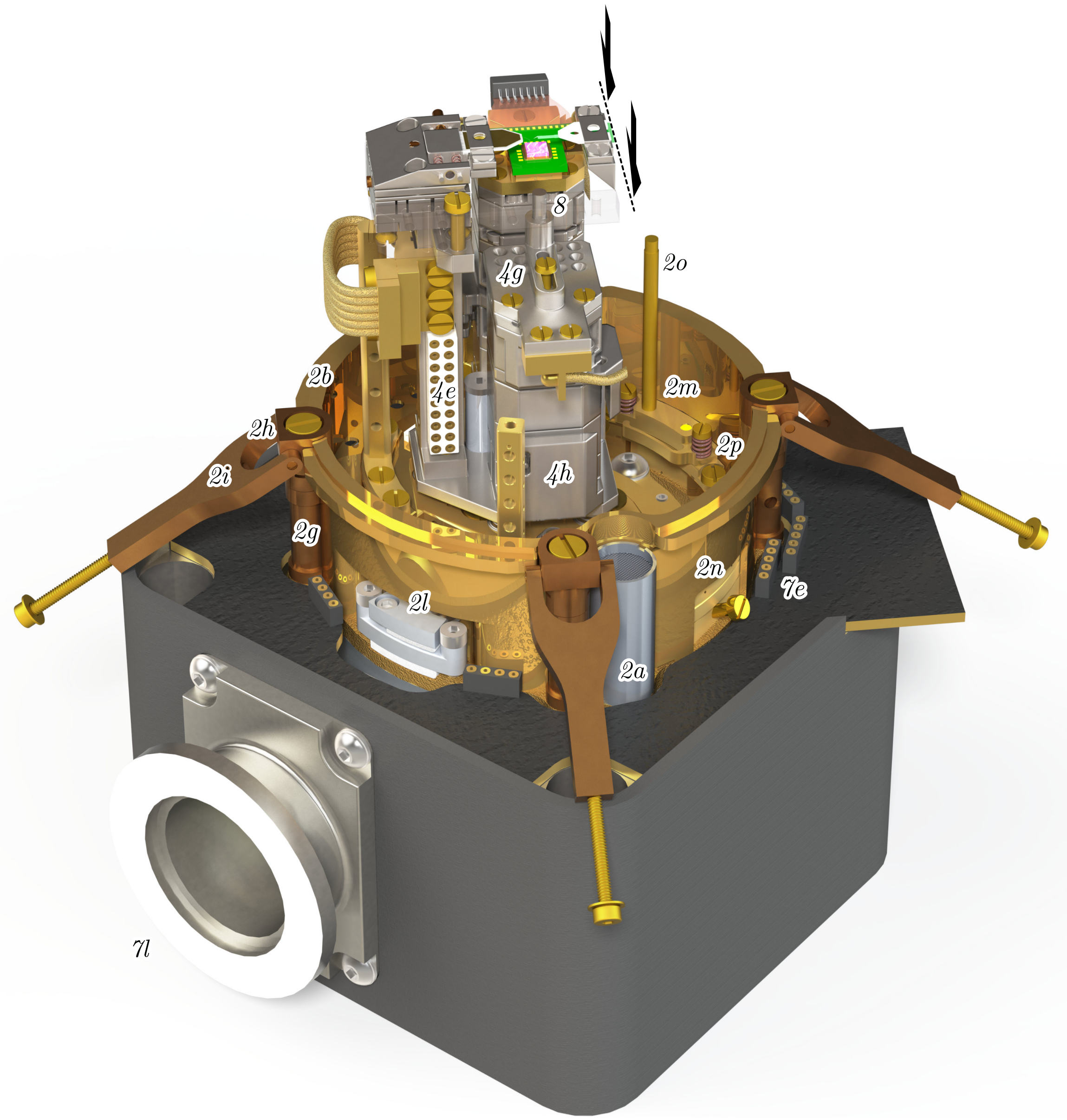

Figure 3.2: CAD design of the VarTMa setup (rear view of Fig. 3.1). The frame of the scanner head (*4f*) is rendered transparent to make the magnet (*8*) visible. The magnet can be placed in coarse discrete steps on the magnet mounting plate (*4g*) and fine-positioned by the attocube magnet stack (*4h*). A part of the 4 K *system* is hidden (cut marked by dashed line and arrows) to make the left own thermal clamp (*2m*) visible. Electrical cables are thermally lagged to the lower halves of the radiation shield (*2b*) by the force of the springs (*2p*). The cables are then plugged into the PCB (*7e*) or guided through the 25-KF panel (*7l*). Electrical cables are shown in Fig. 3.3. Component labels are defined in Tab. 3.1. Some CAD files are property of Montana Instruments®.

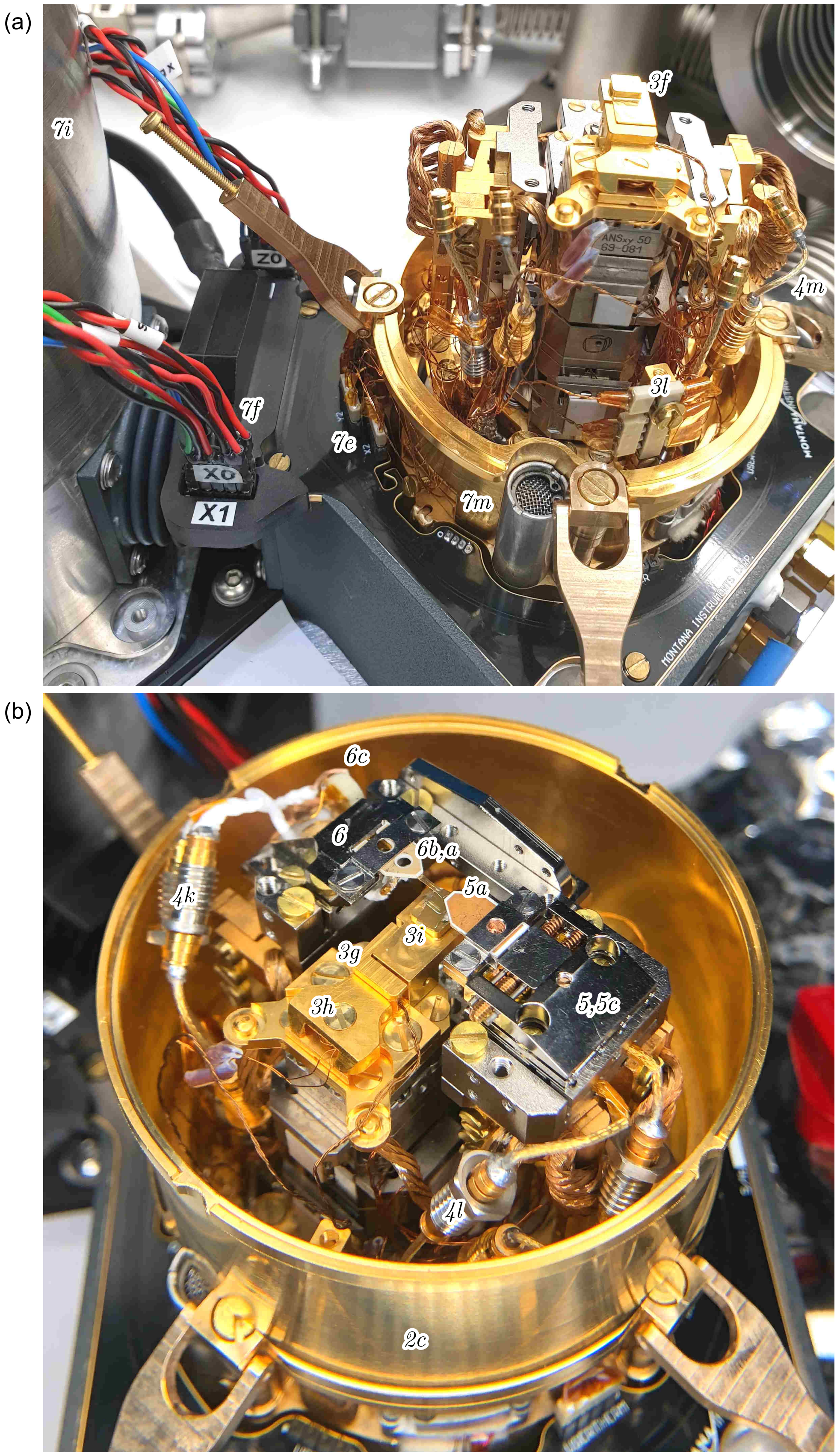
(a)
3f
7i
ZO
4m
3l
7f
7e
X0
X1
7m
ANSxy 50
69-081
(b)
6c
6
6b,a
5a
4k
3i
3g
3h
5,5c
4l
2c

Figure 3.3: Pictures of the VarTMa setup. (a) Sample holder ($3f$) without the scanner head ($4f$) mounted above it. (b) The scanner head ($4f$) (with SMPs ($4k$)($4l$) plugged in) and cylinder surface ($2c$) of the radiation shield are mounted. Components of the scanner head ($4f$) and sample holder ($3f$) are labeled. Component labels are defined in Tab. 3.1.

3.3 Electrical design

3.3.1 Instrumentation

The general electrical design and control software used for our scanning NV microscopes was previously described by Welter [72] and some specific aspects of VarTMa by Lorenzelli [44]. In the following, only a summary of the instruments and their role in the setup is given.

We use a Zurich Instruments Ltd. HDAWG arbitrary waveform generator to compose the pulse sequences like the one depicted in Fig. 2.2(a). Sequences consist of microwave pulses (I and Q signals of 100 MHz) and trigger signals to start data acquisition and to pulse the laser. The laser we use is further addressed in Ch. 6.2.5. The I and Q signals are used with a Marki® IQ-0255 IQ-mixer to modulate the microwave carrier signal from a National Instruments™ QuickSyn FSM-0020 before amplification by a 10 W, 700 MHz – 4000 MHz HD29084 amplifier. This arrangement enables spin operations by pulses of almost arbitrary phase, shape, and duration. Synchronized with a common 10 MHz clock, the photon count events from an Excelitas Technologies® avalanche photodiode are recorded during the pulse sequence. These time stamps are later summed up over the sequence repetitions to obtain the countrate histograms as in Fig. 2.2(c). Further details on the optical system, which is used for confocal excitation of the NV center with a green laser and simultaneous readout of the red photo-emission, are provided in Ref. [44]. National Instruments™ DAQ 6353 and 6363 data acquisition devices are used, also for control of the optical setup and the atomic force microscope, as discussed in the next Sec. 3.3.2. For the distance control of the scanning probe, a Zurich Instruments HF2LI lock-in amplifier with a HF2TA current amplifier is used. Finally, attocube ANC300 and ANC350 controllers are employed to steer the four ANPx51 and two ANPz51 steppers as well as the ANSxy50 sample scanner (see Fig. 3.1).

3.3.2 AFM distance control and tuning fork holder

We use an atomic force microscope (AFM) to control the scanning tip. A visual impression of this was given in Fig. 2.1(c). Our tips are produced by QZabre LLC by ^{15}N ion implantation and etching of a diamond membrane [74], which is cut from a diamond chip grown by chemical vapor deposition by ElementSix™. In this section, a brief overview is given on how we control the z-axis of the sample to keep the tip and the sample surface in soft contact. With this distance control running, the sample can then be raster-scanned under the tip by the x- and y-axis of the attocube scanner.

Our AFM head, which is the tuning fork holder (*6*), has a dither piezo (*6c*), which excites a tuning fork (*6a*) that is oscillating in resonance at around 32.2 kHz parallel to the sample surface. This AFM method is called “shear mode” and maintains a constant distance between tip and sample. We use a mechanical excitation of the tuning fork by the dither piezo, instead of a direct electrical driving of the tuning fork. As explained in Refs. [44, 75], this yields the clean Lorentzian resonance curve needed

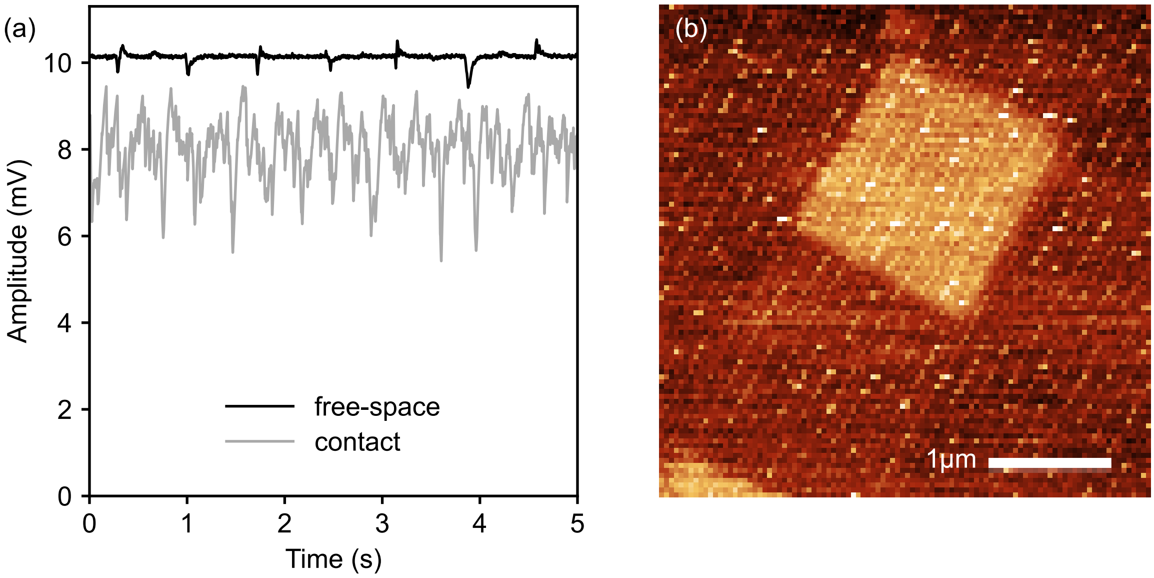

Figure 3.4: Atomic force microscopy (AFM) for distance control. (a) Time trace of AFM control signals when the tip is/is not engaged on the sample, taken at 6.7 K. (b) AFM scan at 12 K with 15 s per line and Q control with $Q = 10\,\mathrm{k}$. The height of the square (NT-MDT TGQ1 silicon test grid) is 20 nm, its size is 1.5 µm. The cryostat vibrations can be observed as spikes in the AFM time traces, resulting in a line pattern in the AFM scan. The mode "High 1" (Compressor: 25 Hz, Head: 70 Hz) of the cryostat is used in the entire figure.

for the Q-control described below. We further found that a titanium clamp that is thick enough not to bend when fastening the tuning fork chip (*6b*) is advantageous for a stable resonance. Likewise, clamping of the dither piezo (*6c*) by beryllium bronze springs yielded no stable resonance. Thus, we returned to gluing the piezo directly to the tuning fork holder (see Fig. 3.3).

We use our lock-in amplifier to implement an amplitude modulation AFM: The dither piezo is excited by a driving signal close to the resonance of the tuning fork. For this, one of the four SMP cables (*4k*) in Fig. 3.3 is used. One prong of the tuning fork is contacted with another SMP cable. A motion of the prongs translates into a small current, which is fed back into the lock-in device after passing the current amplifier. This signal is then demodulated at the driving frequency with a bandwidth of 100 Hz. As the driving frequency, a value slightly (*e.g.* FWHM/10) below the free-space resonance is used. When the tip comes into harder contact with the sample surface, the resonance shifts to higher values. As a consequence of this contact, the amplitude of the demodulated signal drops. Therefore, a PI controller in the lock-in device can be set up to keep the tip at a constant distance from the sample. For this, the PI controller needs to adjust the z-axis position to maintain a constant amplitude of the demodulated signal, *e.g.* around 70 % of the free-space amplitude. The process is explained in more detail for VarTMa in Ref. [44] and for a similar room temperature setup in Ref. [72]. Since this control loop of the z-axis is prone to noise picked up by the cables, the cable shields are connected at several places to the same spot on the optical table in a star-grounding concept. Further, we use a low-pass filter of 160 Hz in the z-axis attocube amplifier and 16 Hz for the x- and y-axis.

A challenge for a variable-temperature SPM setup is the drastic change of the quality

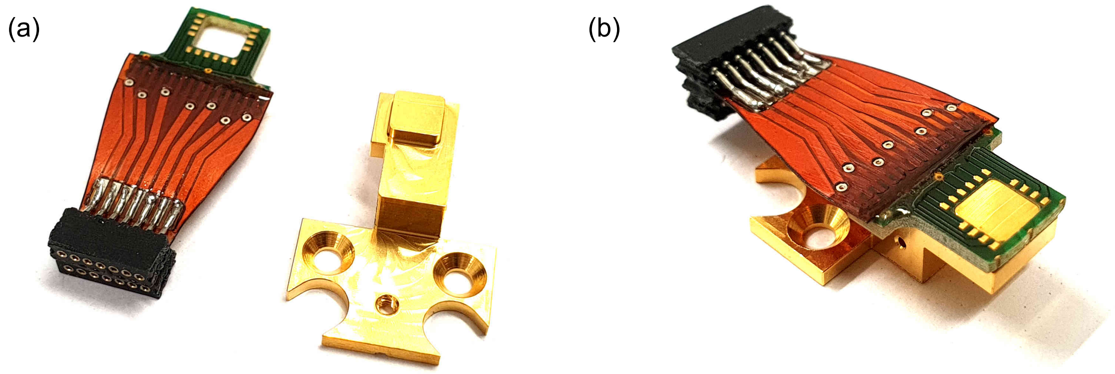

Figure 3.5: Sample holder with electrical contacts. (a) Sample PCB (*3k*) next to the main body of the sample holder (*3f*) without thermometer (*3g*) and heater module (*3h*). The 14 pin plugs are connected by a flexible PCB to the bonding pads on the rigid PCB next to the sample space. One of the lines is connected to the bottom ground plane of the PCB. (b) Sample PCB glued to the main body with conductive epoxy, such that the sample holder is grounded. The length of the sample holder is 2 cm.

factor (Q-factor) of the tuning fork with temperature. In our case, it can change from around 3 k in ambient conditions to well above 30 k at base temperature. Since such high Q-factors lead to ring-down times on the order of seconds, the reaction of the distance control loop is too slow to compensate for vibrations from the cryostat or changes in the sample topography. A possible solution for variable-temperature SPM setups is called “Q control” [76]. Here, the readout signal from the tuning fork is phase-shifted and added onto the driving signal [77]. At the correct phase, this effectively reduces the Q-factor by self-damping the oscillation. The Q-factor can then be adjusted by the amplitude of the added signal, as explained in more detail for VarTMa in Ref. [44]. In addition to an increased reaction time, Q control is found to significantly stabilize the oscillation, even when the tip is not in contact. Exemplary time traces (recorded after all setup updates) for both contact and off-contact are shown in Fig. 3.4(a).

To record AFM scans as in Fig. 3.4(b) or magnetometry scans as in Fig. 3.16, the attocube scanner is “wiggled” (moved along the diagonal of the scan area to be recorded) several times to reduce the image distortion by hysteretic effects of the piezo.

3.3.3 Sample holder

The sample holder (*3f*) can be seen in Figs. 3.1, 3.2 and 3.3. It has a thermometer module (*3g*) with a calibrated Lake Shore® Cernox® CX-SD thermometer. The module is attached by a M1.6 brass screw to the gold-plated OFHC copper main body. Also attached by a M1.6 brass screw to the main body is the heater module (*3h*), which contains a resistive Manganin wire. The thermometer and the heater modules are not touching each other, such that a PID control of the temperature of the main body, and thus the sample (*3i*), is possible. The sample was typically attached with silver paint for good thermal contact.

For samples that have electrical contacts, a sample PCB (*3k*) was designed. The PCB is mounted onto the sample holder, as can be seen in Fig. 3.5. It consists of one rigid PCB (base material FR4) with bonding pads to connect to pads on a sample. However, due to space constraints (*cf.* Fig. 3.1), pin plugs cannot be attached to the rigid PCB directly. Therefore, a second flexible PCB made from polyimide foils is used. Both PCBs were fabricated by Beta LAYOUT Ltd. and connected as follows: The same pattern (a row) of surface mounting contacts exists on the bottom of the flexible and the top of the rigid PCB. Small portions of solder paste are deposited on the contacts of the rigid PCB, and the flexible PCB is then positioned on top of it. Next, the solder paste is melted by placing the two PCBs on a hotplate at 170 °C and applying an additional stream of 250 °C from a heat gun. The flexible PCB self-aligns to the rigid PCB, and the electrical contact is completed. For increased mechanical durability, the flexible PCB is additionally glued to the rigid PCB from the top and the bottom with an epoxy and cured in an oven. Finally, the surface mount pin headers with a pitch of 1 mm are glued onto the flexible PCB, and the pins are soldered to it.

3.3.4 Choice of cables

We will now discuss how the cables are organized inside the cryostat. The main motivation here is to reduce the thermal load. Since wires typically have good electrical conductivity, they also have a high thermal conductivity and, therefore, constitute a major thermal load. The thermal load [78] (unintended heating power) is

$$\dot{Q}_{\mathrm{cond}} = \kappa A \cdot \Delta T / l \,, \tag{3.1}$$

where $\Delta T/l = (T_2 - T_1)/l$ is the temperature gradient over the length l, A is the cross-section, and κ the mean thermal conductivity (over the interval $[T_1, T_2]$). To avoid excessive heating of the 4 K *system*, wires coming from room temperature are first thermally lagged at the 30 K *system* (see next Sec. 3.3.5). We are mostly interested in the heat load on the 4 K *system*, as this determines the temperature of the sample and NV center. To this end, we assume that wires are cooled to $T_2 = 30\,\mathrm{K}$ at the lagging spots and consider the temperature gradient to $T_1 = 4\,\mathrm{K}$ in Eq. 3.1. For this setting, we can approximate the mean thermal conductivity values [79] of the three different wire materials we use:

- copper with $\kappa = 650\,\mathrm{W\,m^{-1}\,K^{-1}}$,
- phosphor-bronze with $\kappa = 6.8\,\mathrm{W\,m^{-1}\,K^{-1}}$,
- Manganin with $\kappa = 3.3\,\mathrm{W\,m^{-1}\,K^{-1}}$.

The electrical conductivity decreases with decreasing thermal conductivity. The choice of wire length l, cross-section A, and material is a trade-off between the electrical resistance and the thermal load. It is ideal to operate at the acceptable resistance limit for best thermal performance.

Cables currently used in the setup can be categorized into three groups: 26 attocube cables, 6 sample cables, and 4 coaxial SMP cables. Their choice of material, based on their electrical properties, is explained in the next three paragraphs. The heat load due to these three groups of wires will be presented later in Tab. 3.2. Pictures of the cabling are given in Fig. 3.3, and the routing of the cables between components can be traced in Figs. 3.1, 3.2. The cables are arranged such that they do not touch the radiation shield and do not harm the movement of the attocube stacks.

In the case of the cabling of the attocube positioners, the resistance of piezo drive loops has to be less than $5\,\Omega$ ($2.5\,\Omega$ one-way), and less than $10\,\Omega$ for their resistive readouts loops (but we use the same cabling as for the drives). We choose phosphor-bronze cables with permissible length here to bridge the 30 K to 4 K step. Moreover, the number of wires should be reduced to a minimum. Therefore, we use a single supply voltage cable and a single ground cable for the readouts of all three stepper motors of each, the sample and the magnet stack. This still leaves 26 cables for the attocube stages.

In the case of the sample heater and thermometer, the resistance of the wires is not critical for their operation. Therefore, we choose thin Manganin wires with a minimal thermal load. Since these cables go directly to the sample, their thermal load has a substantial effect on the achievable base temperature. However, this proximity is required for an accurate readout of the sample temperature and a fast PID control at the setpoint. The thermometer's resistive readout needs four wires to eliminate the effect of the wire resistance, and the resistive heater needs two wires.

The coaxial cables for the dither piezo (*4k*) (see Fig. 3.3), tuning fork readout (*4k*), and MW antenna (*4l*) are semi-rigid SMP cables from the vacuum feed-through at the SMP panel (*7c*) (see Fig. 3.1) over the thermal lagging (*2k*) at the 30 K *system*. To reduce the temperature gradient to the 4 K *system*, these cables wind once around the platform (*1*). At the sample environment, they merge into flexible SMP cables (*4m*) for mechanical isolation and easier (un-)mounting of the scanner head (see Fig. 3.3). These cables are the SC type from Lake Shore Cryotronics® Inc. and were equipped with SMP plugs by Quantum Design GmbH. The plastic jacket of the cables was removed and replaced by PTFE tape where there was a need to increase their flexibility.

3.3.5 Cable organization

As can be seen in Fig. 3.1, three different vacuum feed-through interfaces exist. The first is the SMP panel (*7c*) for AC signals. The second is the PCB sealing the vacuum housing. The pins from the phosphor-bronze wires can be plugged into the PCB inside the vacuum chamber at room temperature (*7e*) (see Fig. 3.3) and accessed by the respective plugs on the ambient side of the PCB (*7f*). The third vacuum feed-through is the D-sub panel (*10*). As can be seen in Fig. 3.13, the 25-KF flange on the vacuum housing (*7l*) continues as a 25-KF bellow and terminates in a 40-KF D-sub feed-through from allectra GmbH in Berlin. The extension by the bellow was necessary due to space constraints under the 50-KF bellow (*12b*) (see Fig. 3.14). The wires inside the bellow are made of copper and are plugged into the pin headers from

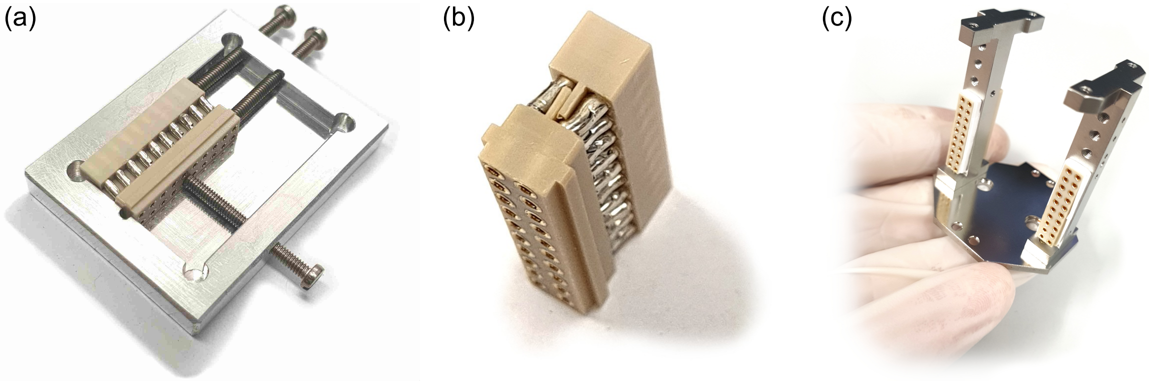

Figure 3.6: Assembly of the pin batteries. (a) PEEK pin battery (*4e*) after soldering inside the assembly tool. (b) Top view of the pin battery after soldering. (c) Pin batteries mounted in the titanium frame structure (*4*) with my hand for scale.

the phosphor-bronze wires. Accessing these plugs only requires opening the 25-KF flange at the vacuum housing (*7l*).

Next, we will follow the wires for the attocube positioners from outside to inside the cryostat and discuss relevant components. The attocube positioners use all of the 20 connections of the PCB vacuum feed-through, and additionally, the sensing wires for position readout use six of the 26 D-sub connections. Inside the cryostat chamber, the wires are thermally lagged at the 30 K *system*. The two thermal clamps (*2k*)(*2l*), which were provided by Montana Instruments, are not sufficient for all attocube wires. Instead, we use two own additional thermal clamps (*2m*)(*2n*) for the lagging of all attocube wires. These laggings are designed such that they can be unmounted from the top, which allows one to take out the two lower halves (*2b*) of the radiation shield without having to open the delicate laggings. For this purpose, handles (*2o*) are attached, which are also used to wrap and sort the long phosphor-bronze wires. From these two thermal clamps, the phosphor-bronze wires for the attocube positioners continue to the 4 K *system*. There, two pin batteries (*4e*) are located in the pillars of the titanium frame structure (see Fig. 3.1) and organize the transition to the native copper wires of the attocube positioners.

The pin batteries are home-built, just as most other pin plugs inside the cryostat. For this, commercial gold-plated brass pins with 2 mm pitch were pressed in self-designed PEEK plastic structures for compatibility with high vacuum and thermal cycling. Additionally, PEEK offers a high melting temperature (343 °C), which is required for the vacuum-compatible solder that is used to connect wires to the pins. The copper cables inside the 25-KF bellow were crimped, though, which is a preferred method over soldering but not applicable for, *e.g.*, the thin phosphor-bronze wires. For the assembly of the pin batteries, the pins were first shortened by CNC-milling before being pressed into the PEEK parts. The resulting pin rows were then pushed together and held in place in a home-build assembly tool, as shown in Fig. 3.6(a,b). Vacuum solder was used to connect the two pin rows, and PTFE tape was used for electrical isolation and to support the press-fitting into the titanium frame structure, as seen in Fig. 3.6(c).

The wires to the sample holder are organized by the sample pin battery (*3l*) (see

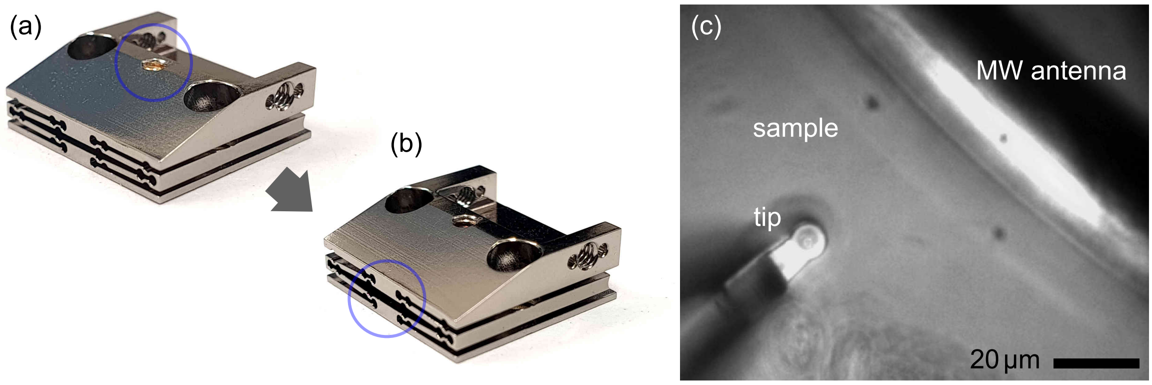

Figure 3.7: Microwave stage. (a) Picture of the z-axis stage of the micropositioner (*5c*) in the microwave holder without extension. (b) The stage is extended along the z-axis by 0.5 mm (blue circle) without tilting by adjustment of the set screw on the top (blue circle in part (a)). (c) Widefield microscope picture of the MW antenna wire aligned to the scanning tip, which is engaged on the sample surface.

Fig. 3.3), which offers easy accessibility for regular (un-)mounting of the sample holder. The two wires from the heater to the battery are phosphor-bronze, and from there, through the thermal lagging (*2l*) to their plugs on the PCB, they are Manganin. The four wires from the sample thermometer to the pin battery and from there over the thermal lagging (*2l*) to their plugs on the PCB are Manganin over the entire length.

For the experiments conducted thus far, the sample PCB (*3k*) was not needed. But for future experiments, which require electrical contacts on the sample, the 14 wires from the sample PCB could be organized at the sample pin battery, then use the lower part of one of the original thermal clamps (*2l*) which was kept empty for this purpose and finally exit the vacuum at the D-sub feed-through (*10*).

3.4 Mechanical design

3.4.1 Microwave holder

The microwave antenna (*5a*) (see Fig. 3.3) cable has to be positioned in sub-100 µm proximity to the NV center since the field strength determines the Rabi-frequency and thus the minimal duration of π-pulses. This can be critical for AC sensing schemes [50]. To achieve such a close alignment, we use a home-built micropositioner (*5c*) based on the elastic deformation of titanium parts. The general design of the microwave holder (*5*) (see Figs. 3.1, 3.2) was already described by Lorenzelli [44]. Compared to Ref. [44], the z-axis stage was adapted to the space constraints of the new radiation shield and to minimize tilting when moving up. The travel range is given by the elastic deformation limit and > 0.5 mm for the z-axis stage (see Fig. 3.7(b)) as well as for the stage that brings the antenna towards the tip.

Since these two stages have a single pivot point given by the tip of their set screw, they are sensitive to pulling forces on the antenna chip. Such forces can arise when (un-)plugging the flexible SMP wires of the microwave delivery (*4l*) (see Fig. 3.3) and harm the previous alignment of the antenna to the NV center. To that end, the first 3 mm of the cable bushing of the microwave holder was designed with a cable clamp (*5b*) for strain relief on the wires at the antenna side. To connect the chip's top ground plane with the coax wire shields, the shields were soldered to the titanium part (or to conductive copper tape attached to the titanium). Further, conductive tape is used between the chip and its top clamp. With this design, a π-pulse time of 80 ns was achieved. Unfortunately, the ground connection with this design and the transmission of microwave signals achieved with the clamping are not as reproducible as desired.

3.4.2 Vibration isolation

The problematic source of vibrations in our system are the helium supply and return valves in the cold head of the cryostat [44]. They open at a frequency of around 2 Hz but occur as sharp beats with high-frequency components (see Fig. 3.4(a)). A complete passive isolation of the spring-mounted structure from these vibrations is not possible. A trade-off in the stiffness of the springs underneath the spring-mounted structure must be found: If they are chosen too soft, very smooth AFM scans were recorded, but the tip moves considerably in the widefield microscope. This makes confocal alignment to the NV center impossible. Further, pulling forces by cables and braids can move the sample and even harm the AFM scans. Overall, the dominating problem in this setting is a too-soft mount for *lateral* displacement. If the springs are chosen too stiff or a rigid connection is made, on the other hand, controlled engagement of the tip on the sample is impaired. Here, the dominating problem is a mount that is too stiff for *vertical* displacement/vibrations. This would suggest mounting the spring not only from the bottom but also from the sides, which is impossible in VarTMa due to space constraints.

By investigation of the movement of the tip in the widefield camera (the frame rate can be adjusted to achieve a stroboscopic effect) and pilot AFM scans, the springs were selected by trial and error. The final result is presented in Ref. [44, Fig. 3.27(b)]. In this setting, with a resonance estimated to be roughly around the bandwidth of the demodulated AFM signal (see Ch. 3.3.2), low-frequency vibrations are transmitted into the spring-mounted structure, but the distance control loop of the AFM can partly compensate them. High-frequency vibrations are reflected and have a reduced influence on the AFM. We also attempted to use passive damping of the spring-mounted structure in the form of PTFE tape on the springs or steel wool (both are compatible with high vacuum and cryogenic temperature). However, these attempts did not yield an improvement, which is expected if vibrations around the resonance play a minor role. More details on the transmissibility for VarTMa are provided in Ref. [44].

Another source of vibration was the roughing pump of the turbo pump. But as presented in Sec. 3.6.3, this was solved by mechanically decoupling them from the system.

An AFM scan at 12 K of an NT-MDT TGQ1 silicon test grid is presented in Fig. 3.4(b). As can be seen, the vibrations do impact the scan, but overall, a good performance is still achieved. This scan was recorded in the "High 1" mode of the cryostation. This mode can also be changed in a few discrete steps when compromising cooling power is an option. Note that the resolution of AFM scans with scanning NV tips is rather poor in comparison to the performance of AFM microscopes due to the bulky nature of the diamond tip (see Fig. 2.1(c)).

3.4.3 Permanent magnet on stages

The magnetic bias field used to generate a Zeeman splitting of the NV spin resonances (see ODMR lines in Fig. 2.2(b)) is provided by a permanent magnet. For the experiments on VarTMa shown in this thesis, Neodymium-Iron-Boron (NdFeB) magnets from supermagnete.ch with a remanence field of 1.35 T are used. The entire inside of the cryostat is built from non-magnetic material to not distort the magnetic field from the bias magnet, introduce uncontrolled magnetic fields on top of the sample field to be measured, and exclude magnetic forces on parts of the setup. The only exception to this is weakly magnetic stainless steel in the SMP cables and in the screws plus Belleville washers that are used at the cold finger to generate a high contact pressure. Here, it should be noted that the brass screws we use are selected: some are, probably due to individual trace amounts of nickel, weakly magnetic. We only use those that show minimal or no magnetic attraction to a touching NdFeB permanent magnet.

A fine alignment of the magnet can be achieved by determining the frequency of the ODMR resonances for slightly varying positions of the magnet [72]. We vary the position of the magnet by moving the steppers in the respective attocube stack (*4h*) (see Figs. 3.1, 3.2). But due to space constraints in VarTMa and the 3 mm travel range of the attocube steppers, a prior rough alignment is necessary. The procedure is presented in Fig. 3.8: we simulate the magnetic field map of a magnet (or stack of magnets in this case), overlay it to a cross-sectional view of the CAD model, and align it to the NV center direction of the tip in use. In doing so, we find a suitable hole in the magnet mounting plate (*4g*). A misalignment below 10° can be achieved with this method.

In practice, it can be helpful to know the precise misalignment and strength of the bias magnetic field based on experimentally obtained values of $f_\pm$ (see Ch. 2.2). The numerical model [43] developed in this thesis provides a function to do this conversion. It is based on the temperature-dependent GS Hamiltonian, which will be presented later in Eq. 4.1. Based on this function, the estimated misalignment for the experiments with NV-5 in this thesis is around 5° at 3.9 mT and 294 K.

The change of this misalignment with temperature is investigated in Fig. 3.9(b–d). A significant change in the magnetic field strength and direction seems to occur. The difference between the optimized (“fitted”) (B, θ_B) solution by the model and the observed position of $f_\pm$ is always significantly lower than 1 MHz, suggesting an overall reliable analysis. But since the position of $f_\pm$ is fairly insensitive to magnet misalignment, as long as θ_B is small, the resulting (B, θ_B) in Fig. 3.9(c,d) have to be treated with caution. For example, the result is sensitive on the assumed position of the ZFS $D_{\mathrm{GS}}(T)$. To be sure, it is generally advisable to determine the ZFS at the respective conditions, as $f_\pm$ can change with strain [14] — especially in small or misaligned magnetic fields. But with the magnet design of VarTMa, it is impossible to

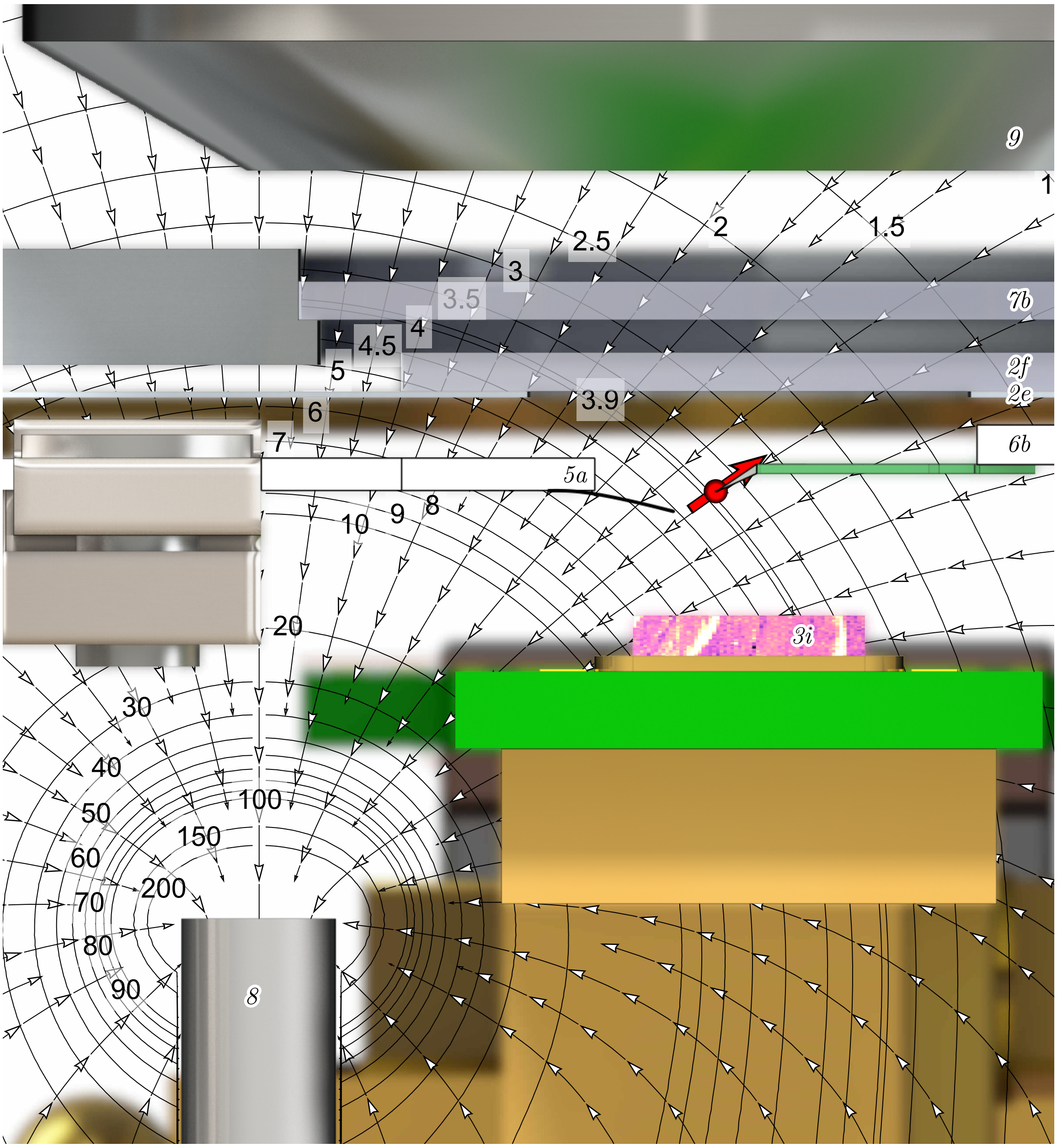

Figure 3.8: Coarse alignment of the bias magnet and optical access. The magnetic field of the bias magnet (*8*) (here $\varnothing = 2\,\mathrm{mm}$, $h = 9\,\mathrm{mm}$, NdFeB with $B_r = 1.35\,\mathrm{T}$) is overlaid with cross-sections of the CAD model of the setup. Field values are given in mT. The red arrow marks the NV center's location and the N-V-axis direction. The field-lines are aligned with the latter, and a bias field of $B \approx 3.9\,\mathrm{mT}$ results (see Fig. 2.2(b) and Fig. 3.9(c,d)). The microscope objective (*9*) is focused on the NV center with a working distance of 4.15 mm. Fitted into this range are the vacuum housing window (*7b*) and the radiation shield window (*2f*), as well as their supporting structures and the QZabre chip (*6b*) and microwave antenna (*5a*) chip. The sample (*3i*) is retracted from the NV tip.

turn off the magnetic field at a given cryogenic temperature. However, we see a good agreement between the literature value [51] and our center frequency in Fig. 3.9(b).

Independent of the fitted (B, θ_B) values, the magnetic field strength along the N-V-axis clearly changes in Fig. 3.9(b). The increase of the splitting during cool-down can have two possible origins: First, the magnet might drift into a position that gives a stronger on-axis component. This seems rather unlikely, also since the magnet was already quite well aligned at room temperature. On top of that, the expected thermal shrinking [78] of the titanium frame is 0.14 % between room and base temperature (14 µm per 1 cm distance). Of this change, only 0.02 % happen between 100 K and 35 K (2 µm per 1 cm distance). Based on the magnetic field simulation in Fig. 3.8, a gradient of [1.1 µT (32 kHz) per 1 µm] can be extracted. The change in Fig. 3.9(b) would amount to an overall thermal drift of ~ 0.5 mm, which is implausible. Further, one would expect a drift in the same direction and significantly less change below 100 K, which is both in contrast to Fig. 3.9(b). This makes the second possible origin of the splitting most likely: the magnetization of the magnet changes as a function of temperature. Indeed, NdFeB has a transition from an easy-axis to an easy-cone magnetization around a temperature of 135 K [80]. A comparison with the reported transition in Ref. [80] shows that the change we see in both angle and field strength has a similar qualitative behavior and the same order of magnitude as Fig. 3.9(c). This motivated the change to a different magnet material, which does not show such a transition. For the future, we change to MG28 grade Samarium Cobalt (Sm_2Co_{17}) magnets from megamagnete.ch with a remanence field of 1.06 T.

3.4.4 Expansion matching design

Another important engineering aspect of a variable-temperature microscope is the thermal expansion of materials. Titanium was chosen as a material for the frame structure (*4*) (see Figs. 3.1, 3.2) for three reasons. First, the attocube stages are also made of titanium. This minimizes the relative movement of components due to thermal expansion/contraction. Second, titanium has a low thermal expansion compared to other metals [78], which further reduces the relative drift of components. Third, threads in titanium do not wear down in contrast to copper, which is used for the parts of the cooling structure (*3*). Fig. 3.9 shows the potential drift of the magnet and the microwave antenna relative to the NV center over two thermal cycles. The confocal spot shows a lateral displacement on the order of 20 µm relative to the objective when cooling from room to base temperature (*cf.* widefield image in Fig. 3.7(c)). At the same time, the confocal spot shifts by around 100 µm downwards, as expected from the size of the titanium frame structure and the thermal expansion coefficient of titanium [78]. However, due to the all-titanium design, the relative distance in z-direction between the sample and the probe only changes on the order of 20 µm. This minimizes the re-alignment effort for scans at variable temperatures and the potential to lose the spot of interest on the sample.

The thermal expansion also needs to be considered in the choice of the screw materials. We will discuss in Sec. 3.5.2 that the force of bolted joints can determine their thermal conductance. Therefore, screws need a higher thermal expansion coefficient than the parts they press together. Brass is a common choice for the material of screws

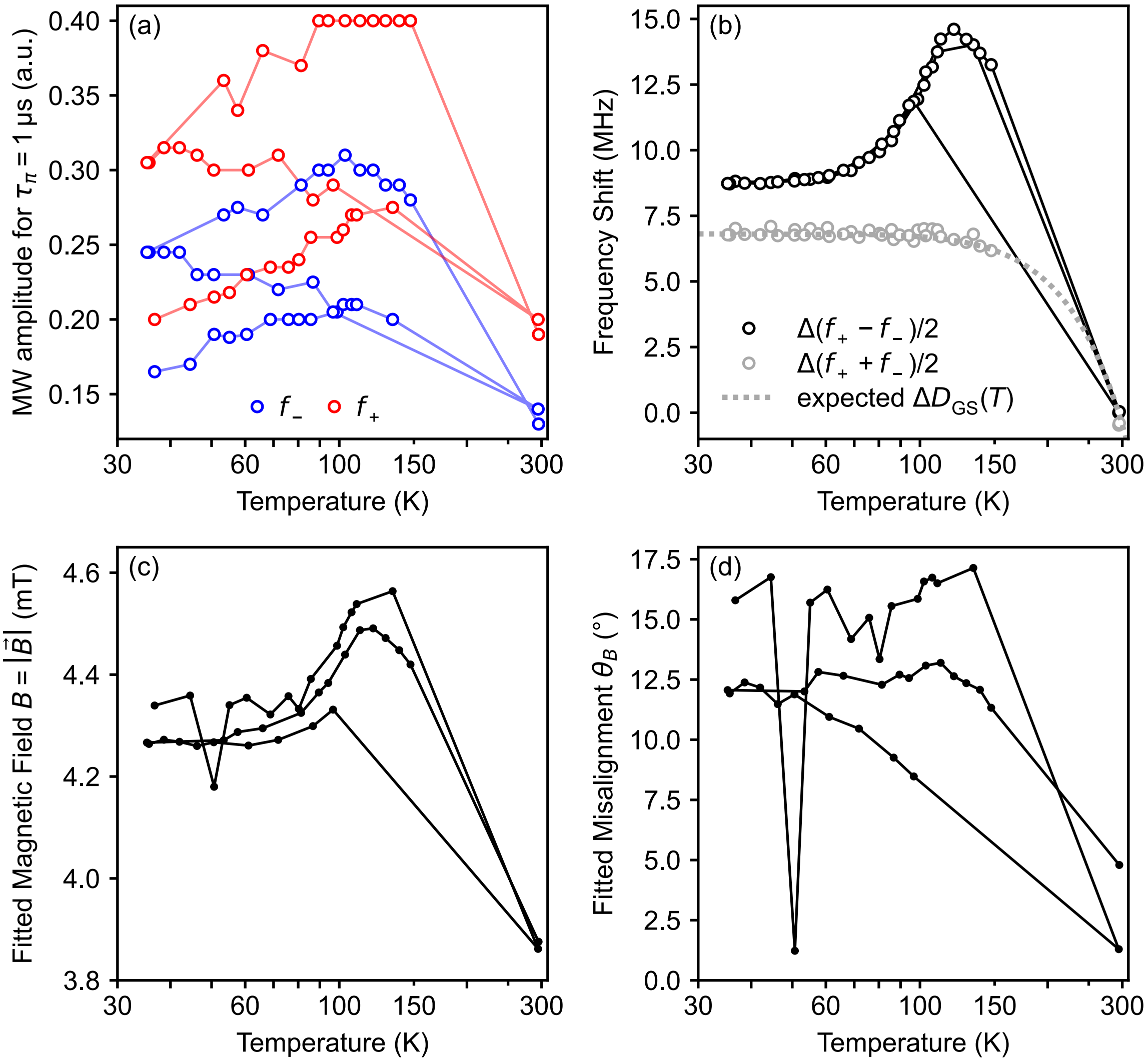

Figure 3.9: Potential thermal drift of components and frequency shift of the NV ZFS. (a) Drift of the microwave antenna relative to the NV center during the experiments with NV-5 from Fig. 2.2(b,d). The drift is plotted by the change of the microwave amplitude needed to obtain a π-pulse with a duration of 1 µs. Solid traces in all panels (a–d) indicate the temporal order of measurements during two thermal cycles. While the magnet drifts in the next panel are reproducible with temperature, the relative movement of the microwave antenna is not reproducible. (b) Change of the ODMR resonances as a function of temperature. To estimate the drift of the magnet position, the relative shift $\Delta(f_+ - f_-)/2$ can be considered. A significant change in the strength of the magnetic field is observed (see Eq. 2.3). As discussed in the text, this might originate from a drift of the magnet induced by the thermal expansion of parts in the setup. But a more likely explanation is a reproducible change of the magnetization of the magnet with temperature. Based on a good agreement between the center frequency $\Delta(f_+ + f_-)/2$ and the expected ZFS from Eq. 2.3, the magnitude and direction of the magnetic field can be fitted with Eq. 4.1. The fit result is shown in parts (c) and (d). The magnet configuration shown in Fig. 3.8 was used.

in cryogenic applications [78] as it fulfills this requirement for copper and titanium parts. A superior choice could be bronze due to a potential zinc out-gassing of brass at elevated temperatures and in high vacuum. But bronze screws are uncommon, and the out-gassing of zinc should not reach a problematic level for us since even at the highest temperature of 350 K, the vapor pressure is significantly lower than our vacuum pressure [78]. Nonetheless, the home-built components with threads are made of bronze (*e.g.* the fastening parts of the radiation shield). It should be noted that a common way to maintain a constant force over temperature is to use (conical spring) Belleville washers. However, placing them with the given space constraints of the setup is difficult, and therefore, they are only used in the platform.

3.5 Temperature management

The motivation for a closer investigation of the temperature management in this thesis was that in a previous design of VarTMa, the base temperature that could be reached at the sample and NV center was around 35 K (see NV-5 in Fig. 2.2(d)). According to Murphy's law, this temperature also constitutes the point of minimal sensing performance, as it will be derived in Ch. 4. Further, the range of sample phenomena that can be investigated is significantly reduced with such a high base temperature. In this section, we will discuss the various engineering steps that allowed us to reach a base temperature of 6.3 K.

In the following, we will first compare the different joints (welded surfaces in Sec. 3.5.1, bolted surfaces in 3.5.2, and cooling braids in 3.5.3) present in the cooling structure (*3*) (see Figs. 3.1, 3.2). For this, we will calculate their thermal conductance (*cf.* Eq. 3.1)

$$\dot{Q}_{\mathrm{cond}}/\Delta T = \kappa A/l\,. \tag{3.2}$$

Afterward, we will calculate the external thermal load from wires in Sec. 3.5.4 and radiation in Sec. 3.5.5. Finally, we will compare these values and discuss the overall performance in Sec. 3.5.6.

3.5.1 Welded joints

Two kinds of welded joints are used in VarTMa. The cooling posts are connected to the cooling braids by electron beam welding conducted by the SwissBeam AG in Rudolfstetten. Before the braids can be welded to the copper parts, a kind of swaging is required (see the top end of the cooling posts in Fig. 3.3). Generally, swaging yields the best results in terms of thermal conductance between a braid and a solid copper part, but the footprint of this technique is too large for the space constraints in our setup.

Therefore, a process for tungsten inert gas (TIG) welding of the braids to the sample mounting plate and ankers was developed. The key steps are explained in the following, together with Fig. 3.10: Initial cleaning of all parts (acetone, isopropanol, ultra-pure water in an ultrasonic bath) is critical to avoid burned contaminations in the welded

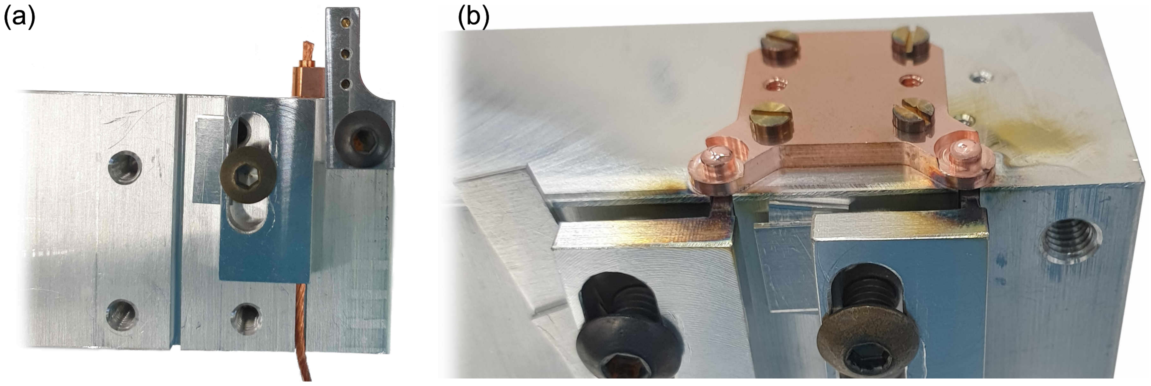

Figure 3.10: Welding of cooling braids. (a) Before TIG welding of an anker part of the copper cooling system. (b) After the welding process of a sample mounting plate. The tarnishing of the copper was minimized by the cooling block design. Afterward, the parts were gold-plated.

joint. For the welding, the parts are tightly mounted on a cooling block designed for this purpose. To prevent oxidation of the braids, they are gently pressed into a gap in the cooling block (see Fig. 3.10(b)). A 50:50 mixture of Helium and Argon gas at a flux of each $11\,\mathrm{L\,min^{-1}}$ is used. The welding should happen during a single strike of the welding arc. For the ankers, a (DC) current of 33 A, for the sample mounting plate of 44 A, is used with several minutes of cooling between the two spots.

3.5.2 Bolted joints

For bolted joints, two factors can improve the thermal conductance (both linearly). First, a larger flat contact area — ideally coated with N-grease. Second, the bolting force (independent from the area) — ideally between gold-plated surfaces. Depending on the contact area and the bolting force, the first or the second can dominate [78]. In our setup, we have examples for both cases: First, an example of an areal contact between polished surfaces is the sample holder to its mounting plate (*3d*) (see Fig. 3.1). Here, large forces should be applied with care due to the delicate attocube stages. Second, an example of a high force between polished gold-plated surfaces is the cold finger to the platform (*1*). The other joints of the cooling structure (*3*) are between these two cases, but space constraints do not allow for large contact surfaces. Thus, the system was designed with as much force by screws as possible, contact surfaces are deburred and were also slightly greased [81]. A small amount of grease was also used for the platform joint. This might limit the conductance, but due to the large contact area, fix it at a very high level. On the other hand, no grease was used at the sample, despite probably increasing the conductivity, since grease can be harmful to the attocube stepper motors, and the sample is changed regularly. Additionally, as we will see below, the bottleneck in the thermal conductance to the sample holder are the cooling braids.

According to the discussion above, a lower bound on the thermal conductance of our bolted joints can be found from the preload force exerted by the screws. The grade of our brass screws should be around 4.6. With known friction values between the screw and the materials, the maximum possible preload can be calculated [82]. It is obtained at the maximum possible tightening torque, which we apply with a torque-meter wrench. In the following, we use a friction value of 0.1. The actual value is probably higher for our cases, which increases the permissible torque and reduces the maximum preload. This estimation yields torques of around 6 cN m/12 cN m/44 cN m for M1.6/M2/M3 screws and maximum possible fores of roughly 24 kg/40 kg/98 kg. The value of the forces needs to be corrected by dividing by a factor of roughly 2 to obtain minimal realistic values. However, we used to tighten the brass screws with a higher torque and have very rarely torn off a screw head. In the scheme from above, this would result in an assumed grade of 5.8 with the torques we use in practice of 11 cN m/22 cN m/77 cN m for M1.6/M2/M3 screws and maximum possible forces of roughly 42 kg/69 kg/171 kg. Given these considerations, we should be able to assume that the force per any screw is higher than 10 kg. Since the gold plating determines the thermal conductance, we find for a force of 10 kg (*i.e.* per screw) a value of around [78]

$$\dot{Q}_{\mathrm{cond}}/\Delta T = 45\,\mathrm{mW\,K^{-1}} \tag{3.3}$$

at 4 K. Remarkably, the value would be a factor 20 smaller if the copper was not gold-plated.

3.5.3 Cooling braids

To obtain the thermal conductance of the cooling braids, we translate them to an effective solid rod. We obtain a cross-section of only $A = 0.74\,\mathrm{mm}^2$ by the weight of a single braid with a certain length and the density of copper. At this point, we can conclude that the cooling braids dominate the thermal conductance when they are in series with solid copper structures. Further, we use the conductivity of OFHC copper at 4 K with $\kappa = 300\,\mathrm{W\,m^{-1}\,K^{-1}}$ [78]. The two braids of length 35 mm between the sample mounting plate and the titanium frame structure are then found to have a thermal conductance per braid of

$$\dot{Q}_{\mathrm{cond}}/\Delta T = 6.3\,\mathrm{mW\,K^{-1}}\,. \tag{3.4}$$

The twelve braids between the cooling posts (*3a*) (see Figs. 3.1, 3.2) and the titanium frame structure have a similar length and thus each a similar thermal conductance.

The cooling of the sample holder through the attocube stack is expected to be negligible. On the one hand, the thermal conductivity of titanium is more than two orders of magnitude lower than for OFHC copper [78]. On the other hand, the bearings inside the attocube steppers are not expected to transmit heat well.

3.5.4 Wires

The choice of the wire material and their length was discussed in Sec. 3.3.4. With Eq. 3.1 the thermal load of each of them can be calculated under the assumption that the laggings, as described there, completely thermalize the wires. The results are presented in this section.

The most temperature-sensitive element, the sample holder, is only connected by long Manganin wires. A 38-AWG wire of length 10 cm contributes with just

$$\dot{Q}_{\mathrm{cond}} = 0.007\,\mathrm{mW} \tag{3.5}$$

here. The sample heater is connected with two of those, while the thermometer has four (but each with length $\sim 20\,\mathrm{cm}$).

The 26 phosphor-bronze cables (17 cm to the lagging, 36-AWG) of the attocube stages contribute with a thermal load per cable of only

$$\dot{Q}_{\mathrm{cond}} = 0.013\,\mathrm{mW}\,. \tag{3.6}$$

At this point, it is interesting to compare their heat load with a setting where the wire material is copper: this would increase their thermal load to 33 mW, which would be the dominating heat source by an order of magnitude and underlines the importance of an appropriate wiring scheme. It is also interesting to consider the effect of the thermal lagging. Under the assumption that the wires do not thermalize at all, and assuming still the same lengths, each thermal load increases by a factor on the order of 50 [78, 79].

Concerning the AC cabling, typical semi-rigid 0.047 inch coax cables with silver-plated stainless steal as a conductor have roughly

$$\dot{Q}_{\mathrm{cond}} \approx 1\,\mathrm{mW} \tag{3.7}$$

at a length of around 20 cm over the 30 K to 4 K step. Comparing the heat load from the four SMP cables to the other sources of heating, they can be identified as the dominating contribution. Since they are only indirectly connected to the sample, their load on the 4 K *system* is comparatively less harmful. However, the one SMP cable to the tuning fork might affect the temperature of the NV center.

3.5.5 Radiation

Since the inside of the cryostat is under high vacuum, thermal radiation is the major heat exchange mechanism between the inner surfaces of the radiation shield and the 4 K *system*. The thermal load [78] by the exchange of radiation between two parallel surfaces of area A and temperature T_i is

$$\dot{Q}_{\mathrm{rad}} = \sigma A \left(T_2^4 - T_1^4\right) \left(\frac{1}{\epsilon_1} + \frac{1}{\epsilon_2} - 1\right)^{-1}\,, \tag{3.8}$$

with the emissivity ϵ_i (the reflectivity is $1 - \epsilon_i$) and the Stefan-Boltzmann constant $\sigma = 5.67 \times 10^{-8}\,\mathrm{W/m^2/K^4}$. The goal of engineering the thermal radiation properties is to reduce the emissivities at the relevant temperature/IR wavelength. The values that ϵ_i assumes range from close to unity for backbody-like surfaces (plastic, glass, organics, water, *etc.*) to values well below 0.1 for polished, and ideally gold-plated metal surfaces. The surface quality alone can alter the emissivity by more than an order of magnitude [78]. Generally, rough, oxidized, or water-absorbing surfaces, as well as fingerprints, are to be avoided. The latter is the reason why, generally, gloves have to be worn when handling parts of the cryostat, together with out-gassing of fingerprints. The former is the reason for the gold plating of the copper parts and the electropolishing of the titanium parts, together with improved thermal contacts.

We now calculate the thermal load on the 4 K *system* due to thermal radiation. For our setting, the surface of the radiation shield is at $T_2 \approx 30\,\mathrm{K}$ and gold-plated, which gives $\epsilon_2 \approx 0.013$ [83]. We approximate the area A to be the inner surface of the radiation shield, which is $A \approx 0.02\,\mathrm{m}^2$. In this, we ignore the bottom face of the cylindrical shape, which is mostly covered by the well-cooled platform of the 4 K *system*. For the dominating surface of the cryostat inside, we assume the polished titanium of the frame structure and attocube stages. This assumption yields $\epsilon_1 \approx 0.05$ at 30 K [83]. In practice, the gold-plated cooling structure with better emissivity, as well as coated cables and plastic pin headers with worse emissivity, are also present. Moreover, cavities in the complex surface of the 4 K *system* result in high absorption. Finally, since the emissivities here drop with temperature, the actual value at $T_2 \approx 4\,\mathrm{K}$ is lower than the 30 K assumed above. We note that the temperature-sensitive area around the sample is designed to have the beneficial emissivity that gold plating yields, but it is also capped with a part of the radiation shield that has significantly worse emissivity (glass window and adhesive bottom layer of the cover tape (*2e*), see Fig. 3.1). Adding radiation-shielding parts mounted on the 4 K *system* around this sensitive area should further reduce radiative heating but are difficult to incorporate due to space constraints.

Overall, due to the complex spatial distribution of materials and temperature, the calculation should only be seen as an estimate of the actual impact on the sample temperature. The assumptions yield in Eq. 3.8 that

$$\dot{Q}_{\mathrm{rad}} \approx 0.01\,\mathrm{mW}\,. \tag{3.9}$$

If we assume instead that the emissivity of the inner surface is like a blackbody with $\epsilon_1 = 1$, the value of $\dot{Q}_{\mathrm{rad}}$ only increases by 20 %. However, if we only (additionally) set $\epsilon_2 = 1$, it increases by a factor 5 ($1/0.013 = 77$), which underlines the importance of our surface engineering. At this point, it is also interesting to investigate the effect of the additional radiation shield window (see Fig. 3.1). If we assume blackbody radiation from the cryostation lid at 300 K through the hole of $A = 100\,\mathrm{mm}^2$ in the cover tape (*2e*) this yields a direct thermal load of 50 mW onto the sample, which would be the dominating heat source by more than an order of magnitude.

Other sources of radiation can also warm up the sample, including the antenna's microwave field. The heating for pulse sequences with low microwave duty cycle or power is found to heat the sample by $\sim 0.3\,\mathrm{K}$, while a continuous microwave excitation at higher power heats the sample by about 2 K (see Fig. 3.11). The heating due to the widefield illumination is around 0.25 K, and heating due to the laser was not observed.

Thermal loads on spring-mounted structure	
radiation from the 30 K *system*	0.01 mW
conduction of the 26 attocube cables	0.34 mW
conduction of the 4 SMP cables	$\sim$ 4 mW
Thermal loads on sample holder	
conduction of the 6 thermometer and heater cables	0.028 mW
Thermal conductance of cooling system	
bolted surfaces per brass screw	$\gtrsim$ 45 mW/K
spring-mounted structure to platform (12 braids)	76 mW/K
spring-mounted structure to sample holder (2 braids)	13 mW/K

Table 3.2: Summary of the thermal budget. The heat load on the 4 K *system* is assumed to be deposited completely on the spring-mounted structure. The lagging of cables is assumed to be perfect and at 30 K.

3.5.6 Overall achieved improvement

We will now compare the unintended heating power to the cooling power of the cooling structure to discuss the base temperature that we reach at the sample. In thermal equilibrium, the cooling power of our cryostat [44] equals the heat load on it. For simplicity, we assumed above that the entire spring-mounted structure is at the same temperature (4 K) as the platform and lower part of the 4 K *system*. In practice, the temperature around the sample holder and scanner head is higher (6.3 K). At the same time, the temperature of the platform (3.8 K) is similar to stage 2 (2.8 K), and the braids at the cooling posts have a high thermal conductance. Thus, there will be a complex temperature gradient within the titanium frame structure. For the calculations of the thermal loads above, the approximation of a common temperature of 4 K of the entire 4 K *system* seems valid compared to the higher temperature of the 30 K *system*, which causes these thermal loads. However, to compare these results with the thermal conductances of the cooling structure, a temperature gradient between the platform and the spring-mounted structure and/or the sample must be assumed. We now assume that the spring-mounted structure, as one unit, receives the entire thermal load. In this picture, its temperature will equilibrate at a value at which the temperature gradient through the cooling posts to the platform results in a thermal conductance equal to the thermal loads.

An overview of the thermal loads and conductances is presented in Tab. 3.2. Among the conductances yielding the cooling power, the cooling braids play the dominating role. This underlines the importance of a design with two braids to the sample instead of only one. In fact, only considering the values in Tab. 3.2, there should be no significant temperature gradient between the spring-mounted structure and the sample thermometer or holder (thanks to the low conductivity of the chosen Manganin wires).

Among all thermal loads on the spring-mounted structure, it can be seen that the dominating one seems to originate from the SMP wires. It should be noted, though, that the assumed value is the least reliable one. When assuming the temperature

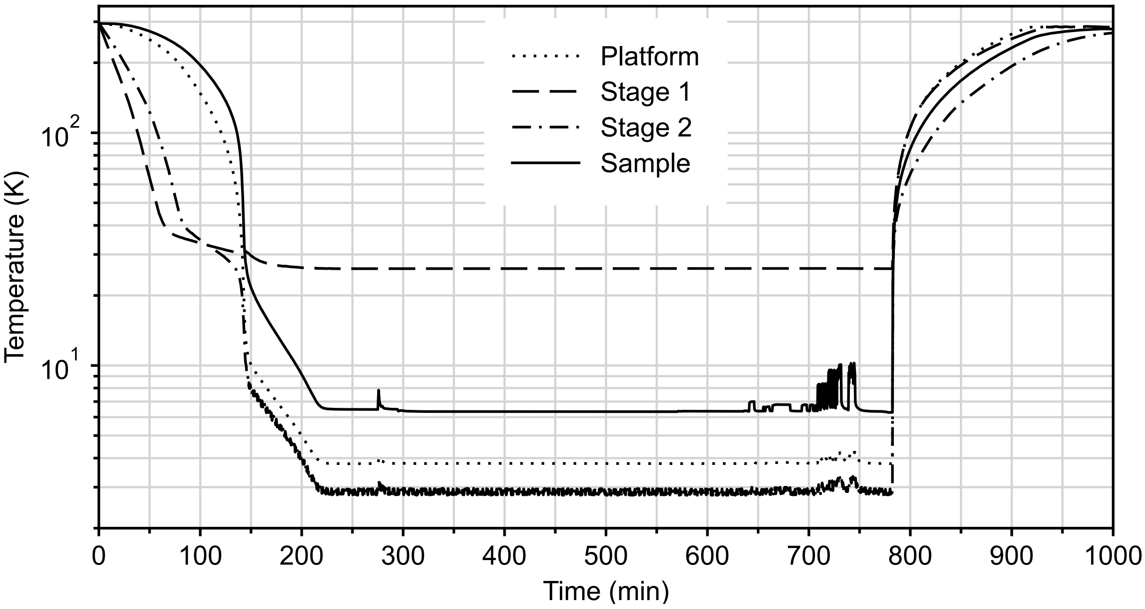

Figure 3.11: Thermal cycle after all modifications to the VarTMa setup. Spikes in the curves originate first from moving the sample into contact (image in Fig. 3.7(c) was recorded here) and second from continuous microwave excitation in ODMRs. When the heat source is turned off, the sample temperature relaxes back within $\sim 10\,\mathrm{s}$.

gradient of $\Delta T = 2.5\,\mathrm{K}$ between the spring-mounted structure and the platform, the braids of the cooling posts yield a cooling power of 190 mW. This value drastically exceeds the thermal loads in Tab. 3.2 by a factor of 43. Based on the discussion in Sec. 3.5.5, the thermal radiation should not be able to cause such a difference. The cooling power from the cooling braids might be lower than anticipated, *e.g.* due to contaminations in the welding spot. But it seems unlikely that this will cause a major deviation in the thermal budget. If the thermal lagging at the 30 K *system* is not ideal, an increase by a factor of up to 50 was given in Sec. 3.5.4. For the phosphor-bronze and Manganin wires, this still cannot explain the deviation — but for the SMP wires, it could. It also seems plausible that these thick wires, with a layered structure including an insulator and a thermally conductive core, do not thermalize well by a single lagging point in a distance of less than 5 cm from the SMP panel at 300 K. Unfortunately, the design of the cryostation makes it difficult to improve this. However, improvements in all other aspects have allowed to reach a satisfying base temperature.

In the past, several copper cables to the 4 K *system* were used; some of the large number of cables could not be thermally lagged by the two original thermal claps; the titanium surfaces were rough from the fabrication by electrical discharge machining; all surfaces were not gold-plated; there were only two long cooling braid to the titanium frame structure and only one from there to the sample; there was no cover tape closing the large gap in the radiation shield lid and no window in it was used. This old design yielded the base temperature of the sample of 35 K. With the improvements described above, the cooldown ($\sim$ 230 min) and warmup ($\sim$ 200 min) speed was significantly enhanced, and a base temperature of less than 7 K during magnetometry scans can be achieved. An exemplary cooldown and warm-up is plotted in Fig. 3.11.

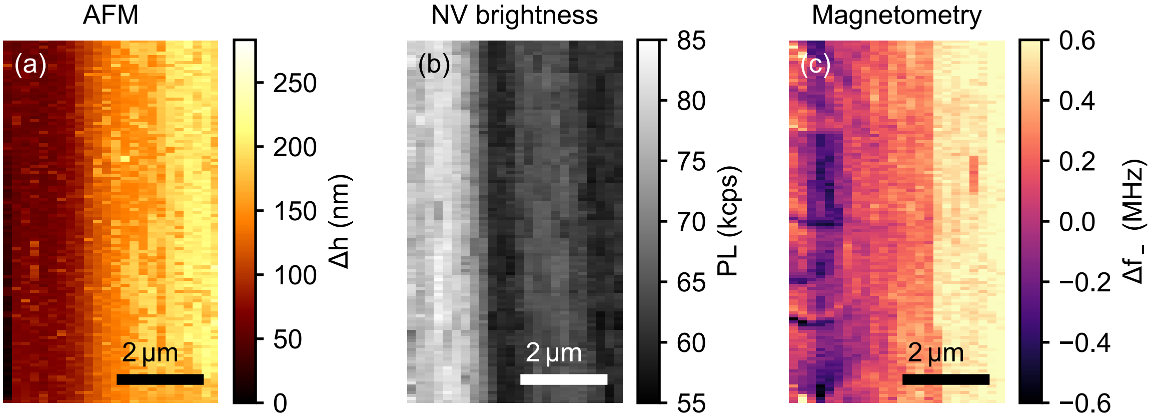

Figure 3.12: Formation of ice during a scan. Simultaneous imaging of different quantities during one magnetometry scan on the same sample as discussed later in Fig. 3.16(a) (here $T = 36\,\mathrm{K}$). The scan starts in the lower left corner, and the vertical axis is the fast scan axis. (a) There is a significant change in the AFM height with increasing time and contamination. The distances are estimated based on the calibration scan in Fig. 3.4(c). (b) The photon count rate (avg. of all photons over the full sequence duration) drops with increasing contamination. This could be due to an increased standoff distance since reflection on the sample surface generates a standing wave, which leads to an oscillation of the PL as a function of the distance [18, SI]. As the PL dropped, the contrast rose slightly to about 120 % of its initial value. (c) The spin resonance frequency first reveals magnetic structures as in Fig. 3.16. But as contaminations between tip and sample accumulate, the weak signal disappears. Measured with NV-5 in the aligned bias field shown in Fig. 3.8.

3.6 Vacuum System

3.6.1 Motivation

Two issues motivated the re-engineering of the vacuum system of VarTMa. The first was that the old design was not user-friendly since a fast turnaround was hindered by an unreliable pump-down process: forces pulling on the cryostat chamber required a person holding it in place. Often, the chamber did not align well, and a severe air leakage rate required a restart. Additionally, mounting of the radiation shield (which was one part instead of the three now: the two lower halves and the cylinder surface) had to be done with great care to not cause thermal leaks by touching the 4 K *system* or even ripping cables off.

The second issue was a poor vacuum when the system was cooled down. This caused the gradual formation of solid contaminations between the sample surface and the scanning tip, most likely due to ice formation. AFM scans above $\sim 100\,\mathrm{K}$ worked very well, while at lower temperatures, the formation of the contamination occurred gradually over timescales of a scan duration. When a large amount of this contamination accumulated at one spot, one could see in the widefield microscope how it disappeared around 200 K at 2×10^{-4} mbar. This roughly matches the sublimation point of water.

Scanning probe microscopy requires clean conditions. As can be seen in a magnetometry scan from then in Fig. 3.12, the formation of the contamination prohibited continuous measurements on the order of several days. Remarkably, the contamination only formed under the scanning tip, since at the beginning of the scan in Fig. 3.12, the system was already cold for around one week. In this section, the steps that were taken to solve the two issues are presented.

3.6.2 Mitigating ice formation

A series of common measures were taken to improve the vacuum:

- Normal leaks were identified with a leak detector and closed. At the SMP panel (*7c*) (see Fig. 3.1), Torr Seal® was applied both along the external perimeter of the plastic plate itself and around the four circular SMA plugs on it. At the D-sub panel (*10*), a LEMO® plug panel was initially used but caused leaks several times. Additionally, it had fewer wire feed-throughs than the new D-sub panel with a 25-KF vacuum connection. Finally, also the external perimeter of the top window (*7b*) was sealed.
- Venting holes were added to all enclosed cavities like tapped holes as they form virtual leaks. Another example are the openings in the platform (*1*) to the large volume under the platform.
- Only materials with low out-gassing, *i.e.* high vacuum compatibility, were used. These include the metals mentioned above, as well as PEEK for plastic parts, PTFE and polyimide and polyvinyl for tape and wire coatings, epoxy resins, ultra-high vacuum (UHV) solder (unless for a few places where the comfort of normal solder is needed) with flux residues removed.
- Mechanical parts were cleaned in an ultrasonic bath of acetone and isopropanol and only handled with gloves afterward.
- To reduce the out-gassing of the KF vacuum O-rings, they were baked out in 200 °C and stored in a dry nitrogen atmosphere. Never, solvent was used to clean them. A small amount of L-Grease was used for those that are not regularly unmounted. By design, a base pressure of 5×10^{-8} mbar can be achieved with a KF vacuum system.
- The system is kept under high vacuum whenever possible; a steady flow of dry nitrogen is used while the system is open for short maintenance like a sample or tip exchange. Purging several times with dry nitrogen helps to achieve a high vacuum faster.
- The charcoal absorbers (*2a*) (see Fig. 3.1) act as small cryopumps for the volume both inside and outside the radiation shield due to their special position within it. They can be baked out occasionally in a vacuum oven (*e.g.* at 160 °C) for reactivation.

Generally, UHV systems are often baked out to remove absorbed water from the surfaces. Our system was only designed for high vacuum (HV) and can be heated up to 350 K with the built-in heaters. This can be used to speed up the pump-down process after the system was exposed to air for a long time. However, the formation of contamination (likely ice) in SPM scans in our system is not due to absorbed water. Rather, the vacuum seals of the cryostat housing are not ideal: the PCB (*7d*) itself is part of the vacuum seal and the O-rings (*7g*) are thin (*cf.* black rings in Fig. 3.1; they leave a distance of 0.1 mm between the neighboring components in compressed state). The vacuum housing is sealed by the force of the negative pressure. Since these parameters constitute given constraints of the setup (and contribute to its user-friendly assembly and small form factor), their negative effects were mitigated by the following two measures:

- Stronger vacuum pumping by larger tube diameters and a short distance to a new, additional getter pump.
- Re-design of the radiation shield to also act as a mechanical shield against the molecular flow of gas particles entering the chamber.

The first measure will be discussed in detail together with the design of the new vacuum system in the next Sec. 3.6.3. Regarding the second measure, it can be seen in Fig. 3.1 that the new radiation shield lid (*2d*) is in close alignment with the inner chamber perimeter (of course, without touching it and creating a large thermal leak). Additionally, the cover tape (*2e*) and radiation shield window (*2f*), which were not used in the past, now avoid a line-of-sight path of gas to the sample.

3.6.3 Design

In the old design used in Fig. 3.12, the roughing pump inside the Montana Instruments control unit was already disconnected, and a turbopump (Pfeiffer Vacuum HiCube™ 80 Eco) with its own roughing pump was connected by a 1.5 m 40-KF vacuum tube to the cryostat housing. Based on this, a new design was developed. It is presented in this section, and a CAD is shown in Fig. 3.13 along with pictures in Fig. 3.15.

The rationale behind the design is the following: A flexible mount of the vacuum system is necessary because the cryostat housing moves slightly during the compression of its O-rings above and below the PCB and under the lid. But flexible vacuum components (*i.e.* bellows and tubes) also compress themselves. Thus, a significant movement is unavoidable and needs to be part of the design.

The solution that was found is: The small movement of the cryostation housing downwards (0.4 mm per O-ring, which is 0.8 mm at the 50-KF flange (*7h*)) is compensated by a 50-KF bellow (*12b*), which offers this flexibility during the pump-down process. This bellow is aligned such that it is in line with the 50-KF flange when the system is under vacuum. For this alignment, a holder (*11*) for the 63-CF T-piece (*11a*) was designed. As it can be seen in Fig. 3.13, it allows for an adjustment of all four required degrees of freedom — the lateral and horizontal position as well as the tilt in both

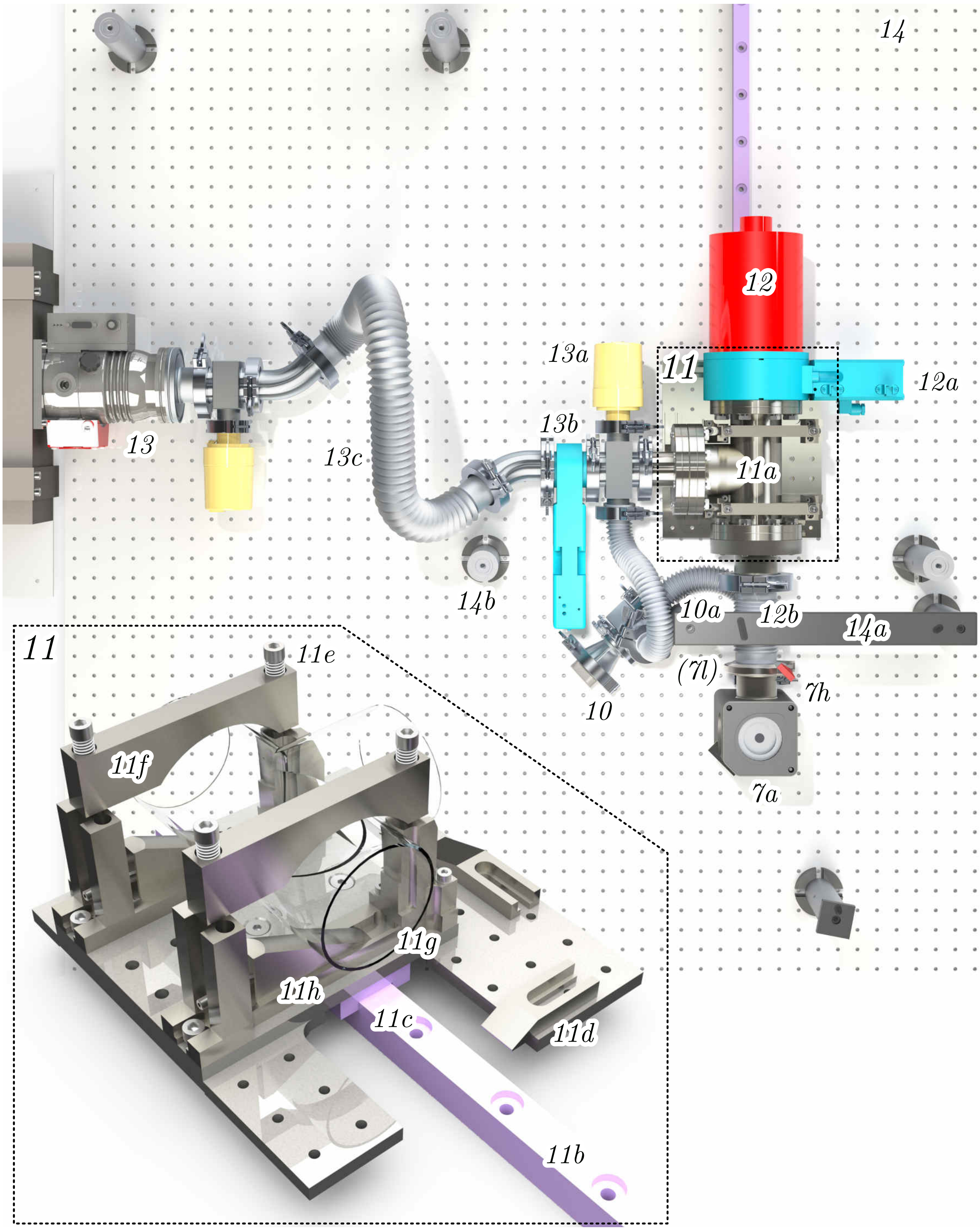

Figure 3.13: CAD model of the new vacuum system. The turbopump (*13*) and getter pump (*12*) are connected to the cryostat housing (*7*). Additionally, the D-sub vacuum feedthrough (*10*) is connected. The vacuum system is mounted with a holder (*11*, dashed line) on a slider (*11c*). The inset on the lower left shows the holder with a glass tube instead of the 63-CF T-piece (*11a*) for clarity of presentation. The design of the holder allows to align the T-piece and thus the 50-KF bellow (*12b*) to the cryostat's 50-KF flange (*7h*) in all four degrees of freedom (two angles, two axes). Component labels are defined in Tab. 3.1. Several CAD files are property of Montana Instruments®, Pfeiffer Vacuum AG, VAT Group AG, and Thorlabs Inc..

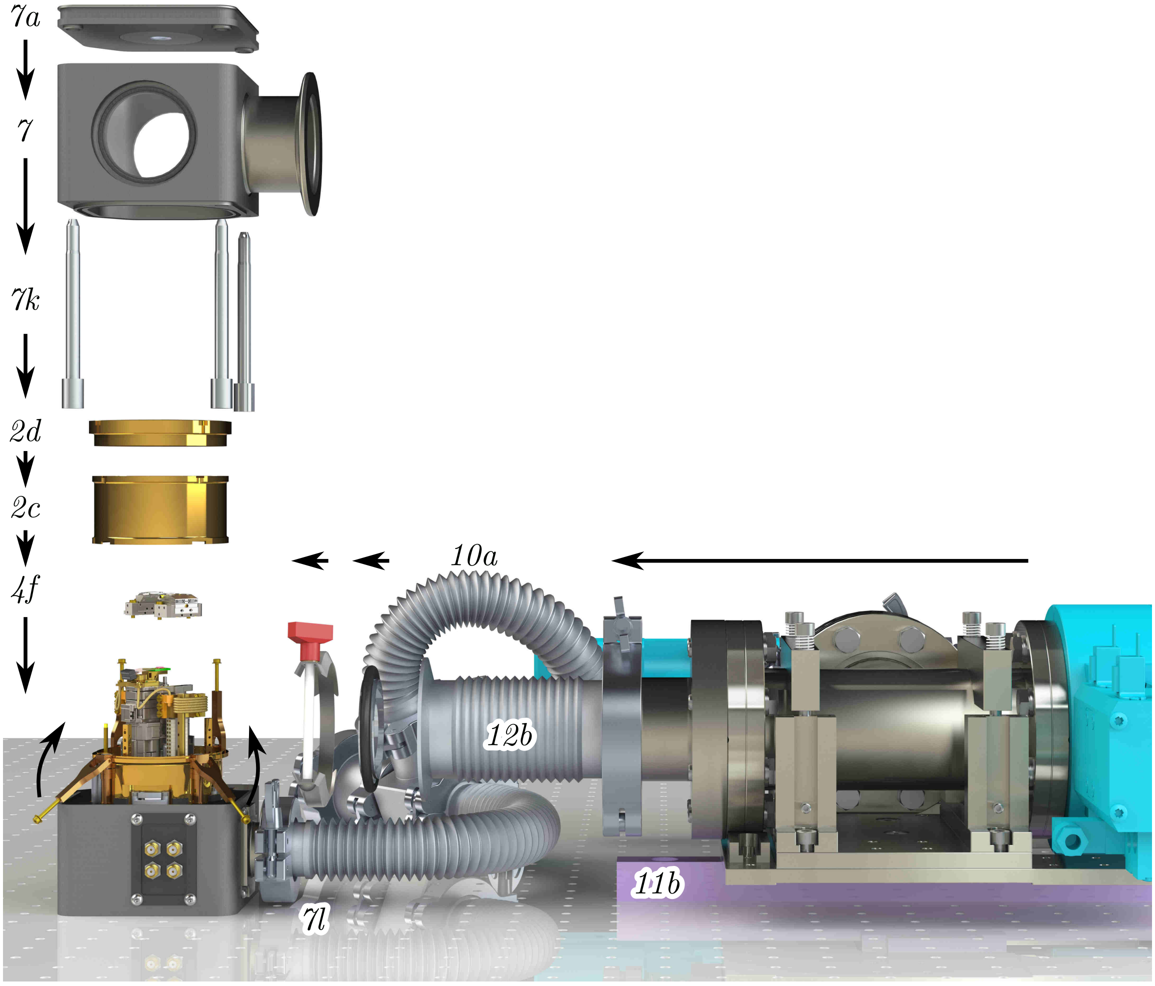

Figure 3.14: CAD models of the assembling procedure. Exploded view illustrating how the vacuum system is assembled after a sample or probe change. During pump-down, the 50-KF bellow (*12b*) compresses, and the entire vacuum system moves forward on the guiding rail (*11b*). Component labels are defined in Tab. 3.1. Several CAD files are property of Montana Instruments®, Pfeiffer Vacuum AG, and VAT Group AG.

directions. Springs (*11e*) clamp the 63-CF T-piece between the rubber-lined (not shown) yokes (*11f*) and adjustment wedges (*11h*). After an initial adjustment, the alignment was ideal and stable. The large compression of the 50-KF bellow (around 1.5 cm) during pump-down is compensated by the entire vacuum system moving forward on a slider (*11c*) (Bosch Rexroth R1651 8), as illustrated in Fig. 3.14. Connected to the T-piece is a Non-Evaporable Getter (NEG) pump (saes CapaciTorr® HV 200) (*12*), which offers a very high pumping speed for getterable gases — among which are water and carbon dioxide. The NEG pump can be decoupled by a pneumatic in-line valve (VAT Vatterfly 204) (*12a*) while the system is vented. The high vacuum rating of the valve and the CF connections in this part of the system prevent an exposure of the NEG material. If the cryostat is open for longer, the 50-KF bellow (*12b*) and 25-KF tube (*10a*) are closed with a blind flange, and the NEG pump is under vacuum provided by the turbopump. The NEG pump should be baked out approximately annually, for which it can be moved on the long guiding rail to the back and thus away from optic components above it (see Fig. 3.15). To improve the pumping speed, it can be internally kept at *e.g.* 200 °C.

The T-piece (*11a*) is further connected by a spirally shaped 40-KF flexible tube (*13c*) to the turbopump (*13*). This arrangement allows for the movement of the T-piece on the slider without strong pulling forces on the turbopump flange. This is useful during maintenance work and necessary while the slider moves forward during the pump-down process. The roughing pump of the turbopump was detached from it and is now connected by a long rubber tube to prevent unnecessary vibrations in the system. The turbopump can also be decoupled from the system by an in-line valve (VAT gate valve, Series 012) (*13b*). A drain tube (*10a*) was added between the 25-KF tube of the D-sub feedthrough (*10*) and the 40-KF tube to the turbopump (*13c*) for efficient pumping (instead of only being connected through the cryostat housing).

As can be seen in Fig. 3.14, guiding rods (*7k*) were added to the cryostat housing. This ensures a safe and accurate placement of the housing without the risk of touching the radiation shield or even exerting forces on it. Fig. 3.14 illustrates the steps to close the vacuum system: First, the cylinder surface and lid of the radiation shield are simply mounted from the top, and the mounting arms are tightened. Second, the housing is slid down on the guiding rods. Third, the 50-KF bellow is connected to the housing. Finally, the turbopump is started. The system moves safely and reliably into its vacuum state without any further interaction required by the user.

3.6.4 Achieved Improvement

In the following, we will try to estimate the improvement of the pumping speed at the cryostat housing. The effective pumping speed is given by

$$S_{\mathrm{eff}} = \left(S_{\mathrm{pump}}^{-1} + C_{\mathrm{tube}}^{-1}\right)^{-1} , \tag{3.10}$$

where S_{pump} is the pumping speed of the pump and

$$C_{\mathrm{tube}} \approx 12.1\,\mathrm{L\,s^{-1}} \cdot \frac{d/1\,\mathrm{cm}}{l/1\,\mathrm{cm}} \cdot c_{\mathrm{stick}} \tag{3.11}$$

is the conductance of the connection between the housing and the pump. For Eq. 3.11, a molecular flow (in HV) through a straight pipe with length l and diameter d was assumed. The correction factor c_{stick} is 1 for non-sticking walls (with sticking coefficient $s = 0$), but decreases rapidly with growing l/d for $s > 0$. As an example on the upper end, it is $c_{\mathrm{stick}} \approx 0.03$ for a sticking coefficient of $s = 1\,\%$ at the length and diameter of the old 40-KF tube [84]. For nitrogen, approximate pumping speeds for the turbopump ($S_{\mathrm{pump}} \approx 32\,\mathrm{L\,s^{-1}}$) and NEG pump ($S_{\mathrm{pump}} \approx 50\,\mathrm{L\,s^{-1}}$, without heating) are given. Plugging in the numbers, we find that the old value was

$$S_{\mathrm{eff}} \approx 2\,\mathrm{L\,s^{-1}} \text{ for } s = 0 \text{ and } 0.1\,\mathrm{L\,s^{-1}} \text{ for } s = 1\,\%\,. \tag{3.12}$$

In this, an additional factor of 0.5 is included for the right angle in the tube. The inverse sum of conductances in series in Eq. 3.10 shows how the capabilities of the pump can get less relevant when long or thin tubing is used. However, the turbopump should not be placed significantly closer to the cryostat due to vibrations. To that end, the NEG pump is used. It yields, with the thicker and shorter new geometry, a value of

$$S_{\text{eff}} \approx 23\,\mathrm{L\,s^{-1}} \text{ for } s = 0 \text{ and } 17\,\mathrm{L\,s^{-1}} \text{ for } s = 1\,\%\,, \tag{3.13}$$

which is relatively independent of the sticking coefficient due to the low l/d. This suggests an improvement of more than a factor of ten. In this, the higher pumping speed of the NEG material for water compared to nitrogen is not even considered.

We achieve a base pressure of $\sim 1 \times 10^{-7}$ mbar at the pressure gauge (*13a*) at room temperature and $\sim 1 \times 10^{-8}$ mbar at low temperature. Typically, we open the valve to the NEG pump at 1×10^{-5} mbar and start the cool-down once the pressure is below 1×10^{-6} mbar. This means we operate between the HV and UHV regimes. The pressure inside the almost enclosed radiation shield might be even better due to cryopumping (also by the charcoal absorbers).

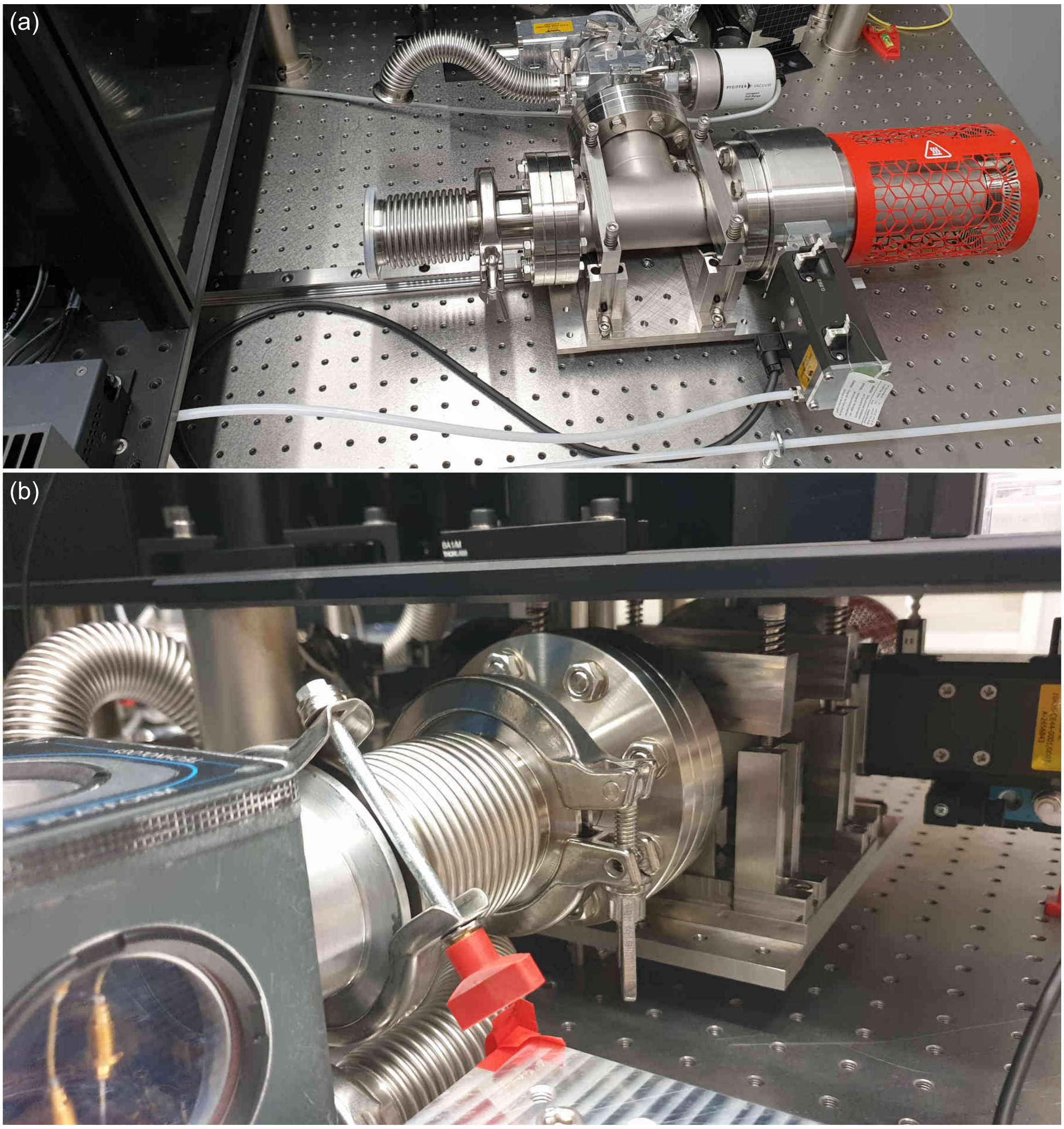

Figure 3.15: Pictures of the new vacuum system. (a) The vacuum system is detached from the cryostat housing and turbo pump and moved on the guiding rail to the back. This way, the getter pump can be baked out, or maintenance on the vacuum system can be done. (b) In normal operation mode, the vacuum system is at the front end of the guiding rail and connected to the cryostat housing. Here, the vacuum system is located underneath a breadboard on which the optical setup (top in part (b) and left in part (a)) is built.

3.7 Performance summary

In the status of the VarTMa setup as described by [44] (*i.e.* before most of the engineering efforts described above), the temperature sweeps on NV-5 were recorded. The data of these measurements is presented in Figs. 2.2, 3.9, 6.8. Here, measurements on VarTMa contributed to the project [35] by covering the temperature range between 80 K and room temperature. Designed as a variable-temperature SPM, VarTMa is relatively free of setup instabilities due to heating, in contrast to the measurements on NV-1 to NV-4 in a large dilution refrigerator (*cf.* Ch. 6). However, the base temperature around 35 K in this status of the setup did not allow us to reveal the revival of the NV performance toward zero temperature (*cf.* Fig. 2.2(d)). The concurrence at 35 K of first, the base temperature for SPM measurements on samples, and second, the NV performance minimum, posed a critical problem: as discussed in the Ch. 2.4, the sensitivity is severely impaired here, and averaging times in measurements are long. Additionally, the investigation of sample phenomena was limited to $T \geq 35\,\mathrm{K}$. Nonetheless, we recorded first quantitative magnetometry images on $\mathrm{ErMnO_3}$. An analysis of these images with respect to the setup performance is given in Fig. 3.16(a) in the next section.

By the engineering efforts described in this chapter, the 1. design goal (*cf.* Sec. 3.1) was achieved: the base temperature could be reduced from 35 K to 6.3 K. This new base temperature is low enough to profit from the revival of the NV performance toward zero temperature. At the same time, the cooldown and warmup speed was significantly enhanced, which was set as the 2. design goal. In the sense of the 3. design goal (user-friendliness), progress has been made by the new assembling architecture presented in Fig. 3.14. Importantly, it contains a more reliable vacuum system design. In the old design, the formation of contaminations under the scanning SPM tip was a severe problem, as was shown in Fig. 3.12. Now, several months of successful and continuous magnetometry scans at base temperature were done without warming up. The formation of surface contaminations seems to be completely mitigated, and we see no photo-bleaching of the NV^- center, as we heard was the case in similar setups with other research groups. We continued the investigation of the multiferroic domains on $\mathrm{ErMnO_3}$. To emphasize the progress achieved in this thesis, a new magnetometry scan at 9 K is shown in Fig. 3.16(b) in the next section.

3.8 Measurements on $\mathrm{ErMnO_3}$

A motivation for the study of rare-earth hexagonal manganites was given in Ch. 2.5. In initial cryogenic experiments on $\mathrm{ErMnO_3}$, we observed the structures shown in Fig. 3.16(a) [44]. The scans were taken after field-cooling the sample in around $0.1\,\mathrm{T} - 0.2\,\mathrm{T}$ through the Néel temperature of $\sim 80\,\mathrm{K}$, where the Mn^{3+} spins undergo a phase transition from paramagnetic to antiferromagnetic order. Instead of the sample holder presented in Fig. 3.5, a specifically designed sample holder was used to provide the field for field-cooling by the permanent bias magnet (shown in inset of Fig. 3.16(a)). After the sample base temperature of 35 K (before the re-engineering from above) was reached, the magnet was retracted and moved laterally to decrease the misalignment with the N-V-axis. Based on the method in Sec. 3.4.3, a misalignment of 63° and field of 7.8 mT is found. For this reason, we do not convert the frequency shift to magnetic field values. Nonetheless, the magnitude of the signal in Fig. 3.16(a) is similar to a theoretical prediction for the canting of the Mn^{3+} spins in the A_2 symmetric phase [70]:

The observable magnetic field above the surface depends only on the domain walls and the transient states that occur in them. In case the A_2 symmetric state occurs as a transient state in such a domain wall (which it can for the B_2 symmetric domains of $\mathrm{ErMnO_3}$ [63]), it is expected to carry a net magnetic moment in the out-of-plane axis due to the slight canting of the Mn^{3+} spins in the trimers [70]. The associated magnetic moment is predicted to be

$$\sigma = \frac{2}{3}\frac{M_{A_2} N l_+}{V_{uc}} = 0.5\frac{\mu_B}{\mathrm{nm}^2} \tag{3.14}$$

per domain wall area (with the same direction as the electric polarization: out-of-plane in our sample). Here $M_{A_2} = 1.4 \cdot 10^{-2}\mu_B$ per Mn^{3+} ion is due to the A_2 state in the domain wall, $N = 6$ the number of Mn^{3+} ions per unit cell, and $V_{uc} = (0.614\,\mathrm{nm})^2 \cdot 1.14\,\mathrm{nm}$ the size of a unit cell [85]. Domain wall sizes are expected to be $l_\pm = 4\,\mathrm{nm}$ to $9\,\mathrm{nm}$ [70]. This would generate a magnetic field of $\sim 20\,\mathrm{\mu T}$ ($\Delta f_- = 0.56\,\mathrm{MHz}$ for aligned bias field in Eq. 2.3) at a typical NV center standoff distance (75 nm were assumed as found in the last paragraph of this section). It shall be noted here that below $\sim 5\,\mathrm{K}$ the Er^{3+} spins can also undergo another phase transition to a ferromagnetic state [63, 69], and a Mn^{3+} ordering in A_2 symmetric domains can be observed [63, 69].

The match between Eq. 3.14 and the first quantitative $\mathrm{ErMnO_3}$ image in Fig. 3.16(a) at 35 K is without considering a significant amplification by coupling to Er^{3+} spins. However, Geng *et al.* [32, 69] attributed their (non-quantitative) signal dominantly to Er^{3+} spins, which couple by Dzyaloshinskii-Moriya interactions to the Mn^{3+} spins. We are investigating the nature of the magnetic signal further by quantitative reconstruction of the surface magnetization as a function of temperature when approaching the Néel temperature of $\sim 80\,\mathrm{K}$. Additionally, our measurements on $\mathrm{YMnO_3}$ showed no magnetic signal [44]. In contrast to $\mathrm{ErMnO_3}$, $\mathrm{YMnO_3}$ forms B_1 symmetric domains [63], and Y^{3+} is not magnetic. In new $\mathrm{ErMnO_3}$ scans at a lower temperature of 9 K (after the re-engineering from above), as in Fig. 3.16(b), magnetic signals are observed without the application of a field while cooling through the Néel temperature.

Finally, some typical scanning NV performance characteristics can be investigated. Based on a calibration of $48\,\mathrm{\mu m\,V^{-1}}$ for our open-loop xy-sample scanner (see Sec. 3.3.1 and Fig. 3.4(b)), the NV standoff distance can be estimated. For this, the expected magnetic field originating from a narrow (infinitely deep) magnetic stripe is fitted to linecuts in the marked area in Fig. 3.16(a). This evaluation yields a value of

$$\text{NV standoff distance} = 75(4)\,\mathrm{nm}\,. \tag{3.15}$$

Further, the field resolution can be estimated from the other marked area in Fig. 3.16(a). A Gaussian distribution with a standard deviation of 67 kHz is found. An averaging time per pixel of 20 s and a FWHM of $\nu \approx 1\,\mathrm{MHz}$ with $C \approx 7\,\%$ is used. Based on

Eqs. 2.3 and 2.4, this gives a magnetic sensitivity of

$$s = 11\,\mathrm{\mu T}\sqrt{\mathrm{s}}\,. \tag{3.16}$$

The sensitivity here is comparatively low since this experiment was conducted in regime (II) in Fig. 2.2(d) with significantly reduced NV sensing performance.

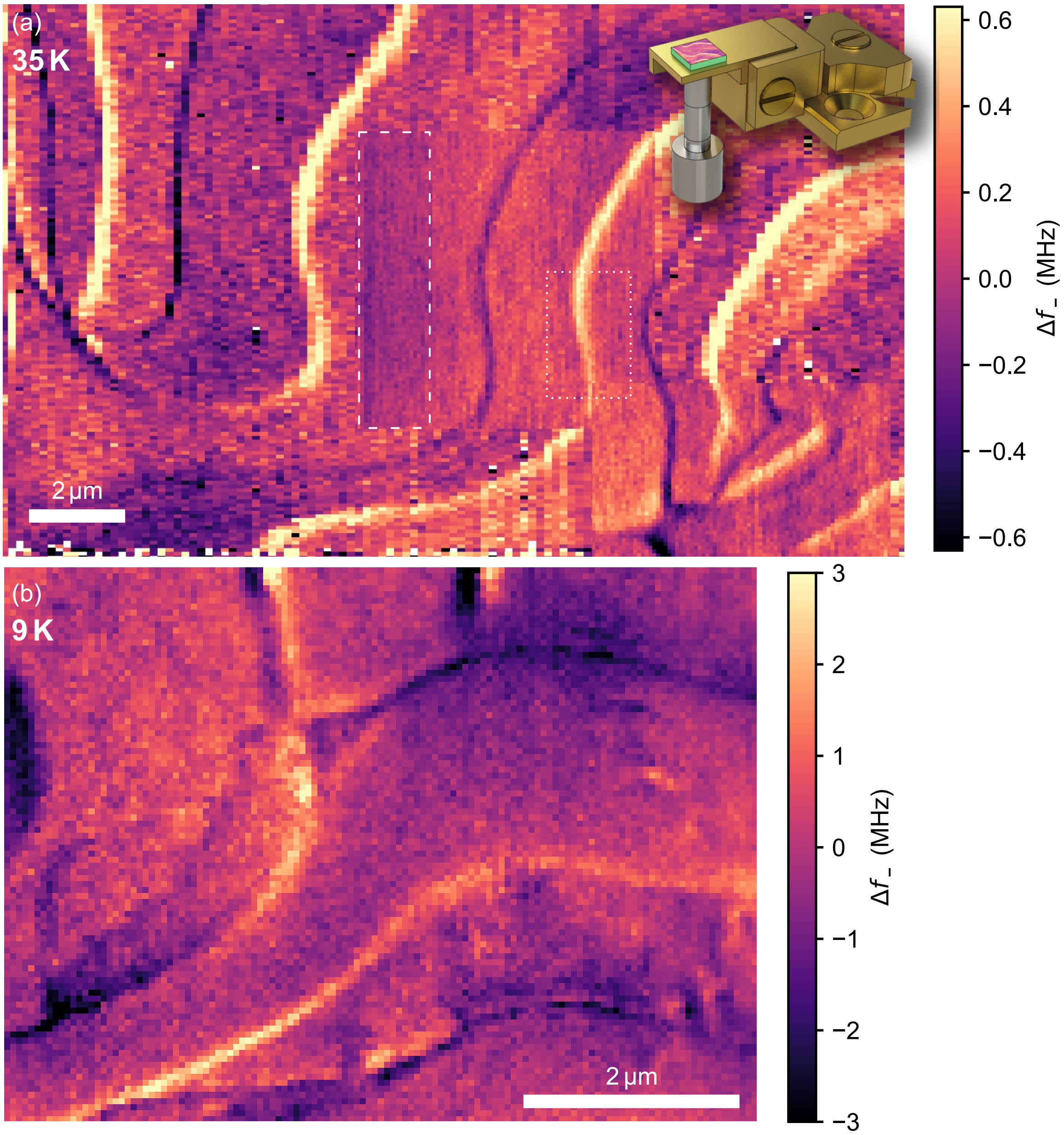

Figure 3.16: Cryogenic magnetometry scans on ErMnO$_3$. (a) Several stitched scans reveal a weak magnetic structure as previously observed by Geng *et al.* [32]. The areas used for a standoff distance (dashed line) and noise (dotted line) evaluation are marked. Inset: render of the sample holder (*3f*) with magnet stack (*8*) and sample (artistic impression) during field-cooling in ~ 0.1 T to 35 K, as used in this measurement. The experiments were performed in the VarTMa setup before the most changes described in this chapter. Reproduced from Lorenzelli [44], where a detailed description of the measurements can be found. (b) Scan on the same sample at 9 K after the setup changes described in this chapter. Here, the sample was cooled through the Néel temperature without an external field. The signal is stronger than in part (a).

CHAPTER 4

Modeling temperature-dependent dynamics in the NV excited state

Most of the text and figures in this chapter were published in Refs. [35, 36]. They were adapted and combined for this thesis. Additionally, parts were added to provide a more complete picture. These parts include the phonon wavelength considerations (Sec. 4.3.4), the comparison to motional averaging (Sec. 4.4.2), the origin of revivals (Sec. 4.4.5), the laser polarization dependence (Sec. 4.4.6), and the classical rate models (Sec. 4.5). For the most part, I developed the considerations presented in this chapter. On numerous topics, exchange with and work by Patrick Scheidegger was essential for our progress in this project. The development of the model presented in this chapter was driven by the experimental observations that are addressed in chapter 6 (see there for detailed contributions) — these measurements were, for the most part, conducted by Patrick Scheidegger and Simon Diesch. Simon Diesch and Christian Degen also supported us in developing the considerations presented in this chapter. In a collaboration during the early phase of the project, discussions with Dominik Irber and Friedemann Reinhard were important. Dominik Irber provided the first version of the code to calculate the low-temperature ES level structure. Further, Assaf Hamo, Konstantin Herb, William Huxter, Erika Janitz, Fedor Jelezko, Patrick Maletinsky, Jörg Wrachtrup, and Jonathan Zopes provided important input.

In this chapter, the development of a model for the temperature-dependent photophysics of the NV$^-$ center is first motivated by an overview of the previous understanding (Sec. 4.1). The framework of our numerical rate model is explained in Sec. 4.2. We present the electronic, spin, and orbital level structure at cryogenic temperature (Sec. 4.2.1) and introduce transition rates between these levels. These include transition rates to model the population dynamics under optical excitation (Sec. 4.2.2), and spin-coherent, phonon-induced transitions between orbital states, which give rise to an additional temperature-dependence (Sec. 4.2.3). We then implement this rate model using the Lindblad master equation approach (Sec. 4.2.4) with jump operators (Sec. 4.2.5), and describe how to obtain experimental observables like the SNR (Sec. 4.2.6). The crucial component in the model is the interaction of the orbital state of the NV$^-$ with the phonon bath. The required phonon-induced transition rates are derived in detail in Sec. 4.3. In Sec. 4.4 we use our model to simulate the temperature dependence of the ES spin dynamics. We identify a prominent spin-lattice relaxation process at intermediate temperatures (Sec. 4.4.1), which we verify with independent Monte Carlo simulations. A comparison with the common phenomena of motional averaging in liquid state NMR is then made (Sec. 4.4.2).

Afterward, we discuss dependencies of the photo-physics on crystal strain and electric field (Sec. 4.4.3), on magnetic field (Sec. 4.4.4), on their combination (Sec. 4.4.5), and finally on the polarization of the excitation laser (Sec. 4.4.6). As a last step, the Lindblad master equation-based model is compared with common classical rate models (Sec. 4.5), which were developed for the so far distinct regimes of cryogenic and room temperature. The model parameters used for the simulations in this chapter are found in Ch. 6 by fitting of measurement data recorded for this purpose.

4.1 Need for a unifying model covering all temperatures

The optical preparation and readout of the spin state relies on an optical cycle that is mostly spin conserving [86, 87] (see Ch. 2.1): Since the ISC is strongly spin-dependent, the NV^- spin states have different average emission rates, and prolonged illumination leads to a preferential population of the $m_\mathrm{S} = 0$ spin state. This mechanism is used for initialization and readout of the quantum spin state, for example, in sensing experiments as discussed in this thesis. Although this basic mechanism for spin contrast and spin polarization is well known, the detailed population dynamics in the ES are not entirely understood [34]. In particular, transitions between the ES sublevels show a marked temperature dependence that can lead to rapid spin relaxation and impair the optical readout, as was preempted in Fig. 2.2(d). At cryogenic temperature, the ES is known to be an orbital-doublet, spin-triplet consisting of six distinct sublevels [87–89]. At room temperature, the ES is averaged to an effective orbital-singlet, spin-triplet [1] through phonon-driven transitions [40, 42, 89, 90]. This phonon interaction within the ES has been attributed to a dynamic Jahn-Teller effect [41, 91]. The phonon-induced mixing rate of the vibronic states of the ES has been determined in cryogenic experiments [92–94]. However, the lack of a fundamental model unifying the rate models at cryogenic [40, 93, 95] with those at room temperature [86, 96] remained a central gap in the understanding of NV center population dynamics.

In this chapter, a comprehensive model of the NV^- center's spin dynamics is presented, spanning the full temperature range from the low- to the high-temperature regime. It is shown that the interplay of spin and orbital dynamics in the ES leads to rapid spin-lattice relaxation at intermediate temperatures, even for NV centers with zero intrinsic strain. Further, the effects of applied magnetic and electric bias fields, as well as crystallographic strain, on the level structure and population dynamics are included in the model. These parameters constitute key quantities in metrology [12–16] and have previously been used to fine-tune the NV^- center properties [97, 98] for information technology. Using a master equation approach, we simulate key experimental observables, including the PL, the spin contrast, and the SNR. Since the experimental methods to probe the ES dynamics involve the full optically active and non-active cycles (*i.e.* GS and SS), this chapter discusses the rate modeling of the entire NV^- center, not just the ES. However, the additional dynamics in the ES are the new addition that allows for a unifying model of the two temperature regimes. Building on this model, this chapter reveals and discusses a rich dependence on the system parameters strain, electric and magnetic fields, and temperature.

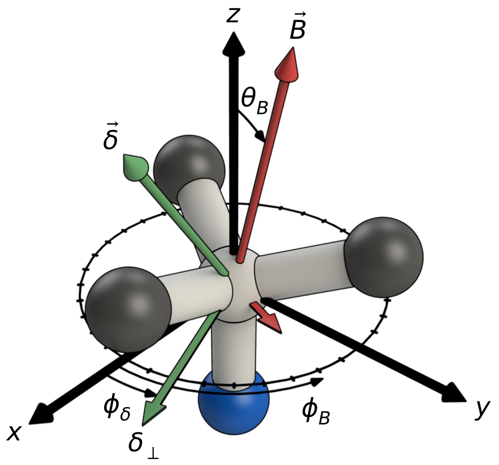

Figure 4.1: NV center coordinate system used in this thesis. Carbon atoms are shown in black, the substitutional nitrogen atom in blue, and the vacancy and covalent bonds in gray. The x-axis is in-plane along one of the carbon bonds. $\overrightarrow{B}$ is the applied magnetic field (red), $\overrightarrow{\delta}$ the strain or electric field (green), and $\delta_\perp$ its in-plane component. The remaining symbols are explained in the text.

4.2 Rate model

4.2.1 Level structure

We begin by introducing the coordinate system of the NV center in the diamond lattice in Fig. 4.1 (see also Fig. 2.1(a)). We define the z-axis by the unit vector along the symmetry axis of the NV center pointing from the nitrogen atom towards the vacancy site, and the x-axis by one of the three in-plane vectors pointing from the vacancy to one of the carbon atoms [1, 71]. The in-plane angles of the magnetic field ϕ_B and the strain ϕ_δ are defined relative to this x-axis in the xy-plane. An electric field is equivalent to strain [1]. The magnetic field misalignment angle θ_B is measured with respect to the z-axis.

Next, we introduce the Hamiltonian of the NV$^-$ center. The detailed level structure is discussed in Refs. [1, 45]. First, the GS is considered. The levels of the $^3\mathrm{A}_2$ electronic GS and their role in sensing experiments were presented in Ch. 2.1. Its Hamiltonian is a spin-triplet-orbital-singlet and is given by

$$\hat{H}_{\mathrm{GS}}/h = D_{\mathrm{GS}}(T)\left(\hat{S}_z^2 - \tfrac{2}{3}\,\hat{\mathbb{I}}_3\right) + \mu_{\mathrm{B}} g_{\mathrm{GS}} \hat{\vec{S}} \cdot \vec{B}\,, \tag{4.1}$$

where we neglect hyperfine interactions and electric and strain fields, since their influence on the GS spin states is minor (for the context of this chapter). Here, $\hat{S}_i$ are spin-1 operators (we will refer to $\hat{O}$ as the operator with matrix representations O_b in basis b) and $\hat{\mathbb{I}}_3$ is the associated identity operator, $\vec{B}$ is the external magnetic field, μ_{B} is the Bohr magneton, and h is the Planck constant which we use in units of $\mathrm{J\,Hz^{-1}}$. Values for the GS ZFS D_{GS} and the g-factor are listed in Tab. 4.1. Note that the ZFS D_{GS} has a temperature dependence (see Eq. 2.3) which is included in the model developed in this thesis. This dependence is relevant when fitting for the GS resonances, for example, during alignment of the bias magnet in Ch. 3.4.3.

But for the purpose of this chapter, this temperature dependence has no influence on the population dynamics. Equally, we neglect the mild temperature and strain dependence [90] of all other interactions listed in Tab. 4.1.

The Hamiltonian of the ^{3}E electronic ES is a spin-triplet-orbital-doublet that is spanned by the composite Hilbert space $\mathcal{H}_{\mathrm{ES}} = \mathcal{H}_{\mathrm{orbit}} \otimes \mathcal{H}_{\mathrm{spin}}$. In the eigenstate basis of the orbital $\hat{\sigma}_z$ and spin $\hat{S}_z$ operators, the ES Hamiltonian reads:

$$
\begin{aligned}
\hat{H}_{\mathrm{ES}}/h = {} & D^{\parallel}_{\mathrm{ES}} \hat{\mathbb{I}}_2 \otimes \left(\hat{S}_z^2 - \tfrac{2}{3}\,\hat{\mathbb{I}}_3\right) - \lambda^{\parallel}_{\mathrm{ES}} \hat{\sigma}_y \otimes \hat{S}_z \\
& + D^{\perp}_{\mathrm{ES}} \left[\hat{\sigma}_z \otimes \left(\hat{S}_y^2 - \hat{S}_x^2\right) - \hat{\sigma}_x \otimes \left(\hat{S}_y \hat{S}_x + \hat{S}_x \hat{S}_y\right)\right] \\
& + \lambda^{\perp}_{\mathrm{ES}} \left[\hat{\sigma}_z \otimes \left(\hat{S}_x \hat{S}_z + \hat{S}_z \hat{S}_x\right) - \hat{\sigma}_x \otimes \left(\hat{S}_y \hat{S}_z + \hat{S}_z \hat{S}_y\right)\right] \\
& + \mu_{\mathrm{B}} g_{\mathrm{ES}} \hat{\mathbb{I}}_2 \otimes \hat{\vec{S}} \cdot \vec{B} + \mu_{\mathrm{B}} g_l B_z \hat{\sigma}_y \otimes \hat{\mathbb{I}}_3 \\
& + d^{\perp}_{\mathrm{ES}} \xi_x \hat{\sigma}_z \otimes \hat{\mathbb{I}}_3 - d^{\perp}_{\mathrm{ES}} \xi_y \hat{\sigma}_x \otimes \hat{\mathbb{I}}_3 + d^{\parallel}_{\mathrm{ES}} \xi_z \hat{\mathbb{I}}_2 \otimes \hat{\mathbb{I}}_3 \,.
\end{aligned}
\tag{4.2}
$$

Here, $\hat{\sigma}_i$ are the Pauli matrices and $\hat{\mathbb{I}}_2$ the identity operator of the orbital subspace, and the vector $\vec{\xi}$ is the sum of the electric and strain-induced fields. The d_i-factors are the respective components of the electric dipole moment. All other parameters are taken from the literature and are collected in Tab. 4.1. Note that an axial strain ξ_z only shifts the overall energy of the ES, which does not affect our analysis and is therefore ignored in the following. For simplicity, we will refer to $\delta_\perp = d^{\perp}_{\mathrm{ES}} \xi_\perp$ as the in-plane strain.

The above Hamiltonians are given in the eigenstate basis of the spin $\hat{S}_z$ and orbital $\hat{\sigma}_z$ operators. We will refer to this basis as the e_z *basis*. The basis states are formed under dominating axial magnetic bias field B_z and in-plane strain $\delta_\perp$ along $\phi_\delta = 0$. These states are given by

$$
\begin{aligned}
e_z \ \textit{basis} = \Big(& \left|+1\right\rangle, \left|0\right\rangle, \left|-1\right\rangle, \\
& \left|E^0_{\mathrm{x},+1}\right\rangle, \left|E^0_{\mathrm{x},0}\right\rangle, \left|E^0_{\mathrm{x},-1}\right\rangle, \left|E^0_{\mathrm{y},+1}\right\rangle, \left|E^0_{\mathrm{y},0}\right\rangle, \left|E^0_{\mathrm{y},-1}\right\rangle, \\
& \left|ss\right\rangle \Big),
\end{aligned}
\tag{4.3}
$$

where the first three states form the spin-triplet of the GS, the next six states form the orbital-doublet-spin-triplet of the ES, and the last state is the spin-singlet of the shelving state (SS). The SS consists of more than one level [1] ($^1\mathrm{A}_1/^1\mathrm{E}$), but for our analysis, it is sufficient to model it by an effective singlet level. x and y denote the two orbital branches $\mathrm{E_x}$ and $\mathrm{E_y}$ of the ES, which form under strain as shown in Fig. 4.2(a).

We will make use of two further sets of basis vectors. For the situation of zero bias field and vanishing strain ($\delta_\perp \to 0$ at $\phi_\delta = 0°$), the eigenvectors approximately assume the zero-field (zf) basis

$$
\begin{aligned}
\textit{zf basis} = \Big(& \left|0\right\rangle, \left|-1\right\rangle, \left|+1\right\rangle, \\
& \left|E_1\right\rangle, \left|E_2\right\rangle, \left|E^0_{\mathrm{y},0}\right\rangle, \left|E^0_{\mathrm{x},0}\right\rangle, \left|A_1\right\rangle, \left|A_2\right\rangle, \\
& \left|ss\right\rangle \Big).
\end{aligned}
\tag{4.4}
$$

Interactions

$D_{\mathsf{GS}}(T)$	GS spin-spin int., value at 0 K:	$2.878\,$GHz [51]
$g_{\mathsf{GS/ES}}$	GS/ES electronic g-factor	2.003 [1]
$D^{\parallel}_{\mathsf{ES}}$	ES axial spin-spin int.	$1.44\,$GHz [99]
$D^{\perp}_{\mathsf{ES}}$	ES transversal spin-spin int.	$1.541\,$GHz/2 [99]
$\lambda^{\parallel}_{\mathsf{ES}}$	ES axial spin-orbit int.	$5.33\,$GHz [99]
$\lambda^{\perp}_{\mathsf{ES}}$	ES transversal spin-spin/orbit int.	$0.154\,$GHz [99]
g_l	ES orbital g-factor	0.1 [40]

Fields

$\delta_{\perp}$	ES in-plane strain/el. field	$40\,$GHz (default)
ϕ_{δ}	strain/el. field in-plane angle	$0°$ (default)
B	mag. field magnitude	$0\,$T* (default)
θ_B	mag. field misalignment angle	$0°$ (default)
ϕ_B	mag. field in-plane angle	$0°$ (default)

Rates

k_r	optical emission rate	$55.7\,\mu\mathrm{s}^{-1}$
$k_{E_{12}}$	avg. ISC rate for $m_{\mathrm{S}} = \pm 1$	$98.7\,\mu\mathrm{s}^{-1}$
$k_{E_{\mathsf{xy}}}$	ISC rate for $m_{\mathrm{S}} = 0$	$8.2\,\mu\mathrm{s}^{-1}$
$r_{\beta} =$	$\beta_{\mathsf{x}}/\beta_{\mathsf{y}}$ optical excitation branching ratio	1
$r_S =$	k_{S0}/k_{S1} SS branching ratio	2.26
ΔE	SS emitted phonon energy	$16.6\,$meV [86]
$\tau_{S,0}$	SS decay time at $T = 0\,$K	$320\,$ns
T	temperature	$0\,$K (default)
η	ES electron-phonon coupling strength	$176\,\mu\mathrm{s}^{-1}\,\mathrm{meV}^{-3}$
Ω	phonon cut-off energy	$168\,$meV

Setup

P	laser power	$2.34\,$mW (default)
b	background	$27.5\,\mathrm{kcps}\,\mathrm{mW}^{-1}$
R	collection over excitation efficiency	$88.4\,$kcps mW µs
A	optical alignment (excitation efficiency)	$136\,\mathrm{W}^{-1}$

Table 4.1: Overview of the parameters used in the rate model. The given values are based on our fit results of sample NV-2 in a nanostructured pillar as given in Tab. 6.3, and additional literature as indicated. For parameters varied throughout this thesis, default values are specified. The sequence timings to determine SNR values are discussed in Sec. 4.2.6. *In this thesis, zero magnetic field means $B \approx 0\,\mathrm{T}$ such that the degeneracy of the GS $m_{\mathrm{S}} = \pm 1$ states is lifted, but their splitting is negligible in comparison to all other parameters in the Hamiltonian.

All ES states of the *zf basis* have $\left\langle \hat{S}_z \right\rangle = 0$ and, apart from $\left|E^0_{\mathrm{x},0}\right\rangle$ and $\left|E^0_{\mathrm{y},0}\right\rangle$, also orbital eigenvalue $\langle \hat{\sigma}_z \rangle = 0$. While $\left|E^0_{\mathrm{y},0}\right\rangle$ and $\left|E^0_{\mathrm{x},0}\right\rangle$ are eigenstates to $m_\mathrm{S} = 0$, the other eigenstates are linear combinations to equal parts of the $m_\mathrm{S} = \pm 1$ and orbit x and y states. The basis transformation $T_{zf \to e_z}$ to the e_z *basis* is given by

$$M_{e_z} = T_{zf \to e_z} M_{zf} \left(T_{zf \to e_z}\right)^{-1} \tag{4.5}$$

for the matrix representation of an operator $\hat{M}$, where [46]

$$T_{zf \to e_z} = \begin{pmatrix} 0 & 0 & 1 & 0 & 0 & 0 & 0 & 0 & 0 & 0 \\ 1 & 0 & 0 & 0 & 0 & 0 & 0 & 0 & 0 & 0 \\ 0 & 1 & 0 & 0 & 0 & 0 & 0 & 0 & 0 & 0 \\ 0 & 0 & 0 & -i/2 & 1/2 & 0 & 0 & -i/2 & -1/2 & 0 \\ 0 & 0 & 0 & 0 & 0 & 0 & 1 & 0 & 0 & 0 \\ 0 & 0 & 0 & -i/2 & -1/2 & 0 & 0 & -i/2 & 1/2 & 0 \\ 0 & 0 & 0 & 1/2 & i/2 & 0 & 0 & -1/2 & i/2 & 0 \\ 0 & 0 & 0 & 0 & 0 & 1 & 0 & 0 & 0 & 0 \\ 0 & 0 & 0 & -1/2 & i/2 & 0 & 0 & 1/2 & i/2 & 0 \\ 0 & 0 & 0 & 0 & 0 & 0 & 0 & 0 & 0 & 1 \end{pmatrix} . \tag{4.6}$$

Finally, under a large axial bias field B_z and large strain $\delta_\perp$ with angle $\phi_\delta \neq 0$, the eigenvectors are given by the high-field (hf) orbit and spin eigenbasis,

$$\begin{aligned} hf\ basis = \Big(& \left|+1\right\rangle, \left|0\right\rangle, \left|-1\right\rangle, \\ & \left|E_{\mathrm{x},+1}\right\rangle, \left|E_{\mathrm{x},0}\right\rangle, \left|E_{\mathrm{x},-1}\right\rangle, \left|E_{\mathrm{y},+1}\right\rangle, \left|E_{\mathrm{y},0}\right\rangle, \left|E_{\mathrm{y},-1}\right\rangle, \\ & \left|ss\right\rangle \Big) . \end{aligned} \tag{4.7}$$

The lower-lying branch is denoted by $\mathrm{E_y}$, and the upper-lying branch by $\mathrm{E_x}$. However, the axes no longer coincide with the x and y directions of the NV center coordinate system (Fig. 4.1), but rather with a coordinate system rotated by ϕ_δ. The emergence of the *hf basis* is shown in Fig. 4.2(c). The basis transformation $T_{hf \to e_z}$ to the e_z *basis* is analogous to Eq. 4.5 and can be constructed as

$$T_{hf \to e_z} = \mathrm{diag}\left(\mathbb{I}_3, T^{\mathrm{ES}}_{hf \to e_z}, 1\right) , \tag{4.8}$$

with $T^{\mathrm{ES}}_{hf \to e_z} = T^{\mathrm{orbit}}_{hf \to e_z} \otimes \mathbb{I}_3$. $T^{\mathrm{orbit}}_{hf \to e_z}$ is construed column-wise from the eigenvectors written in e_z *basis* of the Hamiltonian in the orbital subspace with

$$H_{\mathrm{orbit}} = 1/3\ \mathrm{Tr}_{\mathrm{spin}}\left(H_{\mathrm{ES}}\right) , \tag{4.9}$$

which can be obtained from Eq. 4.2 by the partial trace over the spin subspace. Likewise, we define the Hamiltonian in the spin subspace with

$$H_{\mathrm{spin}} = 1/2\ \mathrm{Tr}_{\mathrm{orbit}}\left(H_{\mathrm{ES}}\right) . \tag{4.10}$$

In Sec. 4.4.1, the degree of mixing between the spin states of $\hat{S}_z$ plays a key role. For the discussion there, Fig. 4.2(b) highlights a specific case. In addition to the evolution of the eigenenergies as a function of the strain and magnetic field in Fig. 4.2(a,c), the respective evolution of the eigenstates $|e_i\rangle$ (*eig basis*) of the Hamiltonian $\hat{H}_{\mathrm{ES}}$ is shown in Fig. 4.3.

4.2.2 Transition rates under optical excitation

We next consider the transition rates between energy levels under optical excitation. The associated rates are collected in Fig. 4.2(d) and Tab. 4.1. Optical excitation from the GS to the ES can be achieved both resonantly (at cryogenic temperatures) and non-resonantly (at all temperatures). If the excitation is non-resonant, it is followed by a rapid phonon relaxation in the phonon sideband. Both excitation methods are largely spin-conserving. Optical transitions with spin-flip occur with $\leq 2\,\%$ [86, 100] and are therefore neglected here. We will focus on the non-resonant case since we aim to describe the population dynamics over a wide temperature range. The resonant case could be covered by introducing individual excitation rates for each ES level. While non-resonant excitation is, in general, not branch-selective, some selectivity can be achieved by adjusting the linear polarization of the laser [41, 95, 101]. The linear polarizations in the xy-plane of the NV center are associated with the $\mathrm{E_x}$ and $\mathrm{E_y}$ orbital branches that are defined by the direction of the strain angle ϕ_δ [88, 89]. Therefore, we introduce the excitation rates into $\mathrm{E_x}$ and $\mathrm{E_y}$ in the *hf basis.* Since these rates depend on the power P of the laser, it is convenient to use the dimensionless optical saturation parameter β and the branching ratio r_β with

$$\beta = \beta_{\mathrm{x}} + \beta_{\mathrm{y}}\,, \tag{4.11}$$

$$r_\beta = \beta_{\mathrm{x}}/\beta_{\mathrm{y}} \tag{4.12}$$

as depicted in Fig. 4.2(d). A value of $\beta > 1$ indicates the onset of saturation [60]. To convert the laser power P into the optical saturation parameter β, we define

$$\beta = PA \tag{4.13}$$

with the alignment A combining the effect of optical excitation efficiency and setup-specific conversion from laser power. We assume a temperature-independent optical excitation efficiency and thus A as suggested by recent findings [38].

The optical decay from the ES to the GS with rate k_r is independent of the spin and the orbital branch and also largely spin-conserving. The value of k_r depends on the microscopic structure the NV center is embedded in. Typical bulk values are around $67\,\mu\mathrm{s}^{-1}$ [102], while those for NV centers in nanostructures, such as nanocrystals [103] or our nanopillars (*cf.* Tab. 6.3 later), can be smaller.

The ES can also decay non-radiatively via the SS. Opposite to the radiative k_r decay, the decay rates from the six ES levels into the SS vary: the two levels associated with the $m_{\mathrm{S}} = 0$ spin states ($\left|E^0_{\mathrm{x},0}\right\rangle$ and $\left|E^0_{\mathrm{y},0}\right\rangle$) have the same and comparatively slow ISC rate $k_{E_{\mathrm{xy}}}$. The average ISC rate of the other four levels associated with the $m_{\mathrm{S}} = \pm 1$ spin states is faster. They vary for the different *zf basis* states, as depicted

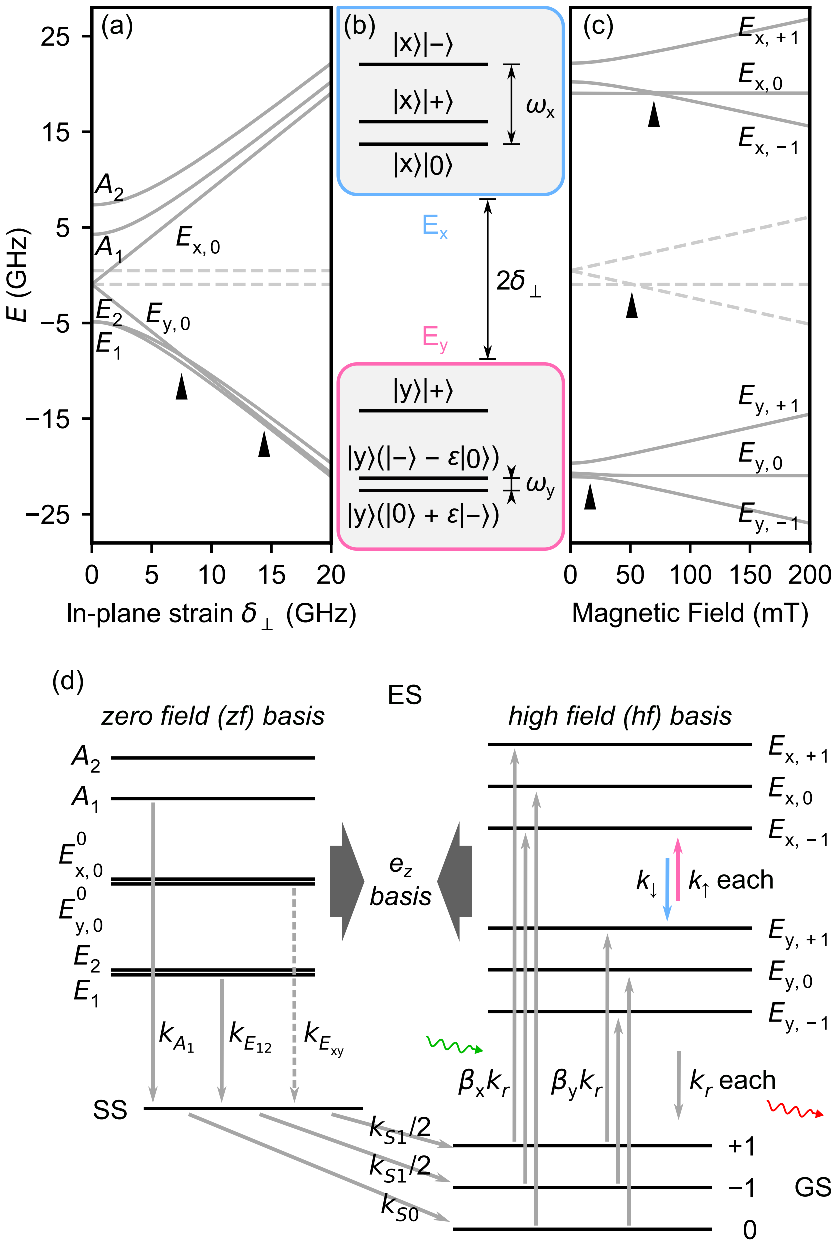
(a)
A2
A1
Ex, 0
E2
Ey, 0
E1
E (GHz)
25
15
5
−5
−15
−25
0
5
10
15
20
In-plane strain δ⊥ (GHz)
(b)
|x⟩|−⟩
|x⟩|+⟩
|x⟩|0⟩
ωx
Ex
2δ⊥
Ey
|y⟩|+⟩
|y⟩(|−⟩ − ε|0⟩)
|y⟩(|0⟩ + ε|−⟩)
ωy
(c)
Ex, +1
Ex, 0
Ex, −1
Ey, +1
Ey, 0
Ey, −1
0
50
100
150
200
Magnetic Field (mT)
(d)
zero field (zf) basis
ES
high field (hf) basis
A2
A1
E0x, 0
E0y, 0
E2
E1
ez
basis
Ex, +1
Ex, 0
Ex, −1
k↓
k↑ each
Ey, +1
Ey, 0
Ey, −1
kA1
kE12
kExy
βxkr
βykr
kr each
SS
kS1/2
kS1/2
kS0
+1
−1
0
GS

Figure 4.2: Level structure of the NV$^-$ center. (a) Energy levels of the ES as a function of strain at zero magnetic field. In parts (a,c), level names are printed where they are approximately eigenstates, and level-anti-crossings (LAC) are indicated by black markers. The dashed traces in parts (a,c) are the eigenlevels of $\mathcal{H}_{\text{spin}}$, obtained by a partial trace over the orbital sub-space $\mathcal{H}_{\text{orbit}}$. They constitute the observed ES energy levels at room temperature. (b) Under strain, the two orbital branches $\mathrm{E_x}$ and $\mathrm{E_y}$ form, split by approximately $2\delta_\perp$. The eigenstates of $\mathcal{H}_{\text{orbit}} \otimes \mathcal{H}_{\text{spin}}$ are composite states of the orbital states $|\mathrm{x}\rangle$ and $|\mathrm{y}\rangle$ and superpositions of the spin states $|0\rangle$ (sometimes also called $|S_z\rangle$) and $|\pm\rangle \propto (|{+1}\rangle \pm |{-1}\rangle)$ (also called $|S_{y/x}\rangle$). Only two spin states mix significantly in this example, with $\varepsilon = \epsilon_{|\mathrm{y}\rangle|0\rangle,|\mathrm{y}\rangle|-\rangle}$, as one can see in Fig. 4.3. Level spacings $\omega_{\mathrm{x/y}}$ are given for the discussion in Fig. 4.5. (c) Energy levels of the ES as a function of an axial magnetic field at $\delta_\perp = 20\,\mathrm{GHz}$. Under high strain and magnetic field, eigenstates of orbit and spin are formed, for example, $|E_{\mathrm{x},+1}\rangle = |\mathrm{x}\rangle\,|{+1}\rangle$. (d) Rate model employed in this thesis. The rates listed in Tab. 4.1 are depicted by arrows. The dashed arrow indicates a low decay probability, allowing for the optical initialization and readout of the GS spin state. Excitation by green light and emission of red light is indicated by wavy arrows. The two bases *zf* (see left in part (a)) and *hf* (right in part (c)) are connected via basis transformations (dark gray arrows) to the e_z *basis* of the ES Hamiltonian.

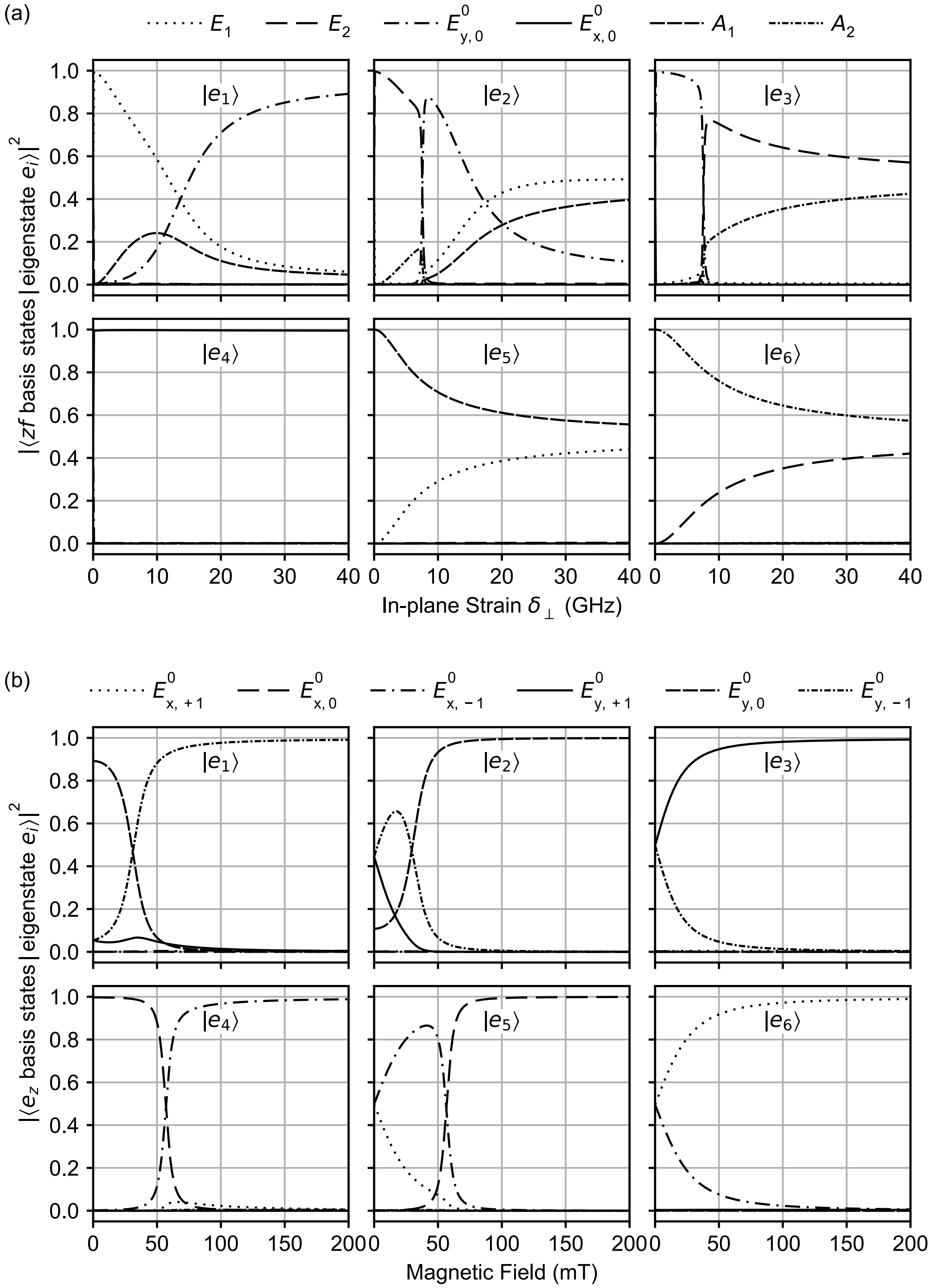

Figure 4.3: Evolution of ES levels under strain and magnetic field. (a) Eigenstates of the ES as a function of strain at zero magnetic field, analogous to Fig. 4.2(a). The probability amplitudes of the ith eigenstate $|e_i\rangle$ are plotted for each of the *zf basis* states. In contrast to Fig. 4.2(a), the angle was set to $\phi_\delta = 5°$ for a finite width of the LAC at $\delta_\perp = 7.5\,\mathrm{GHz}$. (b) Eigenstates of the ES as a function of an axial magnetic field at $\delta_\perp = 40\,\mathrm{GHz}$, similar to Fig. 4.2(c) at $\delta_\perp = 20\,\mathrm{GHz}$. Here, the eigenstates are projected onto the e_z *basis* states, and all angles are set to zero.

in Fig. 4.2(d). Following Goldman *et al.* [93], we use

$$k_{A_1} = k_{E_{12}}/0.52\,, \tag{4.14}$$

$$k_{A_2} = 0\,, \tag{4.15}$$

$$k_{E_1} = k_{E_2} = k_{E_{12}} \tag{4.16}$$

as given in Tab. 4.1. These ISC rates have to be introduced to the model in the *zf basis*. By a basis transformation, we can obtain the corresponding decay rates of the *hf basis* states at a high axial magnetic field and a high strain $\delta_\perp$. Levels with $m_\mathrm{S} = 0$ still decay with the same rate k_{E_xy}. Since the *hf basis* states with $m_\mathrm{S} = \pm 1$ are linear combinations to equal parts of *zf basis* states with $m_\mathrm{S} = \pm 1$, we find their decay rate

$$\overline{k}_{m_\mathrm{S}=\pm 1} = \mathrm{mean}\left(k_{E_1}, k_{E_2}, k_{A_1}, k_{A_2}\right)\,, \tag{4.17}$$

which evaluates to $\approx k_{E_{12}}$ for the values introduced above. Likewise, the two rates k_{E_xy} and $\sim k_{E_{12}}$ are the ISC rates commonly used in room temperature models. We note that there is an additional temperature dependence of these ISC rates [93, 94]. We neglect this effect as it is very small up to room temperature.

Finally, the decay from the spin-singlet SS back to the spin-triplet GS occurs with two characteristic rates k_{S0} and k_{S1} into the GS spin levels $m_\mathrm{S} = 0$ and $m_\mathrm{S} = \pm 1$. It is common to introduce the SS branching ratio as

$$r_S = k_{S0}/k_{S1}\,. \tag{4.18}$$

For example, our branching ratio of $r_S = 2.26$ in Tab. 4.1 results in a 70 % decay probability for $m_s = 0$, and a 15 % probability for each of the $m_s = \pm 1$ states. We assume that r_S is independent of temperature [104]. By contrast, the shelving state lifetime (SSL), defined by

$$\tau_S(T) = \left(k_{S1} + k_{S0}\right)^{-1} = \tau_{S,0}\left(1 - e^{-\frac{\Delta E}{k_\mathrm{B} T}}\right)\,, \tag{4.19}$$

varies with temperature T [86, 87, 104]. This dependence results from a combination of spontaneous emission ($\tau_{S,0}$) and stimulated emission of a phonon with energy ΔE (see Tab. 4.1). k_B is the Boltzmann constant. Since $\tau_S > 100\,\mathrm{ns}$ for all temperatures of relevance here, the SS lifetime dominates the dynamics of the NV$^-$ center under optical excitation together with $1/k_{E_\mathrm{xy}} \approx 100\,\mathrm{ns}$. This combination gives rise to the ability of spin initialization and readout, as discussed in Ch. 2.1.

4.2.3 Phonon-induced transition rates

Next, we consider phonon-driven population dynamics within the ES. The relevant effect for this thesis is phonon-mediated hopping between the two orbital branches. This hopping arises from a coupling to the phonon bath where one- and two-phonon-processes (indices 1 and 2) drive transitions between the orbital states of the NV$^-$ center, as derived in detail in the next Secs. 4.3.2 and 4.3.3. The temperature dependence of the thermal occupation of phonon modes thus dominates the temperature dependence of the NV$^-$ photo-dynamics. We start by introducing the up- and down-rates

$$\mathrm{E_y} \rightarrow \mathrm{E_x}: \quad k_{\uparrow}(T, \delta_{\perp}, \eta) = k_{\uparrow,1} + k_{\uparrow,2}\,, \tag{4.20}$$

$$\mathrm{E_x} \rightarrow \mathrm{E_y}: \quad k_{\downarrow}(T, \delta_{\perp}, \eta) = k_{\downarrow,1} + k_{\downarrow,2}\,, \tag{4.21}$$

respectively, which depend on the temperature T and the strain-induced splitting $\hbar\Delta_{\perp} \approx 2h\delta_{\perp}$ of the orbital branches (*cf.* Fig. 4.2(b) and Eq. 4.44). η parameterizes the coupling strength between electronic orbital states and phonons. Importantly, $k_{\uparrow}$ and $k_{\downarrow}$ only act on the orbital subspace, leaving the state in the spin subspace untouched. The rates are related via the Boltzmann distribution as

$$\frac{k_{\uparrow,1/2}}{k_{\downarrow,1/2}} = e^{-\frac{\hbar\Delta_{\perp}}{k_{\mathrm{B}}T}}\,, \tag{4.22}$$

due to spontaneous emission. Derived in the next Sec. 4.3.2, the downwards one-phonon rate is given by

$$k_{\downarrow,1}(T, \delta_{\perp}) \approx 32\eta h^3 \delta_{\perp}^3 \left[n(2\delta_{\perp}h) + 1\right]\,, \tag{4.23}$$

where n is the Bose-Einstein distribution in Eq. 4.54. Note that the $+1$ term, associated with the spontaneous emission of a phonon, gives a finite and temperature-independent rate that needs to be considered even at $T = 0\,\mathrm{K}$ if the strain $\delta_{\perp}$ is high. For a two-phonon Raman process, we will find in Sec. 4.3.3 that

$$k_{\uparrow,2}(T, \delta_{\perp}) \lesssim k_{\downarrow,2}(T, \delta_{\perp}) = \frac{64\hbar}{\pi}\eta^2 k_{\mathrm{B}}^5 T^5 I(T, \delta_{\perp})\,. \tag{4.24}$$

Here, $I(T, \delta_{\perp})$ is the integral over the phonon mode energies (in units of $k_{\mathrm{B}}T$) in the Debye approximation

$$I(T, \delta_{\perp}) = \int_{x_{\perp}}^{\Omega/k_{\mathrm{B}}T} \frac{e^x x(x - x_{\perp})\left[x^2 + (x - x_{\perp})^2\right]}{2\left(e^x - 1\right)\left(e^{x - x_{\perp}} - 1\right)} dx\,, \tag{4.25}$$

where $x_{\perp} \approx 2\hbar\delta_{\perp}/(k_{\mathrm{B}}T)$. Note that $I(T, \delta_{\perp} \rightarrow 0)$ is non-zero, meaning that two-phonon Raman transitions occur even without strain. The integral is only mildly strain-dependent. Its temperature dependence is negligible if the cut-off energy is larger than the relevant temperature scales ($\Omega \gg k_{\mathrm{B}}T$), which is the case in most parts of this thesis. A thorough discussion of the wavelength of contributing phonon modes is given in Sec. 5.3 and a discussion of the effect of the cut-off energy is given in Ch. 5.3.

Eqs. 4.22–4.24 indicate that $k_{\downarrow,1}$ will dominate for high strain at low temperatures. At elevated temperatures, up- and down-rates converge, and $k_{\uparrow/\downarrow,2}$ will dominate due to their T^5-dependence. The temperature dependence of the hopping rates is further discussed and plotted in Sec. 4.4.1 and Figs. 4.5 and 4.9.

4.2.4 Lindblad master equation

We now discuss how we numerically simulate the population dynamics of the above rate model. Because the phonon-induced transitions $k_{\uparrow/\downarrow}$ only act on the orbital subspace (leaving the coherent spin state undisturbed), dynamics cannot be simulated using classical rate equations commonly used at room temperature [86, 96] and recently also at low temperatures [95]. Instead, we use a Lindblad master equation approach that acts on quantum states yet includes the known classical rates via jump operators. We note that for high strain, the spontaneous emission rate $k_{\downarrow,1}$ can have a significant influence even at zero temperature. Therefore, a classical rate model without phonon transitions can be insufficient in the low-temperature limit.

To combine quantum states of spin and orbit with classical transition rates, we use the master equation in Lindblad form [105]. The Liouville equation describes the time evolution of the density operator $\hat{\rho}$ as

$$\begin{aligned} \frac{\mathrm{d}}{\mathrm{d}t}\hat{\rho} &= -\frac{i}{\hbar}\Big[\hat{H},\hat{\rho}\Big] + \sum_k \left(\hat{L}_k\hat{\rho}\hat{L}_k^\dagger - \frac{1}{2}\Big\{\hat{L}_k^\dagger\hat{L}_k,\hat{\rho}\Big\}\right) \\ &\equiv \mathcal{L}(\hat{\rho})\,, \end{aligned} \tag{4.26}$$

where $[\cdot,\cdot]$ and $\{\cdot,\cdot\}$ are the commutator and anticommutator, $\hat{H}$ is the Hamiltonian, which we write as $H = \mathrm{diag}\,(H_{\mathrm{GS}}, H_{\mathrm{ES}}, 0)$ in matrix-form, and $\mathcal{L}$ is the Liouvillian superoperator. The first term in Eq. 4.26 is the von Neumann equation which describes the unitary part of the time evolution. The second term is the dissipator $\mathcal{D}$, which is also a superoperator. The jump operators $\hat{L}_k$ are used to introduce the transition rates from Fig. 4.2(d). We will discuss them in more detail in the next Sec. 4.2.5.

The rates of the jump operators depend on the temperature and laser power. After they are constructed, we solve the master Eq. 4.26 in Fock-Liouville space with the matrix $\tilde{\mathcal{L}}$ and vectorized density matrix $\vec{\rho}$ as

$$\vec{\rho}(t) = \exp\!\left(\tilde{\mathcal{L}}t\right)\vec{\rho}_0\,. \tag{4.27}$$

This $\vec{\rho}(t)$ is the solution to the differential equation since in our case, $\mathcal{L}$ is time-independent. Parameters like the magnetic field and strain alter the Hamiltonian $\hat{H}$ in Eq. 4.26 and thus lead to a different time evolution. The steady-state ρ_∞ under given jump operators (*e.g.* under optical excitation) is given by the eigenvector of $\tilde{\mathcal{L}}$ to eigenvalue 0.

4.2.5 Jump operators

In the master Eq. 4.26, each decay channel k is assigned a dissipator

$$\mathcal{D}_k(\hat{\rho}) = \hat{L}_k\hat{\rho}\hat{L}_k^\dagger - \frac{1}{2}\Big\{\hat{L}_k^\dagger\hat{L}_k,\hat{\rho}\Big\}\,, \tag{4.28}$$

constructed from its jump operator $\hat{L}_k$. The decay must follow Markovian statistics for the Lindblad master equation to be applicable. We assume that this is the case here. In more detail, the derivation of the Lindblad master equation considers the system of interest coupled to a bath [105, 106]. In our case, this bath is the photons for optical processes and the phonons for orbital interactions. Several assumptions about the interaction with the bath are made in the derivation. These are the assumptions

(i) that the state of the bath and the state of the system are separable at all times and show no correlations (Born approximation), (ii) that the bath has a short memory of the interaction with the system (Markov approximation), and (iii) the rotating wave approximation in the interaction picture (secular approximation). These assumptions hold for the optical processes, but the orbital hopping rates are smaller for low temperatures and then exceed the level spacings (Larmor frequencies) at elevated temperatures or close to LACs. This suggests a conflict with the assumption (iii) and can implicate that the system states are altered under the influence of the phonon bath (vibronic states under the dynamic Jahn-Teller effect [90, 91]; interaction term given in Eq. 4.39), which is not discussed here. Despite this potential conflict, we heuristically find the Lindblad master equation to describe the system dynamics well. We will compare its predictions to analytical expressions of decay rates from literature for a toy model (Sec. 4.4.2), to a Monte Carlo simulation of our system (Sec. 4.4.1), and finally to experimental data (Ch. 5).

To gain a better intuition for the jump operators $\hat{L}_k$ in Eq. 4.28, we will first look at a toy model with two levels. This could be a spin-1/2-system with Zeeman-splitted states $|{+1/2}\rangle$ and $|{-1/2}\rangle$. Written in terms of the density matrix elements in the Hilbert space, a state in Fock-Liouville space is $\vec{\rho} = (\rho_{11}, \rho_{12}, \rho_{21}, \rho_{22})$. If we neglect the unitary time evolution in the Lindblad master equation, we see that $\dot{\vec{\rho}} = \tilde{\mathcal{D}}\vec{\rho}$. Thus, a

$$\tilde{\mathcal{D}}_{T_2} = 1/T_2 \, \mathrm{diag}(0, -1, -1, 0) \tag{4.29}$$

will cause a decoherence rate $k_{T_2} = 1/T_2$, characterized by the exponential decay time T_2. This superoperator can be seen as two incoherent decay processes, one for each of the two states into themselves. It can be constructed as

$$\tilde{\mathcal{D}}_{T_2} = \tilde{\mathcal{D}}_{T_{2,+1/2}} + \tilde{\mathcal{D}}_{T_{2,-1/2}} \text{ with } \hat{L}_{T_{2,i}} = 1/\sqrt{T_2}\ |i\rangle\langle i|\ ,\ i \in \{+1/2, -1/2\} \tag{4.30}$$

in Eq. 4.28.

In the same manner, we can construct an incoherent relaxation process $|{+1/2}\rangle \rightarrow |{-1/2}\rangle$ with decay time T_1. The jump operator

$$\hat{L}_{T_{1,+1/2}} = 1/\sqrt{T_1}\ |{-1/2}\rangle\langle{+1/2}| \tag{4.31}$$

yields a dissipator according to Eq. 4.28 of

$$\tilde{\mathcal{D}}_{T_{1,+1/2}} = 1/T_1 \begin{pmatrix} -1 & 0 & 0 & 0 \\ 0 & -0.5 & 0 & 0 \\ 0 & 0 & -0.5 & 0 \\ +1 & 0 & 0 & 0 \end{pmatrix}. \tag{4.32}$$

As we can see from comparison with Eq. 4.29, a T_1 decay inherently causes a T_2 decay at half the rate. Note that in the context of the NV$^-$ center, a relaxation of the spin state to a 1/3 : 1/3 : 1/3 classical mixture is referred to as a “T_1 process”, as it represents the typical thermal equilibrium. In the toy model, such a relaxation to $\vec{\rho} = (0.5, 0, 0, 0.5)$ is obtained from two parallel relaxation processes as $\tilde{\mathcal{D}}_{T_{1,+1/2}} + \tilde{\mathcal{D}}_{T_{1,-1/2}}$ with decay time $T_{1,+1/2} = T_{1,-1/2} = 2T_1$.

The toy model presented here can easily be implemented with the Python library

QuTiP [106]. One can verify that the jump operators above yield the expected behavior independent of the system's Larmor frequency.

Returning to our rate model of the NV$^-$ center, a decay with Markovian statistics at rate $k_{i,j}$ of basis state $|i\rangle$ into basis state $|j\rangle$ is described by a jump operator

$$\hat{L}_k = \sqrt{k_{i,j}}\,|j\rangle\langle i|\ . \tag{4.33}$$

Each spin-incoherent decay channel in Fig. 4.2(d) has such an individual jump operator. As an example of incoherent transition rates, we use six jump operators to describe the optical decay. An example expressed in states of the *hf basis* (Eq. 4.7) is

$$\hat{L}_{r,+1} = \sqrt{k_r}\,|{+1}\rangle\langle E_{\mathrm{x},+1}|\ . \tag{4.34}$$

We note at this point that the optical transitions are actually largely spin-coherent [107], but this has a negligible influence on the results presented in this thesis (except Sec. 4.4.5, as discussed there). As another example, there is one jump operator to describe the ISC of state $|A_1\rangle$. Thus, expressed in states of the *zf basis* (Eq. 4.4)

$$\hat{L}_{\mathrm{ISC},A_1} = \sqrt{k_{A_1}}\,|ss\rangle\langle A_1|\ . \tag{4.35}$$

To use $\hat{L}_{r,+1}$ and $\hat{L}_{\mathrm{ISC},A_1}$ in the master Eq. 4.26, the matrix representation of it in *hf basis* or *zf basis*, respectively, needs to be basis transformed to the e_z *basis* (basis in which H is written) via the transformation matrices given in Eqs. 4.6 and 4.8. These jump operators destroy coherences between states: a comparison with the relaxation process in the toy model in Eq. 4.31 shows that these jump operators describe T_1-like processes between the two respective states and therefore lead to at T_2 process at half the rate. For example, an initial state $|\psi\rangle = 1/\sqrt{2}\,(|E_{\mathrm{x},+1}\rangle + |E_{\mathrm{x},-1}\rangle)$ will decay to a $1/2 : 1/2$ classical mixture of $|{+1}\rangle$ and $|{-1}\rangle$ in our incoherent implementation under the influence of jump operators $\hat{L}_{r,+1}$ and $\hat{L}_{r,-1}$. This behavior is intended for all rates in this model with the exception of the orbital branch hopping $k_{\downarrow/\uparrow}$. Here, a jump only may only lead to a decay of the orbital state and, therefore, to the destruction of coherences in the orbital subspace $\mathcal{H}_{\mathrm{orbit}}$. Crucially, coherences in the spin subspace $\mathcal{H}_{\mathrm{spin}}$ must be maintained when jumping from one orbital branch to the other. To that end, there are two jump operators for orbital branch hopping:

$$\hat{L}^{\mathrm{ES}}_{\downarrow} = \sqrt{k_\downarrow}\,|\mathrm{y}\rangle\langle \mathrm{x}| \otimes \hat{\mathbb{I}}_3 \tag{4.36}$$

$$\hat{L}^{\mathrm{ES}}_{\uparrow} = \sqrt{k_\uparrow}\,|\mathrm{x}\rangle\langle \mathrm{y}| \otimes \hat{\mathbb{I}}_3 \tag{4.37}$$

To arrive at the representation in the full *hf basis*, the matrix representation has to be extended by 0-block matrices. By comparison with the discussion above, the orbital hopping is like the "T_1 process" at a rate $1/T_1 = 2\overline{k}_{\downarrow/\uparrow}$ on the orbital state towards the mixed orbital state of the detailed balance equilibrium (see Eq. 4.22). It will, therefore, inherently also cause a T_2 process on the coherence of the orbital state, with a rate $\overline{k}_{\downarrow/\uparrow}$.

Finally, it shall be noted that we assumed off-resonant optical excitation here. But with respective adaptions in the jump operators, resonant laser excitation into selected eigenstates of the excited state can also be simulated, as done for Fig. 5.1.

4.2.6 Experimental observables

As discussed in Ch. 2.3, the quantity observed in experiments is the PL intensity. PL is generated by radiative emission (rate constant k_r) of the NV^- center. In addition, contamination of the diamond surface by sp^2 carbon or adsorbed molecules, as well as temporary switching to the NV^0 charge state [57] cause a fluorescent background (further effects of a temporary switching to NV^0 will be discussed in Ch. 6.4.4). We thus model the observed PL of the NV^- center as

$$\mathrm{PL}(t) = AR\left(\sum_{i\in[4\,..\,9]} \rho_{i,i}(t)k_r\right) + bP\,, \tag{4.38}$$

where $\rho_{i,i}$ are the state populations and A, R, b, and P are the setup-specific parameters as explained in Tab. 4.1.

To simulate $\mathrm{PL}(t)$, we first construct the magnetic field- and strain-dependent Hamiltonian H (Eqs. 4.1, 4.2) and determine the *hf basis* (Eq. 4.7). Next, for every rate k_i, we construct the jump operators L_{k_i} in the respective basis needed for that rate (Eq. 4.33). The temperature is required here to calculate the SSL (Eq. 4.19) and orbital hopping rate (Eqs. 4.20, 4.21). We then transform the L_{k_i}'s to the same e_z *basis* as H has and solve the master equation for either the steady-state ρ_∞ or the time evolution $\rho(t)$ (Eq. 4.27). Finally, we calculate the PL for the given setup parameters (Eq. 4.38).

An important figure-of-merit for quantum applications is the SNR [61] in Eq. 2.8. To determine the SNR, we simulate $\mathrm{PL}(t)$ of the pulse sequence that was discussed in Fig. 2.2(a). We use a π-pulse with perfect fidelity of the population swap between the two energetically lowest eigenstates of the GS. For well-aligned or zero magnetic field, these are the $|0\rangle$ and $|-1\rangle$ states. We note that the choice of these states can make a small difference in contrast and thus SNR, since the $m_\mathrm{S} = -1$ and $m_\mathrm{S} = +1$ states do not have the same spin mixing in the low-temperature ES (see Fig. 4.3(b)). In cryogenic experiments, it can therefore be beneficial to measure the contrast of both, the $|-1\rangle$ and $|+1\rangle$ transition, and pick the one with higher contrast. We will use the SNR in the following to simulate the performance of the NV center under different conditions. Note that it accounts for the spin-state initialization as well as the spin readout fidelity, which are both reduced by the spin-lattice relaxation discussed later in Sec. 4.4. Further, we will disentangle the effect of the initialization and readout in Ch. 7.1.

In Sec. 4.4, we will discuss how the NV^- center's photo-dynamics change with temperature, magnetic field, and strain. Therefore, the integration time t_int required for optimal SNR in Eq. 2.8 also changes. In simulations, the t_int for best SNR is thus optimized at the respective conditions. Since a faster spin relaxation in the ES reduces the optimal t_int, a short t_int correlates with a low SNR, as it will be shown in Fig. 7.1(b). Additionally, for best SNR the laser power can also be optimized [108] for each condition. This optimization is also addressed separately in Ch. 7. In simulations, we use the same off-resonant laser power $P = 2.34\,\mathrm{mW}$ (see Tab. 4.1), which corresponds to $\beta = 0.3$ (see Eq. 4.13). For the sequence timings to determine the SNR (see Eq. 2.7), we use t_LaserOn, $t_\mathrm{LaserWait} \to \infty$ to avoid any potential influence by an improper spin initialization.

4.3 Phonon-induced orbital hopping

Before we discuss the simulation results of the model introduced above, we first derive the hopping rates $k_{\downarrow/\uparrow}$ (Eqs. 4.20/4.21) between the orbital electronic states of the NV$^-$ ES via coupling to the phonon bath. In our derivation, we closely follow previous work by Walker *et al.* [109] that was first adapted to the NV$^-$ center by Fu *et al.* [41] and further developed by Abtew *et al.* [91], Goldman *et al.* [93], and Plakhotnik *et al.* [90, 110]. For a recent review of the topic in the context of vibronic states of the NV$^-$ center, the reader is referred to Ref. [34]. But here, in contrast, we aim to provide all steps of the derivation, which allows us to understand how all terms arise. Also, in contrast to the high-temperature and high-strain approximations in Ref. [110] or the low-temperature and low-strain approximations in Ref. [93], we will keep the full equations allowing us to model the wide range of parameters covered in this thesis.

Finally, in Sec. 4.3.4, we will investigate the wavelength range of phonon modes that contribute dominantly to the hopping rates and justify the Debye approximation done in the derivation.

4.3.1 Fermi's Golden Rule

In the following, index i should denote the i^{th} vibrational mode. $p_i \in \{\mathrm{x}, \mathrm{y}\}$ be the polarization of that mode. States $|O\rangle \in \{|\mathrm{x}\rangle, |\mathrm{y}\rangle\}$ are orbital eigenstates (Eq. 4.7). A vibrational level is $|O\rangle|\chi_m\rangle$ with $|\chi_m\rangle = \prod_i |n_i\rangle$ and energy $\epsilon_m = \sum_i n_i \omega_i \hbar$. m denotes the set of occupation numbers $\{n_i\}$ of modes i. In contrast to the rest of this thesis, these ω_i here are in angular frequency units (rad/s) for consistency with the literature. Under the influence of the dynamic Jahn-Teller effect, the electron-phonon interaction with E-symmetric phonons of the ES is [41]

$$
\begin{aligned}
\hat{H}_{\text{e-p}} = \sum_i [&\delta_{p_i,\mathrm{x}} \hbar\lambda_i (|\mathrm{x}\rangle\langle\mathrm{x}| - |\mathrm{y}\rangle\langle\mathrm{y}|)(\hat{a}_i + \hat{a}_i^\dagger) \\
&- \delta_{p_i,\mathrm{y}} \hbar\lambda_i (|\mathrm{x}\rangle\langle\mathrm{y}| + |\mathrm{y}\rangle\langle\mathrm{x}|)(\hat{a}_i + \hat{a}_i^\dagger)] \,.
\end{aligned}
\tag{4.39}
$$

The effect of the annihilation $\hat{a}_i$ and creation $\hat{a}_i^\dagger$ operators for mode i on phonon states is denoted as:

$$\hat{a}_i |\chi_m\rangle = \sqrt{n_{m,i}}\, |\chi_{m,i-}\rangle \tag{4.40}$$

$$\hat{a}_i^\dagger |\chi_m\rangle = \sqrt{n_{m,i}+1}\, |\chi_{m,i+}\rangle \tag{4.41}$$

For the derivation, we will assume to start in a state $|s\rangle$ of the lower branch $\mathrm{E_y}$ and find the rate with which it decays to a final state $|f\rangle$ of the upper branch $\mathrm{E_x}$. Thus,

$$|s\rangle = |\mathrm{y}\rangle|\chi_s\rangle \tag{4.42}$$

$$|f\rangle = |\mathrm{x}\rangle\,|\chi_f\rangle \tag{4.43}$$

and the energy splitting (final minus initial) between the orbital electronic states is given by

$$\hbar\Delta_\perp = \langle\mathrm{x}|\hat{H}_{\text{orbit}}|\mathrm{x}\rangle - \langle\mathrm{y}|\hat{H}_{\text{orbit}}|\mathrm{y}\rangle \approx 2\delta_\perp h > 0\,, \tag{4.44}$$

with the eigenenergies of the orbital subspace H_{orbit} from Eq. 4.9. The approximation holds as long as $g_l B_z$ is small, which is usually the case, but recent observations suggest a larger g_l in high strained NV centers at $B_z \gg 1\,\mathrm{T}$ [95]. The transition rate between the two orbital branches can be calculated by Fermi's Golden Rule

$$k_\uparrow = \frac{2\pi}{\hbar}\sum_f |T_{fs}|^2\delta(\hbar\Delta_\perp + \epsilon_f - \epsilon_s)\,, \tag{4.45}$$

where T_{fs} is the transition matrix element. Up to second order, T_{fs} can be found from

$$T_{fs} = T_{fs}^{(1)} + T_{fs}^{(2)} + \ldots\text{ , with} \tag{4.46}$$

$$T_{fs}^{(1)} = \langle f|\hat{H}_{\text{e-p}}|s\rangle \text{ and} \tag{4.47}$$

$$T_{fs}^{(2)} = \sum_m \frac{1}{E_s - E_m}\,\langle\chi_f|\,\langle\mathrm{x}|\hat{H}_{\text{e-p}}|O_m\rangle\,|\chi_m\rangle\,\,\langle\chi_m|\,\langle O_m|\hat{H}_{\text{e-p}}|\mathrm{y}\rangle\,|\chi_s\rangle\,, \tag{4.48}$$

where we sum over all possible intermediate states $|O_m\rangle\,|\chi_m\rangle$ with energy E_m for the second order process.

We note that coupling to A_1-symmetric phonon modes, instead, leads to an orbital dephasing (T_2) process [110], which we did not include in our model. These modes might only influence the PL in case of resonant optical excitation into levels of the *zf basis*, *i.e.* in very low strain conditions, as *zf basis* states are coherent superpositions of the orbital eigenstates (Eq. 4.6). This might slightly influence the picture given in Fig. 5.1. We further note that apart from Fig. 5.1, our Lindblad master equation approach is only tested and verified for classical mixtures of the orbital states. The validity of our Lindblad master equation approach, as discussed in Sec. 4.2.5, remains to be tested further for coherent orbital states at low temperatures. At elevated temperatures, the orbital hopping destroys such orbital coherences, as discussed in Sec. 4.2.5.

4.3.2 One-phonon process

First, we derive the first-order transition matrix element, which is a one-phonon process. The energy gap $\hbar\Delta_\perp$ is overcome by the absorption of one phonon with exactly that energy.

$$\begin{aligned} T_{fs}^{(1)} &= \langle f|\hat{H}_{\text{e-p}}|s\rangle \\ &= -\sum_i \delta_{p_i,\mathrm{y}}\hbar\lambda_i\left(\langle\chi_f|\hat{a}_i|\chi_s\rangle + \langle\chi_f|\hat{a}_i^\dagger|\chi_s\rangle\right) \\ &= -\sum_i \delta_{p_i,\mathrm{y}}\hbar\lambda_i\left(\sqrt{n_{s,i}}\delta_{f,si-} + \sqrt{n_{s,i}+1}\delta_{f,si+}\right) \end{aligned} \tag{4.49}$$

Here, $\delta_{f,si-}$ denotes that $|\chi_s\rangle$ differs from $|\chi_f\rangle$ only in the occupation number n_i (that has polarization p_i) reduced by one. This is in contrast to $T_{fs}^{(2)}$, where all terms will demand a difference between $|\chi_s\rangle$ and $|\chi_f\rangle$ in exactly two phonon modes. Therefore, in Eq. 4.45 no states $|s\rangle$ and $|f\rangle$ exist that would give a non-vanishing $T_{fs}^{(1)}$ and $T_{fs}^{(2)}$ at the same time. This allows us to separate the overall hopping rate into a one- and a two-phonon contribution as

$$k_\uparrow = k_{\uparrow,1} + k_{\uparrow,2} + \dots \,. \tag{4.50}$$

We then find for

$$\begin{aligned} k_{\uparrow,1} &= \frac{2\pi}{\hbar}\sum_f \left|T_{fs}^{(1)}\right|^2 \delta(\hbar\Delta_\perp + \epsilon_f - \epsilon_s) \qquad (4.51)\\ &= 2\pi\hbar\sum_f \left|\sum_i \delta_{p_i,\mathrm{y}}\lambda_i\Big[\sqrt{n_{s,i}}\delta_{f,si-}\delta(\hbar\Delta_\perp - \hbar\omega_i)\right.\\ &\qquad\qquad \left. + \sqrt{n_{s,i}+1}\delta_{f,si+}\delta(\hbar\Delta_\perp + \hbar\omega_i)\Big]\right|^2 , \end{aligned}$$

where the second term vanishes since $\Delta_\perp, \omega_i > 0$. Note that for each f, there is at most one term in the sum over i that is non-zero. On the other hand, for each i, there is exactly one f. Thus, for any F_i

$$\sum_f \left|\sum_i \delta_{f,si+/-}F_i\right|^2 = \sum_i |F_i|^2 \,. \tag{4.52}$$

Instead of summing over all modes i we integrate over all energies ϵ and use the average $\overline{|F_i|^2}$ of all modes i with energy $\hbar\omega_i = \epsilon$. Inserting the identity $\int_0^\Omega \delta(\epsilon - \hbar\omega_i)d\epsilon$, with the cut-off energy for E-symmetric phonons Ω (see discussion in Ch. 5.3), we find

$$\begin{aligned} k_{\uparrow,1} &= 2\pi\hbar\int_0^\Omega \sum_i \delta_{p_i,\mathrm{y}}|\lambda_i|^2\delta(\epsilon - \hbar\omega_i)n_{s,i}\delta(\hbar\Delta_\perp - \hbar\omega_i)d\epsilon\\ &= 2\pi\hbar\frac{2}{\pi\hbar}\int_0^\Omega J_y(\epsilon)n(\epsilon)\delta(\hbar\Delta_\perp - \epsilon)d\epsilon\\ &= 4J_y(\hbar\Delta_\perp)n(\hbar\Delta_\perp)\,, \end{aligned} \tag{4.53}$$

where the Bose-Einstein distribution

$$n(\epsilon) = \frac{1}{e^{\epsilon/k_\mathrm{B}T} - 1} \tag{4.54}$$

describes the thermal occupation of phonon modes with energy ϵ at temperature T in $|\chi_s\rangle$. Here, the polarization-specific phonon spectral density of E-symmetric phonons

$$\begin{aligned} J_{\mathrm{x/y}}(\epsilon) &= \frac{\pi\hbar}{2}\sum_i \delta_{p_i,\mathrm{x/y}}|\lambda_i|^2\delta(\epsilon - \hbar\omega_i)\\ &= \frac{\pi\hbar}{2}\rho(\epsilon)\,\overline{|\lambda_i|^2}\Big|_{p_i=\mathrm{x/y},\hbar\omega_i=\epsilon} \end{aligned} \tag{4.55}$$

was introduced with the phonon modes density $\rho(\epsilon)$. Assuming a linear dispersion relation and a wavelength of the acoustic phonons much larger than the lattice spacing, the Debye model gives $\rho(\epsilon) \propto \epsilon^2$ and the coupling strength can be approximated [91, 93] to be $\lambda_i \propto \sqrt{\epsilon}$. Then, the spectral density is independent of polarization and given by

$$J(\epsilon) = \eta\epsilon^3 \,. \tag{4.56}$$

Here, η is a measure of the coupling strength to phonons. Finally, we find for the one-phonon orbital hopping rate $\mathrm{E_y} \to \mathrm{E_x}$:

$$\begin{aligned} k_{\uparrow,1}(T,\delta_\perp) &= 4\eta\,[\hbar\Delta_\perp]^3\, n(\hbar\Delta_\perp) \\ &\approx 32\eta h^3\delta_\perp^3 n(2\delta_\perp h) \end{aligned} \tag{4.57}$$

The rates for the opposite direction, $\mathrm{E_x} \to \mathrm{E_y}$, can be found from the detailed balance ratio $k_{\uparrow,1/2}/k_{\downarrow,1/2} = \exp[-\hbar\Delta_\perp/(k_\mathrm{B}T)]$ (Eq. 4.22) which, as a consequence of Eq. 4.50, holds for both the one-phonon and two-phonon processes separately. The result was given in Eq. 4.23:

$$k_{\downarrow,1}(T,\delta_\perp) \approx 32\eta h^3\delta_\perp^3\,[n(2\delta_\perp h)+1]$$

For elevated temperatures $k_\mathrm{B}T \gg 2\delta_\perp h$ ($5\,\mathrm{K} \mathrel{\hat{=}} 50\,\mathrm{GHz}$ strain), the up- and down-rates of Eq. 4.57 and 4.23 become the same and are, to second order in $2\delta_\perp h/k_\mathrm{B}T$, given by [93]:

$$k_1(T \gg 2\delta_\perp h/k_\mathrm{B},\delta_\perp) \approx 16\eta h^2\delta_\perp^2 k_\mathrm{B}T \tag{4.58}$$

4.3.3 Two-phonon process

Next, we derive the second order transition matrix element in Eq. 4.48, again for going from the lower to the upper branch, as given in Eq. 4.42 and 4.43:

$$\begin{aligned} T_{fs}^{(2)} = \sum_m \frac{\hbar^2}{E_s - E_m} & \left(\sum_i \Big[\delta_{p_i,\mathrm{x}}\lambda_i\delta_{O_m,\mathrm{x}} \langle\chi_f|\hat{a}_i + \hat{a}_i^\dagger|\chi_m\rangle \right. \\ & \qquad \left. - \delta_{p_i,\mathrm{y}}\lambda_i\delta_{O_m,\mathrm{y}} \langle\chi_f|\hat{a}_i + \hat{a}_i^\dagger|\chi_m\rangle \Big] \right) \\ & \cdot \left(\sum_j \Big[-\delta_{p_j,\mathrm{x}}\lambda_j\delta_{O_m,\mathrm{y}} \langle\chi_m|\hat{a}_j + \hat{a}_j^\dagger|\chi_s\rangle \right. \\ & \qquad \left. - \delta_{p_j,\mathrm{y}}\lambda_j\delta_{O_m,\mathrm{x}} \langle\chi_m|\hat{a}_j + \hat{a}_j^\dagger|\chi_s\rangle \Big] \right) \end{aligned}$$

Using the same relations as before (Eq. 4.49), this yields:

$$\begin{aligned} T_{fs}^{(2)} = \sum_m \hbar \Bigg(\sum_i \lambda_i \Big[& \underbrace{\sqrt{n_{f,i}+1}\delta_{m,fi+}\delta_{p_i,\mathrm{x}}\delta_{O_m,\mathrm{x}}}_{①} \underbrace{-\sqrt{n_{f,i}+1}\delta_{m,fi+}\delta_{p_i,\mathrm{y}}\delta_{O_m,\mathrm{y}}}_{②} \\ & \underbrace{-\sqrt{n_{f,i}}\delta_{m,fi-}\delta_{p_i,\mathrm{x}}\delta_{O_m,\mathrm{x}}}_{③} \underbrace{-\sqrt{n_{f,i}}\delta_{m,fi-}\delta_{p_i,\mathrm{y}}\delta_{O_m,\mathrm{y}}}_{④} \Big] \Bigg) \end{aligned}$$

$$
\begin{aligned}
\cdot \Bigg(\sum_j \lambda_j \Big[& \underbrace{-\sqrt{n_{s,j}}\delta_{m,sj-}\delta_{p_j,\mathrm{x}}\delta_{O_m,\mathrm{y}}\frac{1}{\omega_j}}_{\text{ⓐ}} \\
& \underbrace{-\sqrt{n_{s,j}}\delta_{m,sj-}\delta_{p_j,\mathrm{y}}\delta_{O_m,\mathrm{x}}\frac{1}{-\Delta_\perp+\omega_j}}_{\text{ⓑ}} \\
& \underbrace{-\sqrt{n_{s,j}+1}\delta_{m,sj+}\delta_{p_j,\mathrm{x}}\delta_{O_m,\mathrm{y}}\frac{1}{-\omega_j}}_{\text{ⓒ}} \\
& \underbrace{-\sqrt{n_{s,j}+1}\delta_{m,sj+}\delta_{p_j,\mathrm{y}}\delta_{O_m,\mathrm{x}}\frac{1}{-\Delta_\perp-\omega_j}}_{\text{ⓓ}} \Big] \Bigg)
\end{aligned}
$$

Since both factors specify attributes of the intermediate state m, less than 16 terms remain in the factored-out equation. For example ①ⓐ: $\delta_{O_m,\mathrm{x}}\delta_{O_m,\mathrm{y}} = 0$. On the remaining terms, we will use relations like

$$
\delta_{m,fi+}\delta_{m,sj-} = \delta_{fi+,sj-}\delta_{m,sj-} = \delta_{f,si-j-}\delta_{m,sj-} \tag{4.59}
$$

and for that specific example,

$$
n_{f,i} = n_{s,i} - 1\,. \tag{4.60}
$$

From the above, one can see that the one intermediate state m for which each term is non-zero is already specified by j and the $\delta_{O_m,\mathrm{x/y}}$. To that end, the sum over m can simply be dropped:

$$
\begin{aligned}
T^{(2)}_{fs} = \sum_{i,j} \hbar\lambda_i\lambda_j \Big[& \sqrt{n_{s,i}}\sqrt{n_{s,j}}\delta_{p_i,\mathrm{x}}\delta_{p_j,\mathrm{y}}\frac{-1}{-\Delta_\perp+\omega_j}\delta_{f,si-j-} && \text{①ⓑ} \\
& +\sqrt{n_{s,i}}\sqrt{n_{s,j}+1}\delta_{p_i,\mathrm{x}}\delta_{p_j,\mathrm{y}}\frac{-1}{-\Delta_\perp-\omega_j}\delta_{f,si-j+} && \text{①ⓓ} \\
& +\sqrt{n_{s,i}}\sqrt{n_{s,j}}\delta_{p_i,\mathrm{y}}\delta_{p_j,\mathrm{x}}\frac{1}{\omega_j}\delta_{f,si-j-} && \text{②ⓐ} \\
& +\sqrt{n_{s,i}}\sqrt{n_{s,j}+1}\delta_{p_i,\mathrm{y}}\delta_{p_j,\mathrm{x}}\frac{1}{-\omega_j}\delta_{f,si-j+} && \text{②ⓒ} \\
& +\sqrt{n_{s,i}+1}\sqrt{n_{s,j}}\delta_{p_i,\mathrm{x}}\delta_{p_j,\mathrm{y}}\frac{-1}{-\Delta_\perp+\omega_j}\delta_{f,si+j-} && \text{③ⓑ} \\
& +\sqrt{n_{s,i}+1}\sqrt{n_{s,j}+1}\delta_{p_i,\mathrm{x}}\delta_{p_j,\mathrm{y}}\frac{-1}{-\Delta_\perp-\omega_j}\delta_{f,si+j+} && \text{③ⓓ} \\
& +\sqrt{n_{s,i}+1}\sqrt{n_{s,j}}\delta_{p_i,\mathrm{y}}\delta_{p_j,\mathrm{x}}\frac{1}{\omega_j}\delta_{f,si+j-} && \text{④ⓐ} \\
& +\sqrt{n_{s,i}+1}\sqrt{n_{s,j}+1}\delta_{p_i,\mathrm{y}}\delta_{p_j,\mathrm{x}}\frac{1}{-\omega_j}\delta_{f,si+j+} \Big] && \text{④ⓒ}
\end{aligned} \tag{4.61}
$$

There are three kinds of processes:

(i) Terms ①ⓓ, ②ⓒ, ③ⓑ, ④ⓐ describe a two-phonon Raman process in which one phonon is absorbed and one is emitted.

(ii) Terms ③ⓓ, ④ⓒ are processes in which two phonons are emitted. Since the orbital state needs energy $\hbar\Delta_\perp$ for the transition $\mathrm{E_y} \to \mathrm{E_x}$ in consideration here, these processes cannot be energy conserving and thus do not contribute.

(iii) Terms ①ⓑ, ②ⓐ are processes in which two phonons are absorbed. Since their sum of energy has to be $\hbar\Delta_\perp$, there are only a few modes that contribute.

To determine the significance of processes where two phonons are absorbed ($\mathrm{E_y} \to \mathrm{E_x}$) or two are emitted ($\mathrm{E_x} \to \mathrm{E_y}$), we compare their rates with the respective Raman process. For most strains studied here ($\delta_\perp < 100\,\mathrm{GHz}$), and for all temperatures where the two-phonon process is relevant ($T > 10\,\mathrm{K}$), the contribution to the hopping rate is below 1 %. We will, therefore, generally neglect two-phonon emission and absorption processes.

We now determine the orbital hopping rate for the two-phonon Raman process. In terms ①ⓓ and ②ⓒ one can swap the names of indices i and j to make their appearance similar to terms ③ⓑ and ④ⓐ. Then, i is the emitted phonon ("$i+$") and j the absorbed ("$j-$"):

$$\begin{aligned}
\tilde{T}^{(2)}_{fs} = \sum_{i,j} & \hbar\lambda_i\lambda_j\sqrt{n_{s,i}+1}\sqrt{n_{s,j}}\delta_{f,si+j-} \\
& \cdot \Bigg[\delta_{p_i,\mathrm{y}}\delta_{p_j,\mathrm{x}}\frac{-1}{-\Delta_\perp-\omega_i} && \text{①ⓓ} \\
& \quad + \delta_{p_i,\mathrm{x}}\delta_{p_j,\mathrm{y}}\frac{1}{-\omega_i} && \text{②ⓒ} \\
& \quad + \delta_{p_i,\mathrm{x}}\delta_{p_j,\mathrm{y}}\frac{-1}{-\Delta_\perp+\omega_j} && \text{③ⓑ} \\
& \quad + \delta_{p_i,\mathrm{y}}\delta_{p_j,\mathrm{x}}\frac{1}{\omega_j}\Bigg] && \text{④ⓐ}
\end{aligned} \tag{4.62}$$

Fermi's Golden Rule requires the conservation of energy, which means for the process we look at

$$\omega_j - \omega_i = \Delta_\perp \geq 0\,. \tag{4.63}$$

With that, terms ①ⓓ and ④ⓐ will become the same, as well as ②ⓒ and ③ⓑ. This gives a factor 2 and two terms in $\tilde{T}^{(2)}_{fs}$ of which only one can be non-zero for given i, j due to the required polarization. The relation in Eq. 4.52 also holds here for $\sum_{i,j}$ and we use the spectral density in Eq. 4.55 twice with $\delta(\epsilon_1 - \hbar\omega_i)$ and $\delta(\epsilon_2 - \hbar\omega_j)$. This gives:

$$\begin{aligned}
k_{\uparrow,2} &= \frac{2\pi}{\hbar}\sum_f \left|\tilde{T}^{(2)}_{fs}\right|^2 \delta(\hbar\Delta_\perp + \epsilon_f - \epsilon_s) \\
&= \frac{2\pi}{\hbar}\left(\frac{2}{\pi\hbar}\right)^2 4\hbar^2 \int_0^\Omega\int_0^\Omega J(\epsilon_1)J(\epsilon_2)\left[n(\epsilon_1)+1\right]n(\epsilon_2) \\
&\qquad\qquad \cdot \left(\left|\frac{\hbar^2}{\hbar\Delta_\perp+\epsilon_1}\right|^2 + \left|\frac{\hbar^2}{\epsilon_1}\right|^2\right)\delta(\hbar\Delta_\perp+\epsilon_1-\epsilon_2)d\epsilon_1 d\epsilon_2
\end{aligned}$$

$$= \frac{32\hbar}{\pi}\int_{\hbar\Delta_\perp}^{\Omega} J(\epsilon-\hbar\Delta_\perp)J(\epsilon)\left[n(\epsilon-\hbar\Delta_\perp)+1\right]n(\epsilon)\left(\frac{1}{\epsilon^2}+\frac{1}{(\epsilon-\hbar\Delta_\perp)^2}\right)d\epsilon \tag{4.64}$$

Likewise, with the detailed balance (Eq. 4.22) we find for the rate $\mathrm{E_x} \rightarrow \mathrm{E_y}$:

$$k_{\downarrow,2} = \frac{32\hbar}{\pi}\int_{\hbar\Delta_\perp}^{\Omega} J(\epsilon-\hbar\Delta_\perp)J(\epsilon)\left[n(\epsilon)+1\right]n(\epsilon-\hbar\Delta_\perp)\left(\frac{1}{\epsilon^2}+\frac{1}{(\epsilon-\hbar\Delta_\perp)^2}\right)d\epsilon \tag{4.65}$$

Using the expressions for $J(\epsilon)$ (Eq. 4.56) and $n(\epsilon)$ (Eq. 4.54) and the substitutions $x=\epsilon/(k_\mathrm{B}T)$ and $x_\perp=\hbar\Delta_\perp/(k_\mathrm{B}T)$ (Eq. 4.44) we find, as already given in Eq. 4.24 and 4.25, that

$$k_{\downarrow,2}(T,\delta_\perp) = \frac{64\hbar}{\pi}\eta^2 k_\mathrm{B}^5 T^5 I(T,\delta_\perp)$$

with the dimensionless phonon integral

$$I(T,\delta_\perp) = \int_{x_\perp}^{\Omega/k_\mathrm{B}T} \frac{e^x x(x-x_\perp)\left[x^2+(x-x_\perp)^2\right]}{2\left(e^x-1\right)\left(e^{x-x_\perp}-1\right)}dx\,.$$

Using the detailed balance, one can directly obtain $k_{\uparrow,2}(T,\delta_\perp)$, which is similar to $k_{\downarrow,2}(T,\delta_\perp)$ at elevated temperature $k_\mathrm{B}T \gg 2\delta_\perp h$ ($5\,\mathrm{K} \mathrel{\widehat{=}} 50\,\mathrm{GHz}$ strain) where the two-phonon process typically dominates. The hopping rates derived in this section as a function of temperature for various strain values will be plotted in Fig. 4.9.

4.3.4 Phonon wavelength considerations

To conclude this section, we will investigate the energy and wavelength of the phonons that contribute to the hopping rates derived above. We will see that we can assume low-energy acoustic phonon modes, which roughly follow the Debye approximation. Further, we will address to what degree our simulations for NV centers in bulk diamond are applicable to shallow NV centers in nanostructures.

Low-energy acoustic phonon modes have a linear dispersion relation with a wavelength λ related to the phonon energy ϵ as

$$\lambda = \frac{v_s h}{\epsilon}\,. \tag{4.66}$$

Here, we used a speed of sound of transversal (shear) waves in diamond of $v_s = 12\,\mathrm{km\,s^{-1}}$ [91, 112]. To find the range of energies ϵ that are relevant for the orbital hopping, we plot the Debye integrand

$$\mathcal{I}\left(x=\frac{\epsilon}{k_\mathrm{B}T},\, x_\perp=\frac{\hbar\Delta_\perp}{k_\mathrm{B}T}\right) = \frac{e^x x(x-x_\perp)\left[x^2+(x-x_\perp)^2\right]}{2\left(e^x-1\right)\left(e^{x-x_\perp}-1\right)} \tag{4.67}$$

from the phonon integral $I(T,\delta_\perp)$ in Eq. 4.25. In Fig. 4.4(a), the Debye integrand $\mathcal{I}$ is plotted for various temperatures and strain values. Relevant values of x lie between 1 and 10. These phonons' temperature-dependent wavelength and energy are given in Fig. 4.4(b). Additionally, the energies of the phonons in the one-phonon process are shown. As we will see in Fig. 4.9, the one-phonon process is typically

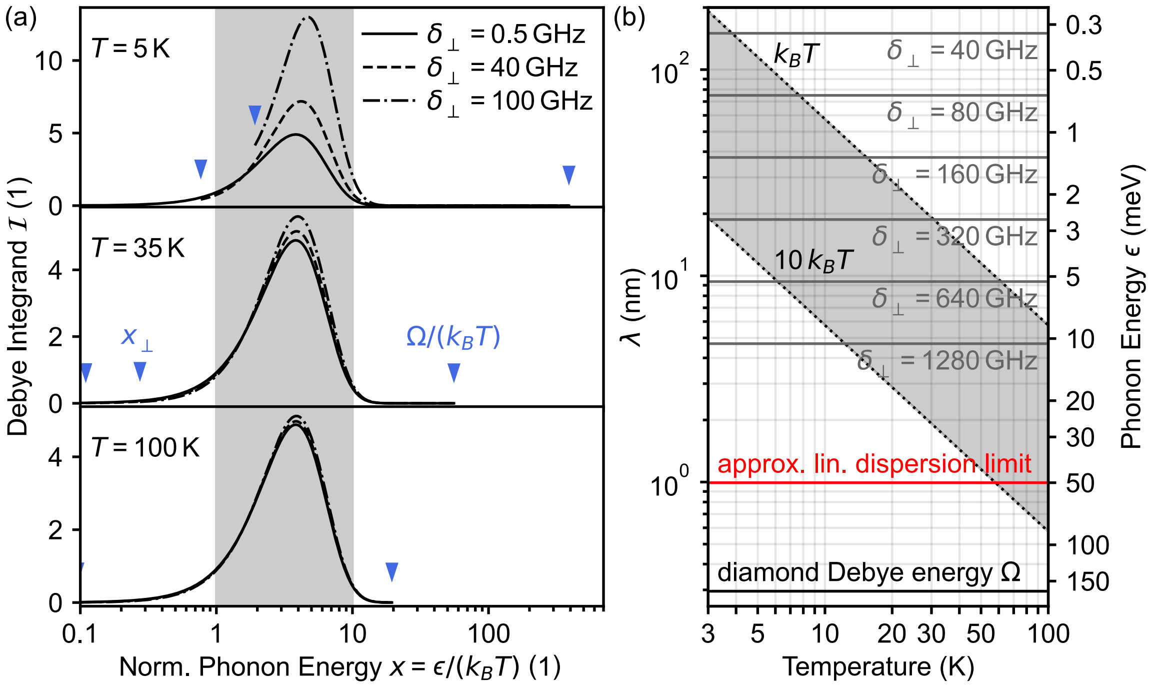

Figure 4.4: Phonon modes driving the orbital hopping process. (a) Debye integrand $\mathcal{I}$ of the two-phonon process for various strain and temperature values. The main contribution to the phonon integral $I(T, \delta_\perp)$ in Eq. 4.25 originates from phonon energies $\epsilon \in [k_\mathrm{B}T,\, 10\, k_\mathrm{B}T]$ (gray shaded area in (a) and (b)). The integrand $\mathcal{I}$ is plotted over the range of the integral $I(T, \delta_\perp)$, and its limits are marked by blue arrows (two per $\delta_\perp$ if within the x-range). For certain conditions, these bounds can become relevant. A similar figure was given by Goldman *et al.* [93] for $\delta_\perp \approx 0$. (b) Contributing phonon energies and wavelength (under Eq. 4.66) as a function of temperature. The approximate linear dispersion limit [111] and diamond Debye energy, which we use as integration bound Ω, are shown. Further, the energies for the one-phonon process (orbital branch splitting) are shown for various strain values in gray.

relevant for $T < 20\,\mathrm{K}$ and $\delta_\perp > 40\,\mathrm{GHz}$. We see in Fig. 4.4(b) that up to 100 K, where the recovered regime (III) in Fig. 2.2(d) starts, the linear dispersion is a good approximation [1, 111]. Above 10 K, where the regime (II) of reduced performance in Fig. 2.2(d) starts, the wavelength is smaller than 60 nm. The same upper wavelength limit is roughly found for relevant contributions to the one-phonon process. In relation to that, the typical scanning-probe pillar structures have a larger diameter $> 100\,\mathrm{nm}$ [113]. But the typical implantation depth of the NV center is around 10 nm. This might cause a small systematic difference between the temperature dependence found in our experiments compared to the bulk simulations done here. Since the orientation of the phonon modes relative to the NV center axis is relevant [91], this difference might even depend on the NV center orientation. The dimensions of the host crystal could become even more relevant for nanodiamonds [103], which often additionally show a very high strain [90] and thus relevant one-phonon processes. Future studies have to show to what degree the temperature-dependent behavior detailed in this thesis will deviate in very small nanostructures. However, the phonon wavelengths responsible for the recovery toward regime (III) are probably still short enough compared to these diamond dimensions and long enough compared to the end of the linear dispersion relation that qualitatively, the same behavior might be observed in all structures. It could be envisioned, though, that targeted engineering of the NV centers depth and orientation could extend the range of regime (I) and thus extend the temperature range of good performance for experiments in the former regime (II).

4.4 Simulation of spin-lattice relaxation and orbital averaging

The phonon-induced hopping between orbital branches results in a strong temperature dependence of the ES spin dynamics. The interplay of orbital branch hopping (Eqs. 4.20, 4.21) and (temperature-independent) spin-state mixing in the ES Hamiltonian (Eq. 4.2, Fig. 4.3) leads to a spin relaxation between the $m_\mathrm{S} = 0$ and $m_\mathrm{S} = \pm 1$ states.

In this section, we first focus on the temperature dependence and how this spin relaxation arises (Sec. 4.4.1). We will then compare it to well-known processes in the field of liquid-state nuclear magnetic resonance (NMR) (Sec. 4.4.2). Finally, we will discuss the influence of crystal strain (or electric field) (Sec. 4.4.3), magnetic field (Sec. 4.4.4), their combination (Sec. 4.4.5), and laser polarization (Sec. 4.4.6) on the temperature dependence of the ES spin dynamics.

4.4.1 Temperature dependence

As an instructive example, we explain the spin relaxation process for the level structure given in Fig. 4.2(b) while assuming a strain of $\delta_\perp = 40\,\mathrm{GHz}$ (Tab. 4.1) — in contrast to $\delta_\perp = 20\,\mathrm{GHz}$ as chosen in Fig. 4.2(b) for clarity of presentation. The state $|+\rangle$ does not mix into the other spin eigenstates in that setting. Therefore, we depict the time evolution in the $|0\rangle$-$|-\rangle$-spin manifold and employ the Bloch sphere picture in Fig. 4.5(b-d). In our description, we write the mixed spin eigenstates as $|0\rangle + \varepsilon\,|-\rangle$ (normalization omitted) *etc.*, where $|\varepsilon|^2 = \left|\epsilon_{|\mathrm{y}\rangle|0\rangle,|\mathrm{y}\rangle|-\rangle}\right|^2 \approx 0.1$ is a small spin-mixing amplitude. Here, $\epsilon_{|i\rangle,|j\rangle}$ between other states $|i\rangle$ and $|j\rangle$ are negligibly small. Crucially, the spin mixing amplitude ε cants the $\mathrm{E_y}$ quantization axis, which is given by the two eigenstates of the $|0\rangle$-$|-\rangle$-spin manifold in the $\mathrm{E_y}$ orbital branch. For comparison, the spin-mixing amplitudes at $\delta_\perp = 40\,\mathrm{GHz}$ and $B = 0\,\mathrm{mT}$ can be found in Fig. 4.3(b). The $|\mathrm{x}\rangle\,|0\rangle$ ($|\mathrm{y}\rangle\,|0\rangle$) state in our example here corresponds to $\left|E^0_{\mathrm{x},0}\right\rangle$ ($\left|E^0_{\mathrm{y},0}\right\rangle$) there. It can be seen that $\left\langle E^0_{\mathrm{x},0}\middle|e_4\right\rangle \approx 1$ while $\left\langle E^0_{\mathrm{y},0}\middle|e_1\right\rangle < 1$.

External magnetic fields, as well as the in-plane strain angle ϕ_δ (here $\phi_\delta = 0^\circ$) and magnitude alter the spin mixing compared to this example. We will address these effects in Secs. 4.4.4–4.4.5, while noting that the general mechanism described here remains valid.

To illustrate the spin relaxation mechanism, we do a Monte Carlo simulation of the time evolution of the spin state in the ES levels. This Monte Carlo approach will later be compared to our full rate model. In these simulations, we exclusively model the coherent evolution in the ES and realize orbital transitions by random, discrete jump

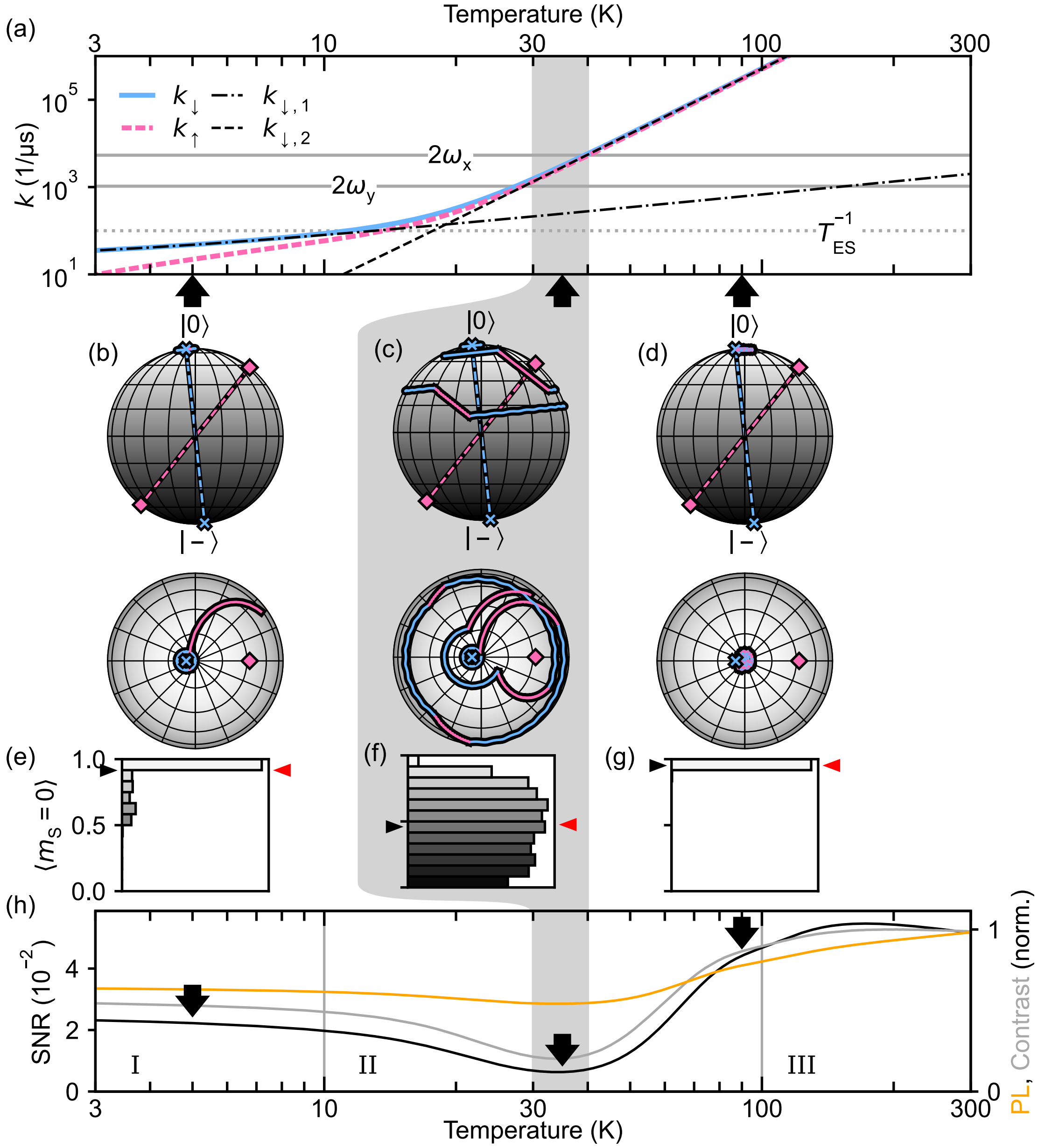

Figure 4.5: Mechanism of the temperature-dependent spin relaxation process in the ES. In the parameter setting of Tab. 4.1, the ES levels are ordered as in Fig. 4.2(b). (a) Orbital hopping rates and their one- and two-phonon contributions as a function of temperature. The inverse lifetime $T_{ES}^{-1} \approx 1/10\,\text{ns}$ of the ES as well as the doubled Larmor frequencies $2\omega_{x/y}$ (units MHz) are indicated by horizontal lines. Spin relaxation is most efficient at temperatures where the hopping rates are resonant with $2\omega_{x/y}$, as indicated by the gray shaded area (here 30 K – 40 K). (b–d) Exemplary realizations of 3 ns time evolution on the side and top views of the Bloch sphere in the |0⟩-|−⟩-spin manifold, plotted for three selected temperatures (marked in parts (a,h)). The color of the time trace encodes the current orbital branch (E_x: blue, E_y: pink). Dashed lines show the quantization axes given by the energy eigenstates in the spin subspace of the two orbital branches, about which Larmor precession occurs. (e–g) Values of m_S after a time evolution of duration T_{ES} under random discrete jumps (average: black arrow) with a corresponding prediction of the master equation with Lindblad jump operators (red arrow). (h) SNR (*cf.* Eq. 2.8), corresponding spin contrast C, and steady-state PL (*cf.* Eq. 2.10) as a function of temperature. The three cases in parts (b–d) mark the three distinct regimes (I–III). Prominently, all three experimental observables reflect the rate of the spin relaxation process.

events with an average frequency given by $k_\downarrow$ and $k_\uparrow$ (Fig. 4.5(a)). The jump events at $t_{n,\downarrow/\uparrow}$, $n \in [0 \mathinner{..} N_{\downarrow/\uparrow}]$, are randomly picked from the interval $t_n \in [0, t]$, while the number of jump events $N_{\downarrow/\uparrow}$ is randomly drawn from the Poisson distribution

$$p(N_{\downarrow/\uparrow}; \lambda = tk_{\downarrow/\uparrow}) = \frac{\lambda^{N_{\downarrow/\uparrow}} e^{-\lambda}}{N_{\downarrow/\uparrow}} . \tag{4.68}$$

We start in the $|E_{\mathrm{x},0}\rangle$ state and evolve the spin state under the von Neumann equation while switching the spin Hamiltonian to fit the respective orbital branch at every jump. The resulting time traces are shown in Fig. 4.5(b–d): Larmor precession at a frequency of the level spacing $\omega_{\mathrm{x/y}}$ occurs (see Fig. 4.2(b)). The time evolution demonstrates the importance of both the spin mixing amplitude ε and the hopping rates $k_{\uparrow/\downarrow}$ in the spin relaxation process: halting the Larmor precession in one orbital branch and continuing it with the same coherent spin state in the other orbital branch can quickly move the spin state away from the Bloch sphere pole where $m_{\mathrm{S}} = 0$.

For hopping rates $k_{\uparrow/\downarrow} \ll T_{\mathrm{ES}}^{-1}$ slower than the ES lifetime, hopping events are rare, and the spin state is mostly conserved. At 5 K, only the $k_{\downarrow,1}$ process leads to a rare decay to the $\mathrm{E_y}$ branch (Fig. 4.5(a)), which happens once in the exemplary time trace shown in Fig. 4.5(b). Nonetheless, the presence of spin mixing (in this example, mostly in the $\mathrm{E_y}$ branch) leads to less-than-optimal conditions. Previous studies established that spin mixing in the ES due to magnetic field [95, 96] or crystal strain [88] is a mechanism for loss of PL. The strain-related spin mixing at low temperatures was found to be partially mitigated by the application of a large magnetic bias field [31, 40, 95], which we will discuss in Sec. 4.4.4.

At elevated temperatures, hopping events become more frequent due to the rapidly increasing two-phonon Raman rates $k_{\uparrow/\downarrow,2}$. Once

$$k_{\downarrow/\uparrow} \approx 2\omega_{\mathrm{x/y}} \tag{4.69}$$

we observe a resonance condition where spin-lattice relaxation is most effective [75]. Here, $\omega_{\mathrm{x/y}}$ are in units Hz as Eq. 4.2 and Fig. 4.2. Intuitively, we find that if precession about each quantization axis completes on average a one-half rotation, the initial spin state is relaxing most efficiently. In our setting, this occurs at around 35 K (Fig. 4.5(c)). This relaxation is a T_1 process of the spin state (*cf.* Sec. 4.2.5).

For hopping rates $k_{\downarrow/\uparrow} \gg 2\omega_{\mathrm{x/y}}$ much faster than the Larmor precession frequency, the initial spin state is barely influenced. This is plotted at 90 K in Fig. 4.5(d). The fast orbital dynamics allow for a description by an effective (time-averaged) room-temperature Hamiltonian, which is obtained by performing a partial trace over the orbital subspace [90] of the low-temperature Hamiltonian (dashed traces in Fig. 4.2(a,c) and Eq. 4.10). In this description, $|0\rangle$ becomes an eigenstate. Thus, at room temperature, this orbital averaging in the ES is critical for the ability to use the NV^- center's outstanding spin properties of the GS through optical excitation.

Finally, we compare the Monte Carlo approach to our rate model (Eq. 4.26), which is used elsewhere in this thesis. In contrast to the discrete jumps in the Monte Carlo approach, the jump operators of the orbital hopping process in our rate model generate a continuous decay of the orbital state. To ensure that our rate model stays in the ES, all decay channels out of the ES were set to 0 for this comparison. In Fig. 4.5(e–g), we plot histograms of the the final population of $m_\mathrm{S} = 0$ in Monte Carlo simulations after a time $t = T_\mathrm{ES}$ spent in the ES, obtained from 10000 (5 K, 35 K) resp. 500 (90 K) realizations of random time traces. As expected, the average of the histogram yields the same result as the expectation value obtained from our rate model, validating both approaches.

In summary, the three regimes that were labeled in Fig. 2.2(d) can be identified. The same qualitative behavior is witnessed in both observables, PL and spin contrast C, and therefore also in the SNR in Fig. 4.5(h):

(I) Around 5 K, the SNR is mostly constant and at a relatively high level.

(II) Around 35 K, the SNR is strongly reduced. The position of the minimum depends on the level spacing and, thus, Larmor frequencies of the given setting, while its depth additionally depends on the degree of spin mixing.

(III) Around 90 K, the SNR has recovered and remains approximately constant up to room temperature. Here, the best SNR is observed.

4.4.2 Comparison to phenomena in the field of NMR

The mechanisms of spin-lattice relaxation and orbital averaging above are related to common textbook examples in the field of NMR: a T_1 relaxation process in a two-level system that is subject to *transversal* random telegraph noise (RTN) and an averaging of NMR resonances that originates from *longitudinal* RTN. Here, transversal/longitudinal components are terms in the Hamiltonian that change/do not change the direction of the system's inherent quantization axis. We will look at these examples in the context of modeling them with the Lindblad master equation and draw parallels to the phonon interactions in the ES of the NV$^-$center.

Longitudinal noise

We start with *longitudinal* RTN on a two-level system and motional averaging. For that, we take up the two-level toy model from Sec. 4.2.5 and add a driving field to it. The Hamiltonian of the system in the rotating frame and under the rotating wave approximation is

$$\hat{H}_\parallel/h = (\omega_0 - \omega)\hat{\sigma}_z/2 + R\hat{\sigma}_x/2 \pm \Delta_z\hat{\sigma}_z/2\,. \tag{4.70}$$

Here, ω_0 is the Larmor frequency and level spacing, ω is the driving field (Rabi) frequency, and R is its amplitude. The system is subject to a fluctuating longitudinal field that randomly takes values of $\pm\Delta_z$ at an average rate k_h of switching ("hopping") from one direction to the other. As before, we always use frequencies and units Hz (not angular frequencies and units rad/s) for energy differences, Larmor frequencies, *etc.*. For very small hopping rates k_h, Eq. 4.70 will show two resonances at $\omega = \omega_0 \pm \Delta_z$. The phenomenon of "motional averaging" refers to the observation that for very high

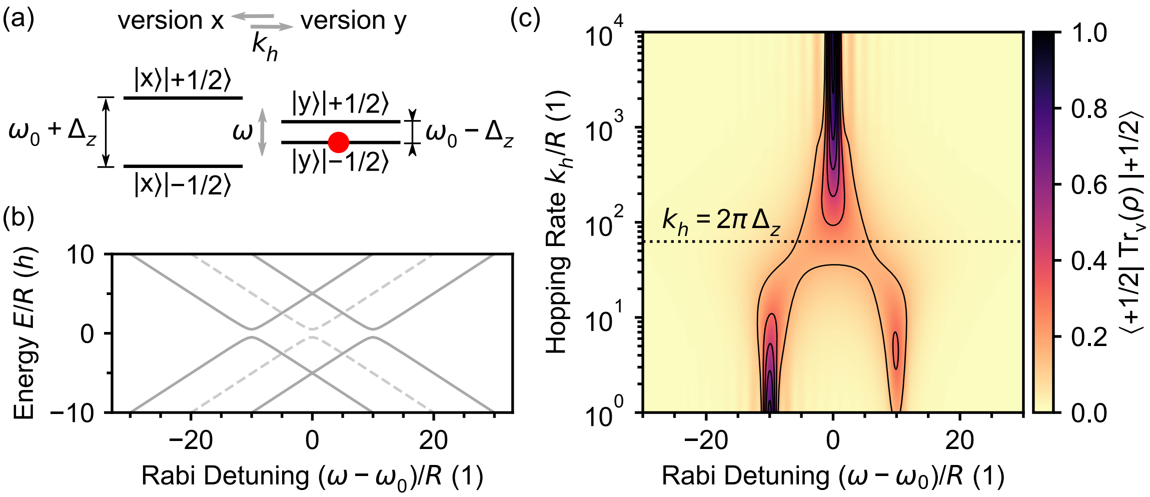

Figure 4.6: Toy model with longitudinal noise to illustrate the process of motional averaging. (a) Level structure of a two-level system ($|{+1/2}\rangle$ and $|{-1/2}\rangle$) with RTN of amplitude $\pm\Delta_z$ and rate k_h is modeled by hopping between two versions ($\mathrm{v} \in [\mathrm{x}, \mathrm{y}]$) of the two-level system. Note the analogy to Fig. 4.2(b). (b) Eigenenergies of the system in the rotating frame under rabi drive with frequency ω and amplitude R (Eq. 4.71). Dashed traces are the eigenenergies of the version-averaged system obtained by a partial trace over the version subspace. We assume $\Delta_z = 10\,R$. Note the analogy to Fig. 4.2(c). (c) Lindblad master equation simulation of the population in the $|{+1/2}\rangle$ state after a duration equal to a π-pulse (when on resonance) as a function of rabi drive frequency and hopping rate. The initial state is marked with a red dot in (a). With increasing hopping rate, the two Rabi resonances first show exchange broadening and the initially empty version x gets populated (right resonance). At the dynamical threshold (dotted trace, see Eq. 4.73), the two resonances show motional averaging to a single resonance, and finally, motional narrowing of the resonance is witnessed.

hopping rates k_h, just a single resonance at $\omega = \omega_0$ is observed instead. This resonance is broad at first, but as the hopping rate grows further, it reaches the linewidth of $k_h = 0$ again — a process called “motional narrowing”. The entire process is presented in Fig. 4.6(c). The mathematical description of this toy model can be approached analytically or numerically. The interested reader is referred to Ref. [114], treating motional averaging and narrowing in the same toy system on a superconducting qubit. There, the method of quantum trajectories [115], a similar approach as our Monte Carlo simulation in Fig. 4.5(b–d), is used to obtain a map as presented in Fig. 4.6(c). Here, however, we will approach the problem with the same method as we generally use for the NV$^-$ photo-physics — the Lindblad master Eq. 4.26.

We imagine hopping between two versions of the two-level system with spin states $|{+1/2}\rangle$ and $|{-1/2}\rangle$. We call the versions x and y, similar to the orbital states of the NV$^-$ ES. One version has a level spacing $\omega_\mathrm{x} = \omega_0 + \Delta_z$, the other $\omega_\mathrm{y} = \omega_0 - \Delta_z$, as depicted in Fig. 4.6(a). In both versions, the quantization axis is the z-axis. The average rate k_h of the RTN becomes the hopping rate. We apply a driving pulse with frequency ω and duration $t = 1/(2R)$ that becomes a π-pulse when ω is in resonance with the level spacing shown in Fig. 4.6(b). For small hopping rates k_h, and assuming a classical mixture of the version as the initial state, a readout of the spin state will then yield a resonance spectrum of two peaks, similar to what we found in a pulsed ODMR experiment in Fig. 2.2(b) (when ignoring the hyperfine splitting). If we start in state $|\mathrm{y}\rangle\,|{-1/2}\rangle$ instead, we obtain a spectrum as the linecut at $k_h \to 0$ in

Fig. 4.6(c). To simulate Fig. 4.6(c), we use the master Eq. 4.26 with a Hamiltonian based on Eq. 4.70 but extended to four levels

$$\hat{H}_{\parallel,4\text{ level}}/h = (\omega_0 - \omega)\,\hat{\mathbb{I}}_2 \otimes \hat{\sigma}_z/2 + R\,\hat{\mathbb{I}}_2 \otimes \hat{\sigma}_x/2 + \Delta_z\,\hat{\sigma}_z \otimes \hat{\sigma}_z/2 \tag{4.71}$$

in the Hilbert space of version and spin $\mathcal{H}_v \otimes \mathcal{H}_{\text{spin}}$, and jump operators

$$\hat{L}_{h,\text{x}} = \sqrt{k_h}\,|\text{y}\rangle\langle\text{x}| \otimes \hat{\mathbb{I}}_2 \text{ and } \hat{L}_{h,\text{y}} = \sqrt{k_h}\,|\text{x}\rangle\langle\text{y}| \otimes \hat{\mathbb{I}}_2 \tag{4.72}$$

for the hopping. Note the similarity to Eq. 4.36 and 4.37. The linewidth of the resonances and faint satellite features in the bottom linecut of Fig. 4.6(c) are given by the power-broadening and spectral components of the square pulse. With increasing hopping rate k_h, the linewidths broaden, which is called "exchange broadening" in the field of NMR. It is caused by a decoherence process on the spin state with $T_2 = 1/k_h$ that originates from the randomization of the Larmor precession at frequencies $\omega_{\text{x/y}}$. While the linewidths broaden, the resonances will start to melt to a single broad resonance at ω_0. This happens around the "dynamical threshold" [114] where

$$k_h = 2\pi\Delta_z\,. \tag{4.73}$$

But when increasing the hopping rate further, this broad resonance becomes narrower again since the decoherence rate of the averaged resonance goes as [116, p. 212]

$$1/T_2 = \frac{(2\pi\Delta_z)^2}{2k_h}\,. \tag{4.74}$$

The system seems to evolve under a time-averaged, effective Hamiltonian obtained by taking the partial trace over the version subspace $\text{Tr}_\text{v}(H_{\parallel,4\text{ level}})$. Similarly, the NV$^-$ ES appears to consist of only the three spin states at room temperature, obtained by a partial trace over the orbit (Eq. 4.10).

Transversal noise

We now switch to the case of *transversal* RTN on a two-level system and the effect of spin relaxation. For this, we exchange the term $\pm\Delta_z\,\hat{\sigma}_z/2$ in Eq. 4.70 with $\pm\Delta_x\,\hat{\sigma}_x/2$ and leave out the Rabi drive. We adopt the scheme of modeling the RTN by hopping between two versions of the two-level system. In the lab frame, the Hamiltonian is then given by

$$\hat{H}_{\perp,4\text{ level}}/h = \omega_0\,\hat{\mathbb{I}}_2 \otimes \hat{\sigma}_z/2 + \Delta_x\,\hat{\sigma}_z \otimes \hat{\sigma}_x/2\,. \tag{4.75}$$

The ratio of ω_0/Δ_x leads to a tilt of the quantization axis and spin state mixing, as shown in Fig. 4.7(a). For comparison, the selected NV$^-$ case in Fig. 4.5 had a mixing $|\varepsilon|^2 \approx 10^{-1}$ (see Fig. 4.3(b)). The mixing, in combination with the hopping rate k_h, leads to a spin relaxation (T_1) process, as discussed for the NV$^-$ in Sec. 4.4.1. For historical reasons, this process is called "spin-lattice relaxation" in the field of NMR. The relaxation rate can be found analytically for this toy model and is given by [116, p. 198]

$$1/T_1 = \frac{(2\pi\Delta_x)^2/(2k_h)}{1 + (2\pi\omega_0)^2/(2k_h)^2}\,, \tag{4.76}$$

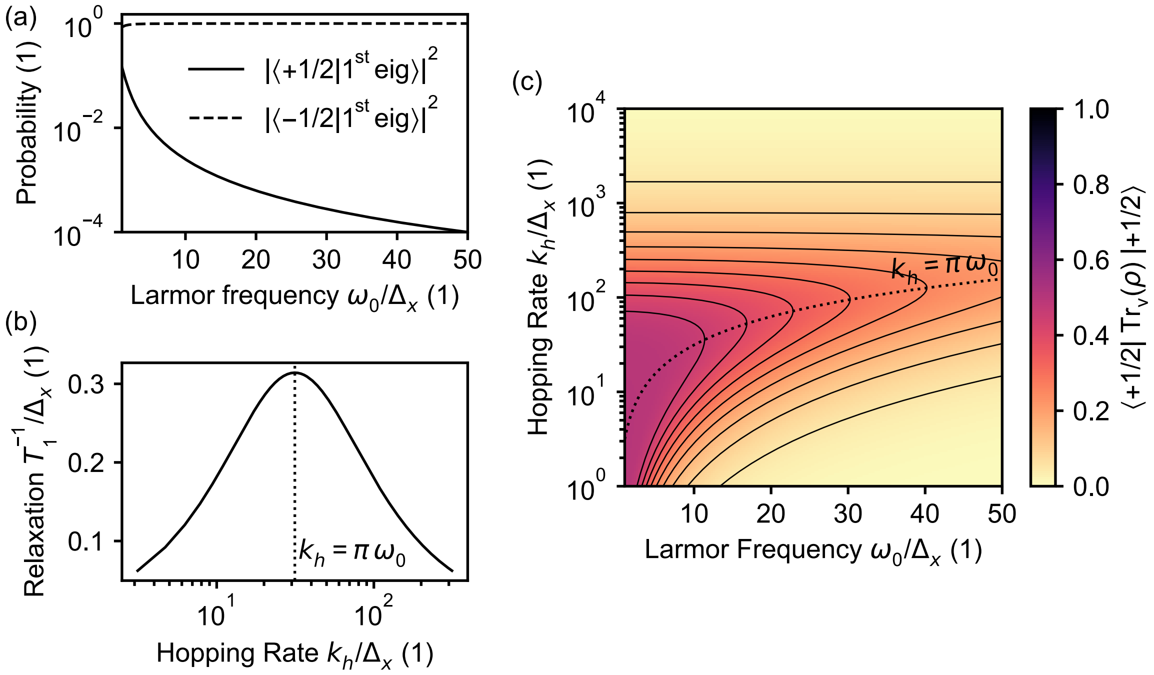

Figure 4.7: Toy model with transversal noise to illustrate the process of spin-lattice relaxation. (a) Spin mixing due to altered eigenstates. The level system from Fig. 4.6(a) is assumed to be subject to the same RTN, but now pointing perpendicular to the quantization axis. This leads to a small tilt of the quantization axis for each version ($\mathrm{v} \in [\mathrm{x}, \mathrm{y}]$), which can be witnessed as a small spin state ($|+1/2\rangle$ and $|-1/2\rangle$) mixing, depending on the ratio ω_0/Δ_x. (b) When the hopping rate k_h is resonant with the level spacing (dotted trace, see Eq. 4.77), the highest relaxation rate is predicted. Here, we assumed a level spacing of $\omega_0/\Delta_x = 10$. (c) Lindblad master equation simulation of the population in the $|+1/2\rangle$ state after a duration $t = T_1(\omega_0 = 30\,\Delta_x, k_h = \pi\omega_0)$ from Eq. 4.76.

which reaches a maximum at

$$k_h = \pi\omega_0 \text{ with } 1/T_1 = \frac{(2\pi\Delta_x)^2}{4\pi\omega_0} \tag{4.77}$$

as plotted in Fig. 4.7(b). An intuition for the resonance condition here can be obtained by viewing the process in the ω_0-rotating frame [116, p. 206]: perturbations with an inverse correlation time (twice the hopping rate k_h) equal to ω_0 become quasi-static and can most effectively alter the state, similar to a π-pulse by a driving field on resonance (as in Eq. 4.70). Again, we can simulate the time evolution numerically with the Hamiltonian from Eq. 4.75 and the jump operators in Eq. 4.72 by using the Lindblad master equation. In Fig. 4.7(c), we do so for varying degrees of spin mixing and hopping rate k_h. We see, as also expected from Eq. 4.77, that the hopping rate required for a relaxation maximum grows as the mixing is reduced. At the same time, the degree of relaxation at this maximum is shrinking but still clearly present even for very small mixing amplitudes (see Fig. 4.7(a)).

We note that a quantitative agreement between the analytical expressions in Eqs. 4.74/4.76 and the simulations with the Lindblad master equation in Figs. 4.6/4.7 is observed. In the derivation of the analytical expressions above, the rotating wave approximation (labeled with (iii) in the Lindblad master equation discussion in

Sec. 4.2.5) was made since the correlation time of the perturbation is shorter than the system time scales [116, p. 199].

Analogy to the NV$^-$ ES

Having discussed the processes of motional averaging and spin-lattice relaxation in this toy model, we can now return to the NV$^-$ ES. In an analogy to our NV$^-$ example in Sec. 4.4.1, the two-level system is the $|0\rangle$-$|-\rangle$-spin space, the RTN is a change in the Hamiltonian when alternating between the orbital branches, and the tilted quantization axis (due to $\varepsilon > 0$) gives rise to the spin relaxation, as it causes transversal noise. This mechanism gives rise to the dip in performance as a function of temperature and is the origin of the regime (II) in Fig. 4.5(h).

We now shift the focus to the orbital averaging that defines regime (III). As we learned from the toy model above, the longitudinal noise causes this process. In the analogy to the NV$^-$ ES, longitudinal noise means that $\omega_\mathrm{x} \neq \omega_\mathrm{y}$ in the two orbital branches. It was first discussed by Rogers *et al.* [40] that the orbital time-averaging process is analogous to motional narrowing in liquid-state NMR spectroscopy. As we saw in Eq. 4.74, a decoherence rate on the spin state arises. This has been used to explain the narrowing of the ES ODMR lines at [42] and above room temperature [90, 110]. However, the decoherence rate is not to be confused with the relaxation rate discussed in this thesis. Since in this thesis, the ES is only used for readout and initialization of the spin state (*i.e.* its projection on the quantization axis), its decoherence rate does not matter — even though it is inherently contained in our model. In these previous studies, *longitudinal* RTN along the z-axis of the NV$^-$ center was examined, while *transversal* components could be neglected. The spin relaxation process introduced in this thesis requires the presence of transversal components in the RTN, which are caused by the different spin mixing in the two branches. This spin mixing requires a finite $\lambda_\mathrm{ES}^\perp$ in the Hamiltonian in Eq. 4.2 [37, 87, 88]. But the magnitude of $\lambda_\mathrm{ES}^\perp$, which is still under debate [1, 104], does not affect the resonance condition in Eq. 4.69 (or Eq. 4.77 for the toy model) — in contrast to the explanation provided in Ref. [37]. The ε (or Δ_x for the toy model) has no influence on the temperature (or rate k_h for the toy model) where the resonance condition is fulfilled. Increasing the magnitude of $\lambda_\mathrm{ES}^\perp$ only broadens and deepens the minimum in NV sensing performance, which can intuitively be understood through an increased ε and canting of the quantization axis in Fig. 4.5(b–d). Setting $\lambda_\mathrm{ES}^\perp = 0$, on the other hand, removes the spin mixing and thus spin-lattice relaxation, leaving behind only the separate mechanism of motional-averaging that defines regime (III) (see later Fig. 4.11(a)). In contrast to $\lambda_\mathrm{ES}^\perp$, the level spacings $\omega_\mathrm{x/y}$ (or ω_0) have a direct influence on the temperature of the minimum according to Eq. 4.69 (or Eq. 4.77). Since strain and magnetic field influence the level spacings, we will discuss them in the next sections.

4.4.3 Strain dependence

The temperature-dependent spin-state relaxation is influenced by an external magnetic bias field as well as the strength and direction of crystallographic strain or, equivalently,

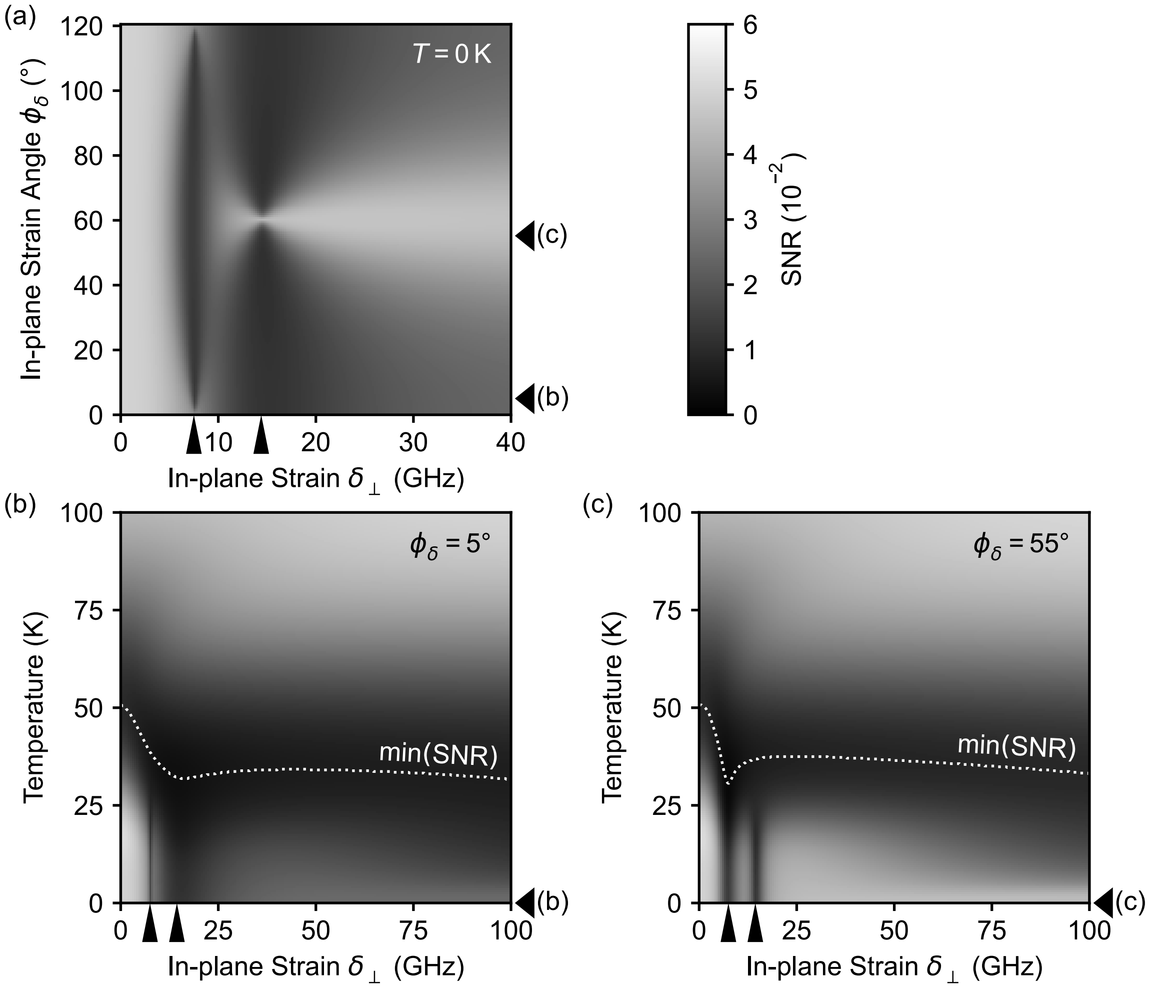

Figure 4.8: Influence of strain on the NV$^-$ performance. (a) Effect of strain $\delta_\perp$ or electric field and its angle ϕ_δ on the SNR. ES LACs, as indicated with the same markers in Fig. 4.2(a), lead to regions of reduced SNR. (b, c) Effect of strain or electric field on the SNR as a function of temperature. The linecuts at 0 K for the two angles ϕ_δ in parts (b) and (c) correspond to the linecuts indicated by the same markers in part (a). A multifaceted landscape of regions with reduced SNR is predicted by these simulations. The numerical minimum in SNR "min(SNR)" is marked per value of $\delta_\perp$ and is the hallmark of the regime (II). For the entire figure, parameters from Tab. 4.1 are used.

an electric field. We first limit ourselves to $B = 0\,\mathrm{mT}$ and address the influence of strain in the distinct regions in parameter space step by step.

We first discuss the effect of the in-plane angle ϕ_δ for strain values $\delta_\perp > 20\,\mathrm{GHz}$ (case from Sec. 4.4.1) at base temperature $T \approx 0\,\mathrm{K}$. The angle alters the degree of spin mixing in the two branches. In the $\mathrm{E_y}$ branch, the degree of spin mixing is maximal at $\phi_\delta = 0°$ and vanishes toward $\phi_\delta = 60°$. In the $\mathrm{E_x}$ branch, this behavior is qualitatively reversed. However, the spin mixing amplitudes in $\mathrm{E_x}$ are generally smaller than the mixing that occurs in the $\mathrm{E_y}$ branch. If we assume equal optical excitation into both branches (*i.e.* $r_\beta = 1$), this results in reduced SNR at a strain angle of $\phi_\delta \approx 0°$ (and multiples of 120°, due to the C_{3v} symmetry of the NV$^-$ center), as plotted in Fig. 4.8(a) and as can be seen when comparing Fig. 4.8(b) and Fig. 4.8(c) for $T \approx 0\,\mathrm{K}$. With increasing temperature, the effect of ϕ_δ disappears in the motional averaging regime (III), as can be seen in Fig. 4.8(b,c) above $T > 50\,\mathrm{K}$. We note that since this effect occurs at cryogenic temperatures, mitigation can be possible by selective resonant excitation into the ES branch with the lower spin mixing at a given ϕ_δ [88]. We will further address the interplay with the optical excitation in Sec. 4.4.6.

We stick to strain values $\delta_\perp > 20\,\mathrm{GHz}$ and discuss the effect of the strain magnitude $\delta_\perp$ next. In Fig. 4.5, we saw that the orbital hopping rates, paired with the spin mixing, cause the observed spin relaxation process. The temperature dependence of the orbital hopping rates up ($k_\uparrow$) and down ($k_\downarrow$) are plotted in Fig. 4.9 for varying in-plane strain $\delta_\perp$. At high strain in Fig. 4.9(a), two effects can be observed: First, at low temperatures, $k_\downarrow$ is significantly higher — a comparison with lower strain is given in Fig. 4.9(d). This is caused by the increase of the phonon mode density with energy: if the orbital branch splitting $\sim 2\delta_\perp$ (Eq. 4.44) is larger, a higher mode density is available for the spontaneous one-phonon emission process (second term in Eq. 4.23). Second, $k_\uparrow$ increases more rapidly with rising temperature — a comparison with lower strain is given in Fig. 4.9(e). This arises since at very low temperature and high strain, the phonon modes required for the one-phonon absorption process are not populated. But as temperature rises, they rapidly become thermally activated, and $k_\uparrow$ reaches the same order of magnitude as $k_\downarrow$. This can be seen in the detailed balance of the rates in Fig. 4.9(f). In both Fig. 4.8(b) and (c), the two effects of the strain-dependent one-phonon process become apparent as a reduction of the SNR with increasing strain (compared at a constant $T < 20\,\mathrm{K}$). At the high strain values, even at $T = 0$, the one-phonon process has a significant influence. Once the temperature is $T > 20\,\mathrm{K}$, the only mildly strain-dependent two-phonon process (Eq. 4.24) dominates and is responsible for the minimum in SNR around $k_{\downarrow/\uparrow} \approx 2\omega_{\mathrm{x/y}}$ (Eq. 4.69). Consequently, as can be seen in Fig. 4.8(b,c), the minimum shows only a small strain dependence for $\delta_\perp > 20\,\mathrm{GHz}$.

Next, we consider the effect of the strain magnitude for $\delta_\perp < 5\,\mathrm{GHz}$ (flat eigenenergies in Fig. 4.2(a)), as found with NV$^-$ centers in bulk diamond. Here, the spin state $|0\rangle$ has very small mixing with the spin states $|\pm1\rangle$ ($\left|\epsilon_{|i\rangle,|j\rangle}\right|^2 \leq 0.03$, see Fig. 4.3(a)). As can be seen in Fig. 4.9(c), the one-phonon hopping rates are also negligibly small. This leads to optimal SNR at cryogenic temperature. Since the level spacing and thus Larmor frequencies ω between eigenstates are large (see Fig. 4.2(a)), the maximal spin relaxation around $k_{\downarrow/\uparrow} \approx 2\omega$ is met at a temperature of around $50\,\mathrm{K}$ in Fig. 4.8(b,c). This constitutes an upward shift from the previously found minimum at $35\,\mathrm{K}$ for higher strain and smaller Larmor frequencies. Even with small spin mixing at zero strain, the minimum is still well-pronounced. This results from two mechanisms that will be explained in the next Sec. 4.4.4. There, these two mechanisms (listed as (i) and (ii) there) explain why a well-pronounced minimum still occurs when a high magnetic field reduces the spin mixing. Interestingly, this also implies that at temperatures above $50\,\mathrm{K}$, higher strain can be beneficial for the SNR since the averaging process is already effective. Below $50\,\mathrm{K}$, low-strained bulk NV centers will yield the best SNR.

Closing the gep in parameter space, between $5\,\mathrm{GHz} < \delta_\perp < 20\,\mathrm{GHz}$ the SNR is dominated by ES LACs (see Fig. 4.2(a)). At these LACs, eigenstates consisting mostly of spin states with $m_\mathrm{S} = 0$ are mixed with those with $m_\mathrm{S} = \pm1$. This leads to a rapid loss of the spin state after optical excitation from the GS and thus destroys the optical initialization and readout process. Since the orbital averaged Hamiltonian has no ES

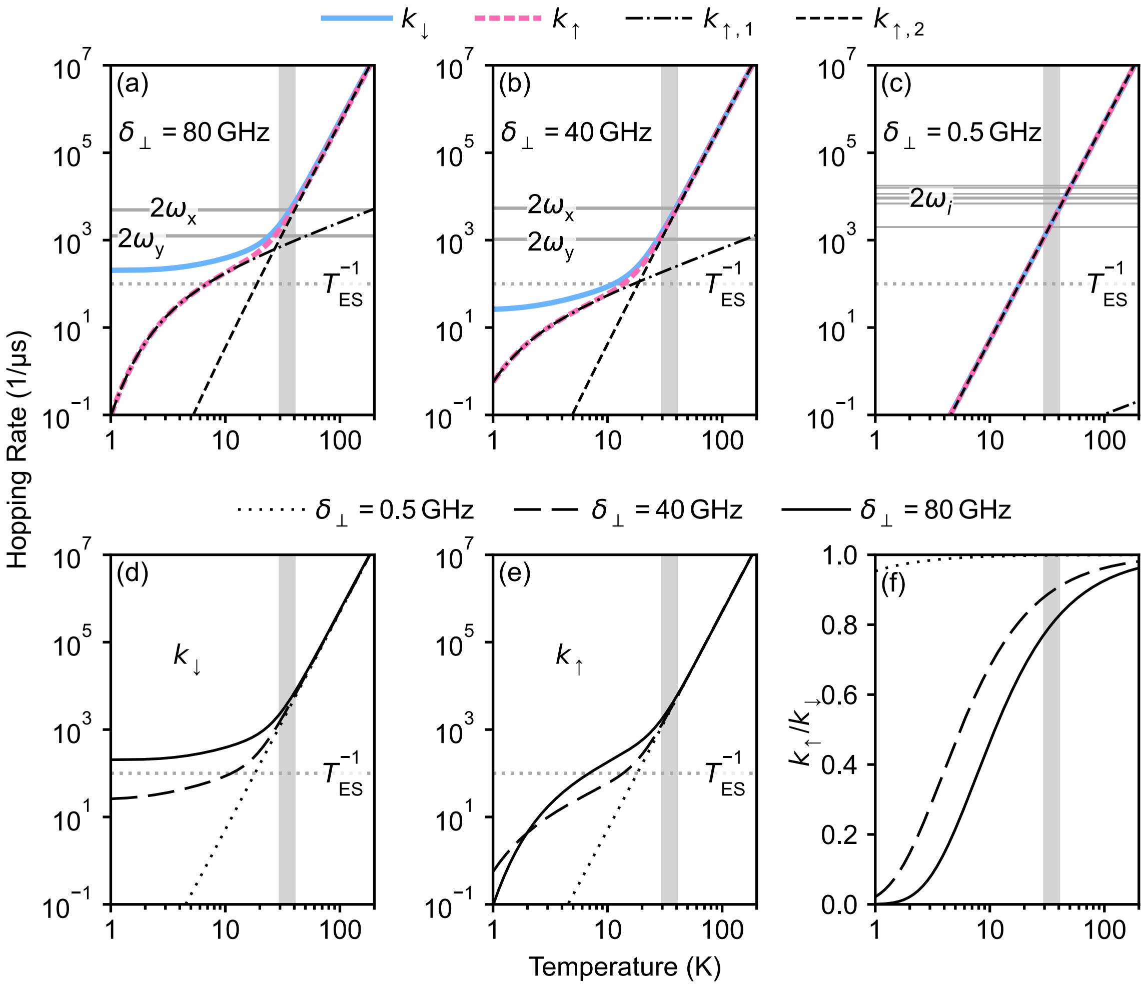

Figure 4.9: Orbital hopping rates under different crystal strains. (a) Rates up and down and contributions to the rate up by the one- and two-phonon processes for high strain (Eqs. 4.20–4.24). Also shown are the inverse optical lifetime T_{ES}^{-1} and twice the Larmor frequencies $2\omega_{x(y)}$ (in MHz) as horizontal lines. A similar plot was introduced for comparatively medium strain $\delta_\perp = 40\,\mathrm{GHz}$ in Fig. 4.5(a). Since a similar level structure is present here at high strain, one can still compare $k_{\downarrow/\uparrow} \approx 2\omega_{\mathrm{x/y}}$ for maximal spin relaxation. The 30 K – 40 K region, where highest spin relaxation was observed there, is also marked here as a reference (gray shading). (b, c) Same plots for $\delta_\perp = 40\,\mathrm{GHz}$ (*i.e.* similar to Fig. 4.5(a)) and $\delta_\perp = 0.5\,\mathrm{GHz}$ strain. Note that at low strain, as in part (c), the concept from Fig. 4.5 with only two Larmor frequencies $\omega_{\mathrm{x/y}}$ breaks down. Instead, twice the Larmor frequencies $2\omega_i$ are shown for all ES levels versus the two $m_S = 0$ states $\left|E^0_{\mathrm{x},0}\right\rangle$ and $\left|E^0_{\mathrm{y},0}\right\rangle$ (almost eigenstates here, see Fig. 4.3(a)). Since these ω_i lie higher than $\omega_{\mathrm{x/y}}$ in parts (a,b), the maximum in spin relaxation is reached at a higher temperature. (d) Overview of the effect of strain on the hopping rate down. (e) Overview of the effect of strain on the hopping rate up. (f) Ratio of rate up and down for different strains. The ratio results in a Boltzmann distribution in the orbital branches after sufficient waiting time. For the entire figure, parameters from Tab. 4.1 are used.

LAC as a function of strain, their effect disappears in the motional averaging regime (see Fig. 4.2(a)).

In summary, targeted application of electric fields [88, 97] or tuning of the strain magnitude and direction [98] can substantially improve the SNR.

4.4.4 Magnetic field dependence

We next focus on the influence that an axial magnetic bias field B has on ES spin relaxation and orbital averaging. The SNR as a function of magnetic field and temperature is plotted in Fig. 4.10.

Addressing the ES LACs in Fig. 4.10(a) first, which dominate the appearance below 70 mT, one can observe how the two LACs at low temperatures average to the single LAC towards room temperature. The origin of these LACs can be inferred from the evolution of eigenenergies in Fig. 4.2(c) with a similar setting. They can be seen as hallmarks of the effective Hamiltonian at the respective temperature [95] and thus allow us to infer at which temperature motional averaging occurs. In Fig. 4.10(a), the averaging evidently happens inside the spin-lattice relaxation regime, which is around 35 K for this strain setting. But the temperature of maximal spin-lattice relaxation and the temperature of the on-set of averaging do not need to coincide. A comparison with the two-level toy model in Fig. 4.6(c) and its Eq. 4.73 for the "dynamical threshold" (on-set of averaging) suggests that when increasing the difference $\omega_x - \omega_y = 2\Delta_z$ in Larmor frequency of the two orbital branches, the hopping rate required for motional averaging is higher. A delayed emergence of the averaged ES is indeed realized in the NV$^-$ ES for low strain, as simulated in Fig. 4.10(b) and observed experimentally in Ref. [37]. Here, the LAC at 51 mT only forms around 100 K since the level spacings and thus their differences are larger than at increased strain (see Fig. 4.2(a)). A direct comparison of the on-set of averaging between these two cases of strain magnitude is easier when the spin-lattice relaxation (at low B) is removed, which is done in Fig. 4.11. In Ref. [37, Fig. 3c], a magnetic field angle ϕ_B dependence is also found to delayed the emergence of the averaged ES, but mostly at strain values $\delta_\perp > 30\,\mathrm{GHz}$. This effect cannot be understood with the concept of the dynamical threshold, as discussed here. Rather, it is highly dependent on the interplay of the magnetic and strain angles and has the same origin as the faint revival feature visible between the ES LACS at intermediate temperatures in Fig. 4.10(a) and will be discussed in the next Sec. 4.4.5. It should be emphasized that a simple averaging of the B-positions of the LACs does not describe the room temperature LAC position, as it seems to be the case in Fig. 4.10(a) and as it was the case in the toy model in Fig. 4.6(c). Only a partial trace over the orbital subspace of the Hamiltonian can provide the correct position, which is independent of strain (see Fig. 4.2(a)).

Around the ES LACs, the min(SNR) trace in Fig. 4.10(a) shows dips in temperature. Here, the $m_\mathrm{S} = 0$ and $m_\mathrm{S} = -1$ levels have the smallest level spacings ω, and the resonance condition for the relaxation maximum $k_{\downarrow/\uparrow}(T) \approx 2\omega$ is met at a lower temperature.

With a magnetic field value above the ES LACs in Fig. 4.10(a), and ignoring the GS

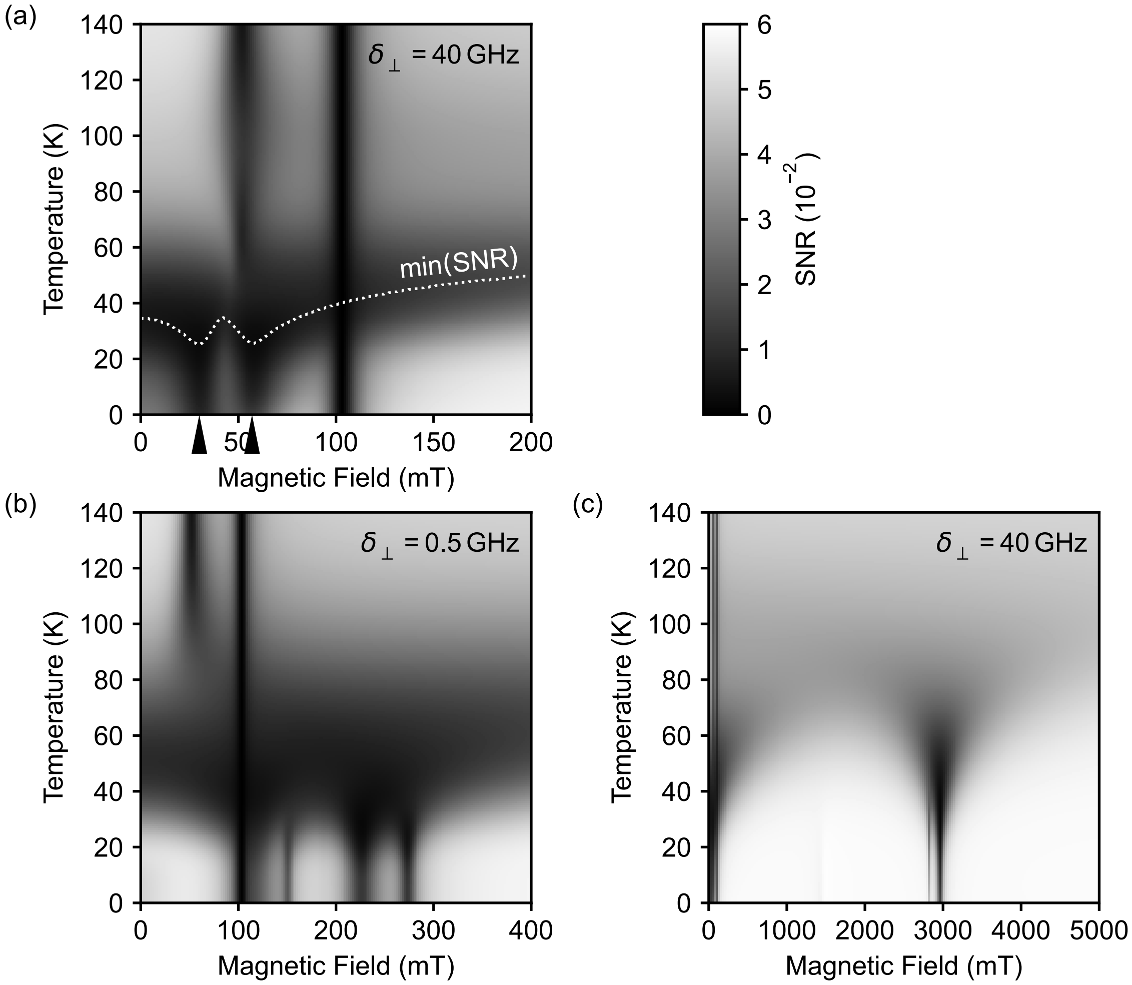

Figure 4.10: Influence of magnetic field on the NV$^-$ performance. (a) Effect of an axial magnetic field and temperature on the SNR. The SNR is strongly reduced at ES LACs (around 30 mT and 57 mT, as indicated with same markers as in Fig. 4.2(c)) and at the GS LAC (103 mT). Additionally, a horizontal minimum occurs in the regime (II). Its numerical minimum "min(SNR)" is marked per temperature. Note the similarity of the B range [0, 90 mT] here to to the toy model with longitudinal noise in Fig. 4.6(c) and the range [70 mT, 200 mT] to the toy model with transversal noise in Fig. 4.7(c). (b) SNR map for an NV center with very low strain splitting of 1 GHz ($\delta_\perp = 0.5$ GHz) as found in bulk diamond. The same qualitative behavior as in part (a) is observed, though the dip in performance is shifted to higher temperatures at low magnetic fields. (c) Same map as in part (a) but extended to very high magnetic fields. Only when approaching $B \sim 5$ T, the dip in performance at intermediate temperatures in regime (II) gradually disappears. It should be noted, though, that this field value is significantly influenced by the position of the LACs above 2.9 T, which were observed to be shifted to significantly higher fields supposedly due to a strain-dependent orbital g_l factor [95]. For the entire figure, parameters from Tab. 4.1 are used, only altered to $\theta_B = 1.9^\circ$ (for $\theta_B = 0$ the GS and averaged ES LACs are not visible), $\phi_\delta = 24.4^\circ$, and $\phi_B = 194.2^\circ$ as found experimentally for NV-2 in Tab. 6.3.

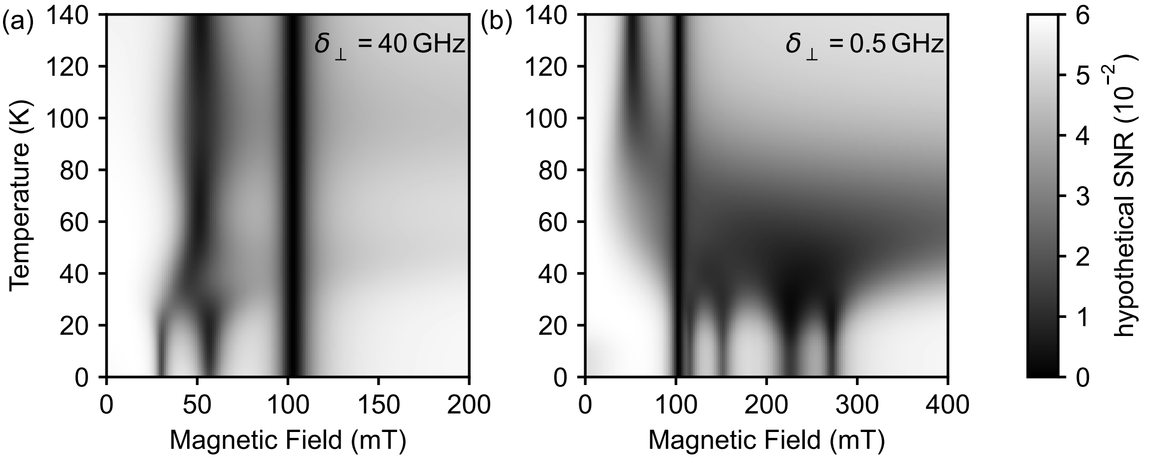

Figure 4.11: Same as Fig. 4.10 but without ES inherent spin mixing. To achieve this, $\lambda_{\mathrm{ES}}^{\perp} = 0$ (see Tab. 4.1) was set. (a) For low magnetic fields, spin mixing due to $\theta_B = 1.9°$ leads to almost no spin-lattice relaxation, and the orbital averaging can be observed without the NV performance minimum. This situation is similar to the toy model with only longitudinal noise in Fig. 4.6. (b) For high magnetic fields and $\theta_B > 0$, the performance minimum forms due to the spin mixing introduced by the misaligned magnetic field.

LAC at 103 mT, two changes to the spin relaxation process can be identified compared to the previous discussion in Sec. 4.4.1 with $B = 0$:

(i) First, increasing the axial magnetic field leads to a dominating Zeeman term in the Hamiltonian and causes the spin states to be better eigenstates. This reduces the spin mixing amplitudes $\epsilon_{|i\rangle,|j\rangle}$ and, consequently, the strength of the spin relaxation. In the Bloch sphere picture of Fig. 4.5(c), this corresponds to a smaller inclination angle of the eigenstate axis. The origin of the spin mixing is either due to a misaligned magnetic field $\theta_B \neq 0$ at $B \gg 0$ or due to $\lambda_{\mathrm{ES}}^{\perp}$. Which of the two dominates can be inferred from a hypothetical setting with $\lambda_{\mathrm{ES}}^{\perp} = 0$ in Fig. 4.11.

(ii) Second, since the Zeeman effect is linear in B, the level spacing and thus Larmor frequencies ω increase. Therefore, the condition $k_{\downarrow/\uparrow} \approx 2\omega$ for maximal spin relaxation shifts linearly to a higher temperature. When only considering the dominant $k_{\downarrow/\uparrow} \propto T^5$ dependence in Eq. 4.24, the shift goes as $B^{1/5}$. This relation is presented well on experimental data in Ref. [37, Fig. 2] and describes the shape of the min(PL) trace in Fig. 4.10(a) above the second LAC (triangle marker). But if the condition for maximal spin relaxation is met at a higher temperature and smaller time scale $1/\omega$, the relaxation rate at resonance is higher. This is because the lifetime T_{ES} of the ES is constant while the number of hopping events increases.

The second effect (ii) partially compensates for the first (i). Therefore, even a very low spin mixing, as found with aligned fields well above 1 T or at low strain and fields (*cf.* Sec. 4.4.3), can still result in an observable minimum in the SNR. This is simulated in Fig. 4.10(c) and was also found experimentally in Ref. [37]. The effect of both changes, (i) and (ii), can also be understood by a comparison with Eq. 4.77 for the relaxation maximum of the two-level toy model. Increasing B is similar to increasing ω_0 there, which makes the B range $[70\,\mathrm{mT}, 200\,\mathrm{mT}]$ in Fig. 4.10(a) similar to Fig. 4.7(c).

In summary, applying an axial magnetic field above 100 mT drastically improves the SNR of NV centers with medium and high strain at low temperatures. At temperatures above 60 K, their SNR at high and low (few mT) magnetic fields becomes comparable.

4.4.5 Combination of strain and magnetic field

The previous sections addressed the dependence of strain and magnetic field on the NV performance independently. This chapter will examine the combined effect of strain and magnetic field.

Investigating the ES LACs at $T = 0\,\mathrm{K}$ first, we see in Fig. 4.12(a) how the LACs from Fig. 4.10 develop as a function of strain. This topic is discussed in more detail in Ref. [95]. For Fig. 4.12(a), magnetic field and strain angles of $\theta_B = 1°$, $\phi_B = 180°$, and $\phi_\delta = 0°$ were assumed. We saw in Fig. 4.8(a) that ϕ_δ has a significant influence on the SNR. Of course, $\theta_B \gg 0$ also impacts the SNR, as a misaligned magnetic field mixes the spin states. But also ϕ_B has an influence, coupled to the value of ϕ_δ. In Fig. 4.12(b), this dependence is plotted at $B = 46\,\mathrm{mT}$ and still using $T = 0\,\mathrm{K}$. One can identify the same pattern six times in the parameter space of $\phi_B, \phi_\delta \in [0°, 360°]$. This periodicity can be easily understood from the C_{3v} symmetry of the NV$^-$ center: in Fig. 4.12(c), six equivalent settings of strain and magnetic field are sketched, and their position in Fig. 4.12(b) is marked. One possible reduced parameter space is $\phi_\delta \in [0°, 60°]$ and $\phi_B \in [0°, 360°]$, as outlined in Fig. 4.12(b).

Next, we discuss $T > 0\,\mathrm{K}$ but stay in the intermediate regime (II) before the orbital averaging happens. Here, a conceptually interesting phenomenon can be observed in simulations: features of SNR revivals, which seem unaffected by the spin relaxation mechanism, can be observed in the parameter space. As a first example, Fig. 4.13(a,b) shows the same strain and magnetic field maps as Fig. 4.12(a,b), only now at $T = 35\,\mathrm{K}$. Regions that differ by a factor of more than three in SNR can be seen, even away from ES LACs. This leads to a clear revival feature in Fig. 4.13(c) at $B = 46\,\mathrm{mT}$, compared to the map shown earlier in Fig. 4.10(a). A second example of a setting in which a significantly altered spin relaxation can be seen around $B \geq 70\,\mathrm{mT}$ is given in Fig. 4.13(d).

Unfortunately, these SNR revivals at intermediate temperatures might not be useful or even difficult to observe in most experiments since they require a rather specific magnetic field and strain setting (*cf.* Fig. 4.13(a,b)). Additionally, the second example is close to the GS LAC and thus also not favorable in terms of the hardware needed for microwave pulses due to a small (large) spacing between $|0\rangle$ and $|-1\rangle$ ($|+1\rangle$). However, the origin of these revivals underlines the intuitive explanation of the spin relaxation process developed in Sec. 4.4.1 and is therefore explained in the following: At temperatures around the spin-relaxation resonance condition (Eq. 4.69), the relaxation rate is sensitive to spin mixing and level spacing. If the strain is sufficient to split the states into two orbital branches, there are regions in the parameter space of the Hamiltonian (Eq. 4.2) that generate similar spin mixing of the $m_\mathrm{S} = 0$ and $m_\mathrm{S} = -1$

spin states in the two orbital branches. This leads to parallel quantization axes of the two orbital branches. As the spin-relaxing effect at intermediate temperature is caused by the different spin evolution in the two orbital branches, it can be mitigated if the Larmor precession axes are parallel. In such a setting, only the spin mixing by and precession about effectively one quantization axis is present, similar to zero temperature.

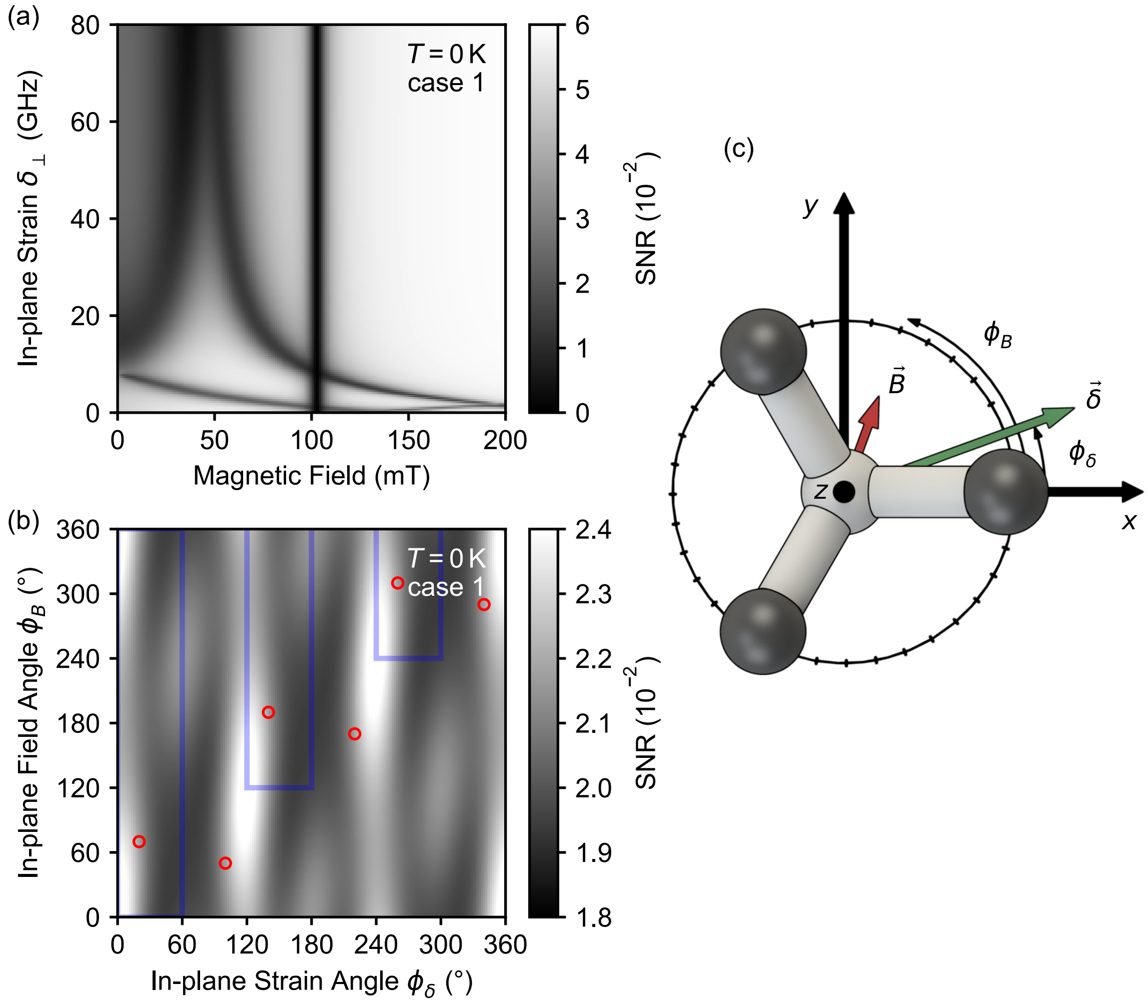

Figure 4.12: Interplay of strain and magnetic field. (a) Evolution of LACs as a function of magnetic field and in-plain strain at zero temperature (see also Ref. [95]). (b) Periodicity of the Hamiltonian of the ES as a function of in-plain strain angle ϕ_δ and in-plain magnetic field angle ϕ_B at zero temperature. Three identical regions are highlighted in blue. Mirrored and shifted versions of this region cover the entire parameter space. (c) Geometric explanation for the identical regions in part (b). Overlaid is the in-plain appearance of the NV$^-$ structure from Fig. 4.1. An example with $\phi_B = 70°$, $\phi_\delta = 20°$ is chosen, and the six equivalent points are marked in (b). For the entire figure, the parameters from Tab. 4.1 are used but adapted to the first example in Fig. 4.13(a–c), which is called “case 1”: $\theta_B = 1°$, $\phi_B = 180°$, $B = 46\,\mathrm{mT}$.

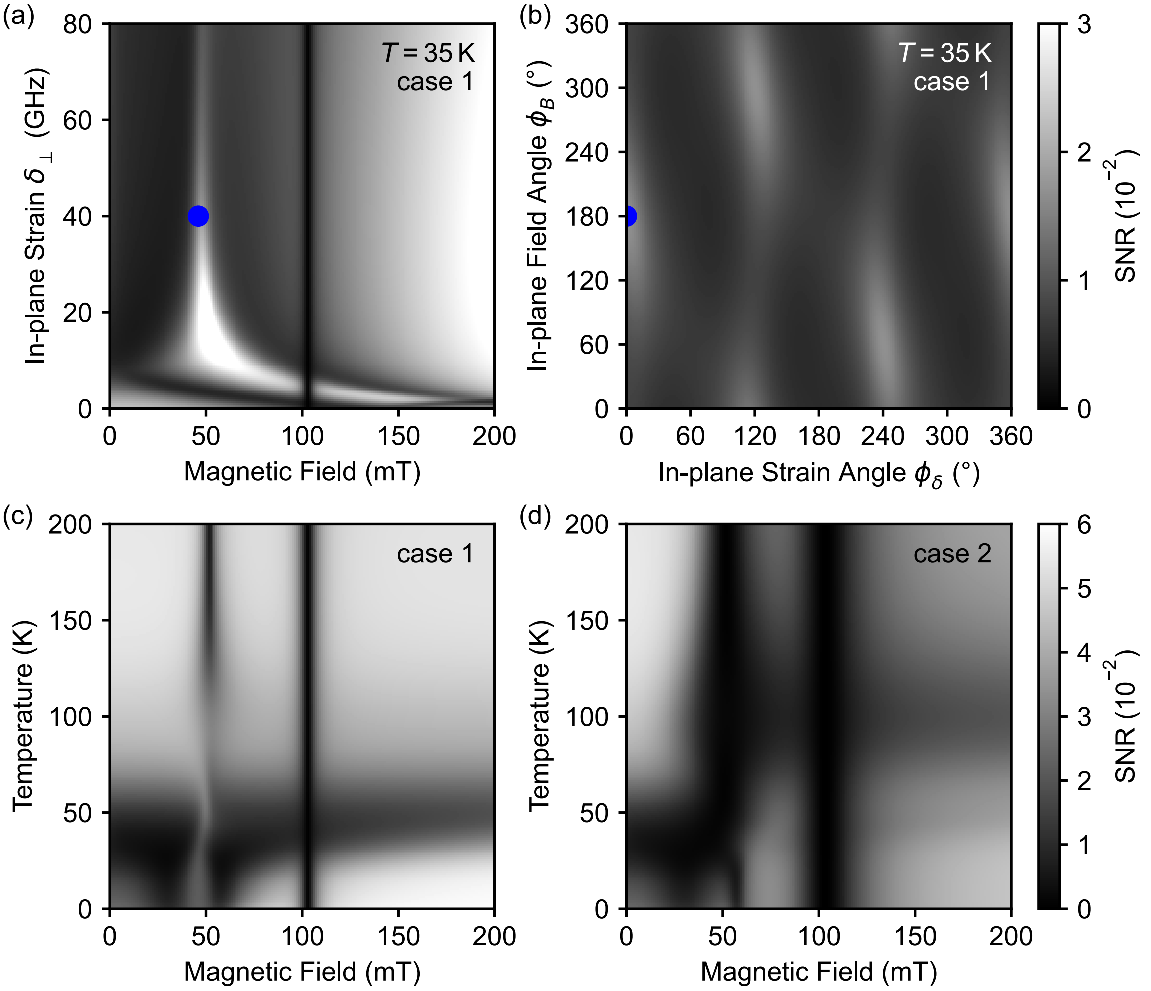

Figure 4.13: Revivals of SNR in the regime (II) of reduced performance. (a, b) Same SNR maps as given in Fig. 4.12(a,b) but for $T = 35\,\mathrm{K}$. Regions with SNR similar to zero temperature can be found in the parameter space. The colorbars for both plots in one row are on the right. (c) SNR as a function of magnetic field and temperature. Compared to a similar Fig. 4.10(a), a revival feature in the SNR at $B \approx 46\,\mathrm{mT}$ occurs in this setting called "case 1" (marked in parts (a,b) by the blue dot). (d) A second example ("case 2") where a high SNR is maintained up to elevated temperature, here for $B \approx 80\,\mathrm{mT}$. The parameters from Tab. 4.1 are used, only altered to $\theta_B = 4.7°$ for case 2 in (d), and only altered to $T = 35\,\mathrm{K}$, $\theta_B = 1°$, $\phi_B = 180°$, $B = 46\,\mathrm{mT}$ for case 1 in (a–c).

To give a visual impression of this mechanism on the Bloch sphere, we need to adapt the states that we have used before in Fig. 4.5 at $B = 0\,\mathrm{mT}$. In the first example here (case 1), the strain of $\delta_\perp = 40\,\mathrm{GHz}$ and magnetic field of $B = 46\,\mathrm{mT}$ causes the *hf basis* states (Eq. 4.7) to be the best approximation of the eigenstates. One can see in Fig. 4.3(b) that the two states with mostly $m_\mathrm{S} = 0$ mix mostly with $m_\mathrm{S} = -1$ states. Therefore, we now choose the $|0\rangle$-$|-1\rangle$-spin manifold for the Bloch spheres. It should be noted that here, $\theta_B, \phi_B \neq 0$, in contrast to Fig. 4.3(b), but the difference is qualitatively irrelevant for this purpose. An exemplary time evolution at 35 K, calculated using the same Monte Carlo approach as in Sec. 4.4.1, is given in Fig. 4.14(a). In the $|0\rangle$-$|-1\rangle$-spin manifold, the two quantization axes are parallel, and the probability of $m_\mathrm{S} = 0$ is largely conserved. The time evolution is not confined to the surface of the $|0\rangle$-$|-1\rangle$-Bloch sphere. Here, this is not due to a classical mixture but since an amplitude also exists in the remaining dimension of $|+1\rangle$. To demonstrate this, the time trace in the $|+1\rangle$-$|-1\rangle$-spin manifold is plotted in Fig. 4.14(b). Due to a start in state $|E_{\mathrm{x},0}\rangle$, the time evolution stays largely in the center of this Bloch sphere. Qualitatively, the same is found for the second example plotted in Fig. 4.13(d) (not shown here).

Finally, another group of conceptually interesting revival conditions is found for weak in-plane magnetic bias fields (*i.e.* $\theta_B = 90°$). As seen in Fig. 4.15(a), maxima in SNR are observed for specific settings of the in-plane angles of magnetic field and strain, here at 35 K. This SNR landscape only arises if the optical excitation and decay are implemented with jump operators that conserve the coherent spin-state [107] (*cf.* discussion in Sec. 4.2.5). At the maxima, a spin eigenstate of the GS, which varies with ϕ_B, becomes very similar to a spin eigenstate of the ES, which mostly varies with ϕ_δ. Spin-coherent optical transitions then allow a transfer from eigenstate to eigenstate. For example, Fig. 4.15(b) highlights a SNR maxima that arises as a result of the $|+\rangle$-state from Fig. 4.2(b). As discussed around Fig. 4.5, the $|+\rangle$-state has very little spin mixing with the $|0\rangle$- and $|-\rangle$-state. Thus, spin-state relaxation under optical excitation is reduced for the $|+\rangle$-state if it is also an eigenstate of the GS. This revival barely alters the steady-state PL but shows the pronounced effect in the contrast and thus SNR if the π-pulse is applied between the $|0\rangle$ and $|+\rangle$ GS MW transition. As presented in Fig. 4.15(b), it is very sensitive to $\theta_B \neq 90°$ and might therefore be useful for in-plane magnetic field alignment for electric field sensing [71] as on the sample presented in Fig. 3.16. The implications of magnetic field sensing with a tilted magnetic field are discussed in Ref. [72, Fig. 2.7].

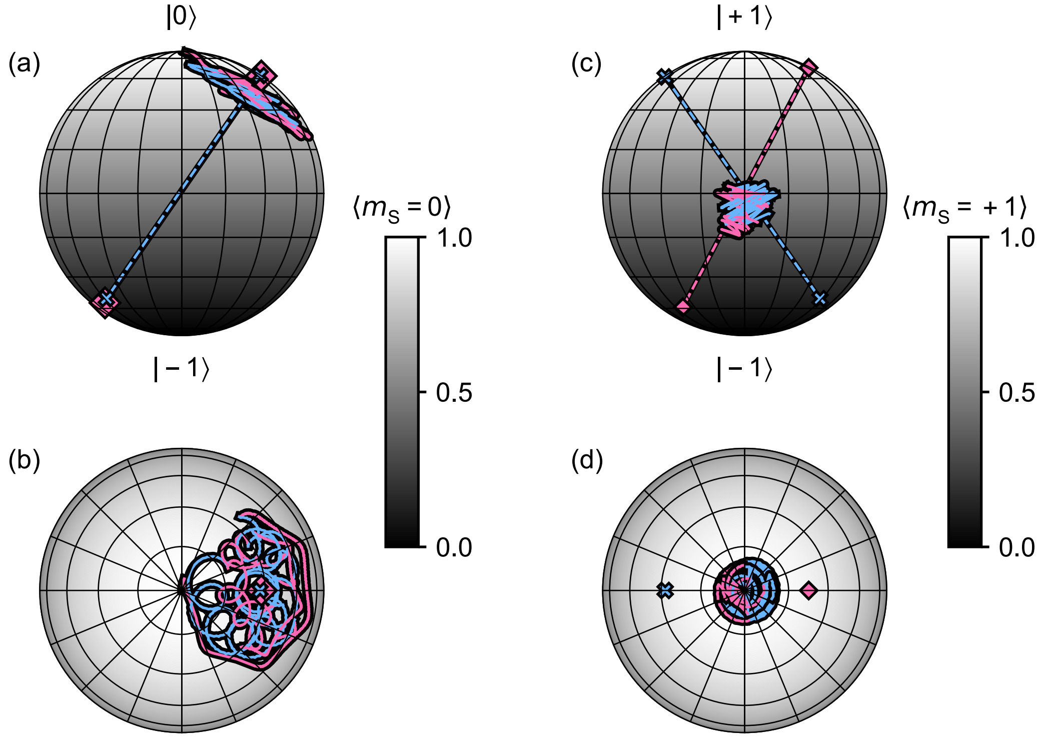

Figure 4.14: Explanation for revivals in the Bloch sphere picture. (a, b) Exemplary time evolution at $T = 35\,\mathrm{K}$ in the $|0\rangle$-$|-1\rangle$-spin manifold simulated with the Monte Carlo method also used in Fig. 4.5(c). A duration of $10\,\mathrm{ns} \approx T_{\mathrm{ES}}$ is shown here. Parallel quantization axes in the two orbital branches almost eliminate the spin-lattice relaxation. (c, d) Same time trace as in (a, b), now plotted in the $|+1\rangle$-$|-1\rangle$-spin manifold. The parameters from Tab. 4.1 are used but adapted to case 1 in Fig. 4.13(a–c): $\theta_B = 1°$, $\phi_B = 180°$, $B = 46\,\mathrm{mT}$.

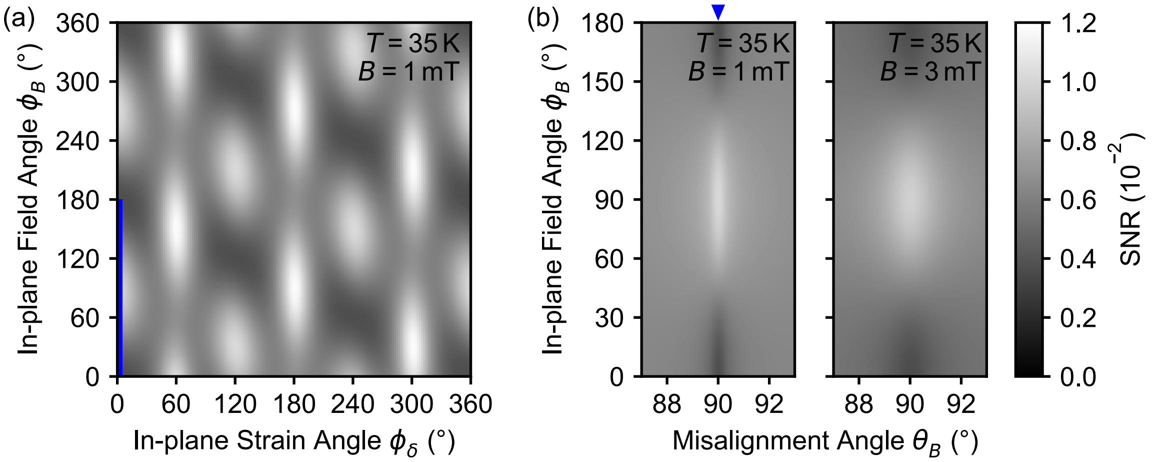

Figure 4.15: Revival of SNR with weak in-plane magnetic field. (a) SNR as a function of the in-plane magnetic field and strain angles for $\theta_B = 90°$ and $T = 35\,\mathrm{K}$. Revivals are predicted in this simulation with coherent optical jump operators. The π-pulse is applied at the lower spin-resonance in the entire figure. (b) SNR for slightly varying values of θ_B and for both $B = 1\,\mathrm{mT}$ and $3\,\mathrm{mT}$. The blue arrow here indicates the same linecut marked by the blue line in part (a). The observation of the revival feature at $\phi_B = 90°$ is due to the $|+\rangle$-state from Fig. 4.2(b) and requires the magnetic field to be precisely aligned in-plane to the N-V-axis. Apart from the values discussed here, the parameters from Tab. 4.1 are used.

4.4.6 Laser polarization and orbital branch selectivity

As a last tuning knob the experimenter has, we will look at the influence of the laser. In the following, we discuss the influence of laser polarization in the context of the spin-lattice relaxation established above. The effect of the laser power will be investigated separately in Ch. 7.1.

So far, we assumed that the two orbital branches are populated equally by the laser, *i.e.* $r_\beta = 1$ in Tab. 4.1. As discussed around Eq. 4.12, the linear polarization of the laser relative to the in-plane direction of strain ϕ_δ can change r_β [41, 95, 101]. We will, therefore, restrict the following discussion to cases where a clear orbital branch splitting is present (*e.g.* by crystal strain). The change of r_β results in a notable effect at the ES LACs in a magnetic field sweep [95] (a horizontal line in Fig. 4.10(a) at base temperature): The depth in PL (or SNR) of these two dips depends on the population in the respective orbital branch. This population is initially set by r_β upon laser excitation and will change due to phonon-driven orbital hopping over the time spent in the ES. This is illustrated in Fig. 4.16 by assuming a perfect branch selectivity of $r_\beta \to 0$ or ∞. In the traces for $r_\beta \to \infty$ the significance of the one-phonon process at low temperature becomes apparent. The spontaneous emission of a phonon (Eq. 4.23) by $\mathrm{E_x} \to \mathrm{E_y}$ and the spin mixing in the $\mathrm{E_y}$ branch due to the broad LAC (here at 30 mT) degrade the performance even at $B = 0$: the dashed trace lies significantly lower than the blue trace. The width (in the B-dimension) of the LACs is altered by the strain direction ϕ_δ. For this reason, the strain (via a stronger spontaneous emission) and its direction show a significant influence in Fig. 4.8(a), even at $B = 0\,\mathrm{T}$. Note that in the example in Fig. 4.16, $\phi_\delta = 24.4°$ was used. With $\phi_\delta \to 60°$, the effect, which the two ES LACs (around 30 mT and 57 mT) still have at $B = 0$, qualitatively reverses. But since the LAC in the $\mathrm{E_x}$ branch is further away from $B = 0$, the effect is less severe, as it was addressed in Sec. 4.4.3.

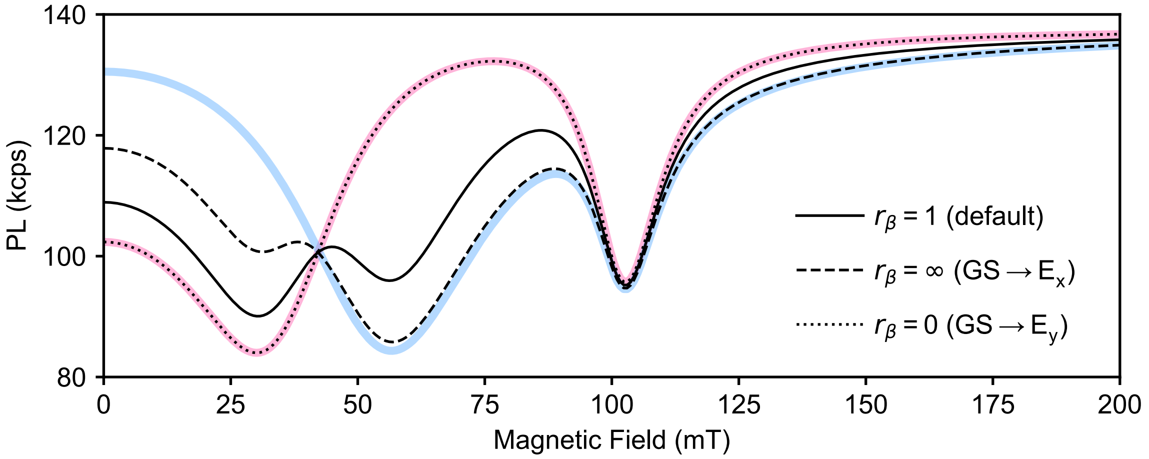

Figure 4.16: Influence of the optical excitation branching ratio. Plotted is the steady-state PL as a function of an axial magnetic field B at $T = 0$ for different laser excitation ratios r_β. A value of $r_\beta \to 0$ ($r_\beta \to \infty$) results in only the E_y (E_x) ES LAC at 30 mT (57 mT) being pronounced, compared to the case with $r_\beta = 1$ where both are pronounced. But while for $r_\beta \to 0$ no signature of the other LAC is present, a clear signature is still seen at the other LAC for $r_\beta \to \infty$. This results from the spontaneous emission term of the one-phonon process, which distributes population from the upper E_x to the lower E_y branch at $T = 0$. For comparison, the thick traces show hypothetical situations without orbital hopping ($\eta = 0$), *i.e.* an orbital state-conserving setting (E_x: blue, E_y: pink). The same parameters as in Fig. 4.10(a) are used.

4.5 Classical rate models

We will now compare the Lindblad master equation model introduced above with classical rate models. First, we will compare the Lindblad master equation model at cryogenic temperature to a classical rate model constructed on the low-temperature level structure. We will see that such a classical model can be sufficient at low temperatures if rates are introduced in the correct basis and if the one-phonon process is included. Second, we verify that the Lindblad master equation model yields the same behavior as the established room-temperature rate model. This will prove that the Lindblad master equation correctly models the recovered room-temperature behavior based on our low-temperature Hamiltonian and rates.

4.5.1 Classical model at cryogenic temperature

Classical rate models [86, 96] are constructed on the level structure of eigenstates of the Hamiltonian H in Eq. 4.1 and 4.2 at given conditions. It is assumed that the system is in an exclusively classical mixture of eigenstates at any time. Therefore, by leaving out coherences, the time evolution of the system is computed on the population probabilities $P_i = \rho_{i,i}$ only, giving a quadratic computational speedup compared to the density matrix ρ in the Lindblad master equation model (see Tab. 6.1). The rates $k_{p,q;b}$ for a transition from state p to q are given for levels of a certain basis b as in Sec. 4.2.2. The rates between the eigenstates (*eig basis*) are then calculated from the rates in b by the projections of the eigenstates onto these basis states of b. Explicitly, the rate $k_{i,j;eig}$ for a transition from eigenstate $|e_i\rangle$ to eigenstate $|e_j\rangle$ is given by the

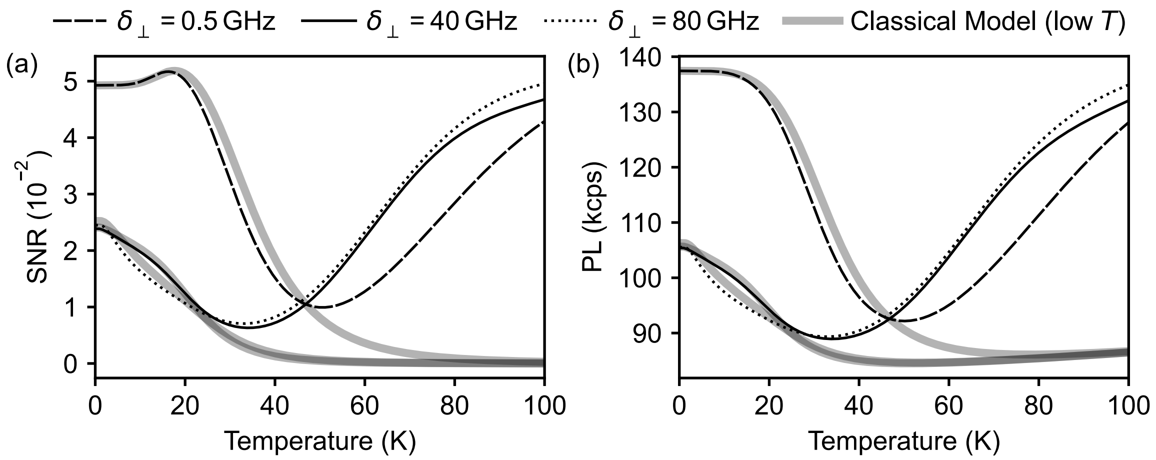

Figure 4.17: Comparison of the Lindblad master equation model to a classical rate model for low temperature. The temperature dependence of the SNR (a) and steady-state PL (b) is simulated for low, medium, and high strain. While the classical model reproduces the Lindblad master equation model well in all aspects at low temperatures, it fails to reproduce the orbital averaging process and recovery toward room temperature. The parameters from Tab. 4.1 are used.

sum of all transition channels in basis b weighted by the probability that $|e_i\rangle$ is in the initial and $|e_j\rangle$ in the final state of that channel:

$$k_{i,j;eig} = \sum_{p,q} |\langle p|e_i\rangle|^2 |\langle q|e_j\rangle|^2 k^b_{p,q} \tag{4.78}$$

Defining

$$\mathcal{T} = |T_{eig\to b}|^2 , \tag{4.79}$$

where $|\cdot|^2$ is computed element-wise and the transformation matrix $T_{eig\to b}$ is constructed column-wise from the eigenvectors of H written in basis b, we can rewrite in matrix from:

$$k_{eig} = \mathcal{T}^T k_b \mathcal{T} \tag{4.80}$$

In our case, where we have several bases b_i (see Fig. 4.2), one has to use

$$k_{eig} = \sum_{b_i} \mathcal{T}^T k_{b_i} \mathcal{T} . \tag{4.81}$$

This is a new requirement arising at low temperature and was thus not used in previous rate models which were constructed for room temperature. Note that $k_{i,i} = 0$ in any basis.

Based on the rate matrix k_{eig}, we will now derive how to compute the time evolution of the system. The population probability of eigenstate $|e_i\rangle$ is P_i with $\sum_i P_i = 1$. The population $P_i(t)$ at time t changes within Δt by:

$$\Delta P_i(t) = \underbrace{\sum_j k_{j,i;eig} \Delta t P_j(t)}_{\text{decay into state } i} - \underbrace{\sum_j k_{i,j;eig} \Delta t P_i(t)}_{\text{decay out of state } i} \tag{4.82}$$

$$\implies \frac{\Delta P_i(t)}{\Delta t} = \dot{P}_i(t) = \sum_j k_{j,i;eig} P_j(t) - \sum_j k_{i,j;eig} P_i(t) \tag{4.83}$$

With the diagonal matrix $S_{i,j} = \delta_{ij} \sum_k k_{i,k;eig}$ we can write in matrix from:

$$\dot{P}_i(t) = \sum_j \left(k_{j,i;eig} - S_{i,j}\right) P_j(t) = \left[\left(k_{eig}^T - S\right) \cdot \vec{P}\right]_i \tag{4.84}$$

$$\implies \dot{\vec{P}}(t) = \left(k_{eig}^T - S\right) \cdot \vec{P} \tag{4.85}$$

As discussed in Sec. 4.2.4, we assume time-independent conditions and thus find

$$\vec{P}(t) = \exp\Big(\big(k_{eig}^T - S\big)t\Big) \cdot \vec{P}_0 \tag{4.86}$$

for the time evolution of an initial population vector $\vec{P}_0$. Eq. 4.86 is the classical analog to Eq. 4.27, and likewise, the steady-state and collected PL can be calculated when using $P_i \equiv \rho_{i,i}$. Note that population vectors are written in *eig basis*. But we can still apply Eq. 4.38 on $\vec{P}(t)$ if we take care not to change the order of (GS, ES, SS) in Eq. 4.79 compared to the other bases, because every ES has the same optical decay rate k_r.

To find the populations $\vec{P}_b$ in a basis b other than the eigenbasis, one can construct a diagonal density matrix $\rho_{i,j;eig} = \delta_{i,j} P_i$. Then, according to Eq. 4.5:

$$\rho_b = T_{eig\to b}\, \rho_{eig}\, T_{eig\to b}^\dagger \tag{4.87}$$

$$\implies \rho_{i,j;b} = \sum_p \langle j|e_p\rangle\, P_p\, \langle i|e_p\rangle^* \tag{4.88}$$

If we are only interested in the populations $\vec{P}_b$ again, then this simplifies to

$$\vec{P}_b = \mathcal{T} \cdot \vec{P}\,. \tag{4.89}$$

But note that Eq. 4.89 is not a basis transformation on population vectors. Information is lost by throwing away the off-diagonal elements in ρ_b. Also, according to Eq. 4.79, $\mathcal{T}$ does not possess the attributes of a transformation matrix (like $T_{b_1\to b_3} = T_{b_2\to b_3} T_{b_1\to b_2}$) and can, in some cases, not be inverted.

Just as for the Lindblad master equation model, it is not sufficient for all strains to introduce the rates in one basis (*cf.* Fig. 4.2 and Fig. 5.1) or to neglect the spontaneous emission of phonons (*cf.* Fig. 4.8). Only at medium strains, which are large enough to form clear orbital branches and low enough for the one-phonon process to play a minor role, these two aspects can be neglected, as pioneered in Ref. [95]. A classical rate model constructed on the low-temperature Hamiltonian, as derived above, largely reproduces the behavior of the Lindblad master equation model at cryogenic temperature. Here, it can be used for the sake of reduced complexity and faster computational speed. Only for increasing temperature, where the coherent spin evolution in the two orbital branches becomes critical for spin relaxation and orbital averaging, does a classical model deviate from the Lindblad master equation model. This can be seen in Fig. 4.17, where both border cases of low strain (like in bulk diamonds) and high strain (like in nanodiamonds), as well as medium strain (as we find in scanning tips in this thesis), are covered.

The simulation of $\delta_\perp = 0.5\,\text{GHz}$ in Fig. 4.17 predicts an interesting behavior, which was not covered in the discussion in Sec. 4.4.3, and is therefore addressed briefly:

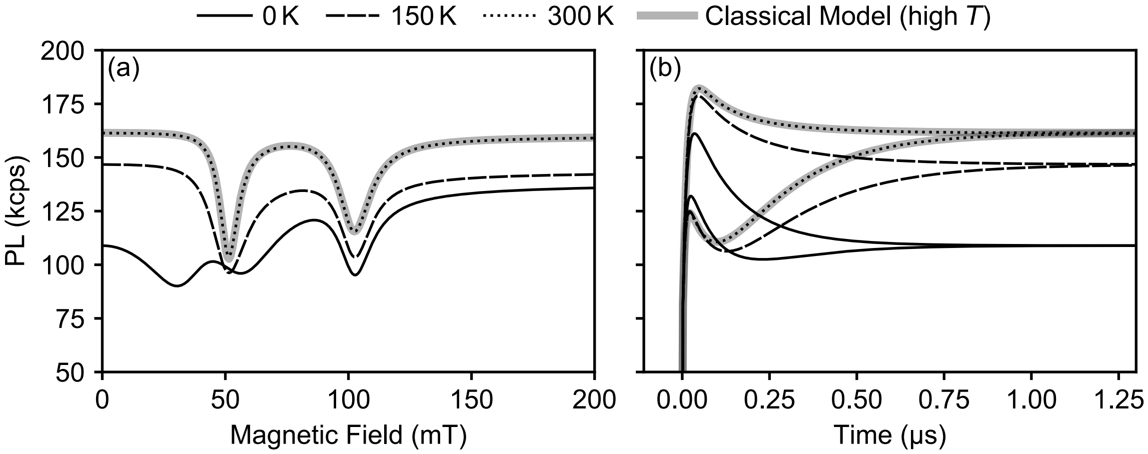

Figure 4.18: Comparison of the Lindblad master equation model to a classical rate model for room temperature. The Lindblad master equation model is evaluated at different temperatures and compared to the common rate model at 300 K. (a) Simulated steady-state PL as a function of magnetic field. The two LACs of the ES average to a single LAC at room temperature (see Fig. 4.10(a)). (b) PL(t) dynamics during a readout laser pulse as in Fig. 2.2(a). A significant change in the dynamics can be witnessed between cryogenic and room temperature. In both panels, complete quantitative agreement with the classical rate model is recovered at room temperature. The same parameters as in Fig. 4.10(a) are used.

The initial peak in SNR around $T = 18\,\mathrm{K}$ arises as a result of the ISC rate $k_{A_2} = 0$ (see Fig. 4.2(d)). At $T \approx 0\,\mathrm{K}$, the two-phonon process is very small (see Fig. 4.9(c)) and the one-phonon process is negligible at $\delta_\perp \approx 0\,\mathrm{GHz}$. As a result, no orbital hopping occurs. Thus, the initial population in $|A_2\rangle$ (after optical excitation from the GS $|\pm1\rangle$) reduces the spin contrast. At $T = 18\,\mathrm{K}$ and with $\delta_\perp = 0.5\,\mathrm{GHz}$, orbital hopping constantly tries to distribute the population evenly between the four $m_\mathrm{S} = \pm1$ states ($|E_1\rangle$, $|E_2\rangle$, $|A_1\rangle$, $|A_2\rangle$). This allows for an ISC decay of the entire $m_\mathrm{S} = \pm1$ population and thus increases the contrast. The peak is not observed in the PL. At higher temperatures, the spin-lattice relaxation with the $m_\mathrm{S} = 0$ states dominates, and the contrast and, thus, SNR drops again.

4.5.2 Classical model at room temperature

When simulating the PL at room temperature, all rates are introduced in the same e_z *basis*. This is possible since the two excited state branches are treated as one averaged spin triplet. Complete averaging makes the ISC rates only dependent on $|m_\mathrm{S}|$ and eliminates the strain dependence. We implement such a common [86, 96] classical rate model for room temperature with only three ES levels and use the same parameters as in the Lindblad master equation model (*e.g.* Eq. 4.17 for the ISC rate of $m_\mathrm{S} = \pm1$ levels). Its ES Hamiltonian was generated by partial-tracing out the orbital subspace of the ES (Eq. 4.10). In Fig. 4.18, we verify that our Lindblad master equation model, which is based on the low-temperature Hamiltonian and rates, recovers complete quantitative agreement with the classical rate model at room temperature.

In the paragraph above, we assumed that the strain dependence of the ES disappears towards room temperature. However, previous studies found a remaining strain dependence of the ES at room temperature. An additional empirical term was initially introduced to the classical room-temperature model [117, 118] to account for observations in highly strained NV centers, as found in nanodiamonds. It was then shown analytically by Plakhotnik *et al.* [90] that this term arises from a sufficiently large imbalance in the Boltzmann-distributed (Eq. 4.22) ES branch population, caused by the large branch-splitting at very high strain ($2\delta_\perp \approx 1\,\mathrm{THz}$ in their work). This prevents the orbital averaging process from completing and thus leads to a remaining influence of the low-temperature strain dependence, even above room temperature.

We will later compare our Lindblad master equation model with the experimentally verified model by Plakhotnik *et al.* in Ch. 5.2. To be able to do so, we need to extend the classical rate model by Plakhotnik *et al.* to take applied magnetic fields into account. Plakhotnik *et al.* derived that in the absence of a magnetic field, an additional term

$$\begin{aligned}\hat{H}_{\mathrm{TRF}}/h = &- D_{\mathrm{ES}}^{\perp}\mathcal{R}(T,\delta_\perp)\Big[\cos\phi_\delta\left(\hat{S}_y^2-\hat{S}_x^2\right)+\sin\phi_\delta\left(\hat{S}_y\hat{S}_x+\hat{S}_x\hat{S}_y\right)\Big] \\ &- \lambda_{\mathrm{ES}}^{\perp}\mathcal{R}(T,\delta_\perp)\Big[\cos\phi_\delta\left(\hat{S}_x\hat{S}_z+\hat{S}_z\hat{S}_x\right)+\sin\phi_\delta\left(\hat{S}_y\hat{S}_z+\hat{S}_z\hat{S}_y\right)\Big]\end{aligned} \tag{4.90}$$

with the temperature reduction factor

$$\mathcal{R}(T,\delta_\perp) = \frac{e^{\hbar\Delta_\perp/k_{\mathrm{B}}T}-1}{e^{\hbar\Delta_\perp/k_{\mathrm{B}}T}+1} \tag{4.91}$$

and the strain splitting $\hbar\Delta_\perp \approx 2h\delta_\perp$ from Eq. 4.44 has to be added to the Hamiltonian of the ES after orbital averaging (Eq. 4.10). We corrected a sign error in Eq. 4.90 compared to the derivation given in Ref. [90]. In this, we still assume that constants as $D_{\mathrm{ES}}^{\perp}$ (see Tab. 4.1) have no temperature and strain dependence. Such intrinsic dependencies are discussed in Ref. [90] but ignored here, as they affect all models equally and thus do not matter for the comparison in Ch. 5.2. In the presence of a magnetic field, Eq. 4.90 is not analytically correct due to the orbital g_l-factor term in the ES Hamiltonian (Eq. 4.2). The ES LAC at $B_z \approx 51\,\mathrm{mT}$, which we will investigate in Ch. 5.2, shows a very small shift of $\Delta B_{\mathrm{LAC}} \approx 2\,\mathrm{\mu T}$ compared to Eq. 4.90 at a strain of $\delta_\perp = 1\,\mathrm{THz}$ and at $300\,\mathrm{K}$ with $g_l = 0.1$ [40] (or $\Delta B_{\mathrm{LAC}} \approx 20\,\mathrm{\mu T}$ with $g_l = 1.0$). Therefore, Eq. 4.90 still constitutes a good approximation as long as the $g_l B_z$ term is small. But at high magnetic fields and if a significant strain dependence of the orbital g_l-factor exists, as recent measurements by Happacher *et al.* [95] indicate, the $g_l B_z$ term could become relevant. In general, the ES averaged Hamiltonian reads

$$\begin{aligned}H_{ES,\mathrm{avg}}/h =&H_{\mathrm{spin}}/h + H_{\mathrm{TRF}}/h \\ =&D_{\mathrm{ES}}^{\parallel}\left(S_z^2-\tfrac{2}{3}\mathbb{I}_3\right)-\lambda_{\mathrm{ES}}^{\parallel}\sigma_2 S_z + D_{\mathrm{ES}}^{\perp}\left[\sigma_3\left(S_y^2-S_x^2\right)-\sigma_1\left(S_yS_x+S_xS_y\right)\right] \\ &+\lambda_{\mathrm{ES}}^{\perp}\left[\sigma_3\left(S_xS_z+S_zS_x\right)-\sigma_1\left(S_yS_z+S_zS_y\right)\right]+\mu_{\mathrm{B}}g_{\mathrm{ES}}\vec{S}\cdot\vec{B} \\ &+\left(\mu_{\mathrm{B}}g_lB_z\sigma_2+d_{\mathrm{ES}}^{\perp}\xi_x\sigma_3-d_{\mathrm{ES}}^{\perp}\xi_y\sigma_1+d_{\mathrm{ES}}^{\parallel}\xi_z\right)\mathbb{I}_3\end{aligned} \tag{4.92}$$

with $\sigma_{1/2/3} = \mathrm{Tr}\left(\sigma_{x/y/z}\rho_{\mathrm{orbit}}\right)$,

$$\rho_{\mathrm{orbit}} = T_{hf\to e_z}^{\mathrm{orbit}}\begin{pmatrix} e^{-\hbar\Delta_\perp/k_{\mathrm{B}}T} & 0 \\ 0 & 1\end{pmatrix}\left(T_{hf\to e_z}^{\mathrm{orbit}}\right)^{-1}\left(1+e^{-\hbar\Delta_\perp/k_{\mathrm{B}}T}\right)^{-1} \tag{4.93}$$

and $T^{\text{orbit}}_{hf\to e_z}$ as used in Eq. 4.8. All $\mathbb{I}_3$ terms in Eq. 4.92 cause an overall energy shift of the ES and are thus irrelevant to our analysis.

CHAPTER 5

Comparing measurements from literature with the model

Most of the text and figures in this chapter were published in Ref. [36]. The considerations presented in this chapter were developed by me but built on the work presented in chapter 4. The contributions are described there. Data from other literature is used and indicated accordingly in the text.

Before comparing the model from the previous sections with our own measurements (Ch. 6), we will now further verify and investigate the predictions of our model. We will do so by comparing it to previous experimental findings in the literature. While excellent agreement is found for two cases in very distinct parameter regimes, as discussed in Secs. 5.1 and 5.2, a gap in the current understanding of the electron-phonon coupling becomes apparent in Sec. 5.3. We discuss how our model might help to close this gap.

5.1 Intersystem crossing rates at cryogenic temperatures

We first examine the validity of our Lindblad master equation model at low strain. In Fig. 5.1, we plot the effective ISC rates k_{ISC} for the different ES levels of the *zf basis* as measured by Goldman *et al.* [92, Fig. 3]. In their work, resonant laser excitation into the individual low-strain ES eigenstates and their Rabi driving was used in the temperature range $5\,\mathrm{K} - 26\,\mathrm{K}$. Remarkable agreement is found between our model and data from Ref. [92]: as the temperature increases, the averaging of the ISC rates with same $|m_{\mathrm{S}}|$ is reproduced by our simulation. We note that the different ISC rates below $20\,\mathrm{K}$ can only result from a model where rates are introduced in the *zf basis*, as discussed in Ch. 4.2.2, independent of whether a classical rate model or a Lindblad master equation model is used. Toward higher temperature, as expected in the regime (II) of maximal spin relaxation, our simulation shows an increase of the effective ISC rate of the $m_{\mathrm{S}} = 0$ states and the corresponding decrease of the $|m_{\mathrm{S}}| = 1$ states. Above $26\,\mathrm{K}$, resonant excitation was experimentally not possible due to the broadening of the spectral lines.

To obtain the ISC rates in Fig. 5.1, we reproduce the experiments by Goldman *et al.* [92] in simulations. First, the system was initialized in the respective eigenstates.

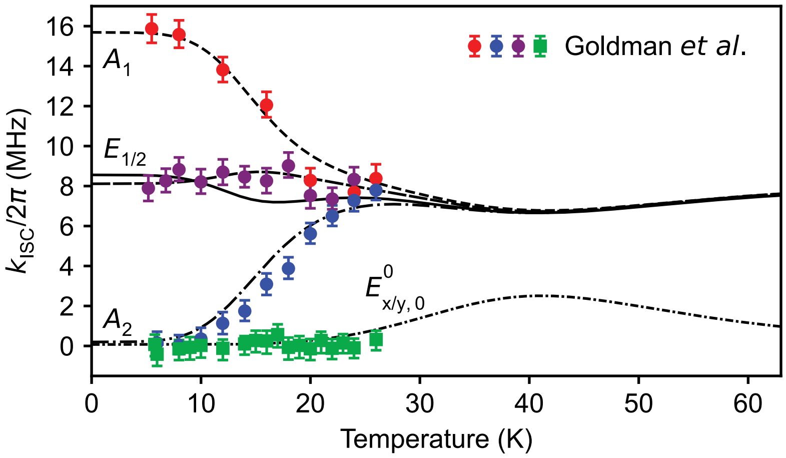

Figure 5.1: Comparison of simulated ISC rates with literature. Experimental data and parameters are taken from Goldman *et al.* [92], while traces are our simulations of the effective ISC rates. They are obtained from a single exponential decay fit of the PL after exciting into the various states of the ES in conditions where *zf basis* states are almost eigenstates (labels).

Then, the state was evolved in time, and the PL was calculated from Eq. 4.38. Finally, a single exponential decay was fitted with a decay rate of k_r (known) plus the effective ISC rate (sought-after). We used the parameters by Goldman *et al.* as an input, namely, $\eta = 276.5\,\mu\text{s}^{-1}\,\text{meV}^{-3}$ and low strain $2\delta_\perp = 3.9\,\text{GHz}$ with $\phi_\delta = 0°$. We did not use their $T_0 = 4.4\,\text{K}$ shift of the phonon temperature, as they did not give an obvious physical motivation for it. The low strain is the reason why the ISC rates of the *zf basis* states are observed to good approximation.

We note that fitting with a single-exponential decay is only an approximation, as around 15 K (where averaging of the ES levels ISC rates occurs, since the optical lifetime is similar to the orbital hopping rate) contributions of the different states can be observed. The ISC rates plotted here should thus be seen as an approximation. The ISC rate difference of E_1 and E_2 at low temperature originates from the non-zero strain, *i.e.* disappears in a setting where E_1 and E_2 are true eigenstates. The experiment could not resolve this behavior since the states are spectrally too close for selective resonant excitation.

We also note that contributions from A_1-symmetric phonon modes might matter here, which are not considered in this thesis (see discussion at the end of Ch. 4.3.1).

5.2 ES Strain dependence at room temperature

To compare our model with the experimentally verified model by Plakhotnik *et al.* [110], we simulate the strain dependence of the averaged ES LAC around 51 mT (see Fig. 4.2(c)). As discussed in Refs. [35, 95], LACs of the GS and time-averaged ES cause a strong reduction in the PL. The LAC position gives insight into the level structure and can be used to compare the levels of a room-temperature model with the numerically time-averaged levels as predicted by our model. The classical rate model with the temperature reduction factor by Plakhotnik *et al.* was derived above in Ch. 4.5.2. We compare the two models in Fig. 5.2(a,b). We first recall that the accepted room-temperature rate model does not contain an explicit dependence on crystal strain in the ES (see dashed traces in Fig. 4.2(a)) — orbital averaging removes any strain dependence of the ES. However, for the high strain values in Fig. 5.2(a), a classical model that includes the Boltzmann distribution predicts a strain dependence of the ES LAC. Likewise, in Fig. 5.2(b), we plot the Lindblad master equation model developed in this thesis. We find full quantitative agreement between the two models. Our model, which includes the Boltzmann distribution using different up- and downward hopping rates (Eq. 4.22), readily predicts the behavior observed under extreme strain at room temperature. This was previously seen as a central challenge for a model covering the entire temperature range [1].

Remarkably, both models predict a non-trivial strain dependence of the width of the LAC, as plotted in Fig. 5.2(a,b). The width of the LAC as a function of the magnetic field varies with the in-plane strain direction ϕ_δ, and the strain position of the smallest width shifts with the magnetic field direction θ_B and ϕ_B. This field dependence could be employed to characterize the order of magnitude of crystal strain and its direction. Since strain strongly affects the SNR of the NV$^-$ center at low temperatures (see Ch. 4.4.3), this feature could be used for all-optical pre-characterization at room temperature. As simulated with the analytical model by Plakhotnik *et al.* in Fig. 5.2(c,d), elevated strain leads to a $\delta_\perp$-characteristic narrowing of the ES LAC at an in-plane magnetic field angle $\phi_B = 180° + \phi_\delta$.

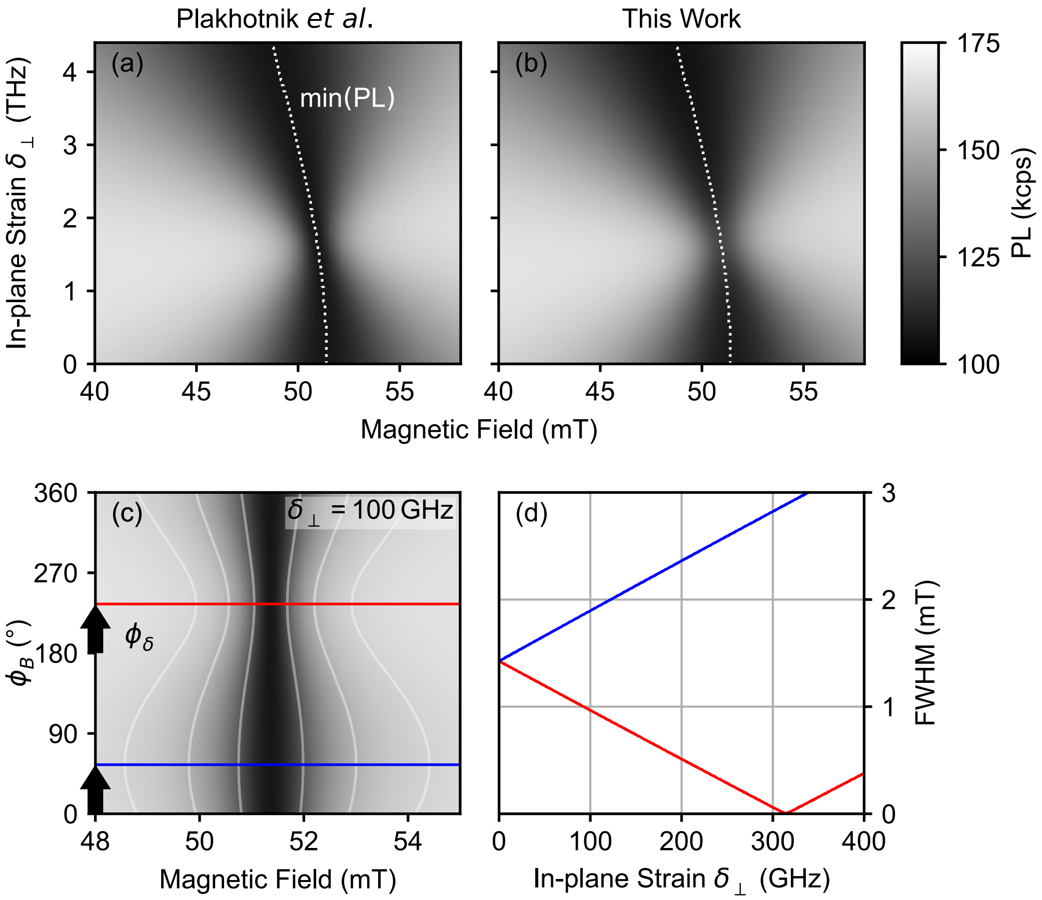

Figure 5.2: Remaining influence of the low-temperature Hamiltonian at room temperature. We simulate the steady-state PL around the ES LAC as a function of magnetic field and strain at 300 K. (a) Room temperature classical rate model with the additional temperature reduction factor in the Hamiltonian as derived by Plakhotnik *et al.* [90]. The dotted trace marks the LAC (minimum in PL). A magnetic field alignment of $\theta_B = 1.9°$ and $\phi_B = 194.2°$ is used, as found experimentally for NV-2 in Tab. 6.3. Other parameters are as in Tab. 4.1. (b) The Lindblad master equation model developed in this thesis. The same dotted trace from part (a) is shown to demonstrate the excellent overlap with the predicted position of the LAC. (c) For a given magnetic field alignment angle θ_B (here: 0.3°), a sweep of the in-plane magnetic field angle ϕ_B is predicted to reveal the strain angle ϕ_δ and magnitude $\delta_\perp$. White traces are contours of constant PL. (d) FWHM of the LAC at the narrowest ($\phi_B = \phi_\delta + 180°$, red line) and widest ($\phi_B = \phi_\delta$, blue line) in-plane magnetic field angle ϕ_B as a function of $\delta_\perp$. Magnetic field sweeps to determine the FWHM are indicated in part (c) for one value of $\delta_\perp$.

5.3 Probing electron-phonon interactions

The spin-lattice relaxation, as well as the orbital averaging, is dependent on the number of available phonons in thermally activated modes and the strength of their coupling to the ES orbital states, as derived in Ch. 4.2.3. Characterizing this spin relaxation process thus suggests a new tool for investigating the interaction of the NV center with the phonon bath. As the temperature dependence of the orbital hopping rate is still under debate [34], we will contextualize recent experimental findings with previous studies and show how our model allows probing electron-phonon interactions based on simple PL measurements.

Multiple studies, including our work, have determined the electron-coupling strength η and reported similar values [35, 37, 91–94, 110]. Determining η requires the evaluation of the integral over the phonon spectrum $I(T, \delta_\perp)$ for the two-phonon Raman process in Eq. 4.24, which all of those studies solve in the Debye approximation. However, different studies use different phonon cut-off energies Ω. One can infer from the upper integration limit in Fig. 4.4(a) that the choice of Ω can have a significant influence at elevated temperatures. We consider the following studies:

1. The study by Goldman *et al.* [92], as already referred to in a different context in Sec. 5.1, uses resonant photoluminescence excitation (PLE) spectroscopy to probe the ES dynamics up to 26 K. At higher temperatures, the spectral broadening does not allow the use of PLE spectroscopy. They use $\Omega = \infty$ and find $\eta = 276\,\mu\text{s}^{-1}\,\text{meV}^{-3}$.

2. Our own experiments and fitted simulations [35, 36], as reported in the next Ch. 6, cover measurements of the ODMR contrast and PL intensity in a temperature range from $T = 3\,\text{K} - 300\,\text{K}$. We assume the Debye energy of diamond $\Omega = 168\,\text{meV}$ for the cut-off and find $\eta = 176\,\mu\text{s}^{-1}\,\text{meV}^{-3} - 268\,\mu\text{s}^{-1}\,\text{meV}^{-3}$, as it will be presented in Tab. 6.3.

3. In an independent and parallel study by Happacher *et al.* [37], similar experiments and fits as our experiments in (2) are reported. There, a fixed cut-off of $\Omega = 60\,\text{meV}$ was used and $\eta = 150\,\mu\text{s}^{-1}\,\text{meV}^{-3}$ was found.

4. Abtew *et al.* [91] determine η from first-principles calculations and vibronic-interaction-model analysis and find good agreement with fit results by Fu *et al.* [41] of the linewidth of the zero phonon line (ZPL) from $T = 3\,\text{K} - 250\,\text{K}$. They assume $\Omega = 50\,\text{meV}$ and find a theoretical value of $\eta = 152\,\mu\text{s}^{-1}\,\text{meV}^{-3}$ and an experimental value of $\eta = 149\,\mu\text{s}^{-1}\,\text{meV}^{-3}$ (in this, we corrected a typo in "$I_4(\infty) = 4\pi^4/15$").

5. Plakhotnik *et al.* [110] perform measurements of the ES ODMR linewidth in the temperature range $300\,\text{K} - 550\,\text{K}$. Since their measurements rely on the time-averaged ES, they extrapolate their model to cryogenic temperatures. They fit a cut-off energy of $\Omega = 13.4\,\text{meV}$.

We test the different cut-off energies by inspecting their effect on our rate model. First, in Fig. 5.3(a), we simulate the temperature-dependent PL to show that there

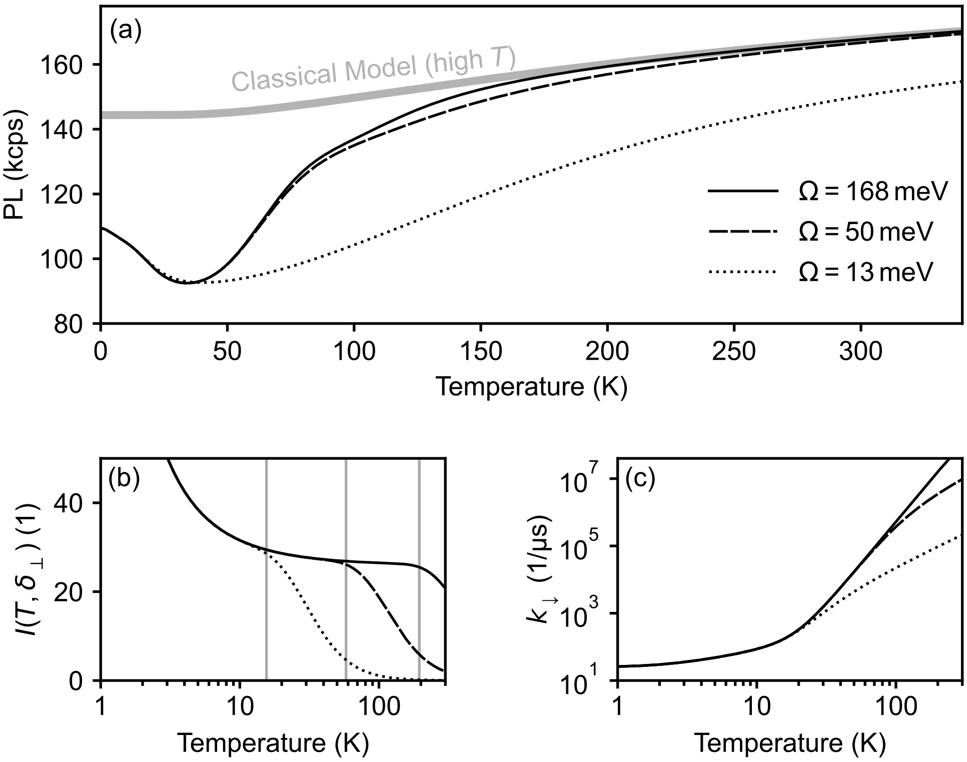

Figure 5.3: Influence of the phonon model on the PL recovery towards room temperature. (a) Steady-state PL as a function of temperature for several phonon cut-off energies Ω. The Ω values correspond to the discussion in the text and are used in the entire figure. The increase in PL above 100 K is due to the decreasing SSL (Eq. 4.19). The effect of the SSL can be distinguished from the ES phonon-driven averaging by comparison with the classical room-temperature model (gray curve). (b) Phonon mode integral $I(T, \delta_\perp)$ plotted for the different Ω values. Vertical gray lines indicate the onset of the cut-offs at $T \approx 0.1 \cdot \Omega/k_B$. (c) $k_\downarrow$ plotted for the different Ω values. Parameters from Tab. 4.1 are used for the entire figure.

is a negligible difference between our cut-off (168 meV) and the lower cut-off from Abtew *et al.* (50 meV) and Happacher *et al.*. This is because the time-averaging sets in at much lower energies ($k_B T \approx 3\,\text{meV}$ for $T = 35\,\text{K}$) than both cut-offs, which was shown above in Fig. 4.4(b). In extension, no discernible effect arises when using $\Omega \to \infty$. Note also from Fig. 4.4(b) that $\Omega \approx 50\,\text{meV}$ marks the approximate limit of the linear dispersion regime of acoustic phonons, for which the phonon spectrum $I(T, \delta_\perp)$ is derived.

By contrast, the low cut-off value of $\Omega = 13.4\,\text{meV}$ from Plakhotnik *et al.* results in a slower increase in the hopping rates toward high temperature (Fig. 5.3(c)). Consequently, the recovery of the PL does not complete up to room temperature (Fig. 5.3(a)). This is in contradiction with several recent experimental studies [35, 37–39], as well as initial work by Rogers *et al.* [40], which found in good agreement that the averaging process and thus the PL recovery completes around 100 K. Plakhotnik *et al.* explain the much higher value of Ω found by Abtew *et al.* for the ZPL linewidth by contributions of A_1-symmetric phonon modes. However, this does not apply to the orbital averaging underlying our rate model, which is caused by E-symmetric phonons.

To gain further quantitative insight, we expect that our model can be used, coupled with a detailed phonon spectrum as well as a detailed PL or spin contrast measurement in the range 80 K to 150 K. For the model, knowledge of the NV center-specific parameters is required. The respective calibration process presented in this thesis requires extensive measurements (see next Ch. 6), including magnetic field sweeps up to 200 mT and a complex calibration process. However, this might not be required for a future study of the phonon model. If measurements are conducted with bulk NV centers that experience negligible crystal strain, the complexity of fitting for the magnetic field and strain vectors would be avoided. This might, additionally, allow for a more reliable fitting of the phonon model. Another approach to probe different phonon modes could be to sweep the controllable crystal strain in a cryogenic anvil cell [119, 120] or by electric fields [88, 97] additional or alternative to a temperature sweep (*cf.* Fig. 4.4(b)).

CHAPTER 6

Fitting model parameters to tailored measurements

Most of the text and figures in this chapter were published in Ref. [35]. They were adapted and extended for this thesis. Additionally, parts were added to provide a more complete picture. These parts include the implementation of data handling (Sec. 6.4.3), parts of the discussion of calibration results (Sec. 6.4.4), and further results on NV-5 (Sec. 6.6). The measurements on NV-5 were recorded by me on the VarTMa setup. Luca Lorenzelli took similar initial measurements on a different NV sample [44], also on the VarTMa setup, which are not shown in this thesis. All other measurements in this chapter (NV-1, NV-2, NV-3, NV-4) were recorded by Patrick Scheidegger and Simon Diesch on the HIMBI setup. These measurements led to the development of the model from chapter 4 and were fitted to it. Patrick Scheidegger, Simon Diesch, and I conceived the experiments in this chapter. I did the data analysis by fitting with the model as presented in this chapter. In a collaboration with Friedemann Reinhard's group, Francesco Poggiali took early-stage measurements on the same ^{12}C *diamond sample and tested resonant optical excitation. Unfortunately, resonant optical excitation seemed impossible due to spectrally broad resonance lines — mostly likely caused by the shallowness of the NV centers in this sample [121]. Matthew Markham (ElementSix™) provided the* ^{12}C *diamond. Jan Rhensius (QZabre LLC) did the nanofabrication of the* ^{12}C *diamond. Assaf Hamo provided critical input on the relevance of applying high magnetic fields.*

In this chapter, an extensive set of experimental data is evaluated with the goal of verifying the model developed in Ch. 4 and characterizing the performance of a variable-temperature scanning NV magnetometer. To that end, NV center-specific parameters need to be fitted. To extract them, different types of measurements are conducted, and their data is simultaneously fitted to the corresponding model simulations. This requires handling of diverse data sets and effective management of fitting procedures. These steps, as well as our final results, are presented in the following. A good agreement is found between simulation and experiment over a wide parameter range.

6.1 Experiment overview

Only some data (NV-5) evaluated in this chapter was actually recorded on the VarTMa setup described in Ch. 3. For the experiments discussed in the following, the ability to continuously sweep large magnetic fields is essential. To that end, the majority of data presented in this chapter was acquired inside a dilution refrigerator [10, 75] (named HIMBI) on an isotopically pure (^{12}C) diamond sample doped with 7 keV NV centers in nanostructured pillars. These are similar to the pillars we use for scanning probe experiments in Fig. 2.1(c). The NV centers from these measurements are called NV-1, NV-2, NV-3, NV-4. In contrast to VarTMa , HIMBI is equipped with a strong, superconducting vector magnet.

The HIMBI data presented here was acquired over the course of three distinct cooldowns. Cooldown #1 was limited to all-optical measurements of PL. Cooldowns #2 and #3 were identical in terms of experimental setup and used a co-planar waveguide for microwave delivery. All contrast versus temperature data on HIMBI was taken during those cooldowns. During cooldown #2, two NV centers (NV-2 and NV-4) bleached, *i.e.* showed a major loss of spin contrast at a reduced PL level. Bringing them to ambient conditions for a short time completely restored their previous properties, and they have not shown signs of bleaching afterward.

Importantly, all our data is consistent across all three cooldowns and in line with the observations in VarTMa (NV-5), which emphasizes the independence of our results from setup-related conditions. Further experimental details on the samples, the setup HIMBI, and the technical challenges of the measurements presented here are provided in Ref. [75] and [35].

6.2 Measurement types

We use six types of experiments to characterize each NV thoroughly and to disentangle the various fitting parameters. Fitting the first three experiment types (Secs. 6.2.1–6.2.3) is a simultaneous effort, further discussed in Sec. 6.4, due to shared parameters between all of them. The fourth experiment type, namely the shelving state lifetime (6.2.4), is determined independently. The fifth type of experiment (Sec. 6.2.5) characterizes the laser pulses and is done once and also independently. Finally, by the sixth type of experiment, we try to verify that we are working with the negative charge state NV$^-$ of the NV center at all temperatures. This section discusses the first five experiments in detail and how they are tailored to extract the model parameters in Tab. 4.1.

Concerning the sixth type of experiment, we see no signs of blinking, as it occurs when the charge state switches, on time scales between 100 µs and 60 s. The procedure of these measurements was described in more detail in Ref. [35, SM]. A temperature-dependent reduction in PL intensity and spin contrast was reported in connection with NV charge state instabilities [122]. However, our model can account for the observed temperature dependence by phonon-induced processes in the ES alone. This

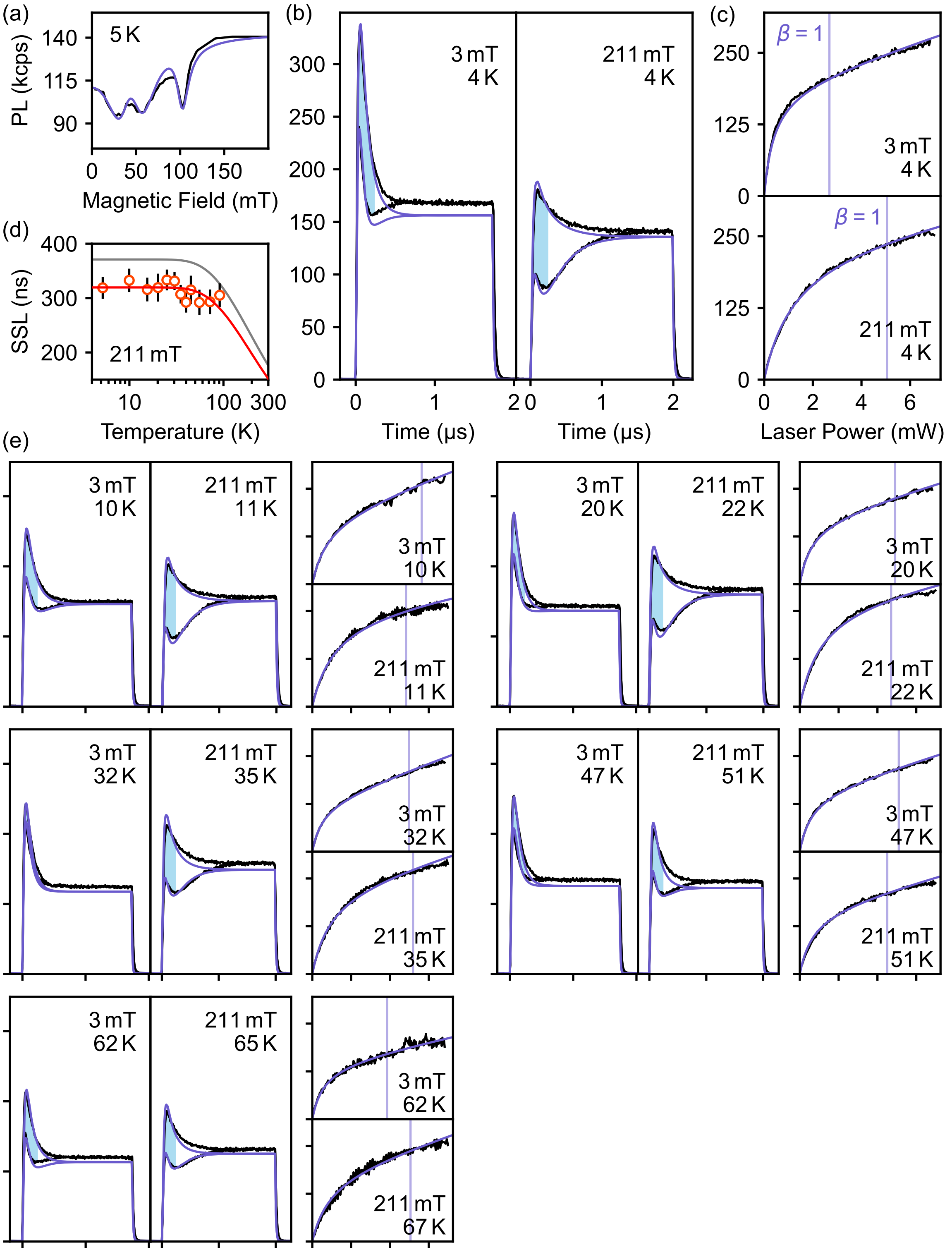

Figure 6.1: Overview of the simultaneous fit result after stage III for NV-2. The complementary measurements with their corresponding fits (solid blue traces) are shown. Parts (a–c) were taken at base temperature ($\sim 5\,\mathrm{K}$) and constitute a typical data set for the simultaneous fitting in stage II described in Sec. 6.4. The vertical axes are PL (kcps). (a) *PL vs. B* measurement. (b) *Time-resolved pulsed ODMR* at low and high magnetic fields. Contrast is integrated over the blue shaded area ($t_{\text{int}} = 250\,\text{ns}$). (c) *Saturation* measurements at the same fields. (d) Measurement and separate fit (red trace) of the temperature dependence of the SSL. For comparison, the findings by Robledo *et al.* [86] are also shown (gray trace). (e) Shown in the same plot pattern as parts (a–c) are all other data sets included in the simultaneous fit in stage III. The fitted parameters are reported in Tab. 6.3 and Fig. 6.5.

suggests that charge-state switching between NV^- and NV^0 does not play a key role in explaining the spin contrast as a function of temperature in our experiments.

6.2.1 PL vs. B

We measure the steady-state PL while sweeping the magnitude of the magnetic field B from high field to low field, as shown in Fig. 6.1(a). At base temperature, such a trace exhibits minima at the LACs of the ES and the GS, which we use to uniquely characterize [40, 95] the in-plane strain $\delta_\perp$ and magnetic field alignment θ_B. These *PL vs. B* measurements are horizontal linecuts in Fig. 4.12(a), and one can easily see that they are well suited to characterize the strain. A magnetic field misalignment, on the other hand, dominantly and uniquely increases the width of the GS LAC (103 mT).

The relative depth of the ES LAC minima at base temperature (*e.g.* 30 mT and 55 mT in Fig. 6.1(a)) is known to depend on the ES branch-selectivity of the optical excitation [95] (called r_β in Tab. 4.1). However, we find an additional dependence on the orbital hopping rate, as discussed in Ch. 4.4.6. Specifically, the spontaneous one-phonon emission process $\mathrm{E_x} \rightarrow \mathrm{E_y}$, which is relevant in the presence of significant in-plane strain, causes the first $\mathrm{E_y}$ LAC minimum to be deeper than the second $\mathrm{E_x}$ LAC minimum when assuming no branch-selectivity (see Fig. 4.16). This observation can also be made upon closer examination of similar *PL vs. B* measurements presented by Happacher *et al.* [95, SM Tab. III]: there, measurements at higher $\delta_\perp$ values showed deeper $\mathrm{E_y}$ LAC minima, which were modeled by smaller r_β values (no phonon processes were included in the model). The rate of the responsible spontaneous emission process (see Eq. 4.23) depends on the electron-phonon coupling strength η, which is a fit parameter in our model. To avoid cross-talk between the fit of η and the branch selectivity r_β, we always assume no orbital branch selectivity in our optical excitation, *i.e.* $r_\beta = \beta_\mathrm{x}/\beta_\mathrm{y} = 1$ (see Fig. 4.2(d)). This assumption is reasonable for the following reasons: (i) we off-resonantly excite NV centers with green laser light into the phonon sideband, where the selectivity is naturally low even with aligned NV and laser polarization axes [41, 101]. (ii) our NV center principal axes are tilted by 55° relative to the diamond surface and optical axis, reducing the possible polarization alignment.

When fitting *PL vs. B* measurements in the following, we exclude points below 15 mT to avoid possible distortions due to the remanent field of the vector magnet, which can dominate at low bias field.

6.2.2 Time-resolved pulsed ODMR

We measure the time-resolved, spin state-dependent PL under excitation with $\sim 2\,\mu\mathrm{s}$ laser pulses as shown in Fig. 6.1(b). This measurement type was discussed in Fig. 2.2(a) and simulated in Ch. 4 to obtain the spin contrast and thus the SNR. Here, in contrast to Fig. 2.2, we use an adiabatic inversion microwave pulse [123] to obtain an experimentally stable spin state inversion fidelity close to 1. Further, in contrast to optimizing the integration time t_int for each parameter setting as in Ch. 4, we use a fixed $t_{\mathrm{int}} = 250\,\mathrm{ns}$ at all conditions. We find that the contrast is fairly resilient against changes in setup-specific parameters (see Tab. 4.1). The PL follows a similar trend (see Fig. 4.5(h)), but is more prone to experimental drift. For this reason, we used contrast to display the temperature dependence of the NV$^-$ center performance in Fig. 2.2(d). Consequently, *time-resolved pulsed ODMR* measurements can be used to fit the temperature dependence (η in Tab. 4.1), as they inherently contain the contrast. Beyond that, the contrast critically depends on the SS branching ratio (r_S in Tab. 4.1).

In addition to the mere contrast value, *time-resolved pulsed ODMR* measurements are well-suited to fit the fast photo-dynamics. Explicitly, these are the rates related to the optical lifetime and ISC process (k_r, $k_{E_{12}}$, $k_{E_{\mathrm{xy}}}$ in Tab. 4.1). We note that setup-specific parameters also change the curve shape.

6.2.3 Saturation measurement

The measurement of the steady-state PL while sweeping the laser power (P in Tab. 4.1) shows a characteristic saturation behavior [124] that arises when the optical excitation rate exceeds the optical decay rate k_r. Then, the laser power-dependent PL becomes linear with a slope given by the fluorescent background (b in Tab. 4.1), as shown in Fig. 6.1(c). The laser power at which the saturation is reached is characteristic of the excitation efficiency. The absolute PL level, on the other hand, is characteristic of the collection efficiency ($R \cdot A$ in Tab. 4.1). Therefore, *saturation* measurements are primarily suited to characterize these three setup-specific parameters and to disentangle them from rate parameters.

Note that the maximal emission rate from the $m_{\mathrm{S}} = 0$ initialized NV$^-$ center with $100\,\%$ collection efficiency ($R \cdot A$) is not around PL $\approx k_r \approx 60\,\mathrm{Mcps}$. The finite chance for a decay to the shelving state, paired with its long lifetime, significantly reduces the maximal emission rate. For the parameters given in Tab. 4.1, the steady-state PL with $R \cdot A = 1\,\mathrm{cps\,s}$, $b = 0$, and $P \to \infty$ is $5.5\,\mathrm{Mcps}$ at $0\,\mathrm{K}$ and $20\,\mathrm{Mcps}$ at $300\,\mathrm{K}$. It shows a similar qualitative behavior as the SNR given as a function of various parameters in Ch. 4.

6.2.4 Shelving state lifetime

The SSL, *i.e.* the time spent in the intermediate singlet levels before decaying back into the GS (*cf.* Fig. 4.2(d)), has a well-known temperature dependence that we included in our model of the NV photo-physics (see Eq. 4.19). We measure the SSL following Refs. [86, 87]. First, we populate the shelving state using a $1.2\,\mu\mathrm{s}$ laser pulse. Second, we wait for a variable duration τ followed by a second laser pulse. The initial photon countrate $\mathrm{PL}_{30\,\mathrm{ns}}$ of this pulse (mean of the counts in the first $30\,\mathrm{ns}$) is a measure for the population that has already decayed out of the SS during τ. When sweeping τ, the resulting exponential rise

$$\mathrm{PL}_{30\,\mathrm{ns}}(\tau) \propto 1 - a e^{-\tau/\tau_S(T)} \tag{6.1}$$

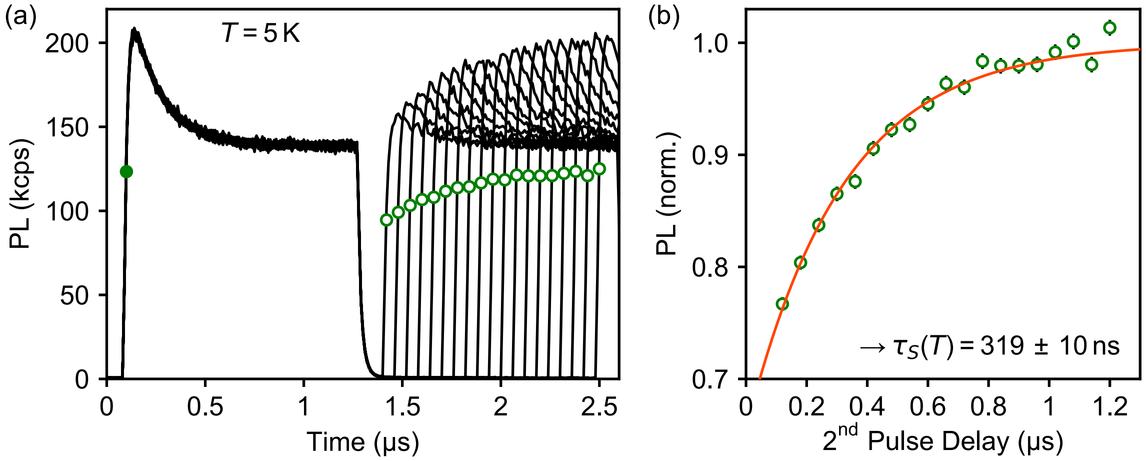

Figure 6.2: SSL evaluation of NV-2 at 5 K **and** 207 mT**.** (a) Subsequent measurements of a pulse sequence with different τ are plotted on top of each other. The rise of the initial PL$_{30\,\mathrm{ns}}$ (averaged, empty green markers) is evaluated for each of the time-resolved PL traces, as explained in the text. (b) The PL$_{30\,\mathrm{ns}}$ values are normalized (filled green marker in (a)) and then fitted to Eq. 6.1 (orange curve). The fit result τ_S is the first data point in Fig. 6.1(d).

can be fitted for the SSL $\tau_S(T)$ at the measurement temperature T. Both evaluation stages are presented in Fig. 6.2. For comparison, the rise in Eq. 6.1 was also visible as the rise of the $\langle m_S = 0\rangle$ between 1 μs − 2 μs in Fig. 2.2(a).

Obtaining the data points $\tau_S(T)$ for several temperatures allows in a second step to fit the parameters of the temperature dependence of the SSL according to Eq. 4.19 ($\tau_{S,0}$ and ΔE in Tab. 4.1). We fit $\tau_{S,0}$ for each NV center individually, as we find significantly different values for different NV centers. The fit results are given in Tab. 6.3 together with their uncertainty. The latter is calculated based on the assumption that there are only statistical errors in the form of photon shot noise (see Ch. 2.3). Fitting $\tau_S(T)$ reliably for ΔE requires a significant amount of measurements in the range $T \gg 100\,\mathrm{K}$, which was not accessible in the experiments on HIMBI. We therefore use $\Delta E = 16.6\,\mathrm{meV}$ as reported by Robledo *et al.* [86]. In Fig. 6.1(d), we present the result of such an evaluation scheme at the example of NV-2.

The slow rise of PL$_{30\,\mathrm{ns}}$ in Eq. 6.1 is characteristic for the negative charge state NV$^-$ of the NV center. Even though the neutral charge state NV^0 also possesses a metastable state, it has only a small influence on the photo-dynamics [108] and does not obscure the characteristic PL profile of the laser pulse sequence (when an off-resonant laser excitation is used or $T > 10\,\mathrm{K}$ [125]). A *shelving state lifetime* measurement can thus be used as a quick and all-optical check whether the negative charge state NV$^-$ is present (on long timescales). This can be useful since during scanning NV experiments, the spin contrast can disappear for various reasons (microwave wire is blown, tip broke off, NV$^-$ permanently switched to NV^0, ...). Another all-optical method is the *saturation* measurement. But in contrast to it, the *shelving state lifetime* measurement does not require a (linear) calibrated laser power. Moreover, the NV^0 also shows a saturation behavior with a time constant similar to the NV$^-$ [125]. But a quantitative difference in the absolute PL exists, which, apart from different photo-dynamics, also originates from partial spectral filtering of the NV^0 PL in typical setups. For a filter setting of 650 nm to 800 nm, the collection of NV$^-$ counts is only around a factor

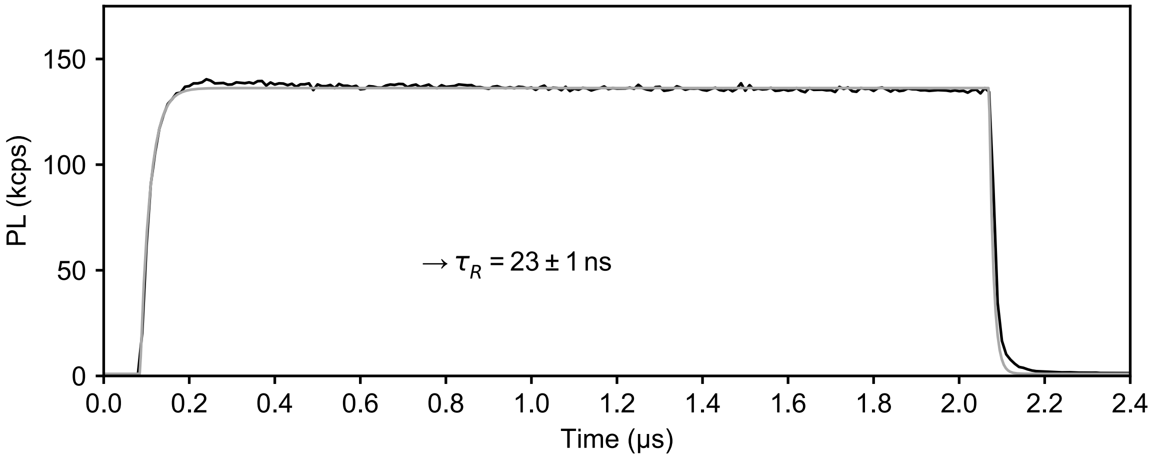

Figure 6.3: Calibration of the laser rise time τ_R. The time-resolved PL of a fluorescent contamination during a laser pulse is measured. The initial rise is fitted to Equ. 6.2. A laser power of $P = 1.45\,\text{mW}$ was used here.

2 more efficient than for NV^0 counts (found by integration of the spectra given in Refs. [126–128]). Additionally, high laser powers give an altered NV^0 population and distort the saturation curve [108], while low laser powers yield a power-independent NV^0 population [124]. Therefore, quantitative knowledge of the setup is needed to use saturation curves to characterize the charge state. The downside of the *shelving state lifetime* measurement, on the other hand, is that it requires long averaging times (due to the small duty cycle $\sim 30\,\text{ns}/5\,\mu\text{s}$) and that the ability to pulse the laser on the sub-100 ns timescale is needed.

6.2.5 Laser characterization

When fitting *time-resolved pulsed ODMR* measurements, the laser rise time τ_R has to be taken into account if it is longer than the time resolution of the photo-detector (10 ns). To simulate this rise, we can use the fact that $\tilde{\mathcal{L}}$ is time-independent (see Eq. 4.27) and ramp up the laser power P, and thus $\tilde{\mathcal{L}}$, in N discrete steps

$$P(t) = \begin{cases} 0 \text{ if } t < t_0 \\ P\left(1 - e^{t_n/\tau_R}\right) \text{ for } t_n = \left\lceil \frac{t-t_0}{\Delta t} \right\rceil \Delta t \\ P \text{ if } t > t_0 + N\tau_R \end{cases} \tag{6.2}$$

and use fix parameters $N = 4$ and $\Delta t = 5\,\text{ns}$ here. We find that the influence of τ_R on the spin contrast is negligibly small. This is in line with the stability of the contrast against other setup-related parameters. In fitting the photo-dynamics in *time-resolved pulsed ODMR* measurements, on the other hand, τ_R is critical. Likewise, we need to individually determine the precise value of t_0 for each measurement. This is done by linear extrapolation to PL = 0 from the first two data points above the dark count level.

For the optical excitation, HIMBI uses a 520 nm diode-laser with home-built modulation circuitry [129]. The data on VarTMa, in contrast, was taken with a 532 nm

Model	creation of model object	SNR at optimal t_{int}	SNR at $t_{\mathsf{int}} = 250\,\mathsf{ns}$	steady-state PL
Lindblad master equation	$15\,\mathsf{ms}$	$100\,\mathsf{ms}$	$90\,\mathsf{ms}$	$16\,\mathsf{ms}$
Classical rate	$0.120\,\mathsf{ms}$	$4\,\mathsf{ms}$	$3\,\mathsf{ms}$	$0.125\,\mathsf{ms}$

Table 6.1: Computational speed of the `nvratemodel` [43] library. The Python implementation of the Lindblad master equation model and the classical room temperature model are compared on a 11th Gen Intel® Core™ i7-11700 @ 2.50GHz, 64bit. The given SNR and PL times contain the creation of the model object.

laser and acousto-optic modulator. We characterize τ_R in HIMBI on fluorescent contamination in proximity to the NV center and assume that it shows an instantaneous reaction, *i.e.* has no significant optical lifetime. As shown in Fig. 6.3, we obtain

$$\tau_R = 23\,\mathrm{ns} \pm 1\,\mathrm{ns}\,. \tag{6.3}$$

We calibrate the power P directly at the laser output and use a conversion factor (called A in Tab. 4.1) to fit the actual excitation rate of the NV center. Heating of the diode slightly alters the output laser power, which is why we find a consistent mismatch by a factor of 1.15 between the steady-state PL value in *time-resolved pulsed ODMR* and the *saturation* measurements. We scale our *saturation* data accordingly with a factor 1.15, which is required to be able to fit both measurement types with the same shared parameters.

6.3 Computational implementation of the models

We implement the models derived in Ch. 4: the Lindblad master equation model, the classical model at low temperature, and the classical model at room temperature with the option for including the temperature reduction factor. The code is openly accessible via GitHub [43] in the form of a (hopefully) easy-to-install and user-friendly Python library, with a high abstraction level — many figures in this thesis can be generated with a single line of code. The library was optimized for computational speed by the open access package numba [130], since fitting the model with a large set of parameters to measurement data can otherwise take prohibitively long. Several functions are inspired by the QuTiP package [106] but were re-implemented for speedup with numba. The gain in computational speed by numba is platform and installation dependent. An exemplary overview is provided in Tab. 6.1. The phonon integral in Eq. 4.25 was implemented as a look-up table for improved computational speed. Our numerical rate model has 10 levels (*cf.* Eq. 4.3). Thus, the Fock-Liouville space of the Lindblad master equation model has a dimension of 100 with $\vec{\rho} \in \mathbb{C}^{100}$ and $\tilde{\mathcal{L}} \in \mathbb{C}^{100\times100}$. It is computationally expensive to calculate the matrix exponential in Eq. 4.27 for each time step in a PL(t) time trace of Eq. 4.38. Therefore, we first calculate $U_{\Delta t} = \exp\left(\tilde{\mathcal{L}}\Delta t\right)$ for a single time step Δt. We then obtain the time trace PL_n over $t_n = n\Delta t$, $n \in [0\,..\,N]$, recursively from $\vec{\rho}_n = U_{\Delta t}\vec{\rho}_{n-1}$ at reduced computational cost. The accumulated numerical errors were found to have a negligible effect on our results. Similarly, in the classical rate models, we calculate the propagation for a small time step Δt in Eq. 4.86 and apply this propagation iteratively at a significantly reduced computational cost.

6.4 Data evaluation

In this section, we describe how we fit our measurements to calibrate the model and, subsequently, simulate the NV PL to compare the model to our measurements.

6.4.1 Overview

When fitting, we distinguish the following sets of fit parameters:

a. *Robust* parameters: They include all NV-intrinsic parameters (*i.e.* strain and rates) and the magnetic bias field, which we have good control over. These parameters are stable against scanning stage movements and other drifts that can occur between measurements, particularly when changing to a new temperature or magnetic field. For an overview, see Tab. 4.1.

b. *Environment-sensitive* parameters: This set is prone to change between measurements. These are the setup parameters listed in Tab. 4.1.

c. Pre-determined parameters: This set was independently determined as discussed in Sec. 6.2 and remains fixed when fitting for sets *a* and *b*.

d. Literature values: Apart from the Hamiltonian parameters in Tab. 4.1, this set contains further parameters or relation of parameters that we take from literature and keep fixed.

An overview of all parameters and their respective categorization will be given in Tab. 6.3 with the fit results. These parameter categories help to distinguish the qualitatively different processes by which we relate our data to the model:

1. *Calibration*: Simultaneous fit of multiple data sets across multiple temperatures T_i and fields B_i with common *robust* parameters but unique *environment-sensitive* parameters for each T_i/B_i. The procedure is described in detail in the next two sections.

2. *Simulation*: Uses the calibration results for the *robust* parameters and a *single* set of *environment-sensitive* parameters (calibration result of the respective base temperature data set) to effectively extrapolate the NV photo-physics to the full range of temperature, magnetic field, and strain. This is used, for example, in the contrast versus temperature curves in Fig. 2.2(d) and Fig. 6.7 and in maps of PL(B,T) in Fig. 6.6(top panels). Deviations from experimental data are found, particularly at high temperatures where drifts in the setup become significant.

3. *Fits*: Fits use the calibration-results for the *robust* parameters but exclusively re-fit the *environment-sensitive* parameters to a given data set at a specific (T, B). This effectively corrects for experimental drifts. Examples are fits of *PL vs. B* measurements in Fig. 6.6(middle panels) and *time-resolved pulsed ODMR* traces in Fig. 2.2(c).

6.4.2 Calibration process

In Sec. 6.2, the various types of measurements were introduced. Each type individually is well-suited to determine some parameters while showing no marked dependence on others. But all generally depend on the same full set of parameters. Thus, to fit this set of parameters, it is necessary to perform a single, consistent fit across different measurements and types. We perform this calibration process in three stages, where each stage informs the set of initial parameters of the subsequent fit.

I. We start by fitting a *PL vs. B* measurement at base temperature ($\sim 5\,\mathrm{K}$) to our full model. We fit for the in-plane strain ($\delta_\perp$, ϕ_δ) and magnetic field alignment (θ_B, ϕ_B) as well as the setup-specific parameters (b, R, A). We use literature-inspired values for all other parameters as they can be found, for example, in Refs. [86, 93, 96, 102].

II. We then simultaneously fit a data set consisting of five different measurements at base temperature ($\sim 5\,\mathrm{K}$), with all parameters being fitted (except for η). This data set includes the *PL vs. B* measurement from before, two *time-resolved pulsed ODMR* traces and two *saturation* measurements at low ($\sim 3\,\mathrm{mT}$) and at high ($\sim 200\,\mathrm{mT}$) magnetic field. Such a data set for NV-2 was shown in Fig. 6.1(a–c) (but with the parameters after stage III).

III. Finally, we fit the same base-temperature set of five measurements together with five (four for NV-4) further sets of each four measurements (*time-resolved pulsed ODMR* and *saturation* measurements at each high and low field), sampled across our full temperature range. This allows us to fit for the electron-phonon coupling strength η, in addition to a final fine-tuning of the full parameter set. Crucially, we use a common set of *robust* parameters across all data sets, but individual *environment-sensitive* parameters are used for each data set, which accounts for mechanical drifts in the experimental setup. Specifically, the two parameters background b and collection over excitation efficiency R are fitted separately to each pair of *saturation* and *time-resolved pulsed ODMR* measurements (at the same field and temperature) and also separately to the base-temperature *PL vs. B* measurement. Further, the alignment parameter A has to be fitted separately for every single measurement. This results in a total of 60 fit parameters simultaneously fitted to 25 distinct measurements.

We find that the simultaneous fit of these 25 measurements in stage III improves the stability of the fit compared to stage II, which contains only the five base-temperature measurements. In this last stage, the computational speed optimization described in Sec. 6.3 becomes very critical, as such a fit can take several days even after the optimization.

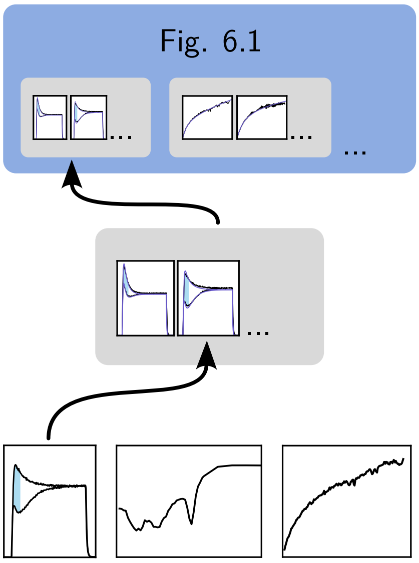

Evaluation per NV center (user interface)
- owns instances of arbitrary Fit-Manager classes
- has one set parameters (each fixed or fittable)
- combine Fit-Manager objects to simultaneous fits
- store and load evaluations

Fit-Manager classes
- for each measurement type
- own multiple instances of same Data class
- manage fit parameters, simulate, plot
- interface for simultaneous fits

Data classes
- for each measurement type
- loading + processing of data & metadata

Figure 6.4: Structure of the Python code developed for data and fit management.

6.4.3 Implementation of data handling

In order to perform the calibration process described above, the data and fit management structure presented in Fig. 6.4 was conceived. It allowed for a modular and flexible handling of the calibration process on a high abstraction level. When performing the least-squares fit over several data sets, special attention must be paid to their relative weights in the cost function. For example, in stage III of the calibration process, the base-temperature *PL vs. B* measurement is only one in 25 data sets. Additionally, for experimental reasons, it is sampled significantly more sparsely than the other measurement types and has y values (*i.e.* PL) lower than, for example, the saturated part in the *saturation* measurements. But the *PL vs. B* measurement is crucial in fitting the strain and magnetic field parameters. To prevent its weight in the fit from being swamped by some statistical or, in particular, systematic errors in the large number of other measurements, we manually alter the weights in the cost function. This process is described in the following.

Conventionally, the weight of each data point (x_j, y_j) in a least-squares fit is given by its inverse statistical variance σ_j^2. The total cost function F, which is minimized in the fitting process by the Python library SciPy [131], is constructed as

$$F = \chi^2 = \sum_{j=0}^{N} \frac{(y_j - f(x_j))^2}{\sigma_j^2} \,. \tag{6.4}$$

In our case, the residuals $(y_j - f(x_j))$ are not dominated by statistical noise, which is given by the shot noise of the photon counting as discussed in Ch. 2.3. Rather, as can be seen in Fig. 6.1, systematic deviations dominate. Therefore, a weighting by σ_j^{-2} does not yield the intended calibration (*i.e.* no visual match between simulation and data). We thus re-define the weights of data points as follows to better represent the information density in the data sets: One part w_B of the weight in the cost function is given to the *PL vs. B* measurement at base temperature, one part w_{sat} to all the

	NV-1	**NV-2**	**NV-3**	**NV-4**
Relative weights				
all sat. meas. w_{sat}	n.a.	$43\,\%$	$51\,\%$	$50\,\%$
all ODMR meas. w_{adia}	$85\,\%$	$46\,\%$	$42\,\%$	$37\,\%$
the *PL vs.* B meas. w_B	$15\,\%$	$11\,\%$	$7\,\%$	$13\,\%$
Final cost contributions				
all sat. meas. F_{sat}	n.a.	$21\,\%$	$40\,\%$	$33\,\%$
all ODMR meas. F_{adia}	$92\,\%$	$75\,\%$	$58\,\%$	$58\,\%$
the *PL vs.* B meas. F_B	$8\,\%$	$4\,\%$	$3\,\%$	$9\,\%$
Final relative errors				
sat. meas. $\sqrt{R_i}$	n.a.	$3(1)\,\%$	$4(1)\,\%$	$4(1)\,\%$
ODMR meas. $\sqrt{R_i}$	$3(2)\,\%$	$6(1)\,\%$	$5(1)\,\%$	$7(2)\,\%$
PL vs. B meas. $\sqrt{R_i}$	$3\,\%$	$3\,\%$	$3\,\%$	$5\,\%$

Table 6.2: Statistics of the least-squares fits performed in the last calibration stage III. The abbreviations sat for *saturation* and adia for *time-resolved pulsed ODMR* measurements (with adiabatic inversion) are used. The manually set weights are presented together with figures of the final outcome of the calibration process. Variables are defined and discussed in the text. Correctly reproducing the dynamics in *time-resolved pulsed ODMR* measurements appears to have the largest relative error and thus dominates the cost function close to the final optimum we found.

saturation measurements together, and one part w_{adia} to all the *time-resolved pulsed ODMR* measurements together. We label each measurement with index i and assign a simulation function f_i (defined by i-individual and shared fit parameters) and data points $(x_{i,j}, y_{i,j})$, $j \in [0, N_i]$. Within

$$w_{\mathsf{sat/adia}} = \sum_{i \in \mathsf{sat/adia}} w_i \,, \tag{6.5}$$

each of the 12 (10 for NV-4) measurements is given a similar weight w_i. We define the total cost function as

$$F = F_B + F_{\mathsf{sat}} + F_{\mathsf{adia}} = \sum_i w_i R_i \tag{6.6}$$

with weights w_i, which we set manually, and R_i given by

$$R_i = \frac{1}{N_i \, \overline{y_{i,j}}\big|_i^2} \sum_{j=0}^{N_i} \left(y_{i,j} - f_i(x_{i,j})\right)^2 \tag{6.7}$$

for the *PL vs. B* and *saturation* measurements. The idea behind this definition is that $\sqrt{R_i}$ is a measure for the relative error between y-data and f-simulation. For the *time-resolved pulsed ODMR* measurements, we calculate R_i as

$$R_i = \frac{1}{N_i \, \overline{y_{i,j}}\big|_i^2 \, \overline{v_{i,j}^2}\Big|_i} \sum_{j=0}^{N_i} v_{i,j}^2 \left(y_{i,j} - f_i(x_{i,j})\right)^2 \tag{6.8}$$

with a data point-specific weighting $v_{i,j}^2$ given by

$$v_{i,j} = \mathcal{G}_j \left(\left| 1 - \frac{\mathrm{sig}_{i,j}}{\mathrm{ref}_{i,j}} \right| \cdot \frac{\mathrm{sig}_{i,j} + \mathrm{ref}_{i,j}}{2} + 1 \right) . \tag{6.9}$$

Here, in the phrasing of Eq. 2.2, $\mathrm{sig}_{i,j}$ ($\mathrm{ref}_{i,j}$) is the $\mathrm{PL}_{m_\mathrm{S}=\pm1}$ ($\mathrm{PL}_{m_\mathrm{S}=0}$) measured at time $x_{i,j}$ in time trace i. The $\mathcal{G}_j$ is a convolution with a Gaussian of width $2\sigma = 90\,\mathrm{ns}$ (spanning nine data points $x_{i,j}$) to smooth out the weighting trace $v_{i,j}$ in the j-dimension. The effect of $v_{i,j}$ is to weight data points by a measure of their spin information content, here roughly contrast times counts. The $+1$ term avoids $v_{i,j} = 0$. Like in Eq. 6.7, also in Eq. 6.8 the $\sqrt{R_i}$ is a measure for the relative error between data and simulation, but now with a focus on the points that have a spin contrast. Note that only this region of spin contrast contains distinctive information from what the corresponding *saturation* measurement already contains.

In our calibration process, systematic errors dominate, and thus, the propagation of statistical errors in the common framework of the least-squares fit does not apply. On top of that, the usage of the fit weights would distort the error propagation from the conventional sense. And finally, there is a significant cross-talk between some fitted parameters. Thus, we do not include any statistical errors in the fits and must refrain from providing errors on the calibration results in Tab. 6.3. The calibration process should rather be seen as a comparison with the model than a fit in the conventional sense, and the fitted parameters should be seen as the best match we could find to a large data set with systematic errors.

6.4.4 Discussion of calibration results

Results of the calibration for the different NV centers are presented in Tab. 6.3 and Fig. 6.5. The latter contains the *environment-sensitive* parameters that have been determined across all temperatures, as described above. Some statistics of the least-squares fits are given in Tab. 6.2. A visual impression of the calibration result was given in Fig. 6.1 for NV-2. For NV-1 we were not able to include *saturation* measurements in the fit as the PL stability required here was not sufficient. We stress that the fitted setup parameters do not show a correlation with temperature. In particular, in Fig. 6.5, we do not see any feature around 35 K, the location of the contrast and PL minimum. Since cooldown #1 has different magnetic field alignment due to changes in the setup, a different in-plane magnetic field angle ϕ_B was used for the *PL vs. B* measurement at base temperature when fitted simultaneously with the *saturation* and *time-resolved pulsed ODMRs* measurements from cooldown #2 and #3. This is the case for NV-1 and NV-2. The alignment angle θ_B had to be assumed to be the same, though, since at the two fields covered by our *saturation* and *time-resolved pulsed ODMRs* measurements, θ_B has a too small effect.

A comparison to previous literature of our calibration results for the electron-phonon coupling strength η and the assumed phonon cutoff energy Ω was given in Ch. 5.3.

Regarding the in-plane magnetic field ϕ_B and strain ϕ_δ angles, we can only determine them relative to one out of three possible crystal axes, which we then call the x-axis

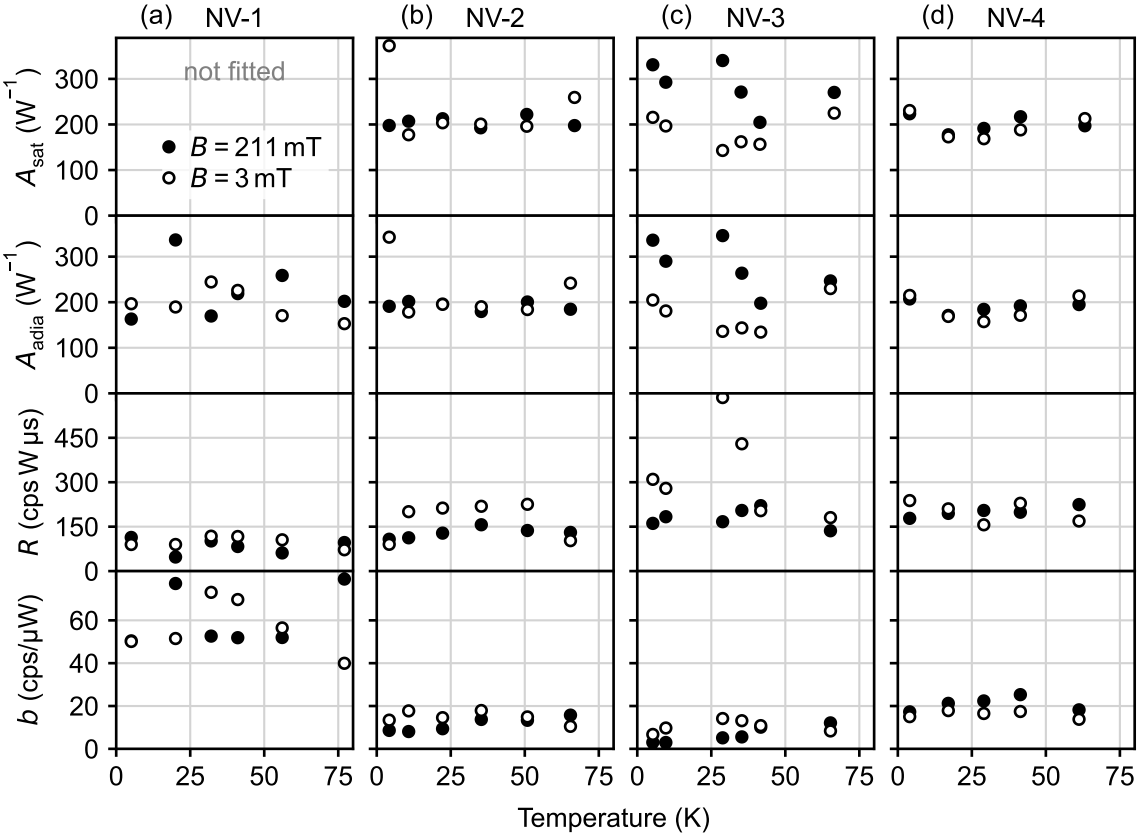

Figure 6.5: Calibration results for the *environment-sensitive* parameters. Shown are the results for the *saturation* (sat) measurements and *time-resolved pulsed ODMRs* (adia, for adiabatic inversion) at low ($3\,\mathrm{mT}$, empty circles) and at high ($\sim 200\,\mathrm{mT}$, filled circles) magnetic field. Temperature-independent results of the same single simultaneous fit per NV center are given in Tab. 6.3. Shown here are the optical alignment A, the ratio of collection over excitation efficiency R (common to both sat and adia), and the background b (also common to both).

of our coordinate system (see Fig. 4.1). Moreover, based on our measurements, we are insensitive to the sign of the z-axis. Therefore, without loss of generality, we limit the fit to $\phi_\delta \in [0°, 60°]$ and $\phi_B \in [0°, 360°]$, as it was discussed in Fig. 4.12(b). In contrast to ϕ_δ (see Fig. 4.8(a)), we note that ϕ_B can have little observable effect on the PL at base temperature but plays a more significant role at intermediate temperature (compare Fig. 4.12(b) and Fig. 4.13(b)). This results in unreliable fit results for ϕ_B in our calibration approach. A better approach was to include also *PL vs. B* measurements at intermediate temperature. Unfortunately, in these measurements, we typically found some point-to-point variations and lower quantitative reproducibility compared to base temperature. This might be due to an increased influence of the magnetic field misalignment or simply due to increased setup instability. Note that the existence of an observable effect of ϕ_B, to begin with, results from an unintended field misalignment θ_B, which was experimentally unavoidable.

		NV-1	NV-2	NV-3	NV-4	
Strain						
$\delta_\perp$	ES in-plane strain (GHz)	31.8	39.9	8.7	80.2	*a*
ϕ_δ	ES in-plane strain angle	39.9°	24.4°	0.8°	59.9°	*a*
Magnetic bias field						
θ_B	mag. field misalignment angle	1.7°	1.9°	1.8°	2.2°	*a*
ϕ_B	mag. field in-plane angle	244.0°	17.6°	106.5°	130.6°	*a*
ϕ_B	cooldown #1	256.2°	194.2°			*a*
Rates						
k_r	opt. emission rate (µs^{-1})	55.1	55.7	45.3	40.5	*a*
$k_{E_{12}}$	ISC rate from $E_{1,2}$ (µs^{-1})	112.4	98.7	101.3	90.7	*a*
k_{A_1}	ISC rate from A_1 (µs^{-1})	$k_{E_{12}}/0.52$ [92]				*d*
$k_{E_{xy}}$	ISC rate from $E_{x,y}$ (µs^{-1})	9.1	8.2	8.6	7.5	*a*
r_β	opt. exc. branching ratio	1				*c*
r_S	SS branching ratio	1.36	2.26	1.44	1.15	*a*
$\tau_{S,0}$	SS decay time at $T = 0\,\mathrm{K}$ (ns)	342(2)	320(3)	292(4)	318(3)	*c*
ΔE	SS emitted phonon energy (meV)	16.6 [86]				*d*
Electron-phonon interaction						
η	ES coupling strength (µs^{-1} meV^{-3})	197	176	268	249	*a*
Ω	phonon cutoff energy (meV)	168				*d*
Setup						
b	background (kcps mW^{-1})	40.8	27.5	52.6	34.7	*b*
R	collection/excit. eff. (kcps mW µs)	67.1	88.4	112.1	178.3	*b*
A	opt. alignment (W^{-1})	245.1	136.2	282.3	188.1	*b*
τ_R	laser rise time (ns)	23				*c*

Table 6.3: Calibration results per NV center. The model parameters were introduced in Tab. 4.1. We fit the NV center intrinsic parameters individually for each center since they are known to vary between NV centers [1]. Fig. 6.5 presents the fit results for setup-related parameters of *saturation* and *time-resolved pulsed ODMR* measurements of the same single simultaneous fit as the respective NV column above. However, the setup-related parameters of the base-temperature *PL vs. B* measurements are provided above. For the laser power *P* and the sequence timings in *time-resolved pulsed ODMRs* we use the values that were set in the respective experiment. The last column specifies the type of parameter as discussed in Sec. 6.4.1: *a*: *robust*, *b*: *environment-sensitive*, *c*: pre-determined, and *d* literature parameters. Errors cannot be given as discussed in Sec. 6.4.3.

Our fit results for the SS branching ratio r_S lie in the broad range of values reported in literature [86, 96, 100, 102, 108] from below 1 to above 10. For a comparison, see Ref. [35, SM], where we converted r_S values of the seven-level-system convention to the five-level system definition in our Eq. 4.18. Theoretical considerations suggest [34] a high $r_S \approx 6$. The effect on the observable spin contrast of $r_S \gg 1$ is similar to the effect of ISC rates $k_{E_{12}}, k_{A_1} \gg k_{E_{\text{xy}}}$: both relations describe reinitialization channels of $m_{\text{S}} = 0$ under optical excitation (see Fig. 4.2(d)). Regarding the latter relation of the ISC rates, a similar spread and potential inconsistency in literature values can be found: while low-temperature studies that employ low-energy resonant laser excitation typically find $k_{E_{\text{xy}}} \approx 0$ [92, 99, 100], experiments with off-resonant green laser excitation typically find values similar to ours (independent of the temperature) [86, 95, 96, 102]. In a very recent study, Monge *et al.* [132] present a direct comparison between off-resonant green and resonant red excitation under comparable conditions. Therein, spin state reinitialization times as typically found with high $k_{E_{\text{xy}}}$ can be witnessed with green excitation, while low-power resonant excitation gives $k_{E_{\text{xy}}} \approx 0$. Another recent experimental study by Wirtitsch *et al.* [108] suggests that this difference might be due to rapid charge state switching. At very low green laser power ($\beta \ll 1$), this switching rate is known to grow quadratically with power and should reach a similar order of magnitude as $k_{E_{\text{xy}}}$ as the power reaches around half saturation [124, 133]. The mechanisms behind this ionization (NV^- GS → NV^- ES → NV^0 GS) and recombination (NV^0 GS → NV^0 ES → NV^- GS) are two-photon processes. But Wirtitsch *et al.* also report on channels from NV^0 ES to the NV^- SS (and in a second step even back to the NV^- ES), which were not anticipated so far [95, 124, 126]. Since a switch of the charge state results in a loss of the spin state [125], rapid charge state switching might be an explanation for misinterpreted low values of r_S and high values of $k_{E_{\text{xy}}}$ so far. The systematic investigation of the role of NV^0 in the spin polarization cycle is further complicated by the fact that the ionization and recombination rates depend on the individual environment around the NV center, which becomes particularly prominent for shallow NV centers as discussed in this thesis [56, 57].

Concerning the in-plane strain direction ϕ_δ, we saw in Fig. 4.8(a) a strong influence on the low-temperature performance at elevated strain. The determination of ϕ_δ through spin mixing, as effectively done in our calibration, is rather indirect and could have significant cross-correlation with rate parameters in the fit since they can yield similar spin-mixing dynamics in *time-resolved pulsed ODMRs*. One could find the strain direction at base temperature independently by turning the linear polarization of the green laser and determining the ES LAC dip depth (of E_x and E_y in *PL vs. B* measurements) versus polarization angle [41, 95]. This was discussed conceptually in Fig. 4.16. Another approach at room temperature for elevated strain values could be the one presented in Fig. 5.2(c).

6.5 Comparison of simulations with data

From the calibration process described above, we obtain all quantities needed to model the PL and contrast of each NV center in dependence on temperature, magnetic field, and strain. When performing these simulations, we fix the *environment-sensitive*

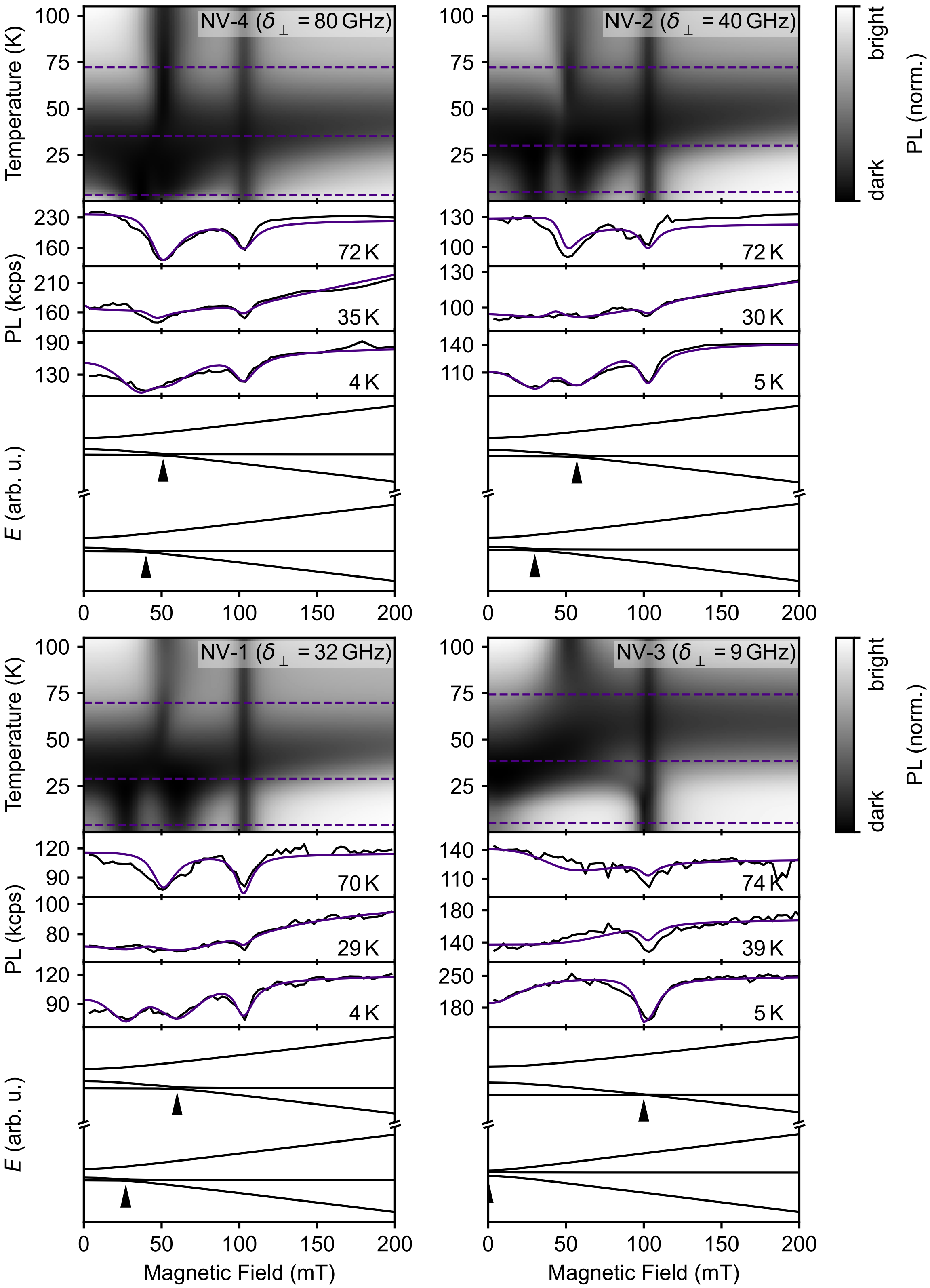

Figure 6.6: Experimental and simulated steady-state PL as a function of temperature and magnetic field. Shown for each NV-4, NV-2, NV-1, and NV-3 are a simulation based on the calibration (top panel), measurements with fits (three middle panels), and ES level structures (bottom panel). The PL is strongly reduced at the ES LACs (triangle symbols) and the GS LAC (103 mT). The temperatures of the fits in the panels below are indicated by dashed lines in the top panel. The PL is normalized for each map individually.

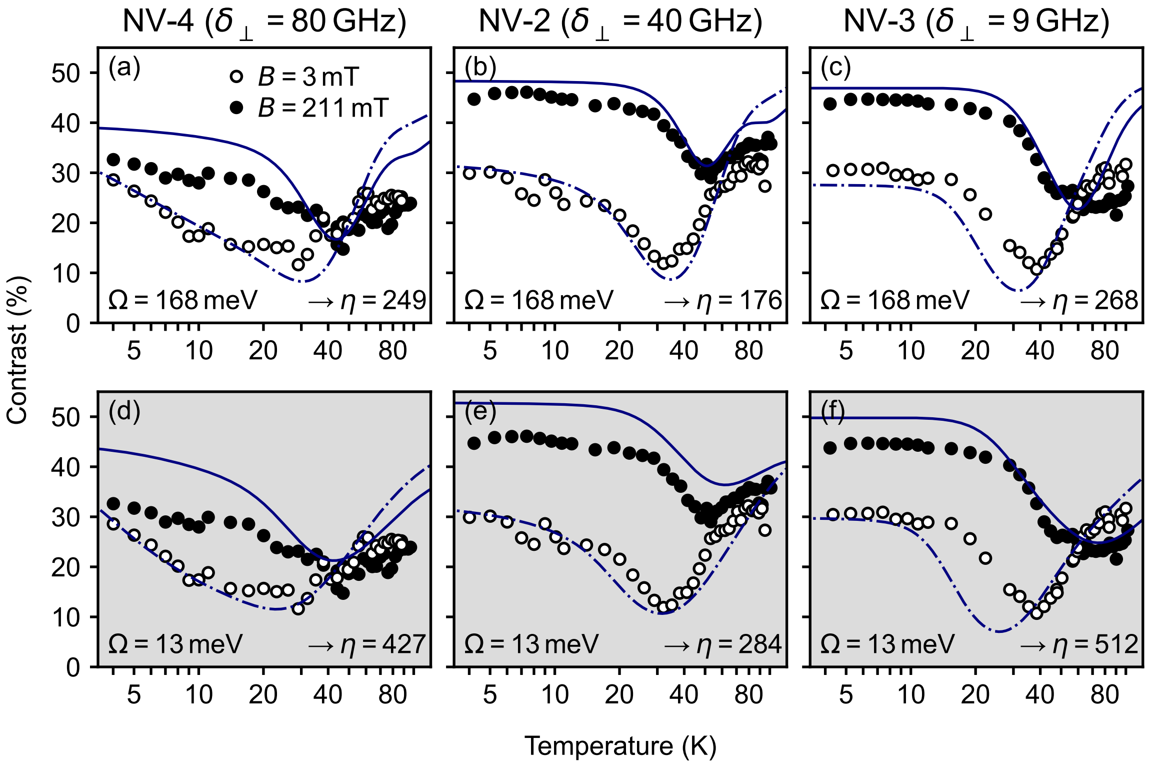

Figure 6.7: Experimental and simulated spin contrast as a function of temperature and magnetic field. (a–c) Contrast as a function of temperature for different strain values $\delta_\perp$. Empty (filled) circles are measurements taken at $\sim 3\,\mathrm{mT}$ ($\sim 200\,\mathrm{mT}$), and blue dashed (solid) traces show the corresponding simulations after the calibration (see text). As an example, for NV-2, the corresponding *time-resolved pulsed ODMR* data and calibration (fit results at base temperature) were shown in Fig. 6.1. (d–f) Comparison to the same evaluation with different cut-off energy Ω. Above, $\Omega = 168\,\mathrm{meV}$ is used, as given in Tab. 4.1. Here, $\Omega = 13.4\,\mathrm{meV}$ [110] is used and yields significantly higher fit results for η (printed values are in units $\mu\mathrm{s}^{-1}\,\mathrm{meV}^{-3}$).

parameters to values obtained at base temperature. For PL(T, B) maps, these are the values given at the bottom of Tab. 6.3. For contrast simulations, we use the lowest-temperature values in Fig. 6.5 at the respective magnetic field. Based on this set of parameters, we extend the simulation of PL and contrast to all temperatures. In this section, we will compare our measurements first to such simulations of PL, and second to such simulations of contrast.

First, for PL(T, B) simulations, this process results in the maps shown in Fig. 6.6(top panels). We compare linecuts of these simulations with *PL vs. B* measurements at select temperatures, covering all three regimes (I–III) of Fig. 4.5(h). For the comparison with the calibrated model in Fig. 6.6(middle panels), we only refit the *environment-sensitive* parameters b and R. This has approximately the same effect as defining a scaling and an offset on our PL data and thus corrects for setup drifts. We use the ϕ_δ values for cooldown #1 in Tab. 6.3 here. A good agreement between measurement and fits is found for all NV centers. We note that when comparing the similarly-strained NV-1 and NV-2, a small revival feature (see discussion in Ch. 4.4.5) is predicted around 50 mT and intermediate temperature for NV-2. However, we were unable to validate or resolve it in the measurements, likely due to a combination of remanent field effects, drift in setup parameters during the magnetic field sweep, and pulse-tube vibration noise limiting our resolution of PL. We assumed the same magnetic field alignment for all measurements, which means that we exclusively used the magnetic field orientation from the calibration fit. However, some drift and/or hysteresis of the vector magnet becomes apparent from the mismatch between data and fit in the width of the dips at the GS LAC at 103 mT in Fig. 6.6(bottom panels).

Second, to compare measurements and simulations of contrast versus temperature, we simulate and evaluate *time-resolved pulsed ODMR* sequences at the desired temperatures. In Fig. 2.2(d), we presented a good match between our simulation and the measured data - despite the fact that the simulation uses fixed *environment-sensitive* parameters. At the same time, we had significant variations of these parameters in the calibration fit at different temperatures in Fig. 6.5. This emphasizes the great stability of contrast measurements against setup drifts. The traces presented in Fig. 2.2(d) were limited to low magnetic field ($\sim 3\,\mathrm{mT}$) and NV centers with medium strain (NV-1, NV-2, NV-5). In Fig. 6.7(a–c) we present the spin contrast for NV centers with high (NV-4, $\delta_\perp = 80\,\mathrm{GHz}$), medium (NV-2, $\delta_\perp = 40\,\mathrm{GHz}$), and low (NV-3, $\delta_\perp = 9\,\mathrm{GHz}$) intrinsic strain within our accessible range. We investigate the contrast at both low and high ($\sim 200\,\mathrm{mT}$) magnetic field. All curves show the same qualitative behavior: a dip in performance at intermediate temperatures. Apart from that, the most prominent feature is a decrease in the spin contrast with increasing strain $\delta_\perp$ already below 10 K. This is in good agreement with the importance of the one-phonon process at high $\delta_\perp$ as theoretically addressed in Fig. 4.8(b,c). The small kink around 90 K in the simulation of the high magnetic field trace for NV-2 originates from a smeared-out revival feature as explained in Ch. 4.4.5. The same kink is not visible in Fig. 6.6 for NV-2 since a different ϕ_B is used there. Also here, the data does not allow us to prove or disprove the existence of such revivals. Generally, towards higher measurement temperatures ($> 60\,\mathrm{K}$), we increasingly find thermal drifts, which we stabilize by frequent optical tracking. Despite our efforts, one can observe that the contrast values measured in the high-temperature limit are systematically lower than the simulated model. We attribute this to increased setup instabilities and possibly some uncertainty in the measured temperature, caused by the large temperature gradient between the sample and the rest of the HIMBI cryostat.

The uncertainty in our high-temperature data raises the question of to what degree our measured data can confirm the phonon model that we used. A detailed discussion of the usage of our model as a novel tool to investigate the nature of contributing phonon modes was given in Ch. 5.3. There, it was concluded that a much lower value of $\Omega = 13.4\,\mathrm{meV}$, as found by Plakhotnik *et al.* [110], is in conflict with our and other experimental findings. To investigate the effect of such a low cut-off energy, we use the value of $\Omega = 13.4\,\mathrm{meV}$ in our model and repeat the calibration of Sec. 6.4.2. As expected, it significantly alters the model, yielding higher fit results of η (NV-2: $284\,\mathrm{\mu s^{-1}\,meV^{-3}}$, NV-3: $512\,\mathrm{\mu s^{-1}\,meV^{-3}}$, NV-4: $427\,\mathrm{\mu s^{-1}\,meV^{-3}}$) and a slower recovery towards room temperature. Comparing the resulting simulations in Fig. 6.7(d–f) with the previous results above, we find that using $\Omega = 168\,\mathrm{meV}$ yields better results at low temperatures, while $\Omega = 13.4\,\mathrm{meV}$ matches the high-temperature data slightly better due to the slower recovery. Thus, presumably due to the setup instabilities and uncertainty in temperature calibration at high temperatures in HIMBI, the data presented here does not allow us to rule out either of the models definitely. But the fitted coupling constant η only agrees well with other literature

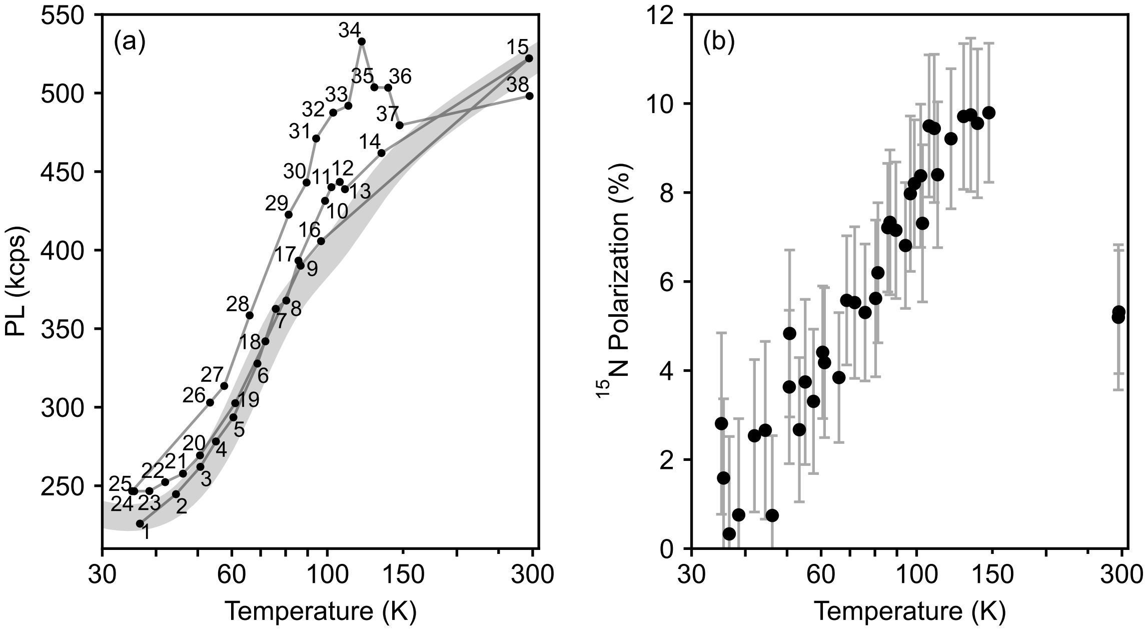

Figure 6.8: Temperature dependence of the PL and ^{15}N nuclear spin polarization. (a) Steady-state PL as a function of temperature measured on NV-5. The numbers indicate the order in which the measurements were recorded, demonstrating the reproducibility found in the VarTMa setup. The broad trace in the background is a simulation with parameters from Tab. 4.1 adjusted to the findings of $B = 4.3\,\mathrm{mT}$ and $\theta_B = 13^\circ$ at low temperature in Fig. 3.9(c,d). To compensate for the non-calibrated setup parameters, R was multiplied by 4 and b by 2. (b) ^{15}N nuclear spin polarization extracted from the relative depth of the hyperfine resonances as shown in Fig. 2.2(b).

when $\Omega \gg 13.4\,\mathrm{meV}$. For future experiments, we expect a more stable contrast versus temperature measurement in the range 80 K to 150 K and a correct phonon spectrum beyond the Debye model (see discussion in Ch. 4.3.4) to give valuable insight into the contributing phonon modes.

To conclude, there is one more type of simulation/fit presented in this thesis: for the explicit comparison of *time-resolved pulsed ODMR* measurements and simulations presented in Fig. 2.2(c) we used the parameters of the calibration and only (re-) fitted the *environment-sensitive* parameters of the time-resolved pulsed ODMR traces together with their respective *saturation* measurement (with shared b and R and individual A, as done in the calibration in Sec. 6.4.2).

6.6 Further results

In this section, we will briefly present further observations in the data set taken on NV-5 in VarTMa. First, Fig. 6.8(a) shows a temperature-dependent plot of the measured steady-state PL. While Happacher *et al.* [37] presented the observation of the temperature dependence of the photo-physics via such PL measurements, we mainly employed the contrast measurements presented in this chapter above [36]. But the NV-5 data set shows a stability sufficient to compare the measured PL with a (non-calibrated) simulation and yields a relatively good agreement without any fitting.

Second, the well-resolved hyperfine resonances as shown in Fig. 2.2(b) allow to extract the polarization of the NV's nuclear spin. Plotted in Fig. 6.8(b) is the ^{15}N polarization determined from the contrast as in Ref. [134]. The observed decrease toward cryogenic temperature is in line with previous literature [134, 135] and was also observed in measurements on HIMBI (not shown here). Focusing on the finite room-temperature value first, the origin of the polarization of the nuclear spin is a flip-flop process, which transfers polarization from the continuously polarized electron spin (by laser illumination) to the nuclear spin. This process is most efficient around the room-temperature ES LAC, due to a matching of the level spacings. But the influence extends even to low fields as used here ($\sim 4\,\mathrm{mT}$). Compared to the results in this previous work, the polarization values in Fig. 6.8(b) are actually lower. Possible explanations for this might be a reduction by a misaligned magnetic field (see Fig. 3.9(d)), the fact that our laser excitation might not be long enough to saturate the polarization transfer [135], and the different nitrogen isotope [136].

As explained by Fischer *et al.* [134], the decrease and loss of a nuclear polarization with decreasing temperature originates from a vanishing of the averaged ES structure (and with it its ES LAC, as we simulated *e.g.* in Fig. 4.10). The low-temperature ES structure might have suitable LACs again, but no revival of the polarization was found experimentally. Probably, this is caused by the spin mixing in the ES, which reduces the polarization and thus gives the same effect as a strong field misalignment at room temperature, where little nuclear polarization is achieved [135].

CHAPTER 7

Examination of spin initialization and readout schemes

Parts of the text and figures in this chapter were published in Ref. [36]. They were extended for this thesis. Additionally, this chapter covers two semester projects which I supervised. First, Ch. 7.3 presents measurements conducted by Leo Šutevski on a room-temperature setup in our group. Second, Ch. 7.3 presents measurements conducted by Tobias Hächler on a QSM setup at QZabre LLC. Martin Stecher from QZabre LLC supported Tobias Hächler in early-stage measurements and simulations with the model from chapter 4. All simulations shown in this chapter were done by me with the model from chapter 4. I conceived the experiments, but several members of the group provided important input or technical support — mainly Konstantin Herb, Erika Janitz, Laura Alicia Voelker, and the QZabre LLC team.

Most spin initialization and readout schemes rely on a low spin-flip probability per optical cycle and are thus affected by the spin-lattice relaxation in the ES during laser excitation. Consequently, both the spin initialization and readout fidelities (and thus the SNR) are strongly temperature-dependent across the three regimes (I–III) discussed earlier in Fig. 4.5(h). With the novel simulation tool that covers the full temperature range at hand, a comprehensive insight into the off-resonant spin initialization and readout can be given in this chapter. Above, we discussed the effects of laser polarization and magnetic and electric fields/strain in Ch. 4.4. Here, we examine the dependence on the laser power and pulse sequence. We will first examine the established single-power initialization and readout scheme (see Fig. 2.2(a)) in Sec. 7.1 and briefly extend the discussion to other existing schemes in Sec. 7.2. This will allow us to investigate improvements to the established scheme in Secs. 7.3 and 7.4. In both simulations and experiments, a higher sensitivity is found for the improved schemes. At the same time, heating by the deposited laser power is significantly reduced. The latter can be crucial in applications with photo-sensitive samples as they occur *e.g.* in bio-sensing [137, 138], or in experiments requiring a low thermal load, such as those at very low temperatures [10]. Further, a reduced laser exposure can be beneficial in avoiding photobleaching of NV centers [139] during long experiments or in environments where a fluorescent background can build up (laser-induced contamination) [140].

It shall be noted that in this chapter, we continue to neglect NV center charge state dynamics, which can become significant at high laser power [108, 124]. These dynamics, which can differ significantly between different NV centers, might alter

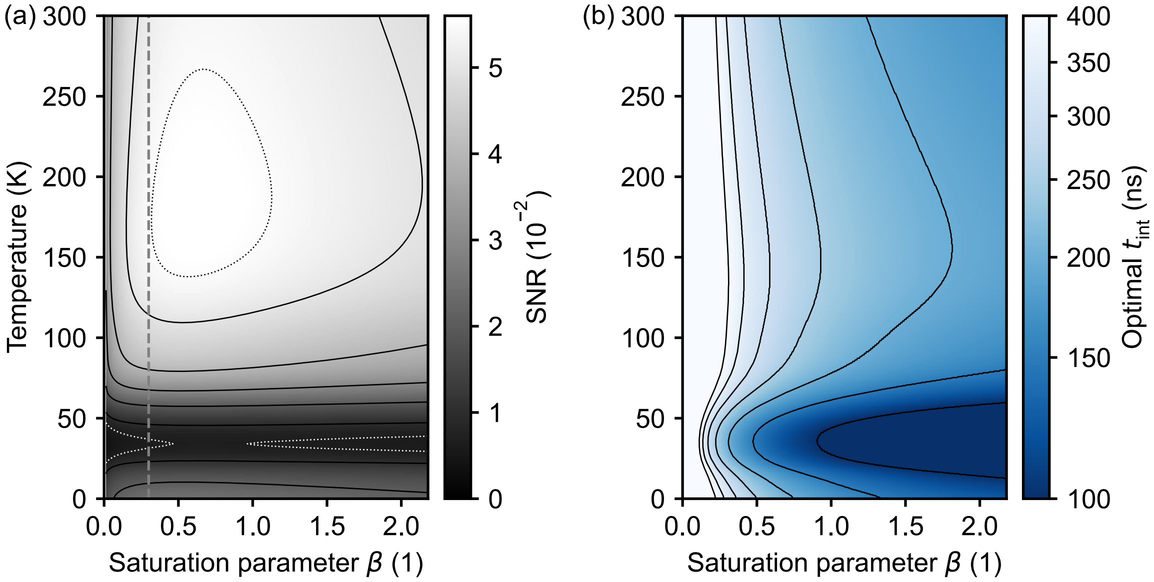

Figure 7.1: Influence of the laser power on the SNR. (a) Simulated SNR as a function of temperature and laser excitation. To convert the saturation parameter β to the laser power P, see Eq. 4.13. The established single-power sequence from Fig. 2.2(a) is used, which has identical laser power for the initialization and readout. The dashed line at $\beta = 0.3$ corresponds to Fig. 4.5(h). Optimal SNR is found at $\beta \approx 0.7$ across all temperatures. (b) The optimal integration time t_{int} used in part (a). The contour lines correspond to the color bar labels, except for the first and last (dotted, at $\text{SNR} = 0.65 \times 10^{-2}$ and 5.5×10^{-2}) in part (a). The parameters from Tab. 4.1 are used, which have a rather high linear background b, contributing to the disadvantage of too-high laser power.

the picture presented here and favor the usage of lower laser power in the readout. A discussion of the meaning of these dynamics in the context of the work presented in this thesis was given in Ch. 6.4.4. However, as our NV centers and thus model parameters have a relatively high background compared to NV centers in the bulk, a high laser power is anyway disadvantageous, and the effects of considering the charge state are therefore expected to be of reduced importance.

7.1 Laser power dependence of spin initialization and readout

Before discussing the initialization and readout separately, we evaluate the laser power and temperature dependence of the SNR, a combined effect of both processes (Fig. 7.1). In the established single-power scheme from Fig. 2.2(a), the spin initialization and readout happen within the same laser pulse and, therefore, also at the same laser power. Around the optimum, the SNR is a flat function of the laser power at all temperatures. The same accounts for the optimal integration time t_{int}. Note that shorter integration times yield higher spin contrast values but less collected photon counts. The optimum is a trade-off of the $\sqrt{\text{PL}}$ growth and drop of spin contrast C with increasing t_{int}, as discussed in Ch. 2.3.

7.1.1 Spin initialization fidelity

We start by considering the spin initialization. We will use the total probability of $m_\mathrm{S} = 0$ in the NV$^-$ GS and ES system (introduced as $\langle m_\mathrm{S} = 0\rangle$ in Ch. 2.2) as a measure for the spin initialization fidelity. A simulation of the initialization fidelity at three different laser powers and for temperatures ranging from 3 K to 300 K is shown in Fig. 7.2(b). Two separate sources of spin polarization (spin selective channels) can be identified: (i) the branching ratio of the SS decay r_S and (ii) the spin-selective ISC rates $k_{E_{12}}$ and k_{A_1} versus $k_{E_{xy}}$.

Addressing (i) first, the statistical initialization fidelity into the GS $m_\mathrm{S} = 0$ after the decay of the SS is given by the probability $p_{\mathrm{SS}\to 0}$ as

$$\text{SS limit: } p_{\mathrm{SS}\to 0} = (1 + 1/r_S)^{-1} = \langle m_\mathrm{S} = 0\rangle|_{\beta\to\infty} \,. \tag{7.1}$$

As stated in the last step of Eq. 7.1, $p_{\mathrm{SS}\to 0}$ constitutes the initialization limit under high optical excitation rates βk_r (see Eq. 4.13). The higher the saturation parameter β, the higher the population P_SS that is trapped in the long-lived SS before the initialization pulse ends (see Fig. 2.2(a) between 1 µs to 2 µs and Ref. [87]). The steady-state value of P_SS is plotted in Fig. 7.2(a) as a function of temperature in the limit of high laser power. In this limit, $P_\mathrm{GS} \to 0$ and $P_\mathrm{ES} = 1 - P_\mathrm{SS}$. Therefore,

$$\dot{P}_\mathrm{SS}(t) = -\frac{1}{\tau_S(T)} P_\mathrm{SS}(t) + \overline{k}_\mathrm{ISC}\,(1 - P_\mathrm{SS}(t)) \tag{7.2}$$

with the effective mean ISC rate $\overline{k}_\mathrm{ISC}$ over all ES populations. Eq. 7.2 yields a steady-state value of

$$P_\mathrm{SS} = \left(1 + 1/\left(\tau_S(T)\,\overline{k}_\mathrm{ISC}\right)\right)^{-1} \,. \tag{7.3}$$

The drop of P_SS in Fig. 7.2(a) with increasing temperature is due to the change in the SSL $\tau_S(T)$ (see Eq. 4.19). This is demonstrated by the dotted trace, which is generated from Eq. 7.3 for a fixed value of $\overline{k}_\mathrm{ISC}$ that was found without spin relaxation (*i.e.* at high temperature). The deviation from the dotted trace at low temperatures originates from the spin relaxation in the ES, which is dominated by spin state mixing at base temperature and spin-lattice relaxation at intermediate temperature (see Ch. 4.4.1). As can be seen in Fig. 7.2(b), the initialization fidelity approaches the limit from Eq. 7.1 with increasing laser power (saturation parameter β). But especially at elevated temperatures, it does not reach this limit since there is a significant ES steady-state population in Fig. 7.2(a).

The second (ii) source of spin polarization is the selectivity of the ISC rates. We now add the effect of the ISC to the SS decay from (i) above. For most rates reported in the literature (including our rates in Tab. 4.1), the ISC has a higher spin selectivity than the SS decay. Therefore, the decay of the ES (*i.e.* the ISC process) dominates the upper limit of the spin initialization fidelity. This upper limit is reached at lower laser power. To investigate the upper limit of the spin initialization fidelity, we thus assume that laser excitation events are so rare that all populations can relax to the GS between them. This minimizes the effect of the lower spin selectivity of the SS decay. For a single decay from the ES to the GS, the probabilities that a spin flip

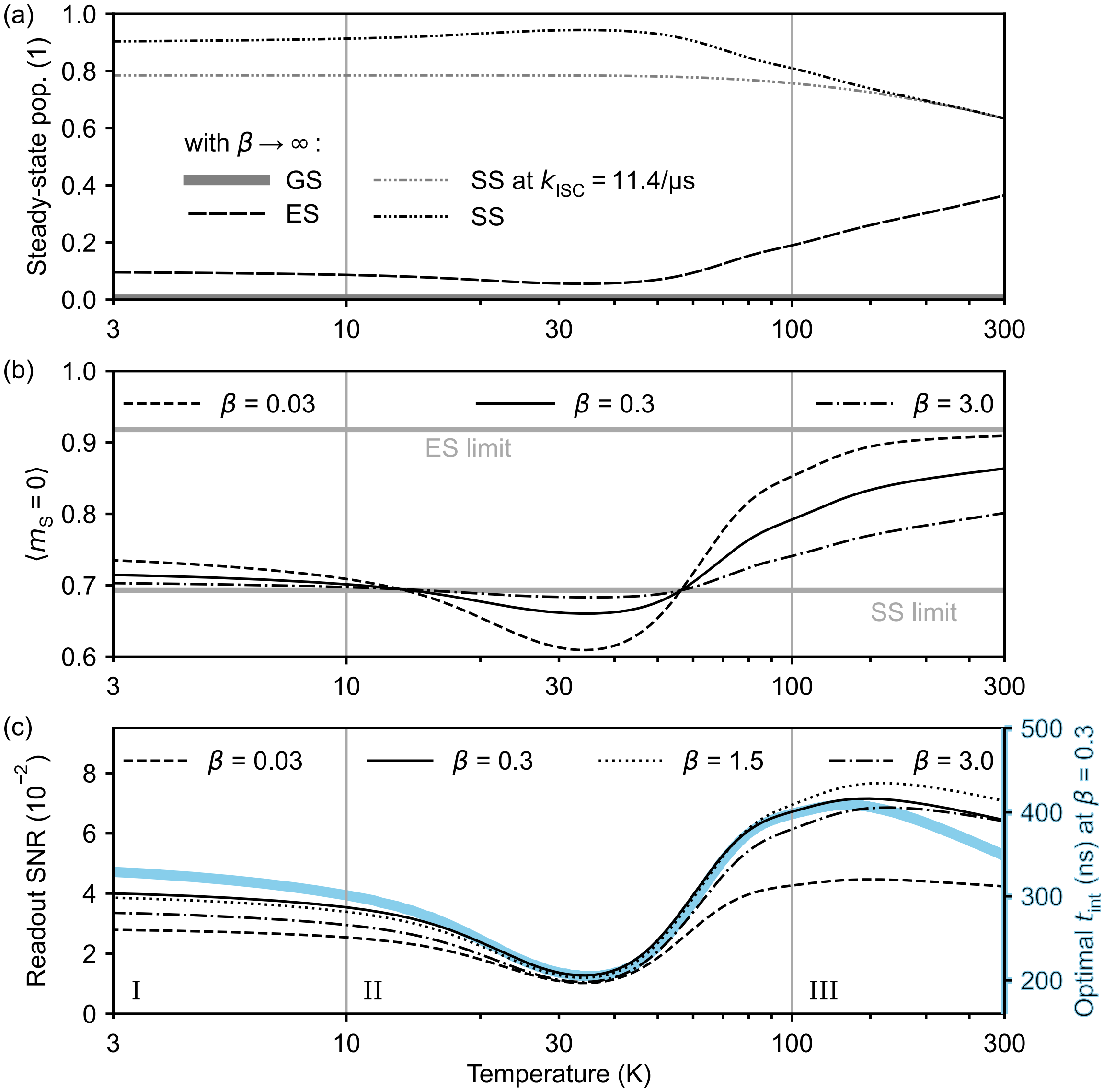

Figure 7.2: Laser power dependence of initialization and readout fidelities. (a) To understand the temperature dependence of the initialization fidelity in the high laser power limit ($\beta \to \infty$), the simulated steady-state population of the SS P_{SS} is plotted. (b) Simulated spin initialization fidelity after a long laser pulse followed by a long waiting time (see Fig. 2.2(a)) at different laser powers β. $\beta = 0.3$ corresponds to the laser power $P = 2.34$ mW in Tab. 4.1 (note the comparatively low optical alignment A there). When spin relaxation is maximal (around 35 K), increasing the laser power is beneficial, approaching the "SS limit" related to the SS branching ratio r_S (lower horizontal gray line, see Eq. 7.1). Outside this regime (II), the opposite behavior occurs: decreasing the laser power is beneficial for the initialization fidelity. Its fundamental "ES limit" is related to the selectivity of the ISC rates (upper horizontal gray line, see Eq. 7.6). (c) Simulated readout fidelity, depicted as the SNR for which we assumed an initialization of $\langle m_S = 0 \rangle = 1$. As always above, the integration time t_{int} (see Fig. 2.1(a)) of the readout is optimized for each temperature and the given β. Note the increase of the optimal laser power to $\beta \approx 1.5$ compared to $\beta \approx 0.6$ of the single-power scheme in Fig. 7.1(a). The resulting optimal t_{int} (blue) follows the same trend as the readout SNR. For the entire figure, the parameters from Tab. 4.1 are used.

occurs are

$$p_{\pm1\to0} = p_{\mathrm{SS}\to0}\,\frac{\overline{k}_{m_{\mathrm{S}}=\pm1}}{\overline{k}_{m_{\mathrm{S}}=\pm1}+k_r}\,, \tag{7.4}$$

$$p_{0\to\pm1} = \left(1-p_{\mathrm{SS}\to0}\right)\frac{k_{E_{\mathrm{xy}}}}{k_{E_{\mathrm{xy}}}+k_r}\,. \tag{7.5}$$

With the same rate approach as used in Eq. 7.2, we then find for the steady state an initialization fidelity of [108]

$$\text{ES limit:}\quad \langle m_{\mathrm{S}}=0\rangle|_{\beta\to0} = \left(1+1/r_S\cdot\frac{k_{E_{\mathrm{xy}}}/\left(k_{E_{\mathrm{xy}}}+k_r\right)}{\overline{k}_{m_{\mathrm{S}}=\pm1}/\left(\overline{k}_{m_{\mathrm{S}}=\pm1}+k_r\right)}\right)^{-1}\,. \tag{7.6}$$

Eq. 7.6 constitutes the upper limit of the achievable initialization fidelity and is reached for a laser power much lower than saturation and respectively long initialization time until a steady state is reached. However, this limit can also only be reached if there is no mechanism of spin relaxation, which is the case in our simulation at elevated temperatures in regime (III) and at base temperature in regime (I) if there is little spin mixing (see Fig. 4.12(a)). In Fig. 7.2(b), one can see that for our medium strain from Tab. 4.1, this limit is only reached at room temperature in regime (III).

The power dependence of the initialization fidelity is reversed in part of the intermediate temperature regime (II). Here, a conceptual switch happens: the spin-lattice relaxation within the ES lifetime is so high that the spin selectivity of the SS decay (temperature independent) becomes the best source of spin polarization within the optical cycle. Consequently, the SS limit (Eq. 7.1) is the upper rather than the lower bound of the initialization fidelity, and higher laser power benefits the initialization. This is in stark contrast to the situation in regimes (I) and (III), where a lower laser power improves the initialization [108]. At the switching points (specifically 13 K and 56 K for the parameters in Fig. 7.2(b)), the spin selectivity of the SS decay equals the spin-lattice relaxation within the ES lifetime. Thus, the laser power cannot improve the situation, and the initialization fidelity becomes independent of the laser power.

7.1.2 Spin readout fidelity

Next, the laser power dependence of the readout is discussed. We use the SNR as elsewhere in this thesis (Eq. 2.8 in *e.g.* Fig. 7.1) and remove the effect of the initialization fidelity by setting it to $\langle m_{\mathrm{S}}=0\rangle = 1$ before the readout (and π pulse). The resulting “readout SNR” is used to quantify the readout fidelity. The temperature dependence of this readout fidelity is shown from 3 K to 300 K in Fig. 7.2(c). In contrast to the initialization fidelity, the readout fidelity shows the same qualitative behavior as a function of laser power at all temperatures: higher laser power yields better readout fidelity, but only if there is no background b in Eq. 4.38. In such a hypothetical case of $b=0$, the readout fidelity shows a saturation-like behavior, and optimal integration times t_{int} at high laser powers are short. This behavior can be understood from the mechanism of spin contrast generation: the more optical cycles a $m_{\mathrm{S}}=0$ state can do while a $m_{\mathrm{S}}=\pm1$ state is trapped in the SS, the higher the SNR.

In practice, with a background $b > 0$ growing linearly with the laser power, there is an optimal power for the readout fidelity, similar to the overall SNR in Fig. 7.1(a) before. Compared to Fig. 7.1(a), the optimal readout power grows mildly when artificially increasing the initialization fidelity. However, the readout fidelity still shows a similar optimal power and t_{int} compared to the overall SNR. This is because the readout fidelity has a weak dependence on the power at the optimum and because the reduction in the readout fidelity typically dominates the temperature dependence of the overall SNR. For the parameters used here, Fig. 7.2(c) shows a drop of $\sim 70\,\%$ in the readout fidelity at the relaxation maximum compared to the low-temperature limit. Conversely, the initialization fidelity is only reduced by $\sim 15\,\%$ in Fig. 7.2(b, $\beta = 0.3$), when put in relation to $\langle m_{\mathrm{S}} = 0 \rangle = 1/3$ in thermal equilibrium.

In summary, with the established initialization and readout scheme of a single off-resonant laser pulse and for established SS and ISC rates, we find: In temperature regime (II), which is newly addressed in this thesis, the SNR is significantly reduced, and the best values are achieved with relatively high laser powers. In the experimentally prominent regimes (I) and (III), in contrast, the established single-power scheme does not yield the best performance since the optimal laser power for the spin readout is relatively high while it is low for the initialization. The next sections will present ways to avoid this trade-off. Before that, a brief review of other initialization and readout schemes will be given.

7.2 Implications of ES spin relaxation for other schemes

So far, we have only discussed off-resonant spin initialization and readout schemes. At low temperatures ($T \lesssim 40\,\mathrm{K}$ [41]), where the spectral lines are sufficiently narrow and stable [121], resonant excitation is possible. By resonant optical pumping, the dominant spin-flip mechanisms in the optical initialization cycle become irrelevant, and a higher $\langle m_{\mathrm{S}} = 0 \rangle$ initialization fidelity of $> 99\,\%$ [8] is achieved. Here, spin mixing in the ES is even beneficial for the duration of the initialization. However, resonant single-shot readout will still suffer from the spin relaxation in the ES [8]. Only the resonant spin-to-charge conversion scheme by Irber *et al.* [9] should be able to avoid destructive effects during spin-state readout largely. Other readout schemes based on spin-to-charge conversion [6, 7, 141], which are available at all temperatures, will equally suffer from the spin relaxation process in the ES.

We also briefly address the implications for the charge state preparation of the NV center. The initialization of the NV^- charge state is typically achieved automatically during the green laser illumination [124] (as in Fig. 2.2(a)). The temperature-dependent relaxation of the spin in the ES of the NV^- is expected to have a small influence on the initialization of the NV^- charge state: previous studies have found spin-dependent ionization rates from the ES [6, 141] and from the SS [95, 126, 142] of the NV^- to the neutral charge state NV^0 under green laser illumination. Since spin relaxation reduces the $m_{\mathrm{S}} = 0$ population, a temperature-dependent ionization rate to NV^0 is expected and was recently observed experimentally by Blakley *et al.* [38]. We neglected this small effect in our model.

7.3 Improved spin initialization by a second laser power

As discussed in Sec. 7.1, at room temperature, a higher spin initialization fidelity is expected for low laser power [108]. At the same time, high laser power is beneficial for the readout at all temperatures, only limited by the background PL (b parameter) or potential switching to NV^0. Therefore, an improved SNR could be achieved if different laser powers were used for the spin initialization and readout. We will now investigate this prediction by experimentally testing a pulse sequence with separate laser powers for the initialization and the readout. The pulse sequence is presented in Fig. 7.3(a). The experiments are carried out on a QZabre LLC tip (NV-6) as shown in Fig. 2.1(c) on a home-built setup at ambient conditions (same as in Ref. [113]). We use two fiber-coupled laser diodes and a fiber coupler to generate the composite laser pulses (same laser design as used for NV-1 to NV-4), since a power switching of our home-built lasers [72] cannot be done on the microsecond timescale. A fixed pulse sequence (*i.e.* fixed time intervals) with a sufficiently long duration is used to avoid complex cross-talk, similar to the discussion around the conventional single-power pulse scheme in Fig. 2.2(a). As can be seen in Fig. 7.3(a), we use a duration $t_{\mathrm{read}} = 0.9\,\mu\mathrm{s}$ for the readout laser (to be able to cover all potential t_{int} in post-processing) and $t_{\mathrm{init}} = 2\,\mu\mathrm{s}$ for the initialization laser. The power of both lasers is swept, and pulsed ODMRs are recorded. In Fig. 7.3(b), we compare these measurements by looking at the SNR (see Eq. 2.8), where the integration time t_{int} is optimized in post-processing. For example, the integration time at the point identified as the approximate optimum in Fig. 7.3(b) is the filled area in Fig. 7.3(a) and found to be $t_{\mathrm{int}} = 230\,\mathrm{ns}$.

Indeed, a better SNR is achieved experimentally when the readout laser power is relatively high and the initialization laser power is relatively low. To obtain a quantitative measure for the improvement over the established single-power scheme from Fig. 2.2(a), we proceed as follows: For each point in Fig. 7.3(b), we determine the steady-state PL during the readout and the initialization, as marked by horizontal lines in the example in Fig. 7.3(a). For each initialization power, we then find the corresponding readout power that yields equal steady-state PL values. The respective points are marked by crosses in Fig. 7.3(b). A line-fit is also shown, and the plots aspect-ratio is then scaled such that this line is diagonal. From the resulting aspect ratio, one can infer that the readout laser yields a $\sim 10\,\%$ higher maximal NV center excitation than the initialization laser (at a factor ~ 2 higher nominal power). This is, for example, due to their different optical paths. For the same reason, note that the absolute values of the laser powers in this chapter are generally not insightful.

The SNR on the linecuts indicated in Fig. 7.3(b) are shown again for quantitative comparison in Fig. 7.3(c). One can see that the SNR peaks early and gradually drops as a function of initialization laser power while keeping the readout laser power fixed. When sweeping the readout laser power, on the other hand, a broad plateau of high

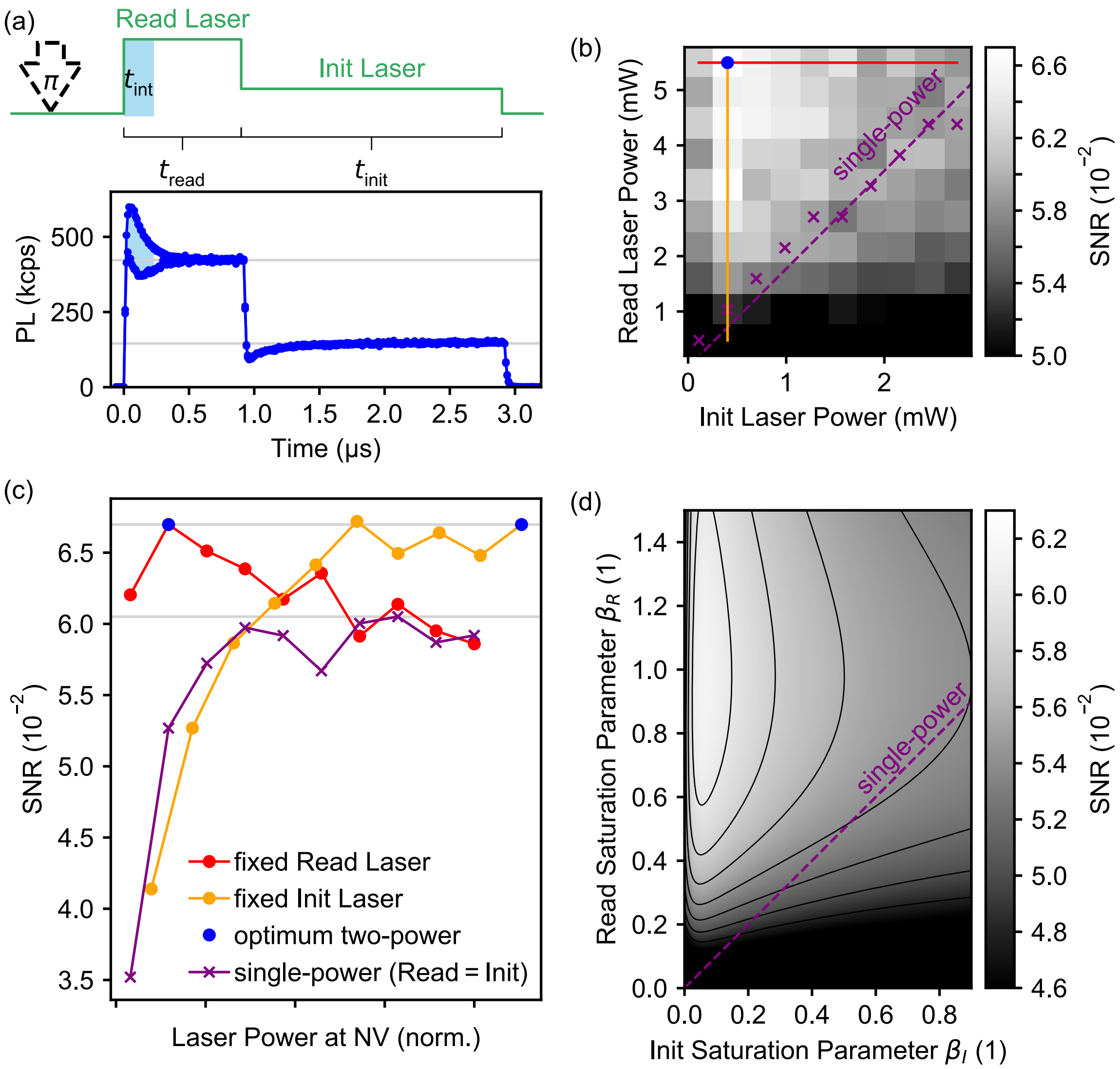

Figure 7.3: Improved SNR by a two-power scheme with NV-6at room temperature. (a) The "two-power" pulsed ODMR scheme is plotted with a corresponding measurement. The spin readout is done with a higher laser power than the spin initialization. If the excitation by both lasers are equal, it is equivalent to the established "single-power" scheme previously presented in Fig. 2.2(a). The integration time t_{int} and the π-pulse are marked as in Fig. 2.2(a). Gray horizontal lines indicate the ratio (here $\sim 1/3$) of the steady-state PL of the two lasers. (b) Experimental sweep of the two laser powers while monitoring the SNR. The optimum within the experimental range is approximated to lie at the blue dot. The corresponding time trace of this measurement is shown in part (a). The performance of the single-power scheme is indicated by the diagonal line (see text). The laser powers are given at the device outputs. (c) The linecuts marked in part (b) are plotted as a function of their normalized laser power (scaling obtained from the dashed line in part (b)). The same optimum (blue dot) from part (b) is marked on them. Also, the SNR achieved with the single-power scheme is plotted by the same markers as used in part (b). Gray horizontal lines indicate the improvement by 10.7 % that the two-power scheme achieves over the single-power scheme. (d) Simulation of the SNR of the two-power scheme. A qualitatively similar laser power range is used as in part (b). Contour lines correspond to the color bar labels. Compared to the maximum on the diagonal (single-power scheme), the two-power scheme yields a predicted gain of 9.5 % at $\beta_R = 1$. An extended view of the single-power linecut can be found in Fig. 7.1(a) at $T = 294$ K. Parameters from Tab. 4.1 are used for the simulations.

SNR is found at high power. The linecuts are taken at the optimal power of the respective other laser that is kept fixed. This is sufficient to obtain SNR values that are always superior or similar to the ones from the single-power scheme at the same laser power at the NV center. At the optimum of the two-power scheme, an SNR improvement by 10.7 % is found over the single-power scheme.

Finally, we simulate the SNR for the two-power scheme in Fig. 7.3(d). The experimental sequence timings are used, and the default parameters from Tab. 4.1 (NV-2) are taken for the model. The simulation qualitatively reproduces the experimental observations. A quantitative comparison cannot be made without calibration fits as done in Ch. 6.4 for other NV centers. However, an intuition for the range of the laser powers used in Fig. 7.3(b) can be gained: The range of the initialization saturation parameters β_I in Fig. 7.3(d) is adjusted to roughly reproduce the behavior in Fig. 7.3(b). The range for the readout saturation parameter β_R is extended a bit compared to part Fig. 7.3(b) to outline the behavior around the optimum better. The SNR values of the simulation lie slightly below the experimental ones here, for example due to a better collection efficiency in the ambient setup (NV-6) compared to HIMBI (NV-2). In the simulation, the optimum of the two-power scheme yields a gain of 9.5 %, compared to the optimum on the diagonal (single-power scheme). At the SNR optimum of the two-power scheme, $t_{\text{int}} = 219\,\text{ns}$ and $\beta_R = 1$. The increase in optimal β_R and simultaneous decrease in t_{int}, compared to the optimal $\beta = 0.7$ that was found for the single-power scheme in Fig. 7.1(a), is a result of decoupling the destructive effect of a high initialization laser power from the readout laser power. From the contour lines in Fig. 7.3(d), one can further infer that optimal readout power β_R is largely independent of the initialization fidelity (*i.e.* β_I).

For a fair comparison of the two-power scheme versus the single-power scheme, the duration of the entire sequence must be taken into account. For this, the SNR of a single initialization and readout cycle is not adequate. Instead, the SNR should be normalized per unit time, including the trade-off of sensing time t_{sens} versus sequence overhead $t_{\text{read}}+t_{\text{init}}$. According to Eq. 2.9, this requirement is fulfilled by the sensitivity. To quantify the gain in sensitivity, the full duration of the pulse sequence would need to be optimized (see Ch. 2.3). This is particularly important since a high initialization fidelity can be achieved with a long, low-power laser pulse. But this duration comes at the cost of fewer sequence repetitions within a fixed experiment duration. Therefore, a sensing sequence-specific trade-off exists here. We will do this full analysis for the measurements in the next section. The two-power scheme was also studied by Wirtitsch *et al.* [108] (but with an additional very-high power pulse for charge state manipulation), where a similar 12.9 % SNR improvement was found for a similar time $t_{\text{read}} + t_{\text{init}} = 3\,\mu\text{s}$. In their work, they also present an optimization of the sensitivity in simulations, complementing our optimization analysis given in the next section.

Despite the improvement in SNR, the two-power scheme has a significant disadvantage in practice: two laser modules or special hardware to generate laser pulses with different power on the sub-microsecond timescale are required and need to be integrated into the optical setup. In the next section, we will replace the second lower-power laser with a fast-pulsed interval of the first high-power laser, obviating the need for two separate lasers.

7.4 Improved spin initialization by fast laser pulses

In this section, we will leverage the advantage of a high laser power readout combined with a lower power initialization, as discussed in the previous section. However, we will achieve this without the disadvantage of the additional hardware requirement of a second laser power. Instead, we reproduce the effect of the lower laser power by a pulse-width-modulated (PWM) operation of the first, high-power laser. The new sequence scheme ("pulsed") is presented in Fig. 7.4(a). Such a scheme was demonstrated to achieve a 10 % contrast improvement for very long measurement times by Song *et al.* [143]. However, the authors did not consider the readout process nor optimize the sequence overhead for optimal sensitivity. Instead, they focused on the case of very long measurement times with $t_{\text{sens}} \gg t_{\text{init}}$, where this overhead is negligible.

Thus, the first goal of this section is to demonstrate that the pulsed scheme is superior to the established single-power scheme, also for shorter sensing times t_{sens} as used, for example, in scanning probe microscopy with pulsed ODMR (see Fig. 2.2). Since a pulsed laser is already used in most experiments with NV centers (in the form of a direct-modulation diode or by an acousto-optic modulator), the pulsed scheme presented here is readily available in most setups. In the single-power readout and initialization scheme, a sub-20 ns rise time of the laser (*cf.* Eq. 6.2) offers no benefit. Therefore, 4 ns-fast pulses, as described as ideal by Song *et al.*, might not be available in many setups. In this context, the second goal of this section is to demonstrate that such short pulses are neither needed for the pulsed scheme's success nor ideal in cases with background PL values we typically encounter.

7.4.1 Optimization concept

The sequence of the pulsed scheme in Fig. 7.4(a) has a duration of

$$T_{\text{seq}} = t_{\text{sens}} + \underbrace{t_{\text{read}} + \underbrace{N\left(t_{\text{on}} + t_{\text{off}}\right)}_{t_{\text{init}}}}_{t_{\text{LaserOn}}} + t_{\text{LaserWait}}\,, \tag{7.7}$$

with N being the number of pulses within the initialization phase. For an optimal initialization, the process described in the derivation of the upper achievable initialization limit ("ES limit") in Eq. 7.6 has to be reproduced in the experiment. This means [143] a long ($N \gg 1$) initialization with very short ($t_{\text{on}} \ll T_{\text{ES}}$) and strong ($\beta \gg 1$) laser pulses for the excitation, as well as a long waiting time ($t_{\text{off}} \gg \tau_S(294\,\text{K})$). In that sense, the picture of a PWM does not capture the full concept since the two-power scheme does this pump-wait cycle only statistically. However, we will show in simulations that this difference is small. Further, using a high laser power might be limited by an increase in background PL or a two-photon conversion to NV^0 [124] harming the readout. Also, a trade-off has to be made between the measuring time t_{sens} and the sequence overhead from an excessively long t_{init}. We will discuss this trade-off in the following.

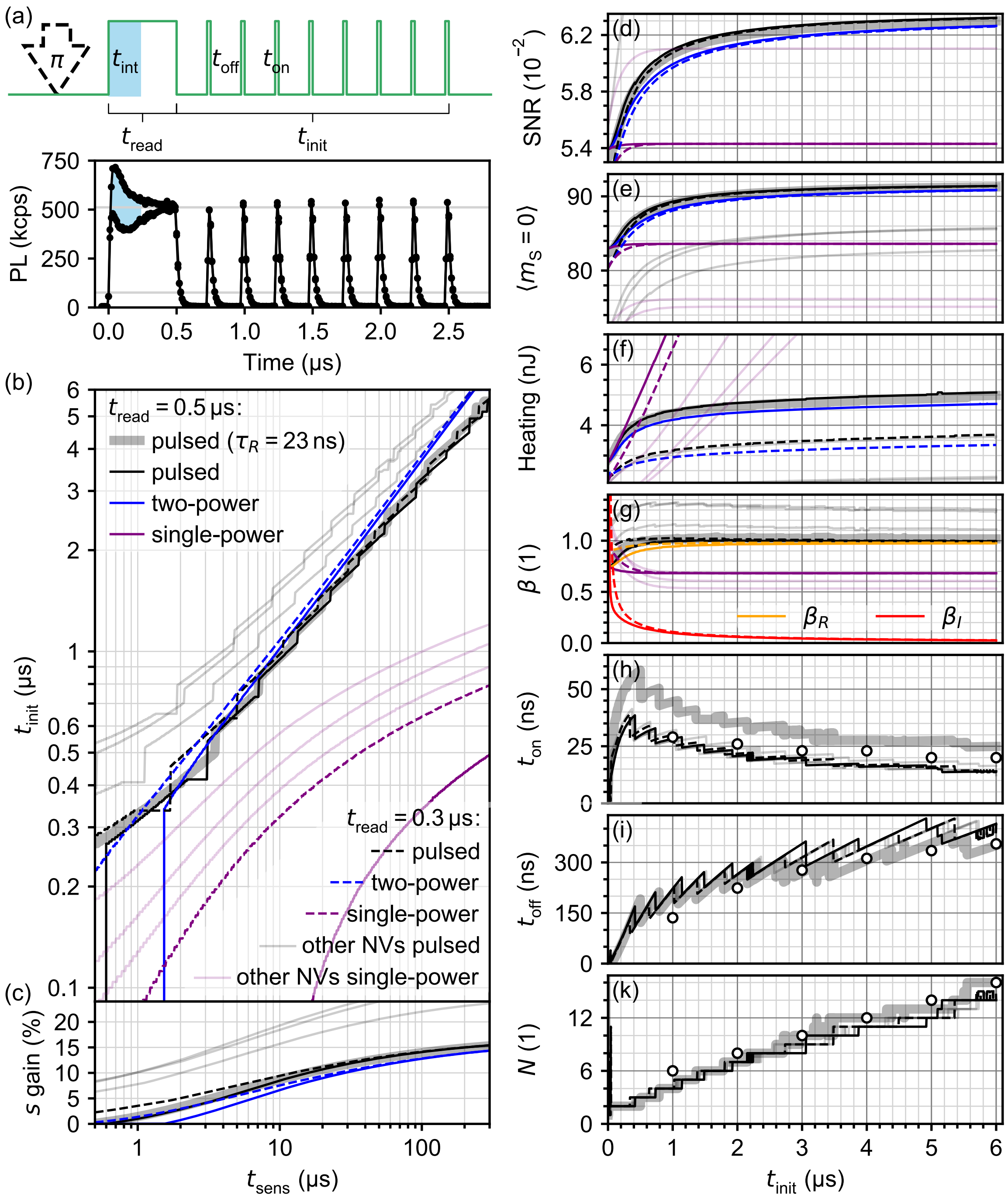

Figure 7.4: Optimized sensitivity by a fast-pulsed laser scheme at room temperature. (a) The fast-pulsed ("pulsed") pulsed ODMR scheme is plotted with a corresponding measurement (yellow marker in Fig. 7.5(b)). The spin readout is done with a high laser power while the same laser performs the spin initialization in a fast-pulsed manner. This is conceptually similar to the "two-power" scheme in Fig. 7.3(a). As there, gray horizontal lines indicate the ratio (here $\sim 1/7$) of the steady-state PL (mean PL taken for the initialization). The "single-power" scheme was presented in Fig. 2.2(a). (b) Simulation of optimal t_{init} as a function of the MW sequence duration t_{sens} for different schemes and settings. The optimization minimized the sensitivity s in Eq. 7.8. (c) Corresponding gain in s over the single-power scheme. The performance characteristics of one sequence repetition are shown in (d – f) and the corresponding optimal sequence parameters in (g – k), all as a function of t_{init}. Parameters from Tab. 4.1 are used for the simulations. For the faint thin traces, the parameters of the other three NV centers in Tab. 6.3 are used with $t_{\text{read}} = 0.3\,\mu\text{s}$.

For a fair comparison of performance between schemes, we use the sensitivity s as a figure of merit. One example is the sensitivity of a pulsed ODMR given by Eq. 2.6. For more advanced quantum sensing protocols, different microwave sequences are used and the factors in Eq. 2.6 vary [50]. However, these constants do not alter the general trade-off discussed in the following. To this end, we will refer to the general Eq. 2.9 in the following, which states that

$$s \propto \mathrm{SNR}^{-1}\sqrt{t_{\mathrm{sens}} + t_{\mathrm{read}} + t_{\mathrm{init}} + t_{\mathrm{LaserWait}}}\,. \tag{7.8}$$

To be able to discuss the performance without limiting us to one case-specific t_{sens}, we will maximize the SNR as a function of fixed sequence timings. We use fixed, typical values $t_{\mathrm{read}} = 0.5\,\mu\mathrm{s} \geq t_{\mathrm{int}}$ and $t_{\mathrm{LaserWait}} = 1\,\mu\mathrm{s} \gg \tau_S(294\,\mathrm{K}) \approx 150\,\mathrm{ns}$. t_{int} is always optimized in post-processing. This leaves a variable SNR (t_{init}) for optimization. In this optimization, the laser power P (or equivalently, the saturation parameter β), the on-time t_{on}, and the number of repetitions N are varied. The off-time t_{off} is implicitly set by optimizing for a given t_{init}. The function of optimal $\mathrm{SNR}(t_{\mathrm{init}})$ and the case-specific t_{sens} are then plugged into Eq. 7.8. The resulting $s_{t_{\mathrm{sens}}}(t_{\mathrm{init}})$ is minimized, which finally yields the optimal t_{init} value for that t_{sens}. With the knowledge of optimal t_{init}, one can then look up the corresponding optimized parameters ($\beta(t_{\mathrm{init}})$, $t_{\mathrm{on}}(t_{\mathrm{init}})$, $N(t_{\mathrm{init}})$). The same optimization concept is applicable to the other two schemes: the single-power scheme with only the laser power β as an optimization parameter and the two-power scheme with the two laser powers β_R and β_I as optimization parameters.

The optimization process described above is executed on simulations in Fig. 7.4 for a large range of t_{sens}. Fig. 7.4 can be used as follows: selecting *e.g.* a sensing sequence duration of $t_{\mathrm{sens}} = 10\,\mu\mathrm{s}$, Fig. 7.4(b) suggests an initialization time of $t_{\mathrm{init}} \approx 1\,\mu\mathrm{s}$. This t_{init} is more or less independent of t_{read} and whether the two-power or pulsed scheme is used. If one performs a pulsed scheme (best performance as depicted in Fig. 7.4(d–f)), the simulation suggests parameters $\beta = 1$, $t_{\mathrm{on}} = 28\,\mathrm{ns}$, and $N = 4$ in Fig. 7.4(g–k). They are predicted to offer a gain in sensitivity of 8.5 % (with $t_{\mathrm{read}} = 0.5\,\mu\mathrm{s}$), as shown in Fig. 7.4(c).

7.4.2 Simulation results

We will now examine the predictions of Fig. 7.4 more closely. We first discuss how these simulations are implemented, then compare the three different schemes, discuss the effect of the laser rise time and the ideal duration of the fast pulses, and finally, investigate the effect of altered NV center model parameters.

Implementation

The pulse sequence, as shown for one exemplary sequence in Fig.7.4(a), is applied on an initial start state ρ_0 to initialize the spin state. Then, an optional π-pulse is applied. Finally, the sequence is applied a second time for the spin readout, and the optimal integration time t_{int} is used. For the single-power scheme in Fig. 2.2(a), the thermal state was used as a natural choice for the start state ρ_0. However, we will now allow the optimization algorithm to use short t_{LaserOn} values. Therefore, it is better to increase the penalty for improper initialization by using the worst possible case of ρ_0. We thus use, without loss of generality, the GS $m_{\mathrm{S}} = -1$ as ρ_0. Note that an incomplete initialization does not erase the state from the previous sensing repetition, which could be a MW pulse at a different frequency in the pulsed ODMR example of Fig. 2.2(b).

In optimizing the single-power scheme in Fig. 7.4, the laser is simply left on during t_{init}. For the two-power scheme, a different laser power β_I is used during t_{init} compared to the value β_R during t_{read} (see Fig. 7.3(a)).

Steps in the optimized traces of the pulsed scheme in Fig. 7.4 originate from having to fit an integer number N of $t_{\mathrm{on}} + t_{\mathrm{off}}$ into fixed t_{init}. Due to the discontinuous nature of the optimization function, a gradient descent to the optimum in parameter space is not possible. The optimization algorithm thus coarsely samples the full parameter space first to find a good initial guess. From there, the (gradient-free) Nelder-Mead simplex algorithm is used to find the optimum, which is provided by the Python library SciPy [131].

Comparison of schemes

We will first focus our discussion on the thin solid traces in Fig. 7.4, which use $t_{\mathrm{read}} = 0.5\,\mu\mathrm{s}$ as the experiments in Sec. 7.4.3. Further, the parameters from Tab. 4.1 are used at room temperature.

The single-power scheme shows a simple optimal behavior: as we saw in Fig. 7.1(a), the optimal laser power is around a saturation parameter of 0.7 with these NV model parameters — largely independent of t_{init}, as seen in Fig. 7.4(g). Since the initialization is not improved by leaving the laser on for long t_{init}, the initialization fidelity and SNR are flat functions in Fig. 7.4(d, e). Thus, in order to optimize the sensitivity, the algorithm suggests using $t_{\mathrm{init}} = 0$ in Fig. 7.4(b) for measurement times of $t_{\mathrm{sens}} < 10\,\mu\mathrm{s}$.

The two-power scheme quickly converges to a readout laser power $\beta_R = 1$ with increasing t_{init} in Fig. 7.4(g). We identified this to be the optimum readout power in Fig. 7.3(d) for the same background PL value b. At the same time, the optimal initialization laser power β_I continues to drop towards 0 with increasing t_{init}. The same behavior can be identified for the pulsed scheme: $\beta_R \to 1$, and the duration of the pulses $t_{\mathrm{on}} \to 45\,\mathrm{ns}$ is adjusted accordingly in Fig. 7.4(h). The number N of pulses is quickly adjusted such that a $t_{\mathrm{on}} \sim \tau_S(294\,\mathrm{K}) \approx 150\,\mathrm{ns}$ is reached. As t_{init} increases further, the number of pulses N that can be made can be increased. With each repetition of the above-mentioned pump-wait cycle, the initialization fidelity increases. Further, there is room to increase t_{off} to obtain a more complete decay of the SS before the next pump pulse.

The simulations suggest an improvement of up to $15\,\%$ in s with the pulsed scheme compared to the single-power scheme. This is seen in Fig. 7.4(c) for measurement times of $t_{\mathrm{sens}} \approx 300\,\mu\mathrm{s}$. The gain with the two-power scheme is very similar and only $1\,\% - 2\,\%$ lower than the pulsed scheme. On the other hand, the deposited laser energy during one sequence repetition shown in Fig. 7.4(f) is slightly lower for the two-power scheme since it excites the NV center without wasting power in the saturated regime.

Laser pulse duration and rise time

For short measurement times $t_{\mathrm{sens}} \lesssim 5\,\mu\mathrm{s}$, optimal $t_{\mathrm{init}} \lesssim 0.7\,\mu\mathrm{s}$ are suggested by the simulation. In this regime, the duration of t_{read} becomes relevant. Since relatively high laser powers are used in the pulsed and two-power scheme, the readout pulse with $t_{\mathrm{read}} = 0.5\,\mu\mathrm{s}$ already serves as an initialization. Also the experimental data shown in Fig. 7.3(a) and Fig. 7.4(a) show that at $t = 0.5\,\mu\mathrm{s}$, the initial state is erased. The rationale behind this is that $t_{\mathrm{read}} > \tau_S(294\,\mathrm{K})$. While decreasing t_{sens}, there is even a point where a better sensitivity is achieved with $t_{\mathrm{init}} = 0$ (*i.e.* the single-power scheme with $t_{\mathrm{LaserOn}} = t_{\mathrm{read}}$). The pulsed (two-power) scheme shows this drop in Fig. 7.4(b) around $t_{\mathrm{sens}} = 0.6\,\mu\mathrm{s}$ ($t_{\mathrm{sens}} = 1.5\,\mu\mathrm{s}$).

When we decrease t_{read} to the minimum of $t_{\mathrm{read}} = 0.3\,\mu\mathrm{s} \gtrsim t_{\mathrm{int}}$ (dashed traces in Fig. 7.4), the initialization is not completed during t_{read}. When followed by a fast-pulsed initialization, $t_{\mathrm{init}} = 0.3\,\mu\mathrm{s}$ achieves a significantly higher gain in sensitivity and is an advantageous scheme over the single-power one, even for pulsed ODMR with $t_{\mathrm{sens}} \approx 1\,\mu\mathrm{s}$. In this regime, the pulsed scheme also clearly outperforms the two-power scheme in Fig. 7.4(c). And in terms of the sample heating, a shorter t_{read} is also beneficial.

As a last element of the timings in the pulsed scheme, we address the duration of the fast pulses. In the optimization in Fig. 7.4)(h), t_{on} reduces gradually with increasing t_{init}. This decreases the chances of exciting an $m_{\mathrm{S}} = 0$ state twice and, thereby, potentially destroying it by the finite chance of an ISC process (*cf.* Sec. 7.1.1). But t_{on} roughly stays in the 20 ns range, in contrast to the 4 ns-fast pulses suggested in Ref. [143]. Consequently, one would also expect laser rise times on the order of 20 ns to be sufficiently fast for the pulsed scheme. This is confirmed by the simulations shown as thick traces in Fig. 7.4 for $\tau_R = 23\,\mathrm{ns}$ from Eq. 6.3. Finally, we note that the optimization would look different if a second laser were used for the pulsed scheme. Then, no bound other than two-photon charge state switching exists for the pump-wait cycle of the initialization. In that case, the optimization would indeed yield the parameter regime of as short and intense laser pulses as possible.

Variation across NV centers

The simulation results shown in Fig. 7.4 depend on the NV center parameters. In particular, the ISC rates and the SS branching ratio and lifetime play a critical role in the improved performance with the pulsed and two-power schemes (see discussion in Sec. 7.1). Thus, one may ask the question to what degree simulations performed on one set of NV center parameters can be used for a general set of NV center parameters. Unfortunately, this cannot be answered with certainty here. But two partial answers can be provided:

First, the Python library developed in this thesis (see Ch. 6.3) provides a high-level function that returns optimization results as plotted in Fig. 7.4. If the parameters of an NV center are known, this might answer the question (still only including the NV^0 by its effect on the effective NV^- model parameters).

Second, we use the parameters of the other three NV centers (NV-1, NV-3, NV-4) in Tab. 6.3 and compare them to the parameters discussed so far (NV-2). These simulations are shown for the single-power and the pulsed scheme as faint thin traces in Fig. 7.4. As can be seen, the optimal parameters t_{on} and N barely change. Optimal t_{init} for given t_{sens} lie higher, though. A variation in the optimal laser power can also be witnessed. This originates from a lower background in these model parameters: at $\beta = 0.5$, the background PL counts bP (see Eq. 4.38) make up 43 % of the total steady-state PL for NV-2. For NV-1, NV-3, and NV-4, it is only 35 %, 26 %, and 26 %. A lower background yields a higher SNR with a higher optimal readout laser power. Note that the alignment parameter A in Tab. 6.3 is significantly higher for NV-1, NV-3, and NV-4. Thus, lower absolute laser power is needed, and less laser energy is deposited in Fig. 7.4(f), despite a higher optimal β in Fig. 7.4(g).

7.4.3 Experimental results

In the following, measurements with the pulsed scheme are presented. We observe a gain in SNR of $\sim 5\,\%$ over the traditional single-power scheme and subsequently discuss a sensitivity optimization. Then, we address the deposited laser energy. Here, our experiments reduce the heating by a factor of two or more compared to the single-power scheme. Finally, we compare the pulsed scheme experiment with the two-power scheme experiment from Sec. 7.3.

Pulsed scheme measurements

The pulsed scheme is tested in experiment at room temperature on another QZabre LLC tip (NV-7). Measurements are conducted in the commercial QSM setup by QZabre LLC. The setup is equipped with an Toptica Photonics iBeam Smart 515 laser with a specified rise time of around $\tau_R \approx 1\,\mathrm{ns}$. A readout laser time of $t_{\mathrm{read}} = 0.5\,\mu\mathrm{s}$ is used and t_{init} is varied. The other timing parameters are indicated by the circular markers in Fig. 7.4(h–k). The laser power is swept for each case of t_{init} and for both the single-power and the pulsed scheme. The resulting SNR is shown in Fig. 7.5. We find that the pulsed scheme outperforms the established single-power scheme at almost all points for the same given laser power and sequence duration.

Sensitivity gain of the pulsed scheme

For a better comparison between the two schemes, the SNR is plotted against the deposited laser energy in Fig. 7.6(a) at the example of $t_{\mathrm{init}} = 1\,\mu\mathrm{s}$ from Fig. 7.5(a). Here, the data of the single-power scheme was averaged over all six t_{init} measurements in Fig. 7.5. This is motivated by the fact that for $t_{\mathrm{read}} = 0.5\,\mu\mathrm{s}$, the single-power scheme is not expected to yield a significantly different result for $t_{\mathrm{init}} > 0$ compared to $t_{\mathrm{init}} = 0$. As discussed in Sec. 7.4.2, the optimal t_{init} of the single-power scheme is expected to be 0 up to $t_{\mathrm{sens}} \gtrsim 10\,\mu\mathrm{s}$. And at higher values of t_{sens}, the value of t_{init} barely has an influence, as it can be seen in Fig. 7.4(d,e,g). One can see that this is

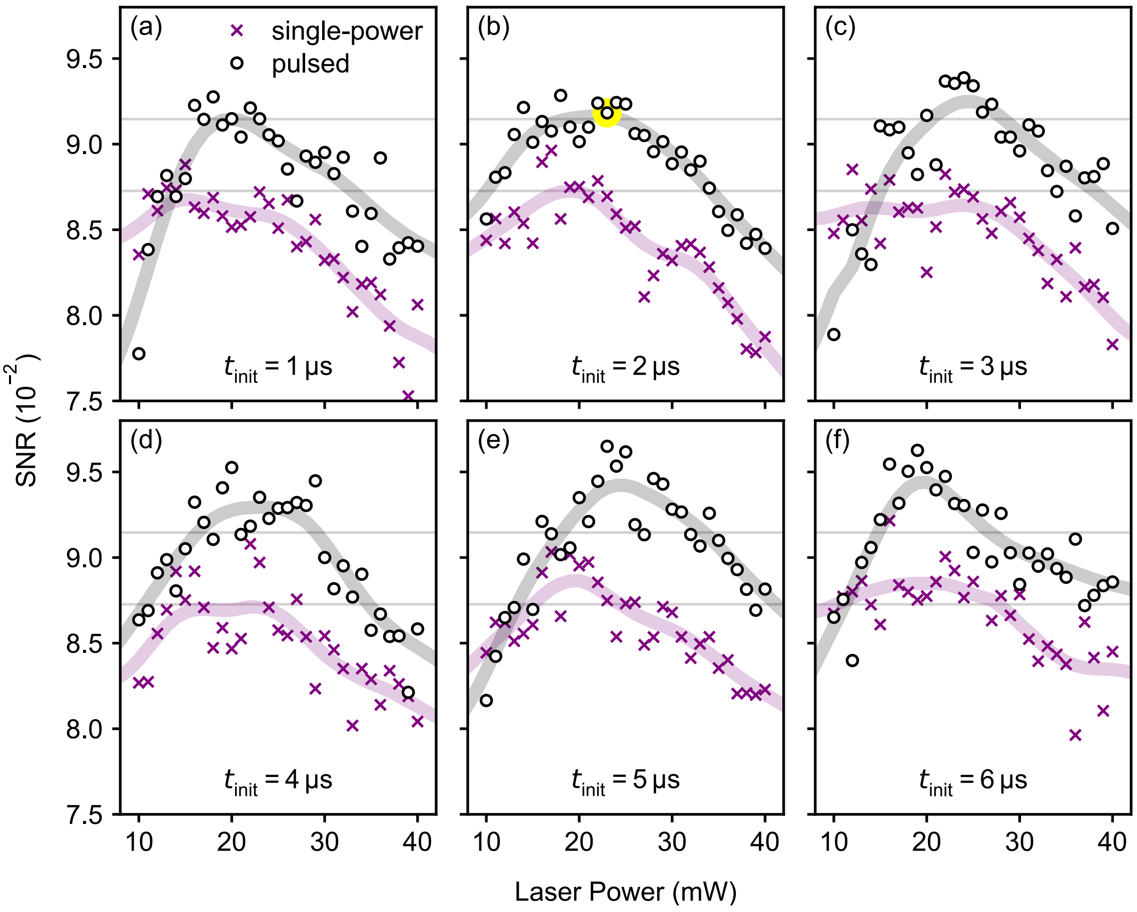

Figure 7.5: Comparison of the fast-pulsed vs. single-power pulsed ODMR scheme with NV-7 at room temperature. (a–f) Plotted is the measured SNR of a single sequence repetition (as always used above) as a function of laser power at the device output. The laser power is strongly attenuated before reaching the NV center. Different initialization times t_{init} are used, as shown in the scheme in Fig. 7.4(a). The SNR of the time trace shown there is marked by a yellow dot in part (b) and constitutes the approximate optimum of the pulsed scheme for $t_{\mathrm{init}} = 2\,\mu\mathrm{s}$. The same t_{init} was used for all two-power scheme measurements in Fig. 7.3. Thick solid traces are moving averages (smoothed by convolution with a Gaussian of $\sigma = 3\,\mathrm{mA}$). Gray horizontal lines are given for comparison with Fig. 7.6.

also the case in the experiment from the reach of the steady-state PL in Fig. 7.4(a) after $t_{\mathrm{read}} = 0.5\,\mu\mathrm{s}$.

An overview of the gain in SNR for all other t_{init} measurements is presented in Fig. 7.6(b). At the same t_{init}, the fast-pulsed scheme is found to have about 5 % more SNR than the single-power scheme for our measurements on NV-7. In practice, laser pulse durations around $t_{\mathrm{LaserOn}} \approx 1.5\,\mu\mathrm{s}$ (*i.e.* $t_{\mathrm{init}} = 1\,\mu\mathrm{s}$ for the experimental data here) are established. In this context, if one wants to use $t_{\mathrm{LaserOn}} = 1.5\,\mu\mathrm{s}$, the observed SNR gain of 5 % in Fig. 7.6(b) directly translates to an equal gain in sensitivity.

However, it is important to emphasize that this does not mean that the pulsed scheme has superior *optimized* sensitivity s compared to the single-power scheme. For a given t_{sens}, one has to compare the sensitivity of an optimized t_{init} for the pulsed scheme with an optimized t_{init} for the single-power scheme. This is done by minimizing Eq. 7.8 under varying t_{init} with the respective functional behavior of SNR(t_{init}) presented in

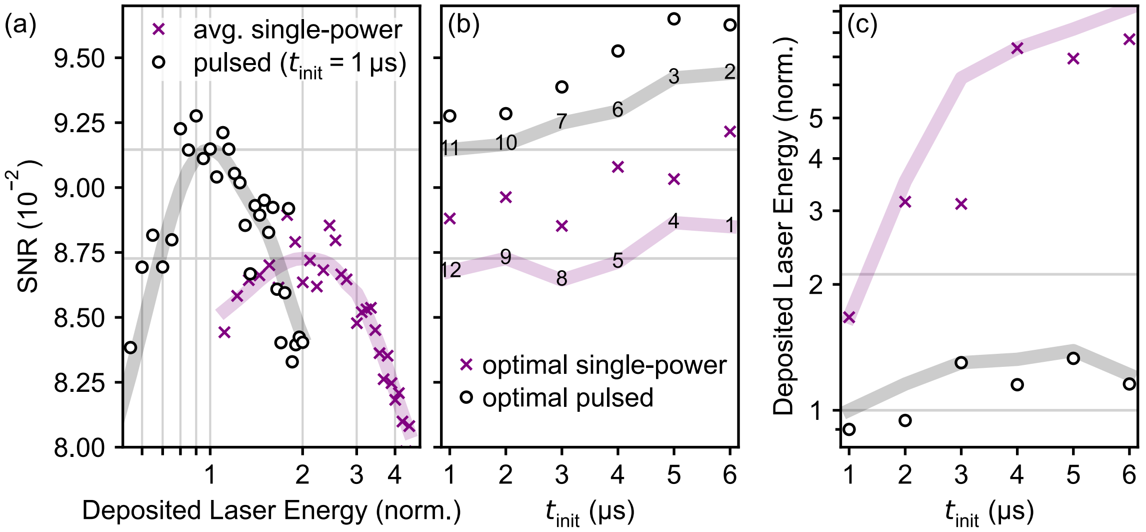

Figure 7.6: SNR gain and reduced heating of the fast-pulsed over the single-power pulsed ODMR scheme with NV-7. (a) SNR as a function of deposited laser energy during one sequence repetition for $t_{\mathrm{init}} = 1\,\mu\mathrm{s}$. The pulsed scheme data is the same as in Fig. 7.5(a). The data shown for the single-power scheme is obtained by averaging all traces in Fig. 7.5(a–f) and assuming $t_{\mathrm{init}} = 1\,\mu\mathrm{s}$ for the deposited energy. Also shown are the SNR (b) and the heating due to deposited laser energy (c) at the SNR maximum of the data points (marker) and averaged curves (thick traces) from Fig. 7.5(a–f). The numbers on the averaged curves in part (b) indicate the temporal order in which the measurements were recorded. Gray horizontal lines in parts (b,c) indicate the gain as derived from the maximum of the moving averages in part (a). For the same t_{init}, the fast-pulsed scheme has about 5 % more SNR and a factor ≥ 2 lower deposited laser energy.

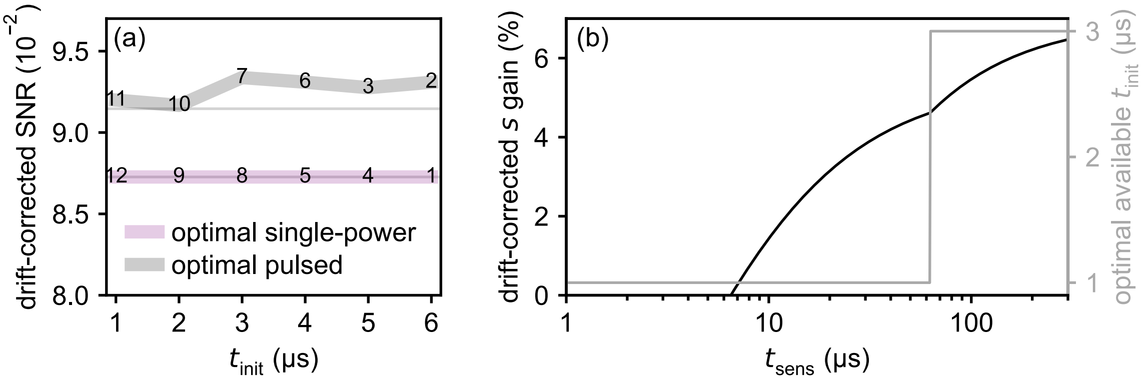

Figure 7.7: Sensitivity gain of the fast-pulsed over the single-power pulsed ODMR scheme with NV-7. (a) Same as Fig. 7.6(b) but after a drift correction based on the single-power data. Gray horizontal lines are given for comparison with Fig. 7.6. Corresponding simulations were shown in Fig. 7.4(d). (b) Sensitivity optimization of the fast-pulsed scheme based on the measurements. Part (a) is used to optimize the initialization time t_{init} in Eq. 7.8. Due to the discrete (integer) cases of t_{init} to pick from in part (a), and their scattering, only two values of t_{init} yield optimal sensitivity, dependent on the chosen t_{sens}. Corresponding simulations were shown in Fig. 7.4(b,c).

Fig. 7.6(b). To perform this analysis, we need to ensure equal experimental conditions for all t_{init}. But various drifts in the experimental conditions are often unavoidable in experiments. Examples are changing optical alignment, changing background PL, changing actual laser power due to a varying diode temperature, *etc.*. We, therefore, use the SNR of the single-power scheme in Fig. 7.6(b) for a best-effort correction of such drifts and record the data in the temporal order indicated in Fig. 7.6(b). As discussed above, no significant t_{init} dependence is expected for the SNR of the single-power scheme. The drift-corrected SNR is presented in Fig. 7.7(a). In corresponding simulations of the SNR gain in Fig. 7.4(d), qualitatively similar behavior is found but with a higher absolute gain (12 % there compared to 5 % here at $t_{\mathrm{init}} = 1\,\mu\mathrm{s}$). Deviation is expected here due to different parameters of NV-7 compared to Tab. 4.1 and different sequence timing (*cf.* Fig. 7.4(h–k)). Fig. 7.7(a) can now be used to determine the optimal t_{init} for best sensitivity s. The result of this optimization is shown in Fig. 7.7(b). To obtain the lower bound for the gain in sensitivity shown here, we assume an optimal $t_{\mathrm{init}} = 0$ for the single-power scheme with the averaged SNR value from Fig. 7.7(a), as motivated above. Similar to the SNR, the experimentally observed gain in sensitivity with NV-7 is smaller than the one found in simulations in Fig. 7.4(c).

It should finally be noted that usage of a shorter $t_{\mathrm{read}} = 0.3\,\mu\mathrm{s}$ is expected to increase the observed gain in sensitivity (*cf.* Fig. 7.4(c)) but requires an initialization $t_{\mathrm{init}} > 0$ as the previous spin state is not erased during t_{read}.

Reduced heating with the pulsed scheme

Apart from the SNR gain, the pulsed scheme also offers an advantage in terms of the deposited laser energy per sequence repetition. Fig. 7.6(c) shows that heating is reduced by a factor of two or more when exchanging the initialization phase of the single-power scheme with the fast-pulsed scheme. A trade-off exists between optimizing for low heating and the best SNR. However, compared to the readout, the pulsed or low-power initialization has only a small influence on the heating, as seen in the experimental data (Fig. 7.6(b) vs. (c)) as well as the simulation (Fig. 7.4(d) vs. (f)). When calculating the deposited energy, the laser rise time τ_R should be considered in case it is on the same time scale as t_{on}. This was done for the $\tau_R = 23\,\mathrm{ns}$ case in Fig. 7.4. For the experimental data and other simulations, $\tau_R = 0$ was assumed. If a shorter $t_{\mathrm{read}} \approx 0.3\,\mu\mathrm{s}$ would be used, the reduction in laser exposure would be even higher.

The two benefits (increased SNR and reduced heating) from employing the pulsed scheme are highlighted in Fig. 7.6(a).

Comparison of the pulsed and two-power measurements

Highlighted in yellow in Fig. 7.5(b) is an approximately optimal case for the pulsed scheme with $t_{\mathrm{init}} = 2\,\mu\mathrm{s}$, which achieved around 5 % gain in SNR in experiment. The same t_{init} was used in the best case of the two-power scheme, which achieved a gain around 11 % in experiment. As seen in Fig. 7.4(a), the pulsed scheme uses a $\sim 1/7$ ratio of the steady-state PL during initialization over readout. The best two-power scheme in Fig. 7.4(a) had a $\sim 1/3$ ratio. Likely, the latter was not the optimum and only identified as such due to the coarse sampling resolution in β_I. Recalling the discussion about the two mechanisms of spin polarization (ISC and SS decay) in Sec. 7.1.1 and the uncertainty in present literature about the values of the parameters therein (*cf.* Ch. 6.4.4), we can use our experimental findings and developed understanding to draw a conclusion: the fact that a clearly measurable gain is obtained with the two schemes proves that the ISC is dominating the spin polarization process at room temperature. This limits the value of r_S or $k_{E_{12}}$. This inference can most likely be made without having to include charge state switching since the laser power in the initialization is low in the two-power scheme.

7.4.4 Utilizing the improved scheme

From a theoretical point of view, the pulsed and two-power schemes utilize the same effect and give a similar gain in sensitivity and reduction in sample heating. In an intuitive picture, one can thus see the pulsed scheme as a way to achieve a low average laser power during initialization without using a second laser. An alternative approach would be to pulse the laser diode much faster than the rise time to achieve an effectively continuous and lower laser power for the initialization. Either way, the average steady-state PL during initialization should be around a factor 5 to 10 smaller than during the readout, depending on the chosen duration of the initialization. It should be recalled that the advantage of both schemes is only predicted to exist in the temperature regimes I and III in Fig. 7.2(b). In regime II, an inverse effect is expected: here, best initialization is achieved with high laser power pumping to the SS. The two schemes should, therefore, perform worse than the single-power scheme.

As a rule of thumb in setting up the pulsed scheme, one can proceed as follows (for pulse scheme see Fig. 7.4 and Eq. 7.7):

- *Characterizing the laser*: A laser power around saturation should be used here. Generally, also for the single-power scheme, the laser power should be optimized since it is setup- and probe-dependent. To do this, one can, for example, run a sequence with very long initialization time (*e.g.* $t_{\text{init}} = 20 \times (3 \times \tau_S + 10\,\text{ns} + \tau_R)$) and short laser pulses (*e.g.* $t_{\text{on}} = 10\,\text{ns} + \tau_R$) with long waiting times in-between (*e.g.* $t_{\text{off}} = 3 \times \tau_S$), and set $t_{\text{read}} = 1\,\mu\text{s}$. Here, τ_R is the exponential laser rise time and typically $\tau_S \approx 150\,\text{ns}$ at room temperature and $\tau_S \approx 300\,\text{ns}$ at cryogenic temperature. A sweep of the laser power then reveals the optimal readout power for the highest SNR (see simple Eq. 2.10). The result of a similar measurement was shown in Fig. 7.5(f). In this, t_{int} should be optimized in post-processing for the highest SNR per laser power — this also applies to the single-power scheme. A Python function to do this is offered in the GitHub library (see Ch. 6.3), or Fig. 7.1(b) can be used as guidance.
- *Sequence timings for good sensitivity*: The high laser power pulse should not be considerably longer than the integration time, which means $t_{\text{read}} \lesssim 500\,\text{ns}$. The parameters of the pump-wait cycles (N, t_{on} and t_{off}) can be taken from Fig. 7.4 with $t_{\text{init}} \geq 1\,\mu\text{s}$.

- *Sequence timings for reducing the laser exposure of the sample*: A $t_{\mathrm{read}} = 0.3\,\mu\mathrm{s}$ is advisable, followed *e.g.* by a reliable initialization sequence of $t_{\mathrm{init}} = 2\,\mu\mathrm{s}$ with N and t_{on} as given in Fig. 7.4.

Note that this is only a rough guide. The process of a full optimization was described in Sec. 7.4.1.

We showed here that in contrast to the mantra of extremely short and powerful laser pulses in Ref. [143] for bulk NV centers, 4 ns-fast pulses are not ideal when background limits the readout around laser saturation. This is, today, often the case in the technologically prominent field of shallow NV centers for quantum sensing applications. Instead, around 20 ns pulses, as seen in Fig. 7.4(h), are optimal for the regime discussed in Ref. [143] ($t_{\mathrm{sens}} \geq 100\,\mu\mathrm{s}$ with $t_{\mathrm{int}} \approx 3\,\mu\mathrm{s}$). Our simulations with the parameters from Tab. 4.1 yield in this regime a contrast improvement of 6.5 %, compared to the 10 % found in their work. This is, to some degree, due to the different NV center-specific parameters but crucially also because in the simulations here, the relevant quantity SNR is optimized and not the contrast (similar to Ref. [108] for the two-power scheme). Finally, we showed that the advantage found in Ref. [143] can also be utilized with slower laser rise times. This greatly extends the number of experiential setups readily able to utilize the scheme by only an adjustment of the pulse sequence in the control software. With respect to charge state switching of shallow NV centers [57, 124, 128], the less powerful and longer laser pulses we use here might offer an additional advantage over the pulses used in Ref. [143], but the dependence might be complex [108]. It can be envisioned that our fast-pulsed scheme is routinely used to extend the lifetime (or reduce the heating) of samples and NV^- centers due to a reduced deposited laser energy at simultaneously increased SNR.

CHAPTER 8

Conclusion and Outlook

In this thesis, an instrument was set up for variable-temperature scanning probe microscopy based on sensing with single NV centers. The performance of the microscope was analyzed in detail to gain a thorough understanding of its engineering and NV center inherent characteristics. The instrument and data recorded on other setups were used to gain a fundamental understanding of the photo-physics of the NV center over a wide temperature range, covering 4 K to 300 K. This effort ultimately resulted in an openly accessible Python library [43] enabling the simulation of standard optical readout quantities over a wide parameter space of temperature, strain or electric field, and magnetic field. Further, the library was used to examine improvements in the established optical initialization and readout scheme.

Setup

Regarding the engineering of the setup, a very compact (teacup-sized) design was presented. It enables fast turn-around times (around 7 h) and a base temperature below 7 K. Solutions to various challenges of temperature management were discussed. After the implementation of a new design, coaxial cables were identified as the major remaining heat load. Moreover, the vacuum system design was greatly improved. A high vacuum was essential to avoid contamination aggregation on the sample surface under the scanning tip.

The strength of the setup presented in this thesis is its easy access to all temperatures between 7 K and 350 K. As a sensor, the NV center contributes quantitative imaging of magnetic and electric fields with nanometer-scale resolution. In future experiments, studies of phase transitions in multiferroics and current transport regimes are envisioned. The low base temperature, the ability to switch temperatures quickly, and the developed understanding of the photo-physical aspects of the sensing performance will facilitate this effort.

Temperature-dependent NV center photo-physics

A Lindblad master equation model of the NV^- center population dynamics was presented. It unifies the existing separate rate models developed for the low- and high-temperature limits. The effect of temperature is included by phonon-induced hopping between the ES energy levels, which, together with their spin mixing, was identified as the key mechanism for a discovered spin-state relaxation in the excited state. The relaxation process is most effective when the hopping rate between the orbital states is resonant with the ES spin level spacing, explaining the reduction in the sensing performance around 30 K to 60 K. Since the ES level spacing and mixing are dependent on strain and magnetic field, these parameters can tune the resonance condition. Further, the wavelength of contributing phonon modes was analyzed. For structures like nanodiamonds, the dimensions of the host crystal could become relevant to the spin-state relaxation. Thus, improving the performance of NV centers at intermediate temperatures through targeted engineering of their depth, orientation, magnetic field, or strain/electric field can be envisioned.

Using numerical simulations of the population dynamics, several important experimental observables were extracted, including the dynamic and steady-state PL intensity, as well as the SNR for spin-state readout, which are relevant for quantum applications. After an NV center-specific calibration of the model, simulated observables were compared with an extensive set of experimental data. A good agreement was found between simulation and experiment over a wide parameter range of 4 K to 300 K, 0 mT to 200 mT, and an ES branch splitting due to crystal strain of 18 GHz to 160 GHz.

It was further shown that a probing of the electron-phonon coupling is possible by comparison of PL measurements with a systematic modeling of the PL intensity as a function of temperature. This approach is applicable in regimes where resonant PL excitation spectroscopy and measurements of motional narrowing on ES ODMR lines are unavailable, providing a new avenue for experimental probing of the contributing phonon modes. In particular, the transition from the low- to the high-temperature regime critically depends on the phonon model. A simple Debye model was used here, in line with previous literature. However, by the aid of our simulations, some aspects of this state-of-the-art description were found to be inconsistent with some experimental observations reported in the literature. Using more accurate phonon models in our master equation description, as they are currently being developed, might provide a well-motivated and more precise description of the NV photo-physics. Here, more stable PL measurements with bulk NV centers at the crossover temperature might provide valuable input when fitted with the model.

The model successfully describes subtle reminders of the low-temperature Hamiltonian in the room-temperature PL at high crystal strain. In previous literature, these were observed experimentally (called the "temperature reduction factor") and also included in a classical room temperature rate model. In this thesis, simulations at the ES LAC were presented that suggest the use of these reminders at room temperature for an all-optical pre-characterization of the crystal strain. Selected NV probes could then be used at cryogenic temperature, where the crystal strain has a strong impact on the sensing performance. Another aspect predicted by the model are revival features in the regime of suppressed performance at intermediate temperature. The mechanisms of both, the revival features and the temperature reduction factor, are directly related to the interplay between magnetic fields and crystal strain/electric fields. They were theoretically explained in this thesis, but investigating these experimentally might further validate the model or improve the understanding of NV photo-physics.

Improved initialization and readout schemes

Having an easy-to-use tool to simulate the photo-physics of the NV center at hand, the established optical spin initialization and readout scheme was analyzed over the full temperature range. A reversed initialization behavior at intermediate temperature was found. Its occurrence is in close interplay with the ES and shelving state branching ratios — two quantities that vary widely in the literature and that are difficult to disentangle, also in conjunction with the neutral charge state. Here, future experiments based on this reversed initialization behavior might provide a new approach to the discussion.

Further, improvements to the established single-power initialization and readout scheme were investigated: a fast pulse train (a few tens of nanoseconds) at high laser power for the initialization, followed by a conventional readout (but also at the same high laser power). Alternatively, a scheme that uses a second, lower-power laser for the initialization was investigated. At room temperature, an improvement between 5 % to 10 % in the sensitivity was found experimentally and in simulations, even for short sensing sequences like in pulsed ODMR. This means a 10 % to 20 % speed-up in measurements. Additionally, this scheme reduces the deposited energy by the laser, which is beneficial for photo-sensitive samples or thermal load-critical experiments at cryogenic temperatures. Conveniently, this scheme can be readily implemented in setups that have pulsed ($\lesssim 30\,\mathrm{ns}$) laser capability.

Simulation library

The simulation library for Python is now available for researchers and customers of scanning NV microscopes. It could help them find the best operating conditions for their experiments. For the first time, it is possible to simulate the NV center photo-physics over the commonly covered range of temperature (cryogenic to room temperature) and magnetic field. For this, the `MEmodel` class was implemented. Beyond this, the library can simulate room-temperature photo-physics at high computational speed. The `HighTmodel` class, which is a commonly used classical rate model, was implemented for this purpose. Despite this prevalence, the accessibility of simulating, for example, contrast or SNR vs. key parameters with just a few lines of code, as well as the inclusion of the temperature reduction factor, make this part of the library also a helpful tool. Additionally, it offers a routine to optimize the optical initialization and readout sequence. In the future, the library could be extended to simulate quantum gates on the spin (other than instantaneous π-pulses) or non-classical optical processes. Also, so far, it does not include the hyperfine structure, the effects of strain/electric field on the ground state, the absolute positions of the energy levels of the NV^-, and the NV^0 levels.

Bibliography

[1] M. W. Doherty, N. B. Manson, P. Delaney, F. Jelezko, J. Wrachtrup, and L. C. Hollenberg, “The nitrogen-vacancy colour centre in diamond”, Phys. Rep. **528**, 1–45 (2013).

[2] R. Schirhagl, K. Chang, M. Loretz, and C. L. Degen, “Nitrogen-vacancy centers in diamond: nanoscale sensors for physics and biology”, Annu. Rev. Phys. Chem. **65**, 83 (2014).

[3] L. Childress and R. Hanson, “Diamond NV centers for quantum computing and quantum networks”, MRS Bulletin **38**, 134–138 (2013).

[4] E. D. Herbschleb, H. Kato, Y. Maruyama, T. Danjo, T. Makino, S. Yamasaki, I. Ohki, K. Hayashi, H. Morishita, M. Fujiwara, and N. Mizuochi, “Ultra-long coherence times amongst room-temperature solid-state spins”, Nat. Commun. **10**, 3766 (2019).

[5] A. Gruber, A. Drabenstedt, C. Tietz, L. Fleury, J. Wrachtrup, and C. von Borczyskowski, “Scanning confocal optical microscopy and magnetic resonance on single defect centers”, Science **276**, 2012, 2012 (1997).

[6] B. Shields, Q. P. Unterreithmeier, N. P. de Leon, H. Park, and M. D. Lukin, “Efficient readout of a single spin state in diamond via spin-to-charge conversion”, Phys. Rev. Lett. **114**, 136402 (2015).

[7] D. A. Hopper, R. R. Grote, A. L. Exarhos, and L. C. Bassett, “Near-infrared-assisted charge control and spin readout of the nitrogen-vacancy center in diamond”, Phys. Rev. B **94**, 241201 (2016).

[8] L. Robledo, L. Childress, H. Bernien, B. Hensen, P. F. A. Alkemade, and R. Hanson, “High-fidelity projective read-out of a solid-state spin quantum register”, Nature **477**, 574–578 (2011).

[9] D. M. Irber, F. Poggiali, F. Kong, M. Kieschnick, T. Luhmann, D. Kwiatkowski, J. Meojer, J. Du, F. Shi, and F. Reinhard, “Robust all-optical single-shot readout of nitrogen-vacancy centers in diamond”, Nat. Commun. **12**, 532 (2021).

[10] P. J. Scheidegger, S. Diesch, M. L. Palm, and C. L. Degen, “Scanning nitrogen-vacancy magnetometry down to 350 mK”, Appl. Phys. Lett. **120**, 224001 (2022).

[11] D. M. Toyli, D. J. Christle, A. Alkauskas, B. B. Buckley, C. G. van de Walle, and D. D. Awschalom, “Measurement and control of single nitrogen-vacancy center spins above 600K”, Phys. Rev. X **2**, 031001 (2012).

[12] J. R. Maze, P. L. Stanwix, J. S. Hodges, S. Hong, J. M. Taylor, P. Cappellaro, L. Jiang, M. V. G. Dutt, E. Togan, A. S. Zibrov, A. Yacoby, R. L. Walsworth, and M. D. Lukin, “Nanoscale magnetic sensing with an individual electronic spin in diamond”, Nature **455**, 644, 644 (2008).

[13] G. Balasubramanian, I. Y. Chan, R. Kolesov, M. Al-Hmoud, J. Tisler, C. Shin, C. Kim, A. Wojcik, P. R. Hemmer, A. Krueger, T. Hanke, A. Leitenstorfer, R. Bratschitsch, F. Jelezko, and J. Wrachtrup, “Nanoscale imaging magnetometry with diamond spins under ambient conditions”, Nature **455**, 648, 648 (2008).

[14] F. Dolde, H. Fedder, M. W. Doherty, T. Noebauer, F. Rempp, G. Balasubramanian, T. Wolf, F. Reinhard, L. C. L. Hollenberg, F. Jelezko, and J. Wrachtrup, “Electric-field sensing using single diamond spins”, Nat. Phys. **7**, 459–463 (2011).

[15] G. Kucsko, P. C. Maurer, N. Y. Yao, M. Kubo, H. J. Noh, P. K. Lo, H. Park, and M. D. Lukin, “Nanometre-scale thermometry in a living cell”, Nature **500**, 54–58 (2013).

[16] V. M. Acosta, E. Bauch, M. P. Ledbetter, A. Waxman, L. S. Bouchard, and D. Budker, “Temperature dependence of the nitrogen-vacancy magnetic resonance in diamond”, Phys. Rev. Lett. **104**, 070801 (2010).

[17] J. Tisler, T. Oeckinghaus, R. J. Stohr, R. Kolesov, R. Reuter, F. Reinhard, and J. Wrachtrup, “Single defect center scanning near-field optical microscopy on graphene”, Nano Lett. **13**, 3152–3156 (2013).

[18] S. Ernst, D. M. Irber, A. M. Waeber, G. Braunbeck, and F. Reinhard, “A planar scanning probe microscope”, ACS Photonics **6**, 327–331 (2019).

[19] C. Bradley, J. Randall, M. Abobeih, R. Berrevoets, M. Degen, M. Bakker, M. Markham, D. Twitchen, and T. Taminiau, “A ten-qubit solid-state spin register with quantum memory up to one minute”, Phys. Rev. X **9**, 031045 (2019).

[20] M. Pompili, S. L. N. Hermans, S. Baier, H. K. C. Beukers, P. C. Humphreys, R. N. Schouten, R. F. L. Vermeulen, M. J. Tiggelman, L. dos Santos Martins, B. Dirkse, S. Wehner, and R. Hanson, “Realization of a multinode quantum network of remote solid-state qubits”, Science **372**, 259–264 (2021).

[21] B. M. Chernobrod and G. P. Berman, “Spin microscope based on optically detected magnetic resonance”, J. Appl. Phys. **97**, 014903, 014903 (2005).

[22] C. L. Degen, “Scanning magnetic field microscope with a diamond single-spin sensor”, Appl. Phys. Lett. **92**, 243111, 243111 (2008).

[23] J. M. Taylor, P. Cappellaro, L. Childress, L. Jiang, D. Budker, P. R. Hemmer, A.Yacoby, R. Walsworth, and M. D. Lukin, “High-sensitivity diamond magnetometer with nanoscale resolution”, Nat. Phys. **4**, 810, 810 (2008).

[24] P. Maletinsky, S. Hong, M. S. Grinolds, B. Hausmann, M. D. Lukin, R. L. Walsworth, M. Loncar, and A. Yacoby, “A robust scanning diamond sensor for nanoscale imaging with single nitrogen-vacancy centres”, Nat. Nanotechnol. **7**, 320–324 (2012).

[25] L. Rondin, J. P. Tetienne, P. Spinicelli, C. dal Savio, K. Karrai, G. Dantelle, A. Thiaville, S. Rohart, J. F. Roch, and V. Jacques, “Nanoscale magnetic field mapping with a single spin scanning probe magnetometer”, Appl. Phys. Lett. **100**, 153118 (2012).

[26] T. Song, Q. C. Sun, E. Anderson, C. Wang, J. Qian, T. Taniguchi, K. Watanabe, M. A. McGuire, R. Stohr, D. Xiao, T. Cao, J. Wrachtrup, and X. Xu, “Direct visualization of magnetic domains and Moire magnetism in twisted 2D magnets”, Science **374**, 1140–1144 (2021).

[27] Q. Sun, T. Song, E. Anderson, A. Brunner, J. Forster, T. Shalomayeva, T. Taniguchi, K. Watanabe, J. Grafe, R. Stohr, X. Xu, and J. Wrachtrup, “Magnetic domains and domain wall pinning in atomically thin $CrBr_3$ revealed by nanoscale imaging”, Nat. Commun. **12**, 1989 (2021).

[28] L. Thiel, D. Rohner, M. Ganzhorn, P. Appel, E. Neu, B. Muller, R. Kleiner, D. Koelle, and P. Maletinsky, “Quantitative nanoscale vortex imaging using a cryogenic quantum magnetometer”, Nat. Nanotechnol. **11**, 677 (2016).

[29] L. Thiel, Z. Wang, M. A. Tschudin, D. Rohner, I. Gutierrez-lezama, N. Ubrig, M. Gibertini, E. Giannini, A. F. Morpurgo, and P. Maletinsky, “Probing magnetism in 2D materials at the nanoscale with single-spin microscopy”, Science **364**, 973 (2019).

[30] M. Pelliccione, A. Jenkins, P. Ovartchaiyapong, C. Reetz, E. Emmanouilidou, N. Ni, and A. C. B. Jayich, “Scanned probe imaging of nanoscale magnetism at cryogenic temperatures”, Nat. Nanotechnol. **11**, 700–705 (2016).

[31] U. Vool, A. Hamo, G. Varnavides, Y. Wang, T. X. Zhou, N. Kumar, Y. Dovzhenko, Z. Qiu, C. A. C. Garcia, A. T. Pierce, J. Gooth, P. Anikeeva, C. Felser, P. Narang, and A. Yacoby, “Imaging phonon-mediated hydrodynamic flow in WTe_2”, Nat. Phys. **17**, 1216 (2021).

[32] Y. Geng, N. Lee, Y. J. Choi, S. Cheong, and W. Wu, “Collective magnetism at multiferroic vortex domain walls”, Nano Lett. **12**, 6055–6059 (2012).

[33] D. A. Bandurin, I. Torre, R. K. Kumar, M. B. Shalom, A. Tomadin, A. Principi, G. H. Auton, E. Khestanova, K. S. Novoselov, I. V. Grigorieva, L. A. Ponomarenko, A. K. Geim, and M. Polini, “Negative local resistance caused by viscous electron backflow in graphene”, Science **351**, 1055–1058 (2016).

[34] Á. Gali, “Ab initio theory of the nitrogen-vacancy center in diamond”, Nanophotonics **8**, 1907–1943 (2019).

[35] S. Ernst, P. J. Scheidegger, S. Diesch, L. Lorenzelli, and C. L. Degen, “Temperature dependence of photoluminescence intensity and spin contrast in nitrogen-vacancy centers”, Phys. Rev. Lett. **131**, 086903 (2023).

[36] S. Ernst, P. J. Scheidegger, S. Diesch, and C. L. Degen, “Modeling temperature-dependent population dynamics in the excited state of the nitrogen-vacancy center in diamond”, Phys. Rev. B **108**, 085203 (2023).

[37] J. Happacher, J. Bocquel, H. T. Dinani, M. A. Tschudin, P. Reiser, D. A. Broadway, J. R. Maze, and P. Maletinsky, “Temperature dependent photophysics of single NV centers in diamond”, Phys. Rev. Lett. **131**, 086904 (2023).

[38] S. M. Blakley, T. T. Mai, S. J. Moxim, J. T. Ryan, A. J. Biacchi, A. R. H. Walker, and R. D. McMichael, “Spectroscopy of photoionization from the ^1E singlet state in nitrogen-vacancy centers in diamond”, arXiv:2301.10383 (2023).

[39] N. B. Manson, M. S. J. Barson, M. Hedges, P. Singh, S. Stearn, Y. Chen, L. Oberg, C. A. Meriles, and M. W. Doherty, “NV^- with nitrogen”, arXiv:2311.09570 (2023).

[40] L. J. Rogers, R. L. Mcmurtrie, M. J. Sellars, and N. B. Manson, “Time-averaging within the excited state of the nitrogen-vacancy centre in diamond”, New J. Phys. **11**, 063007 (2009).

[41] K. C. Fu, C. Santori, P. E. Barclay, L. J. Rogers, N. B. Manson, and R. G. Beausoleil, "Observation of the dynamic Jahn-Teller effect in the excited states of nitrogen-vacancy centers in diamond", Phys. Rev. Lett. **103**, 256404 (2009).

[42] G. D. Fuchs, V. V. Dobrovitski, D. M. Toyli, F. J. Heremans, C. D. Weis, T. Schenkel, and D. D. Awschalom, "Excited-state spin coherence of a single nitrogen-vacancy centre in diamond", Nat. Phys. **6**, 668–672 (2010).

[43] S. Ernst, *nvratemodel*, GitHub, (2023) `https://github.com/sernstETH/nvratemodel`.

[44] L. Lorenzelli, "Development of a scanning nitrogen-vacancy-center magnetometer for variable temperature experiments", PhD Thesis (ETH Zurich, Zurich, 2021), DOI: 10.3929/ethz-b-000488879.

[45] J. R. Maze, A. Gali, E. Togan, Y. Chu, A. Trifonov, E. Kaxiras, and M. D. Lukin, "Properties of nitrogen-vacancy centers in diamond: the group theoretic approach", New J. Phys. **13**, 025025 (2011).

[46] M. W. Doherty, N. B. Manson, P. Delaney, and L. C. L. Hollenberg, "The negatively charged nitrogen-vacancy centre in diamond: the electronic solution", New J. Phys. **13**, 025019 (2011).

[47] F. Jelezko, T. Gaebel, I. Popa, A. Gruber, and J. Wrachtrup, "Observation of coherent oscillations in a single electron spin", Phys. Rev. Lett. **92**, 076401 (2004).

[48] E. V. Oort, N. Manson, and M. Glasbeek, "Optically detected spin coherence of the diamond n-v center in its triplet ground-state", Journal of Physics C: Solid State Physics **21**, 4385 (1988).

[49] M. Palm, W. Huxter, P. Welter, S. Ernst, P. Scheidegger, S. Diesch, K. Chang, P. Rickhaus, T. Taniguchi, K. Watanabe, K. Ensslin, and C. Degen, "Imaging of submicroampere currents in bilayer graphene using a scanning diamond magnetometer", Phys. Rev. Appl. **17**, 054008 (2022).

[50] C. Degen, F. Reinhard, and P. Cappellaro, "Quantum sensing", Rev. Mod. Phys. **89**, 035002 (2017).

[51] X. D. Chen, C. H. Dong, F. W. Sun, C. L. Zou, J. M. Cui, Z. F. Han, and G. C. Guo, "Temperature dependent energy level shifts of nitrogen-vacancy centers in diamond", Appl. Phys. Lett. **99**, 161903 (2011).

[52] S. Lourette, A. Jarmola, V. M. Acosta, A. G. Birdwell, D. Budker, M. W. Doherty, T. Ivanov, and V. S. Malinovsky, "Temperature sensitivity of ^{14}NV and ^{15}NV ground state manifolds", Phys. Rev. Appl. **19**, 064084 (2023).

[53] J. R. Rabeau, P. Reichart, G. Tamanyan, D. N. Jamieson, S. Prawer, F. Jelezko, T. Gaebel, I. Popa, M. Domhan, and J. Wrachtrup, "Implantation of labelled single nitrogen vacancy centers in diamond using 15n", Appl. Phys. Lett. **88**, 023113, 023113 (2006).

[54] J. F. Barry, M. J. Turner, J. M. Schloss, D. R. Glenn, Y. Song, M. D. Lukin, H. Park, and R. L. Walsworth, "Optical magnetic detection of single-neuron action potentials using quantum defects in diamond", Proc. Natl. Acad. Sci. USA **113**, 14133 (2016).

[55] M. S. Wornle, “Nanoscale scanning diamond magnetometry of antiferromagnets”, PhD Thesis (ETH Zurich, Zurich, 2021), DOI: 10.3929/ethz-b-000488794.

[56] B. K. Ofori-Okai, S. Pezzagna, K. Chang, M. Loretz, R. Schirhagl, Y. Tao, B. A. Moores, K. Groot-Berning, J. Meijer, and C. L. Degen, “Spin properties of very shallow nitrogen vacancy defects in diamond”, Phys. Rev. B **86**, 081406 (2012).

[57] D. Bluvstein, Z. Zhang, and A. C. B. Jayich, “Identifying and mitigating charge instabilities in shallow diamond nitrogen-vacancy centers”, Phys. Rev. Lett. **122**, 076101 (2019).

[58] S. Sangtawesin, B. L. Dwyer, S. Srinivasan, J. J. Allred, L. V. Rodgers, K. D. Greve, A. Stacey, N. Dontschuk, K. M. ODonnell, D. Hu, D. A. Evans, C. Jaye, D. A. Fischer, M. L. Markham, D. J. Twitchen, H. Park, M. D. Lukin, and N. P. de Leon, “Origins of diamond surface noise probed by correlating single-spin measurements with surface spectroscopy”, Phys. Rev. X **9**, 031052 (2019).

[59] P. L. Stanwix, L. M. Pham, J. R. Maze, D. L. sage, T. K. Yeung, P. Cappellaro, P. R. Hemmer, A. Yacoby, M. D. Lukin, and R. L. Walsworth, “Coherence of nitrogen-vacancy electronic spin ensembles in diamond”, Phys. Rev. B **82**, 201201 (2010).

[60] A. Dreau, M. Lesik, L. Rondin, P. Spinicelli, O. Arcizet, J. F. Roch, and V. Jacques, “Avoiding power broadening in optically detected magnetic resonance of single NV defects for enhanced dc magnetic field sensitivity”, Phys. Rev. B **84**, 195204 (2011).

[61] D. A. Hopper, H. J. Shulevitz, and L. C. Bassett, “Spin readout techniques of the nitrogen-vacancy center in diamond”, Micromachines **9**, 437 (2018).

[62] D. P. DiVincenzo, “The physical implementation of quantum computation”, Fortschr. Phys. **48**, 771–783 (2000).

[63] M. Fiebig, T. Lottermoser, and R. V. Pisarev, “Spin-rotation phenomena and magnetic phase diagrams of hexagonal $\mathrm{RMnO_3}$”, J. Appl. Phys. **93**, 8194–8196 (2003).

[64] M. Fiebig, T. Lottermoser, D. Meier, and M. Trassin, “The evolution of multiferroics”, Nat. Rev. Mater. **1**, 16046 (2016).

[65] M. Giraldo, Q. N. Meier, A. Bortis, D. Nowak, N. A. Spaldin, M. Fiebig, M. C. Weber, and T. Lottermoser, “Magnetoelectric coupling of domains, domain walls and vortices in a multiferroic with independent magnetic and electric order”, Nat. Commun. **12**, 3093 (2021).

[66] T. Choi, Y. Horibe, H. T. Yi, Y. J. Choi, W. Wu, and S.-W. Cheong, “Insulating interlocked ferroelectric and structural antiphase domain walls in multiferroic $\mathrm{YMnO_3}$”, Nature Mater. **9**, 253–258 (2010).

[67] C. J. Fennie and K. M. Rabe, “Ferroelectric transition in $\mathrm{YMnO_3}$ from first principles”, Phys. Rev. B **72**, 100103 (2005).

[68] M. Fiebig, T. Lottermoser, D. Frohlich, A. V. Goltsev, and R. V. Pisarev, “Observation of coupled magnetic and electric domains”, Nature **419**, 818–820 (2002).

[69] Y. Geng, H. Das, A. L. Wysocki, X. Wang, S. W. Cheong, M. Mostovoy, C. J. Fennie, and W. Wu, “Direct visualization of magnetoelectric domains”, Nature Mater. **13**, 163–167 (2014).

[70] S. Artyukhin, K. T. Delaney, N. A. Spaldin, and M. Mostovoy, “Landau theory of topological defects in multiferroic hexagonal manganites”, Nature Mater. **13**, 42–49 (2014).

[71] W. S. Huxter, M. F. Sarott, M. Trassin, and C. L. Degen, “Imaging ferroelectric domains with a single-spin scanning quantum sensor”, Nat. Phys. **19**, 644–648 (2023).

[72] P. Welter, “Microscopy of magnetic fields by scanning diamond magnetometry”, PhD Thesis (ETH Zurich, Zurich, 2022), DOI: 10.3929/ethz-b-000530838.

[73] Z. Yan, D. Meier, J. Schaab, R. Ramesh, E. Samulon, and E. Bourret, “Growth of high-quality hexagonal $ErMnO_3$ single crystals by the pressurized floating-zone method”, J. Crystal Growth **409**, 75–79 (2015).

[74] K. Chang, “Scanning magnetometry with NV centers in diamond”, PhD Thesis (ETH Zurich, Zurich, 2017), DOI: 10.3929/ethz-a-010863681.

[75] P. Scheidegger, PhD Thesis (ETH Zurich, Zurich, in preparation).

[76] G. Ctistis, E. H. Frater, S. R. Huisman, J. P. Korterik, J. L. Herek, W. L. Vos, and P. W. H. Pinkse, “Controlling the quality factor of a tuning-fork resonance between 9 and 300 K for scanning-probe microscopy”, J. Phys. D: Appl. Phys. **44**, 375502 (2011).

[77] T. R. Rodríguez and R. García, “Theory of Q control in atomic force microscopy”, Appl. Phys. Lett. **82**, 4821–4823 (2003).

[78] J. Ekin, *Experimental techniques for low-temperature measurements* (Oxford University Press, 2006), DOI: 10.1093/acprof:oso/9780198570547.001.0001.

[79] Montana Instruments, *Cryogenic wiring guide*, Product Documentation, (2021) `https://www.montanainstruments.com/support/product-documentation`.

[80] L. M. García, J. Chaboy, F. Bartolomé, and J. B. Goedkoop, “Orbital magnetic moment instability at the spin reorientation transition of $Nd_2Fe_{14}B$”, Phys. Rev. Lett. **85**, 429–432 (2000).

[81] Montana Instruments, *Cryogenic sample mounting guide*, Product Documentation, (2021) `https://www.montanainstruments.com/support/product-documentation`.

[82] Bossard Group, *Torque and preload calculator*, Online Calculators and Converters, (2024) `https://www.bossard.com/global-en/assembly-technology-expert/technical-information-and-tools/online-calculators-and-converters/torque-and-preload-calculator/`.

[83] J. Frolec, T. Králík, V. Musilová, P. Hanzelka, A. Srnka, and J. Jelínek, “A database of metallic materials emissivities and absorptivities for cryogenics”, Cryogenics **97**, 85–99 (2019).

[84] C. G. Smith and G. Lewin, “Free molecular conductance of a cylindrical tube with wall sorption”, J. Vac. Sci. Technol. **3**, 92–95 (1966).

[85] T. J. Sato, S. .-. Lee, T. Katsufuji, M. Masaki, S. Park, J. R. D. Copley, and H. Takagi, “Unconventional spin fluctuations in the hexagonal antiferromagnet $YMnO_3$”, Phys. Rev. B **68**, 014432 (2003).

[86] L. Robledo, H. Bernien, T. van der Sar, and R. Hanson, “Spin dynamics in the optical cycle of single nitrogen-vacancy centres in diamond”, New J. Phys. **13**, 025013 (2011).

[87] N. Manson, J. Harrison, and M. Sellars, “Nitrogen-vacancy center in diamond: model of the electronic structure”, Phys. Rev. B **74**, 104303 (2006).

[88] P. Tamarat, N. B. Manson, J. P. Harrison, R. L. McMurtrie, A. Nizovtsev, C. Santori, R. G. Beausoleil, P. Neumann, T. Gaebel, F. Jelezko, P. Hemmer, and J. Wrachtrup, “Spin-flip and spin-conserving optical transitions of the nitrogen-vacancy centre in diamond”, New J. Phys. **10**, 045004 (2008).

[89] A. Batalov, V. Jacques, F. Kaiser, P. Siyushev, P. Neumann, L. J. Rogers, R. L. McMurtrie, N. B. Manson, F. Jelezko, and J. Wrachtrup, “Low temperature studies of the excited-state structure of negatively charged nitrogen-vacancy color centers in diamond”, Phys. Rev. Lett. **102**, 195506 (2009).

[90] T. Plakhotnik, M. W. Doherty, J. H. Cole, R. Chapman, and N. B. Manson, “All-optical thermometry and thermal properties of the optically detected spin resonances of the NV– center in nanodiamond”, Nano Lett. **14**, 4989–4996 (2014).

[91] T. A. Abtew, Y. Y. Sun, B. Shih, P. Dev, S. B. Zhang, and P. Zhang, “Dynamic Jahn-Teller effect in the NV^- center in diamond”, Phys. Rev. Lett. **107**, 146403 (2011).

[92] M. L. Goldman, A. Sipahigil, M. W. Doherty, N. Y. Yao, S. D. Bennett, M. Markham, D. J. Twitchen, N. B. Manson, A. Kubanek, and M. D. Lukin, “Phonon-induced population dynamics and intersystem crossing in nitrogen-vacancy centers”, Phys. Rev. Lett. **114**, 145502 (2015).

[93] M. L. Goldman, M. W. Doherty, A. Sipahigil, N. Y. Yao, S. D. Bennett, N. B. Manson, A. Kubanek, and M. D. Lukin, “State-selective intersystem crossing in nitrogen-vacancy centers”, Phys. Rev. B **91**, 165201 (2015).

[94] M. L. Goldman, M. W. Doherty, A. Sipahigil, N. Y. Yao, S. D. Bennett, N. B. Manson, A. Kubanek, and M. D. Lukin, “Erratum: state-selective intersystem crossing in nitrogen-vacancy centers [Phys. Rev. B 91, 165201 (2015)]”, Phys. Rev. B **96**, 039905 (2017).

[95] J. Happacher, D. A. Broadway, J. Bocquel, P. Reiser, A. Jimenéz, M. A. Tschudin, L. Thiel, D. Rohner, M. l. G. Puigibert, B. Shields, J. R. Maze, V. Jacques, and P. Maletinsky, “Low-temperature photophysics of single nitrogen-vacancy centers in diamond”, Phys. Rev. Lett. **128**, 177401 (2022).

[96] J. Tetienne, L. Rondin, P. Spinicelli, M. Chipaux, T. Debuisschert, J. Roch, and V. Jacques, “Magnetic-field-dependent photodynamics of single NV defects in diamond: an application to qualitative all-optical magnetic imaging”, New J. Phys. **14**, 103033 (2012).

[97] L. C. Bassett, F. J. Heremans, C. G. Yale, B. B. Buckley, and D. D. Awschalom, “Electrical tuning of single nitrogen-vacancy center optical transitions enhanced by photoinduced fields”, Phys. Rev. Lett. **107**, 266403 (2011).

[98] K. W. Lee, D. Lee, P. Ovartchaiyapong, J. Minguzzi, J. R. Maze, and A. C. B. Jayich, "Strain coupling of a mechanical resonator to a single quantum emitter in diamond", Phys. Rev. Applied **6**, 034005 (2016).

[99] L. C. Bassett, F. J. Heremans, D. J. Christle, C. G. Yale, G. Burkard, B. B. Buckley, and D. D. Awschalom, "Ultrafast optical control of orbital and spin dynamics in a solid-state defect", Science **345**, 1333–1337 (2014).

[100] N. Kalb, P. C. Humphreys, J. J. Slim, and R. Hanson, "Dephasing mechanisms of diamond-based nuclear-spin memories for quantum networks", Phys. Rev. A **97**, 062330 (2018).

[101] R. Ulbricht, S. Dong, I. Chang, B. M. K. Mariserla, K. M. Dani, K. Hyeon-Deuk, and Z. Loh, "Jahn-teller-induced femtosecond electronic depolarization dynamics of the nitrogen-vacancy defect in diamond", Nat. Commun. **7**, 13510 (2016).

[102] A. Gupta, L. Hacquebard, and L. Childress, "Efficient signal processing for time-resolved fluorescence detection of nitrogen-vacancy spins in diamond", J. Opt. Soc. Am. B **33**, B28–B34 (2016).

[103] P. Reineck, L. F. Trindade, J. Havlik, J. Stursa, A. Heffernan, A. Elbourne, A. Orth, M. Capelli, P. Cigler, D. A. Simpson, and B. C. Gibson, "Not all fluorescent nanodiamonds are created equal: a comparative study", Particle & Particle Systems Characterization **36**, 1900009 (2019).

[104] G. Thiering and A. Gali, "Theory of the optical spin-polarization loop of the nitrogen-vacancy center in diamond", Phys. Rev. B **98**, 085207 (2018).

[105] D. Manzano, "A short introduction to the lindblad master equation", AIP Advances **10**, 025106 (2020).

[106] J. Johansson, P. Nation, and F. Nori, "Qutip 2: a python framework for the dynamics of open quantum systems", Computer Physics Communications **184**, 1234–1240 (2013).

[107] G. D. Fuchs, A. L. Falk, V. V. Dobrovitski, and D. D. Awschalom, "Spin coherence during optical excitation of a single nitrogen-vacancy center in diamond", Phys. Rev. Lett. **108**, 157602 (2012).

[108] D. Wirtitsch, G. Wachter, S. Reisenbauer, M. Gulka, V. Ivády, F. Jelezko, A. Gali, M. Nesladek, and M. Trupke, "Exploiting ionization dynamics in the nitrogen vacancy center for rapid, high-contrast spin, and charge state initialization", Phys. Rev. Research **5**, 013014 (2023).

[109] M. B. Walker, "A T^5 spin–lattice relaxation rate for non-Kramers ions", Canadian Journal of Physics **46**, 1347–1353 (1968).

[110] T. Plakhotnik, M. W. Doherty, and N. B. Manson, "Electron-phonon processes of the nitrogen-vacancy center in diamond", Phys. Rev. B **92**, 081203 (2015).

[111] P. Pavone, K. Karch, O. Schütt, D. Strauch, W. Windl, P. Giannozzi, and S. Baroni, "Ab initio lattice dynamics of diamond", Phys. Rev. B **48**, 3156–3163 (1993).

[112] H. J. McSkimin and J. Andreatch P., "Elastic moduli of diamond as a function of pressure and temperature", J. Appl. Phys. **43**, 2944–2948 (1972).

[113] T. Zhu, J. Rhensius, K. Herb, V. Damle, G. Puebla-Hellmann, C. L. Degen, and E. Janitz, “Multicone diamond waveguides for nanoscale quantum sensing”, Nano Lett. **23**, 10110–10117 (2023).

[114] J. Li, M. P. Silveri, K. S. Kumar, J.-M. Pirkkalainen, A. Vepsäläinen, W. C. Chien, J. Tuorila, M. A. Sillanpää, P. J. Hakonen, E. V. Thuneberg, and G. S. Paraoanu, “Motional averaging in a superconducting qubit”, Nat. Commun. **4**, 1420 (2013).

[115] C. Gardiner and P. Zoller, “The stochastic schrodinger equation”, in *Quantum noise: a handbook of markovian and non-markovian quantum stochastic methods with applications to quantum optics*, Springer Series in Synergetics (Springer, Berlin, Heidelberg, 2004), pp. 341–396.

[116] C. P. Slichter, “Spin-lattice relaxation and motional narrowing of resonance lines”, in *Principles of magnetic resonance*, Springer Series in Solid-State Sciences (Springer, Berlin, Heidelberg, 1990), pp. 145–218, DOI: 10.1007/978-3-662-09441-9_5.

[117] G. D. Fuchs, V. V. Dobrovitski, R. Hanson, A. Batra, C. D. Weis, T. Schenkel, and D. D. Awschalom, “Excited-state spectroscopy using single spin manipulation in diamond”, Phys. Rev. Lett. **101**, 117601 (2008).

[118] P. Neumann, R. Kolesov, V. Jacques, J. Beck, J. Tisler, A. Batalov, L. Rogers, N. B. Manson, G. Balasubramanian, F. Jelezko, and J. Wrachtrup, “Excited-state spectroscopy of single NV defects in diamond using optically detected magnetic resonance”, New J. Phys. **11**, 013017 (2009).

[119] A. Hilberer, L. Toraille, C. Dailledouze, M.-P. Adam, L. Hanlon, G. Weck, M. Schmidt, P. Loubeyre, and J.-F. Roch, “Enabling quantum sensing under extreme pressure: nitrogen-vacancy magnetometry up to 130 GPa”, Phys. Rev. B **107**, L220102 (2023).

[120] M. Lesik, T. Plisson, L. Toraille, J. Renaud, F. Occelli, M. Schmidt, O. Salord, A. Delobbe, T. Debuisschert, L. Rondin, P. Loubeyre, and J.-F. Roch, “Magnetic measurements on micrometer-sized samples under high pressure using designed NV centers”, Science **366**, 1359–1362 (2019).

[121] Y. Chu, N. D. leon, B. Shields, B. Hausmann, R. Evans, E. Togan, M. J. Burek, M. Markham, A. Stacey, A. Zibrov, A. Yacoby, D. Twitchen, M. Loncar, H. Park, P. Maletinsky, and M. Lukin, “Coherent optical transitions in implanted nitrogen vacancy centers”, Nano Lett. **14**, 1982–1986 (2014).

[122] D. F. Wise, “Could NV centres in diamond be used to measure donor spins in silicon?”, PhD Thesis (University College London, London, 2021).

[123] E. Kupce and R. Freeman, “Adiabatic pulses for wideband inversion and broadband decoupling”, Journal of Magnetic Resonance, Series A **115**, 273–276 (1995).

[124] N. Aslam, G. Waldherr, P. Neumann, F. Jelezko, and J. Wrachtrup, “Photo-induced ionization dynamics of the nitrogen vacancy defect in diamond investigated by single-shot charge state detection”, New Journal Of Physics **15**, 013064 (2013).

[125] S. Baier, C. Bradley, T. Middelburg, V. Dobrovitski, T. Taminiau, and R. Hanson, "Orbital and spin dynamics of single neutrally-charged nitrogen-vacancy centers in diamond", Phys. Rev. Lett. **125**, 193601 (2020).

[126] D. A. Craik, P. Kehayias, A. Greenspon, X. Zhang, M. Turner, J. Schloss, E. Bauch, C. Hart, E. Hu, and R. Walsworth, "Microwave-assisted spectroscopy technique for studying charge state in nitrogen-vacancy ensembles in diamond", Phys. Rev. Applied **14**, 014009 (2020).

[127] J. Jeske, D. W. M. Lau, X. Vidal, L. P. McGuinness, P. Reineck, B. C. Johnson, M. W. Doherty, J. C. McCallum, S. Onoda, F. Jelezko, T. Ohshima, T. Volz, J. H. Cole, B. C. Gibson, and A. D. Greentree, "Stimulated emission from nitrogen-vacancy centres in diamond", Nat. Commun. **8**, 14000 (2017).

[128] L. Rondin, G. Dantelle, A. Slablab, F. Grosshans, F. Treussart, P. Bergonzo, S. Perruchas, T. Gacoin, M. Chaigneau, H. Chang, V. Jacques, and J. Roch, "Surface-induced charge state conversion of nitrogen-vacancy defects in nanodiamonds", Phys. Rev. B **82**, 115449 (2010).

[129] P. Welter, J. Rhensius, A. Morales, M. S. Wornle, C.-H. Lambert, G. Puebla-Hellmann, P. Gambardella, and C. L. Degen, "Scanning nitrogen-vacancy center magnetometry in large in-plane magnetic fields", Appl. Phys. Lett. **120**, 074003 (2022).

[130] S. K. Lam, A. Pitrou, and S. Seibert, "Numba: a LLVM-based python JIT compiler", in Proceedings of the second workshop on the LLVM compiler infrastructure in HPC, LLVM '15 (2015), pp. 1–6, DOI: 10.1145/2833157.2833162.

[131] P. Virtanen, R. Gommers, T. E. Oliphant, M. Haberland, T. Reddy, D. Cournapeau, E. Burovski, P. Peterson, W. Weckesser, J. Bright, S. J. van der Walt, M. Brett, J. Wilson, K. J. Millman, N. Mayorov, A. R. J. Nelson, E. Jones, R. Kern, E. Larson, C. J. Carey, İ. Polat, Y. Feng, E. W. Moore, J. VanderPlas, D. Laxalde, J. Perktold, R. Cimrman, I. Henriksen, E. A. Quintero, C. R. Harris, A. M. Archibald, A. H. Ribeiro, F. Pedregosa, P. van Mulbregt, and SciPy 1.0 Contributors, "SciPy 1.0: Fundamental Algorithms for Scientific Computing in Python", Nature Methods **17**, 261–272 (2020).

[132] R. Monge, T. Delord, G. Thiering, Á. Gali, and C. Meriles, "Resonant versus nonresonant spin readout of a nitrogen-vacancy center in diamond under cryogenic conditions", Phys. Rev. Lett. **131**, 236901 (2023).

[133] T. Gaebel, M. Domhan, C. Wittmann, I. Popa, F. Jelezko, J. Rabeau, A. Greentree, S. Prawer, E. Trajkov, P. Hemmer, and J. Wrachtrup, "Photochromism in single nitrogen-vacancy defect in diamond", Appl. Phys. B **82**, 243–246 (2006).

[134] R. Fischer, C. O. Bretschneider, P. London, D. Budker, D. Gershoni, and L. Frydman, "Bulk nuclear polarization enhanced at room temperature by optical pumping", Phys. Rev. Lett. **111**, 057601 (2013).

[135] F. Poggiali, P. Cappellaro, and N. Fabbri, "Measurement of the excited-state transverse hyperfine coupling in NV centers via dynamic nuclear polarization", Phys. Rev. B **95**, 195308 (2017).

[136] J. T. Oon, J. Tang, C. A. Hart, K. S. Olsson, M. J. Turner, J. M. Schloss, and R. L. Walsworth, "Ramsey envelope modulation in NV diamond magnetometry", Physical Review B **106**, 054110 (2022).

[137] G. Petrini, E. Moreva, E. Bernardi, P. Traina, G. Tomagra, V. Carabelli, I. P. Degiovanni, and M. Genovese, "Is a quantum biosensing revolution approaching? perspectives in NV-assisted current and thermal biosensing in living cells", Adv. Quantum Technol. **3**, 2000066 (2020).

[138] T. Zhang, G. Pramanik, K. Zhang, M. Gulka, L. Wang, J. Jing, F. Xu, Z. Li, Q. Wei, P. Cigler, and Z. Chu, "Toward quantitative bio-sensing with nitrogen–vacancy center in diamond", ACS Sens. **6**, 2077–2107 (2021).

[139] J. Aspinall, S. O. Adekanye, I. Brown, A. R. Dhawan, and J. M. Smith, "Instabilities in nanodiamond nitrogen-vacancy centre single photon sources under prolonged pulsed excitation", Opt. Mater. Express **10**, 332–341 (2020).

[140] S. Parthasarathy, M. Joos, L. B. Hughes, S. A. Meynell, T. A. Morrison, J. D. Risner-Jamtgaard, D. M. Weld, K. Mukherjee, and A. C. B. Jayich, "Role of oxygen in laser induced contamination at diamond-vacuum interfaces", arXiv:2401.06942 (2024).

[141] E. Bourgeois, A. Jarmola, P. Siyushev, M. Gulka, J. Hruby, F. Jelezko, D. Budker, and M. Nesladek, "Photoelectric detection of electron spin resonance of nitrogen-vacancy centres in diamond", Nat. Commun. **6**, 8577 (2015).

[142] S. Wolf, I. Meirzada, G. Haim, and N. Bar-Gill, "Nitrogen-vacancy singlet-manifold ionization energy", Phys. Rev. Applied **19**, 034076 (2023).

[143] Y. Song, Y. Tian, Z. Hu, F. Zhou, T. Xing, D. Lu, B. Chen, B. Chen, Y. Wang, Y. Wang, Y. Wang, N. Xu, N. Xu, J. Du, J. Du, J. Du, and J. Du, "Pulse-width-induced polarization enhancement of optically pumped N-V electron spin in diamond", Photon. Res. **8**, 1289–1295 (2020).

Curriculum vitae

Personal data

Name	Stefan Ernst
Date of Birth	July 24th, 1991
Nationality	German
Email	sternst@ethz.ch

Education

2018 – 2024	**ETH Zürich**, *Zurich, Switzerland* Doctoral student in Physics Spin Physics group (Laboratory for Solid State Physics)
2014 – 2017	**Technische Universität München (TUM)**, *Munich, Germany* Master of Science in Condensed Matter Physics
2011 – 2014	**Technische Universität München (TUM)**, *Munich, Germany* Bachelor of Science in Physics

Awards

2018	Award for Best Thesis 2018 *Walter Schottky Institut (TUM)*
2018	Shortlisted Candidate for Nano Innovation Award 2018 *Center for NanoScience (LMU)*

List of publications

1. S. Ernst, D. M. Irber, A. M. Waeber, G. Braunbeck, and F. Reinhard, “A planar scanning probe microscope”, *ACS Photonics* **6**, 327–331 (2019).

2. M. L. Palm[†], W. S. Huxter[†], P. Welter, S. Ernst, P. J. Scheidegger, S. Diesch, K. Chang, P. Rickhaus, T. Taniguchi, K. Watanabe, K. Ensslin, and C. L. Degen. “Imaging of submicroampere currents in bilayer graphene using a scanning diamond magnetometer”. *Phys. Rev. Applied* **17**, 054008 (2022).

3. S. Ernst[†], P. J. Scheidegger[†], S. Diesch, L. Lorenzelli, and C. L. Degen, “Temperature dependence of photoluminescence intensity and spin contrast in nitrogenvacancy centers”, *Phys. Rev. Lett.* **131**, 086903 (2023).

4. S. Ernst[†], P. J. Scheidegger[†], S. Diesch, and C. L. Degen, “Modeling temperaturedependent population dynamics in the excited state of the nitrogen-vacancy center in diamond”, *Phys. Rev. B* **108**, 085203 (2023).

[†]: These authors contributed equally.

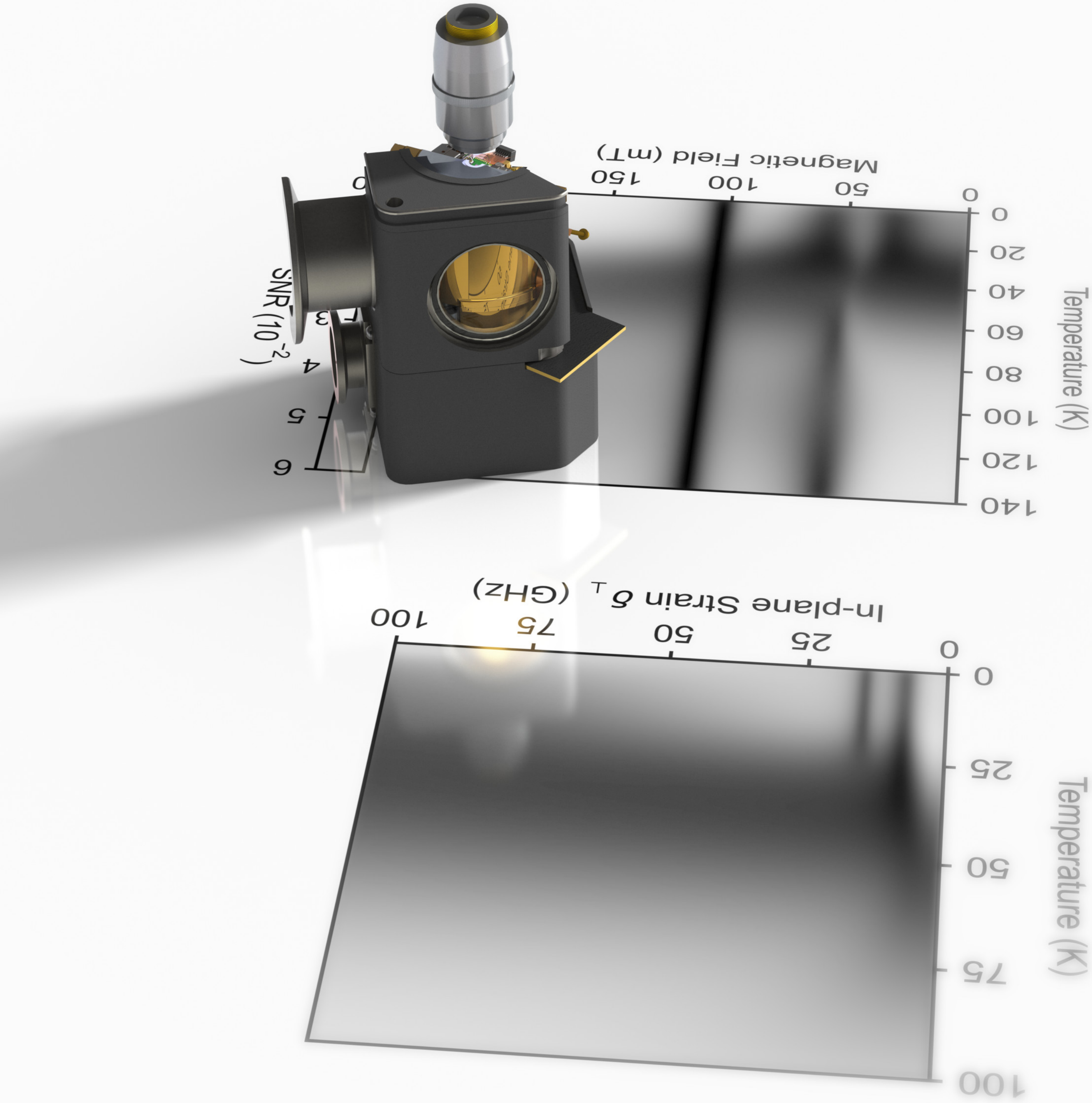
Magnetic Field (mT)
0
50
100
150
0
Temperature (K)
0
20
40
60
80
100
120
140
SNR (10^-2)
3
4
5
6
In-plane Strain δ⊥ (GHz)
0
25
50
75
100
Temperature (K)
0
25
50
75
100